High-multiplicity space-division multiplexed transmission systems

High-Multiplicity Space-Division Multiplexed Transmission Systems

PROEFSCHRIFT

ter verkrijging van de graad van doctor aan de Technische Universiteit Eindhoven, op gezag van de rector magnificus prof.dr.ir. F. P. T. Baaijens, voor een commissie aangewezen door het College voor Promoties, in het openbaar te verdedigen op woensdag 9 oktober 2019 om 13:30 uur

door

John Johannes Arnoldus van Weerdenburg

geboren te West Maas en Waal

Dit proefschrift is goedgekeurd door de promotoren en de samenstelling van de promotiecommissie is als volgt:

voorzitter:	prof.dr.ir. P.M.J. van den Hof
1e promotor:	dr.ir. H. de Waardt
2e promotor:	prof.ir. A.M.J. Koonen
copromotor:	dr. C.M. Okonkwo
leden:	prof.dr.-ing. N. Hanik (Technische Universität München)
	prof.dr. S. Randel (Karlsruhe Institute of Technology)
	dr. J.J.G.M van der Tol
	dr. R. Ryf (Nokia Bell Labs, Crawford Hill, USA)

Het onderzoek of ontwerp dat in dit proefschrift wordt beschreven is uitgevoerd in overeenstemming met de TU/e Gedragscode Wetenschapsbeoefening.

A catalogue record is available from the Eindhoven University of Technology library.

High-Multiplicity Space-Division Multiplexed Transmission Systems
Author: J.J.A. (John) van Weerdenburg
Eindhoven University of Technology, 2019
ISBN: 978-90-386-4860-6
NUR: 959

Keywords: Optical fiber communication / Space division multiplexing / Digital signal processing / Modulation

This work was performed in the Electro-optical communications (ECO) group at the department of Electrical Engineering at Eindhoven University of Technology.

This work was partially funded by "de Nederlandse Organisatie voor Wetenschappelijk Onderzoek" (NWO) Photonics Graduate programme under grant 022.005.011.

Typeset using LaTeX
printed by ADC Dereumaux, Eindhoven, the Netherlands

Summary

High-Spatial Multiplicity Space-Division Multiplexed Transmission Systems

The modern information-driven society ever increasing demand for bandwidth has been supported by rapid technological advancements in the field of optical fibre communications. The low-attenuation and lack of modal dispersion led to the vast deployment of optical connections based on single-mode fibres. Within the available optical amplification band, digital signal processing has been exploited to improve spectral efficiency by increasing the modulation order and symbol rate as well as utilize both polarizations. Due to the nonlinear material properties of optical fibres, a maximum achievable capacity is in the order of 100 terabit/s. Meanwhile, the compound annual growth rate (CAGR) of data traffic continues at 20 % to 60 %, at several points in the optical communication network.

Addressing the impending capacity crunch is a subject of ongoing research in the field of optical fibre communications. A straight-forward approach of operating multiple parallel single-mode systems would result in an approximate linear scaling in cost per bit, which rapidly becomes unsustainable with exponential growth in demand. Space-division multiplexing (SDM) techniques exploiting multiple cores, modes and combinations thereof has been proposed as a solution for increasing capacity within a single fibre. The potential integration of fibres, transceivers and other system components can lead to a reduction in cost per bit which scales with the number of channels. Hence, this thesis focuses on the characterisation and analysis of components and fibres for space-division multiplexing and their evaluation in both short-reach and long-distance transmission systems.

These novel fibre designs introduce new challenges and impairments to optical fibre communications. One challenge is managing or unravelling spatial channel crosstalk introduced during propagation and by other system components such as spatial multiplexers, optical amplifiers, and switches. Minimizing this crosstalk allows independent operation of spatial channels employing conventional polarisation-

multiplexed coherent transceivers. This low crosstalk regime can be realised by ensuring significant spatial separation of the spatial channels, i.e. core pitch in a multi-core fibre.

Alternatively, the typically larger spatial channel mixing occurring in mode division multiplexed transmission over few-mode or multi-mode fibres is resolved by digital signal processing algorithms. As computational complexity increases with the number of spatial channels and contribution of transmission effects, managing this complexity is key towards future deployment of SDM technology. For optimal performance of these algorithms, the complete impulse response needs to be available in the digital domain. differential mode group delay (DMGD) as a result of the different propagation speeds of the individual channels, broadens this impulse response, thereby imposing memory requirements of the digital receiver. Furthermore, differences in losses between the spatial channels referred to as mode dependent loss (MDL) is a fundamental capacity limiting impairment.

A key aspect of this thesis is the detailed understanding of the sources of transmission impairments both at component and system level. For characterization of components and subsystems, an optical vector network analyser (OVNA) has been developed, which is capable of measuring linear device parameters, which includes MDL and DMGD. This instrument can measure the frequency transfer function matrix and time domain impulse response matrix for the C- and L-wavelength bands in a single measurement with both high temporal and spectral resolution as well as high dynamic range. This measurement technique is applied in the characterization process of multi-mode and few-mode multi-core fibres and components.

The thesis also addresses multiple transmission experiments employing SDM, both for single span (<80 km) reach and concatenated longer amplified transmission distances. The first-ever transmission of 10 spatial modes in a few-mode fibre has been investigated, which can increase the capacity of a single fibre by one order of magnitude. In addition, the enabling components and transmission techniques by a combination of spatial (de)multiplexers with low MDL, of a low DMGD 6-LP few-mode fibre and of advanced digital signal processing is provided. A similar data rate was transmitted over 50 µm core diameter multi-mode fibre, which can support up to 55 spatial mode channels.

The final part of the thesis addresses the work to further demonstrate the increased transmission capacity of SDM fibres. By placing few-mode fibre spans in a recirculating loop setup, two record capacity × distance transmission experiments were achieved: 138 Tbit/s 6-mode transmission over 590 km and 2400 km transmission over 3-mode fibre. The performance analyses of these systems are addressed in detail.

In summary, this thesis demonstrates the rapid progress of space division multiplexing and its potential to provide a breakthrough in addressing the capacity limits in currently deployed optical transmission systems.

Table of Contents

Chapter 1

Introduction

In this introductory chapter, the motivation for high-multiplicity space-division multiplexed optical transmission systems will be explained by discussing the impact of the growing demand for bandwidth on telecommunication systems. The evolution of telecommunication systems towards the optical fibre infrastructure of today will be provided. Next, a brief overview of the topics covered in the following chapters is presented. Finally, a summary of the author's contribution and acknowledgements will be given at the end of this chapter.

1.1 Motivation

Telecommunication, or the exchange of information at a distance, has progressed enormously from the fire signals used by ancient Greece to the modern smartphone users of today. Prior to the introduction of electrical systems, communication was generally limited by line of sight and small alphabet sizes. This changed with the invention of the electrical telegraph by Samuel Morse in 1838, followed by two other important inventions that shaped the field of communications of the 19th century. These inventions were the telephone by Alexander Graham Bell in 1876, and Marconi's radio in 1896.

Halfway through the twentieth century, worldwide telephone networks based on wire pairs were replaced by coaxial cables, increasing the bandwidth to support 300 voice channels. However, the high attenuation of such cables required a small repeater spacing, which sparked the introduction of microwave communication, where data is modulated onto an electrical carrier wave of several GHz. As the bitrate was limited for higher carrier frequencies, both systems had a comparable bit-rate-distance product limited to approximately $100\,\text{Mbit/s} \times \text{km}$.

An increase in the bit-rate-distance product of several orders of magnitude was foreseen by employing optical waves with frequencies in the order of hundred of THz as carriers. However, no coherent light source and suitable medium were available in the 1950s. The first issue was resolved by the invention of the semiconductor

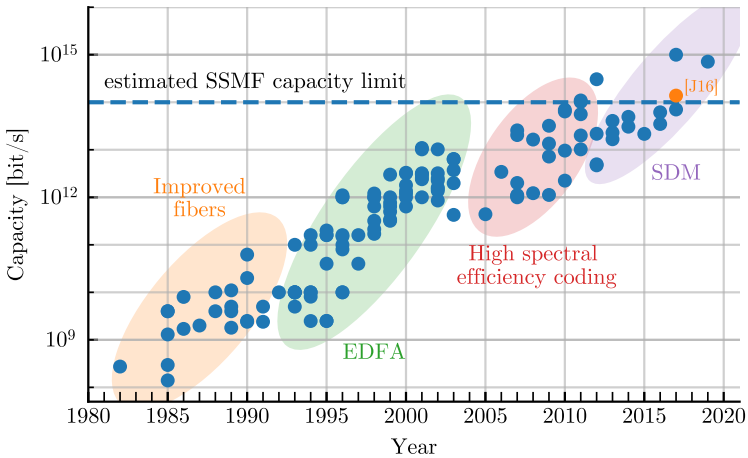

Figure 1.1: Capacity of transmission results presented in post-deadline sessions. Roughly each decade a new technology emerges that results in exponential growth in capacity. Figure after [4].

optical laser in 1960 [1]. The development of optical fibres took an additional 10 years [2], after its proposal in 1966 [3]. The optical fibre not only provided more bandwidth but also offered a 10 times increase in repeater spacing. Furthermore, smaller footprint and lower weight simplified installation. These factors led to the rapid evolution from electrical-based communication towards the highly cost-efficient low power consumption of multi-mode optical fibre systems.

The capacity of optical fibre systems has rapidly developed over the last 40 years, as can be seen from the reported transmission experiments at post-deadline sessions at the Optical Fiber Communication Conference (OFC) and the European Conference on Optical Communication (ECOC) shown in Fig. 1.1. Since the first introduction of lightwave systems, the capacity-distance product has roughly increased by a factor of four every ten years. This exponential growth has been supported by various technological improvements. The first being the transition from the 800 nm transmission window towards the lower attenuation and minimum dispersion range around 1310 nm in the 1970s. However, with increasing bit rates, the modal dispersion amongst other factors becomes a capacity limiting factor. Therefore, single-mode fibres swiftly replaced multi-mode fibres from 1986 onwards for long-distance communication. It was discussed that the minimum attenuation in silica optical fibres is around 1550 nm [5]. However, the high chromatic dispersion delayed the transition to this transmission window until the introduction of single-mode lasers and dispersion-shifted fibres, which have their minimum dispersion around 1550 nm. To further increase the repeater distance beyond 60 km, coherent transmission systems were proposed. In this type of systems, a high power local oscillator is employed to improve the sensitivity of the receiver. Furthermore,

it would enable quadrature modulation at the transmitter as both cosine (real) and sine (imaginary) components of the optical carrier could be exploited. Moreover, digital dispersion compensation can be exploited, thereby averting the undesired nonlinear properties of dispersion-shifted fibre and dispersion compensation modules. Due to the more complex receiver architecture, the introduction of coherent systems was postponed, as the discovery of optical amplifiers led to a more efficient method to improve system capacity [6, 7]. Besides increasing repeater spacing, optical amplifiers are capable of amplifying multiple wavelength channels simultaneously. This wavelength-division multiplexing (WDM) technology boosted optical fibre capacity with unseen growth, as it roughly doubled every 6 months in the early 1990s.

The erbium doped fibre amplifier (EDFA) rapidly became the most popular optical amplifier type for long-distance fibre communication, as it enabled repeaterless pure optical transoceanic links. However, for conventional C-band EDFAs, the gain spectrum is limited to 4.4 THz. After exhausting the available spectrum, increasing the spectral efficiency became the next endeavour towards a capacity increase in the first decade of this millennium. Additional capacity was unlocked through the introduction of digital signal processing, which enabled higher-order modulation formats that carry multiple bits in each symbol, pulse shaping to reduce gaps between adjacent WDM channels, the exploitation of both polarizations of light, and advanced forward error correction codes.

The rapid pace at which capacity of optical fibre systems developed has been pushed by an exponentially growing demand for bandwidth by emerging applications. One of the more recent drivers is video streaming services, which rapidly overtook user-generated data from web browsing and file sharing as video qual-

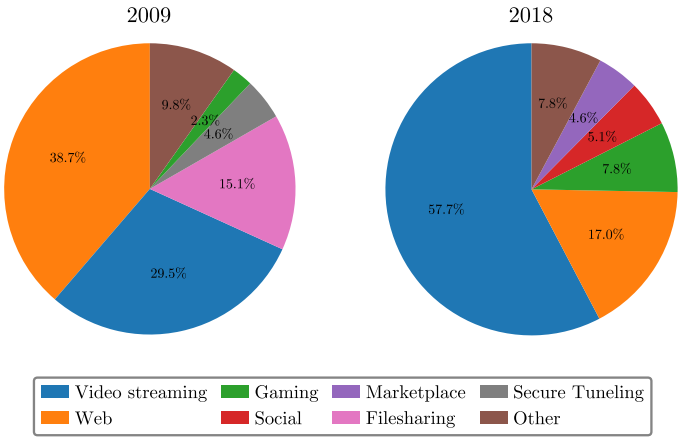

Figure 1.2: Composition of global internet traffic in 2009 [8] and 2018 [9].

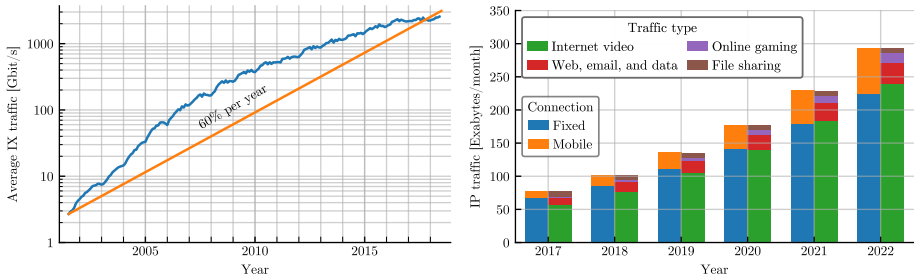

(a) (b)

Figure 1.3: (a) Monthly internet traffic passing through the Amsterdam Internet Exchange (AMS-IX) over the past 16 years [11], showing an average annual growth of 60 %. (b) Monthly IP traffic generated by fixed and mobile connections [10], showing a steady 22 % growth of user generated traffic.

ity increased in the 2010s. Figure 1.2 shows the five applications responsible for largest contribution towards user-generated internet protocol (IP) traffic in 2009 and 2018. Although already clearly present in 2009, video streaming dominates the user-generated traffic in 2018, thereby diminishing the impact of web browsing and file sharing. As of 2018, 58 % of downstream traffic is consumed by streaming platforms such as Netflix (14.97 %), Youtube (11.35 %), and other platforms (13.07 %) [9]. With the focus on cloud services and computing, machine-to-machine traffic (not included in Fig. 1.2) is increasing at a tremendous pace which is expected to be boosted with the enormous amount of connections from emerging Internet of Things (IOT) applications [10].

Although it is challenging to predict the next dominant traffic generator, a lot of effort is taken into predicting compound annual growth rates (CAGRs) based on monitoring data flows. An example is given by Fig. 1.3a, which shows the monthly data passing through the Amsterdam Internet Exchange (AMS-IX) over the last 16 years [11]. After an astonishing growth of almost 120 % from 2002 to 2008, it saturated to 30 % annual increase of traffic, resulting in a yearly average of 60 %. CAGR ranging from 20 % to 60 % are observed at various points in the optical networks [12]. A similar trend is observed from the yearly presented forecast by Cisco, reporting an approximate 25 % monthly increase in traffic. The latest forecast is shown in Fig. 1.3b. It predicts almost 300 ExaByte of user-generated traffic by 2022 based on available statistics from 2017 and 2018 [10]. Observe that a continuing growth for internet video is expected, as well as a shift from fixed connections toward mobile with the introduction of 5G networks.

Although the exact growth rate can vary, numerous sources predict an exponential increase in traffic, which require the capacity of optical fibres to scale accordingly. This can be realised by more efficient use of the five physical properties available for multiplexing in optical fibres: time, quadrature, frequency,

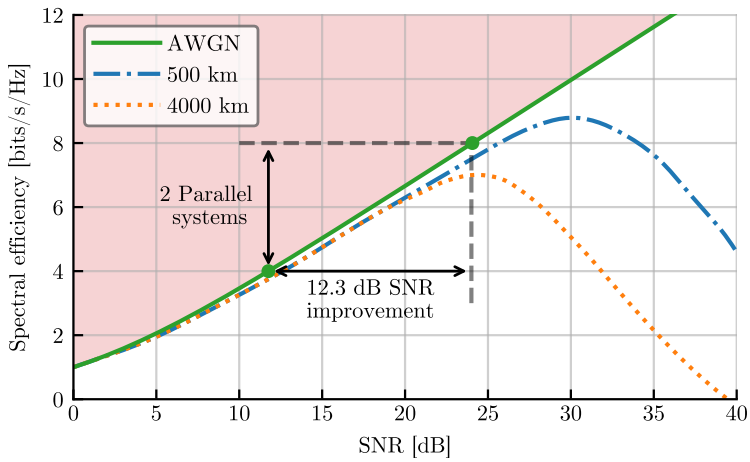

Figure 1.4: Spectral efficiency of the AWGN and single-mode optical fibre channels of lengths 500 km and 4000 km [13]. The shaded area is inaccessible without parallelism. Two options to double the spectral efficiency of an exemplary system are given.

polarisation, and space. By applying Shannon's theorem to describe the maximum information that can be transmitted over an additive white Gaussian noise (AWGN) as upper bound [14], the system capacity over the five dimensions can be written as [15]:

$$C = M \times B \times 2 \times \log_2 (1 + \mathrm{SNR}) \,, \tag{1.1}$$

where M is the number of spatial channels, B represents the system bandwidth, and the last term equals the Shannon capacity of a single-polarisation quadrature modulated signal given a certain signal-to-noise ratio (SNR). Improving system capacity by optimizing the time and quadrature dimensions in the form of high symbol rate, high cardinality modulation formats that transport a larger number of bits in shorter time intervals requires an improvement in signal-to-noise ratio (SNR). According to Eq. (1.1), increasing system capacity by a factor of k requires a k-th power improvement in SNR. As the term suggests, this can be achieved by either increasing the signal power or reducing the noise energy. As noise accumulates with transmission distance, this generally results in a reach reduction. Furthermore, a limitation is reached due to the nonlinear response of fibres, when high power signals are injected. This is illustrated in Fig. 1.4, where the fibre capacity follows Shannon's law for the AWGN channel [14] for low SNR but falls off at higher signal powers [13, 16]. This phenomenon limits the achievable gain from the time and quadrature dimensions towards the capacity. Another limiting factor to increasing the symbol rate and modulation order is imposed by the bandwidth and resolution of the digital-to-analog converter (DAC) and analog-to-digital converter (ADC). Furthermore, the standardised channel spacing on the International Tele-

communications Union (ITU) grid imposes constraints to the channel bandwidth and thus symbol rate. Traditionally, this grid employed a 50 GHz or 100 GHz spacing. The modern, flexible dense wavelength-division multiplexing (DWDM) grid defines channel granularity of 6.25 GHz, thereby alleviating this constraint [17].

A linear, and thus better way to scale capacity can be achieved by improving the terms in front of the logarithm in Eq. (1.1). The two polarisations of light, represented by the factor of 2, are already exploited in deployed systems. Furthermore, the 4.4 THz available in the C-band is rapidly exhausting in WDM transmission systems. Even though EDFAs are less efficient outside the C-band, they are adapted to provide an additional 7 THz of bandwidth in the L-band. Including the other defined telecommunication bands a total of 53.5 THz of bandwidth is available, which would result in an improvement by a factor of 12 at best. However, due to the higher attenuation for lower wavelengths, the high absorption around 1380 nm in legacy fibre, and the combination of different optical sources and amplifier technologies to provide a broad gain spectrum, a lower capacity increase is to be expected. Ultra low-loss hollow-core fibres can offer an additional 37 THz of bandwidth in the 2 µm range, outside of conventional telecom frequencies. Consequently, it is incompatible with deployed fibre technology, and can thus not benefit from the low costs of well-developed components. Note that due to the logarithmic relation of SNR and capacity, the effect of reducing the attenuation of optical fibres rapidly diminishes.

The last variable in Eq. (1.1) relates to parallelism in the spatial domain [4, 12, 18]. A straightforward approach is the deployment of M single-mode systems operated in parallel, resulting in linear growth of capacity. However, this requires M times the number of components as each link operates individually. Similar to the multi-core microcontrollers, parallelism can be exploited to reduce costs by integration. Therefore research is focused on novel fibre types (Section 3.2), that exploit multiple modes in a multi-mode core, multiple cores within a single cladding, or a combination thereof. However, in contrast to WDM, spatial channels can experience linear mixing during propagation. Hence, two design strategies for space-division multiplexing (SDM) systems exist. The first focuses on minimizing the inter-channel crosstalk, such that each channel can be exploited similarly to single-mode fibre. One example is the multi-core fibre (MCF), where the core pitch is kept sufficiently large to transmit conventional polarisation-multiplexed signals over each core. As the spatial channels are not allowed to interact, the capacity gains are limited by the cladding diameter. Deviating from the standardized 250 µm diameter leads to incompatibility with cabling and fibre processing instruments. Furthermore, increasing the cladding size negatively impacts the mechanical structural properties.

The other strategy employs multiple-input multiple-output (MIMO) digital signal processing (DSP) to unravel the spatial channel mixing, which is discussed in more detail in Chapter 4. To regulate the computational complexity of the power-hungry DSP, a short channel impulse response is preferable. Consequently, the differential mode dispersion has to be carefully managed in both fibre, component,

and system design. In addition to modal dispersion, the varying losses among the modes, or unevenly distributed gain in optical amplifiers, collectively referred to as mode dependent loss (MDL) introduces a fundamental capacity limiting impairment. Although mode dependent attenuation of fibres is present, the optical amplifiers and spatial multiplexer contribute stronger to this impairment, thus has to be addressed in their design and production. These spatial multiplexers are a necessary interface between existing single-mode and the proposed SDM technology. The various methods developed over the years are discussed in Section 3.3.

The proposal for SDM dates back to 1979 for multi-core [19], and 1982 for mode division multiplexing [20]. At the time, there was no need to develop a complete system. However, with the impending capacity crunch of single-mode fibres [21], research towards exploiting the spatial domain gained interest around 2005 [22, 23], and developed at a tremendous pace in the 2010s. Resulting in numerous demonstrations of multiplexing over 3 modes within a few-mode fibre (FMF) [24–27], exceeding distances over a 1000 km [28, 29]. The possibility to transmit over more than 3 modes was demonstrated by the first 6 mode transmission in 2012 [30]. Simultaneously, the development of MCF technology has shown a spatial multiplicity of 19, with impressive transmission rates [31, 32]. And by combining both mode and core multiplexing, an even higher spatial multiplicity was demonstrated by transmitting 255 Tbit/s over a 7-core 3-mode fibre in 2014 [33], although at a very limited distance. This led to the target of this dissertation, where the scaling towards a higher number of spatial channels and longer-reach transmission is investigated.

1.2 Thesis structure

The eight chapters in this thesis cover the challenges in scaling the established 3-mode transmission research towards higher spatial-multiplicity for both short-reach and long-distance optical systems.

In Chapter 2, the optical fibre as a transmission medium is introduced. First, the light-guiding properties and the concept of fibre modes are intuitively explained using geometric optics. Subsequently, a more detailed analysis of these modes is obtained by solving Maxwell's equations. Finally, pulse propagation is discussed covering both linear and non-linear effects.

Chapter 3 introduces the components found in an SDM transmission system, including the signal modulation applied at the transmitter, the spatial multiplexer converting between single-mode and multi-mode domains, various types of SDM fibres, optical amplifiers, and means to detect the signal at the receiver.

The digital signal processing applied to the detected signals to recover the transmitted symbols is described in Chapter 4. At the core is the MIMO equaliser, unravelling the spatial channel crosstalk and mitigating various linear impairments. Additional modules in front of the equaliser are employed to compensate receiver

impairments and timing issues. Finally, frequency and phase errors are removed by carrier phase estimation before symbols are detected and demapped to bits.

In Chapter 5, the development of a spatially-diverse optical vector network analyser (OVNA) for SDM component characterisation is presented. By employing a fast sweeping laser source, low bandwidth but high-gain photodetectors, and high-resolution analogue-to-digital conversion, the complex transfer function matrix of multi-port devices can be directly measured over several THz of bandwidth in a single and fast measurement. This matrix describes the complete linear response of optical components, from which parameters such as insertion and mode-dependent loss, cross-talk, group delay, and chromatic dispersion can be extracted by applying digital signal processing. The optical vector network analyser (OVNA) is employed for characterisation of spatial multiplexers, few-mode fibres, and few-mode multi-core fibres. The latter being the largest spatial multiplicity fibre to be analysed at a detailed level as provided by optical vector network analysis.

Three short reach mode-division multiplexing (MDM) transmission experiments are presented in Chapter 6, including the first-ever reported 10 mode transmission over FMF. As managing differential mode group delay (DMGD) in few-mode fibres becomes more difficult for higher mode counts, a 50 µm core diameter multi-mode fibre (MMF) is employed to increase transmission distance for 10 mode transmission to 40 km. The higher coupling between modes within a single mode-group of the MMF is exploited to achieve MDM transmission with reduced DMGD. This is demonstrated by comparing two 3-mode transmission systems over two sets of spatial channels of 53.4 km MMF.

Chapter 7 covers record transmission experiments over 3-mode and 6-mode fibre. The first is designed with a larger effective area, and as such allows for higher signal powers before introducing nonlinear impairments. Its performance is compared to standard single-mode fibre (SSMF), and shown to outperform it up to transmission distances of 2400 km. A record throughput of 138 Tbit/s is achieved by transmitting 120 wavelength and 12 spatial channels in a combined WDM/SDM experiment over 590 km FMF.

Finally, the conclusions and a future outlook are given in Chapter 8.

1.3 Contributions and acknowledgements

The author is responsible for all design, theoretical analysis and experimental work reported in this thesis. The work was also a result of a collaboration between several industrial partners and academic institutions. The experimental data presented in Chapter 5 with the exception of Section 5.6, was obtained using the OVNA developed by the author. The measurements for Section 5.6 were obtained by Dr. Simon Rommel at the National Institute of Information and Communications Technology (NICT) in Japan. The analysis based on these measurements as presented in this dissertation is performed by the author. The data for Section 5.7 was obtained at NICT by the author using his software applied to the provided hardware.

This research visit was supervised by Dr. José Manuel Delgado Mendinueta and dr. Werner Klaus.

The transmission experiments of Chapter 6 were conducted at Eindhoven University of Technology employing fibres provided by the Prysmian Group, and mode-multiplexers manufactured by CREOL (The College of Optics and Photonics, University of Central Florida). The employed DSP processing techniques and TDM-SDM receiver are adaptations and improvements on the implementation provided by Dr. Roy van Uden.

Experiments presented in Chapter 7 were taken at the Crawford Hill research site of Nokia Bell Labs in New Jersey under the supervision of Dr. Roland Ryf and Dr. Nicolas Fontaine. The transmission fibres were manufactured by OFS, and the 3D-waveguide spatial multiplexer was developed in collaboration with MQ Photonics Research Centre (Sydney, Australia) and the University of South Australia. The digital signal processing implementation was provided by Dr. Roland Ryf. The author was responsible for the design and optimization of the transmission link and analysis.

This PhD project has been carried out under the supervision of Prof. Ir. Ton Koonen, Dr. Ir. Huug de Waardt and Dr. Chigo Okonkwo from Eindhoven University of technology and was partially funded by ”de Nederlandse Organisatie voor Wetenschappelijk Onderzoek” (NWO) Photonics Graduate programme under Grant 022.005.011.

This research has resulted in the publications listed in the publication listed on page 192. Where this is referenced in the text, the notation [J#] is used.

Chapter 2

The optical fibre channel

Before the twentieth-century glass fibres or rods were mainly used for decorative purposes, and not much attention was paid to the optical properties of the material [34]. This changed in the 1950s, with the invention of cladding layer fibre that improved the light-guiding properties by exploiting the concept of total internal reflection [35–37]. However, 1000 dB/km losses limited the practical use of optical fibres for communication, and their main application was found in short distance medical imaging [38]. In 1966, Kao and Hockham predicted that the attenuation could be reduced to below 20 dB/km by removing impurities in the silica [3]. Four years later, Corning produced the first fibre below this predicted limit [2]. In the 1980s, optical fibres with an attenuation of less than than 0.2 dB/km could be manufactured [5], and would reduce further to 0.1419 dB/km, which is the lowest reported attenuation in single-mode fibre to date [39]. The fast improvement of attenuation in the 1970s and 1980s has led to this medium forming the backbone of our digital society.

This chapter focusses on the main component in optical fibre communications, the fibre. In Section 2.1 the concept of light propagation in optical fibres is illustrated by a geometric optic description of the medium. In the same section, the concept of modes in fibres is presented in an intuitive matter. A more in-depth analysis of these modes is derived from Maxwell's equations in Section 2.2. Under the weakly guiding approximation (WGA), the waveguide modes resolve to linearly polarised (LP) modes, which are commonly employed as a basis in mode-division multiplexing (MDM) transmission. Whereas the modes describe the transverse distribution of the optical field, the evolution of the longitudinal field is described by the generalized nonlinear Schrödinger equation (GNSE). This differential equation can be applied to model linear and nonlinear propagation effects. In Section 2.3, the primary propagation effects such as attenuation, dispersion and non-linear impairments are introduced. Finally, the coupled GNSE are presented to include the interaction between the spatial channels.

2.1 Fibres as optical waveguides

Optical fibres are dielectric waveguides, generally cylindrical in form, that confines electromagnetic energy in the form of light, and guides it in a direction along its z axis. The transmission properties depend on its structure, which determines the transmission capacity of the fibre. The cross-section of a typical optical fibre is shown in Fig. 2.1a. It has a central glass core with radius a, surrounded by a cladding layer with a lower refractive index and radius b. Most fibres are encapsulated in a plastic jacket or coating to add additional mechanical strength to the fibre. The boundary between core and cladding can be abrupt, resulting in a step-index profile as depicted in Fig. 2.1b. Graded-index profiles, as illustrated in Fig. 2.1c, have a gradual decreasing refractive index for increasing radius, which will result in a lower modal dispersion as will be explained later in this section.

The light-guiding property of optical fibres is based on Snell's law of total internal reflection of light. This concept will be explained by applying geometric optics to a step-index multi-mode fibre. The cross-section along the propagation axis of the fibre is shown in Fig. 2.2. The coloured lines in this figure correspond to a ray congruence, which represents a fibre mode. When this beam encounters the boundary with the cladding, a part is reflected into the core and the remainder is refracted into the cladding, as can be seen for the blue beam in Fig. 2.2. The refraction or bending of the ray is the result of different propagation speeds of light in both materials, which is denoted by v and is related to the speed of light in vacuum c by:

$$n = \frac{c}{v}, \tag{2.1}$$

where n is the refractive index of the medium. The speed of light in vacuum is 299 792 458 m/s, often approximated as 3×10^8 m/s. The refractive index is used

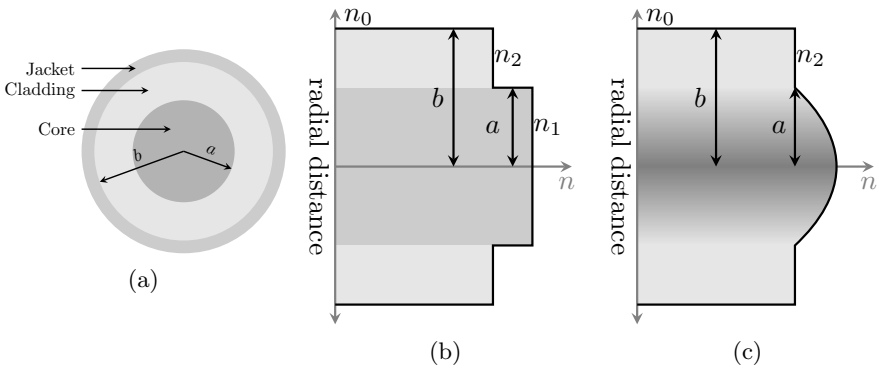

Figure 2.1: (a) Cross section of an optical fibre. (b) Refractive index profile of a step-index fibre. (c) Refractive index profile of a graded-index fibre.

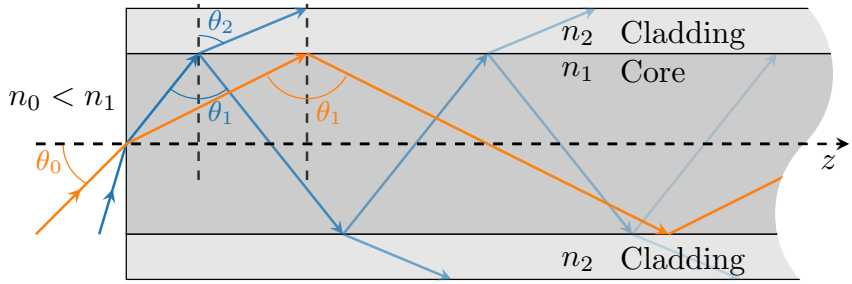

Figure 2.2: Two rays entering a step-index fibre under different angles. The orange ray propagates through the fibre as it is totally reflected on the boundary interface. At each reflection of the blue ray, energy leaks through the cladding, and the ray will fade out.

to relate the angles of two rays at the boundary as:

$$n_1 \sin\theta_1 = n_2 \sin\theta_2, \tag{2.2}$$

where θ_1 and θ_2 are the angles with respect to the normal of the incident and refracted beams respectively. This expression is known as Snell's law. For increasing incident angle, the angle of the refractive beam reduces, up to a point where the ray propagates parallel to the boundary interface. The corresponding incident angle is known as the critical angle θ_c, given as:

$$\sin\theta_c = \frac{n_2}{n_1} \tag{2.3}$$

When the incidence angle is increased beyond the critical angle, the light is fully reflected back into the core. In practice, there is always some tunnelling of optical energy through the interface, which can be explained by the electromagnetic wave theory of light [40].

The outside medium of the fibre has refractive index n_0, which in general is smaller than that of the core material. All rays entering with angle θ_0 that result in total internal reflected beams will be guided by the waveguide. The range of angles accepted by the optical fibre is given by the numerical aperture (NA), which can be linked to the critical angle by applying Snell's law at the interface of the core and outside medium:

$$\mathrm{NA} = n_0 \sin\theta_{0,\max} = n_1 \sin\theta_c = \sqrt{n_1^2 - n_2^2} \approx n_1\sqrt{2\Delta}, \tag{2.4}$$

Where Δ is the core-cladding index difference. The numerical aperture (NA) is a dimensionless quantity less than unity, that can be applied to calculate optical power coupling efficiencies between media.

Equation (2.4) suggests that all beams entering the fibre with an angle smaller than θ_0 are guided through the fibre. However, in practice, only a set of discrete

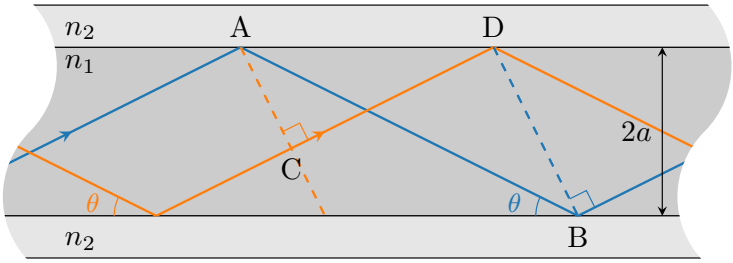

Figure 2.3: Two rays and their orthogonal phase fronts as they propagate through a step-index fibre.

angles are accepted. This can be understood, when considering that a wave consists of multiple rays, of which two are drawn in Fig. 2.3. The constant phase fronts, represented by the dashed lines, are orthogonal to the rays. For a guided wave, constructive interference of both waveforms is required. Therefore the phase shift over path AB minus the shift over CD must be a multiple of 2π. After some basic geometry, the wave propagation requirement can be expressed as:

$$\frac{2\pi n_1}{\lambda}(AB - CD) + 2\delta = 2m\pi \tag{2.5}$$

$$\frac{4\pi a n_1 \sin\theta}{\lambda} + \delta = m\pi, \tag{2.6}$$

where a is the core radius, λ is the wavelength of the light, m is an integer number, and δ is the phase shift introduced at the refraction on the core-cladding boundary. Since m is an integer number, the acceptance angles θ has to be discrete. Thus light can only be accepted at certain discrete angles within the NA. This discretization result in the formation of optical fibre modes. The number of modes supported by a fibre is reflected in the normalized frequency V, given as:

$$V = \frac{2\pi a}{\lambda}\mathrm{NA}. \tag{2.7}$$

The derivation of this formula will be explained in Section 2.2. Fibres with a higher V parameter support a larger number of modes. A special case holds for $V \leq 2.405$, which is the cut-off frequency of the first higher-order mode. Hence, only the mode $m = 0$ is within the maximum angle of acceptance. Fibres of this type are called single-mode fibre (SMF), and are widely deployed in long-distance optical communication systems.

The same geometric approach can be applied to graded-index fibres, which refractive index profile is described by Eq. (2.8), where α determines the curvature of the profile and the index difference Δ is given by Eq. (2.9). Note that for large

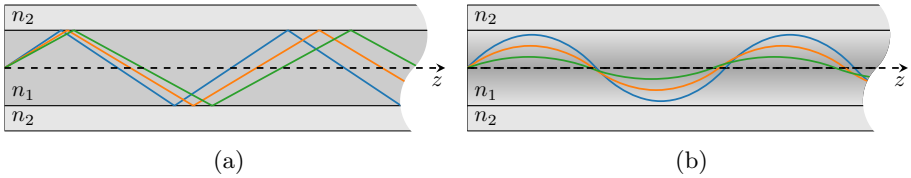

Figure 2.4: Light travelling through an optical fibre with a step-index profile (a) and graded-index profile (b).

values of α, the profile converges towards a step-index fibre.

$$n(r) = \begin{cases} n_1 \left[1 - 2\Delta(r/a)^a\right]^{1/2} & \text{for } 0 \leq r \leq a \\ n_1(1-2\Delta)^{1/2} \simeq n_1(1-\Delta) = n_2 & \text{for } r > a \end{cases}, \tag{2.8}$$

$$\Delta = \frac{n_1^2 - n_2^2}{2n_1^2} \simeq \frac{n_1 - n_2}{n_1} \tag{2.9}$$

A gradual decrease in refractive index towards the cladding can be seen from Eq. (2.8). Since the propagation speed is inversely proportional to the refractive index, light will travel faster towards the cladding. Therefore the rays propagate through the fibre in a parabolic manner, as can be seen in Fig. 2.4b. For both index profiles holds that more oblique rays travel a longer path through the medium, as can be seen in Fig. 2.4, but only in graded-index fibre will they propagate faster. Consequently, the propagation time difference, or differential mode delay (DMD), can be smaller for graded-index fibres. As will be discussed in more detail later, the differential mode delay is an important design parameter for mode-division multiplexed transmission systems as it imposes memory requirements of the digital receiver.

2.2 Modes in optical fibres

A more detailed analysis of the propagation of light is obtained by solving Maxwell's equations for an optical fibre. Solving these equations for an electromagnetic field in hollow metallic waveguides, yields only transverse electric (TE) and transverse magnetic (TM) modes. Transverse modes are perpendicular to the propagation direction, hence do not have a field component in propagation direction z. However, at the boundary of core and cladding both electric and magnetic fields couple, resulting in hybrid modes. These modes are denoted as EH when the transverse electric field is dominant, or HE when the magnetic field is stronger. While these solutions are known, numerical methods are required to obtain them. These methods can be simplified by applying the weakly guiding approximation (WGA), which presumes a small refraction index difference between core and cladding material. With this approximation, the LP modes of the fibre are found. These

modes, labelled with integer indices l, m as $\mathrm{LP}_{\mathrm{lm}}$, are a combination of the TE, TM, HE, and EH modes of the fibre.

In Section 2.2.1, the wave equation for the electromagnetic field is derived from Maxwell's equations under the WGA. Next, the wave equations are solved in Section 2.2.2 to obtain the LP modes for a step-index fibre profile.

2.2.1 Wave equations

As all electromagnetic fields, the propagation of light in fibres is governed by Maxwell's equations. For this analysis, the optical fibre medium is assumed to be linear, isotropic, time-invariant, and source free material. Under these assumptions, Maxwell's equations in the frequency domain take the form of [41]:

$$\nabla \times \mathbf{E} = -j\omega\mathbf{B} \tag{2.10a}$$

$$\nabla \times \mathbf{H} = j\omega\mathbf{D} \tag{2.10b}$$

$$\nabla \cdot \mathbf{D} = 0 \tag{2.10c}$$

$$\nabla \cdot \mathbf{B} = 0 \tag{2.10d}$$

Where $\nabla\times$ and $\nabla\cdot$ denote the curl and divergence operators, respectively. For simplicity of notation, the tilde over the field expressions is dropped and the frequency dependence is implicitly understood. The electric flux density $\mathbf{D}\left[\mathrm{C/m^2}\right]$ is related to the electric field intensity $\mathbf{E}[\mathrm{V/m}]$ via the permittivity ϵ of the material. Similarly, the magnetic flux density $\mathbf{B}\left[\mathrm{Wb/m^2}\right]$ is related to the magnetic field intensity $\mathbf{H}[\mathrm{A/m}]$ via the permeability μ of the material. This relation is described by the constitutive relations [42]:

$$\mathbf{D} = \epsilon\mathbf{E} \tag{2.11a}$$

$$\mathbf{B} = \mu\mathbf{H} \tag{2.11b}$$

It is common to operate on the relative permittivity and permeability of a material, which are related to their absolute variants in vacuum as:

$$\epsilon = \epsilon_r\epsilon_0 \tag{2.12}$$

$$\mu = \mu_r\mu_0 \tag{2.13}$$

where μ_0 is defined as $4\pi \times 10^{-7}\,\mathrm{N/m}$, and the value of ϵ_0 follows from the relation $\epsilon_0\mu_0c^2 = 1$. The refractive index n as used to explain the concepts of reflection and refraction in the previous section is related to the relative material parameters by:

$$n = \sqrt{\epsilon_r\mu_r} \tag{2.14}$$

From Eq. (2.10), an equation defining the wave phenomena of the electromagnetic field can be derived. The wave equation for the electrical field is obtained by first

taking the curl of Eq. (2.10a). Subsequently inserting Eq. (2.10c), Eq. (2.10b), and Eq. (2.10d) yields:

$$\begin{aligned}\nabla \times (\nabla \times \mathbf{E}) &= -j\omega(\nabla \times \mathbf{B}) \\ &= -j\mu\omega(\nabla \times \mathbf{H}) \\ &= -j\mu\omega(j\omega\mathbf{D}) = \mu\omega^2\mathbf{D} \\ &= \epsilon\mu\omega^2\mathbf{E} \\ &= \epsilon_0\mu_0 n^2\omega^2\mathbf{E} \end{aligned} \tag{2.15}$$

Note that Eqs. (2.12) to (2.14) have been applied to derive the last step. Next, the following vector identity,

$$\nabla \times (\nabla \times \mathbf{A}) = \nabla(\nabla \cdot \mathbf{A}) - \nabla^2\mathbf{A}, \tag{2.16}$$

where ∇^2 is the vector Laplacian is applied to the left hand side of Eq. (2.15), which yields:

$$\nabla(\nabla \cdot \mathbf{E}) - \nabla^2\mathbf{E} = \epsilon_0\mu_0 n^2\omega^2\mathbf{E} \tag{2.17}$$

Since the refractive index difference between core and cladding is small, it can be considered constant under the WGA to simplify the wave equation [43]. Hence, the first term on the left hand side of Eq. (2.17) approaches zero. Therefore, the wave equation for the electrical field is found to be:

$$\nabla^2\mathbf{E} + \epsilon_0\mu_0 n^2\omega^2\mathbf{E} = 0 \tag{2.18}$$

Analogue to the derivation of the wave equation for the electrical field, the wave equation for the magnetic field is given by:

$$\nabla^2\mathbf{H} + \epsilon_0\mu_0 n^2\omega^2\mathbf{H} = 0 \tag{2.19}$$

For the constant relative permittivity ϵ_r of the isotropic medium, these vectorial wave equations can be rewritten to the standard form of the Helmholtz equation by introducing the wave number k as:

$$k = k_0 n = \omega\sqrt{\epsilon_0\mu_0}n = \frac{\omega n}{c} \tag{2.20}$$

where k_0 is the wave number in vacuum. Finally, the wave equation for the electrical and magnetic field are given by:

$$\nabla^2\mathbf{E} + k^2\mathbf{E} = 0 \tag{2.21a}$$

$$\nabla^2\mathbf{H} + k^2\mathbf{H} = 0 \tag{2.21b}$$

This set of equations will be solved in the next section.

Since the structure of the fibre is uniform with propagation direction z, the derivative of the electromagnetic field with respect to z must satisfy [44]:

$$\frac{\partial}{\partial z} = -j\beta, \tag{2.22}$$

where β is the propagation constant in direction z of the wave number k. The propagation constant will be covered in more detail in Section 2.3.

2.2.2 Linearly polarised modes

To solve the wave equations, a cylindrical system of coordinates $\{r, \phi, z\}$ is employed to describe the electromagnetic fields in the radial, angular, and propagational directions. The Laplacian operator ∇^2 for an axially symmetric optical fibre in a cylindrical coordinate system is given by:

$$\begin{aligned}\nabla^2 &= \frac{\partial^2}{\partial x^2} + \frac{\partial^2}{\partial y^2} + \frac{\partial^2}{\partial z^2} \\ &= \frac{1}{r}\frac{\partial}{\partial r}\left(r\frac{\partial}{\partial r}\right) + \frac{1}{r^2}\frac{\partial^2}{\partial \phi^2} + \frac{\partial^2}{\partial z^2} \\ &= \frac{\partial^2}{\partial r^2} + \frac{1}{r}\frac{\partial}{\partial r} + \frac{1}{r^2}\frac{\partial^2}{\partial \phi^2} + \frac{\partial^2}{\partial z^2},\end{aligned} \tag{2.23}$$

Furthermore, the tangential electric field components E_x and E_y are assumed to be in the form of [44]:

$$E(r, \phi) = R(r)\Phi(\phi) \tag{2.24}$$

Substituting this expression for the electrical field and Laplacian in Eq. (2.21a) yields:

$$\begin{aligned}\frac{1}{R(r)}\left(\frac{\partial^2 R(r)}{\partial r^2} + \frac{1}{r}\frac{\partial R(r)}{\partial r}\right) + \frac{1}{r^2}\frac{1}{\Phi(\phi)}\frac{\partial^2 \Phi(\phi)}{\partial \phi^2} + k_0^2 n^2 - \beta^2 = 0 \\ \frac{r^2}{R(r)}\left(\frac{\partial^2 R(r)}{\partial r^2} + \frac{1}{r}\frac{\partial R(r)}{\partial r}\right) + k_0^2 n^2 - \beta^2 = -\frac{1}{\Phi(\phi)}\frac{\partial^2 \Phi(\phi)}{\partial \phi^2}\end{aligned} \tag{2.25}$$

Note that the elements on the left hand side of Eq. (2.25) are functions of only r and the right hand side only of ϕ, and thus have to be constant. Hence, Eq. (2.25) can be rewritten as two ordinary differential equations (ODEs) for a given constant l:

$$\frac{\mathrm{d}^2 R(r)}{\mathrm{d}r^2} + \frac{1}{r}\frac{\mathrm{d}R(r)}{\mathrm{d}r} + \left(k_0^2 n^2 - \beta^2 - \frac{l^2}{r^2}\right) R(r) = 0, \tag{2.26}$$

and

$$\frac{\mathrm{d}^2 \Phi(\phi)}{\mathrm{d}\phi^2} + l^2 \Phi(\phi) = 0 \tag{2.27}$$

The solution of Eq. (2.27) is a periodic function given by [45]:

$$\Phi(\phi) = \sin(l\phi + \varphi), \tag{2.28}$$

where φ is an arbitrary constant phase. Since the field must be periodic with a period of 2π because of the symmetry of the optical fibre, l has to be an integer. For a step-index fibre, with core radius a, Eq. (2.26) has two solutions. The first describing the electromagnetic wave inside the core with refractive index n_1, and a second solution defining the wave in the cladding material with refractive index

n_2. Since Eq. (2.26) are in the form of Bessel's differential equation, the solutions comprises of Bessel functions [46]. The solution for $R(r)$ can be written as:

$$R(r) = \begin{cases} AJ_l\left(\frac{ur}{a}\right) + BY_l\left(\frac{ur}{a}\right) & \text{for } r \leq a, \\ CK_l\left(\frac{wr}{a}\right) + DI_l\left(\frac{wr}{a}\right) & \text{for } r \geq a. \end{cases} \tag{2.29}$$

where, J_l and Y_l are the lth-order Bessel functions of the first and second kind, and K_l and I_l are the lth-order modified Bessel functions of the first and second kind. Since the field must remain finite, and Bessel functions of the second kind diverge at zero, coefficient B has to be zero. As the modified Bessel function of the first kind diverges, and the electromagnetic field should decay to zero towards infinity, coefficient D can also be dropped from Eq. (2.29). Hence, the solutions of the wave equations for step-index fibre are given by:

$$R(r) = \begin{cases} AJ_l\left(\frac{ur}{a}\right) & \text{for } r \leq a, \\ CK_l\left(\frac{wr}{a}\right) & \text{for } r \geq a. \end{cases} \tag{2.30}$$

The newly introduced parameters u and w are considered to be the normalized lateral propagation constants in the core and the normalized lateral decay constant in the cladding, and are defined as [43]:

$$u^2 = a^2\left(k_0^2 n_1^2 - \beta^2\right) \tag{2.31a}$$

$$w^2 = a^2\left(\beta^2 - k_0^2 n_2^2\right) \tag{2.31b}$$

Furthermore, u and w describe the normalized frequency V, which is related to the cut-off conditions of modes in optical fibres as introduced in Section 2.1 as:

$$V = \sqrt{u^2 + w^2} = ak_0\sqrt{n_1^2 - n_2^2} = ak_0\text{NA} \tag{2.32}$$

The boundary conditions imply that the electromagnetic field must be continuous at the interface between core and cladding. Hence, both Eq. (2.30) and its derivative with respect to r, evaluated at $r = a \pm 0$ must be equal to zero. This set of two equations can be written in matrix form as:

$$\begin{bmatrix} J_l(u) & -K_l(w) \\ uJ_l'(u) & -wK_l'(w) \end{bmatrix} \begin{bmatrix} A \\ C \end{bmatrix} = 0 \tag{2.33}$$

where $'$ denotes the derivate with respect to r. For non-trivial solutions, the determinant of the left matrix in Eq. (2.33) has to be zero. Finally, by applying the Bessel functions properties [46]:

$$J_\nu'(z) = J_{\nu-1}(z) - \nu z^{-1} J_\nu(z), \tag{2.34a}$$

$$zK_\nu'(z) = -zK_{\nu-1}(z) - \nu K_\nu(z) \tag{2.34b}$$

the characteristic equation under the WGA, is obtained as:

$$\frac{uJ_{l-1}(u)}{J_l(u)} = -\frac{wK_{l-1}(w)}{K_l(w)} \tag{2.35}$$

The solutions of Eq. (2.35) are the linearly polarised modes, labelled as $\mathrm{LP_{lm}}$. The indices relate to the combination of EH and HE waveguide modes within each LP mode. These waveguide or vectorial modes are obtained by solving Maxwell's equations without applying the WGA. The relation between the first 10 LP modes and the waveguide modes are given in Table 2.1 for step-index fibres [40]. In general, an $\mathrm{LP_{0m}}$ mode consists of an $\mathrm{HE_{1m}}$ mode. Each $\mathrm{LP_{1m}}$ mode is a combination of $\mathrm{HE_{0m}}$, $\mathrm{EH_{0m}}$ and $\mathrm{HE_{2m}}$ modes. For $l \geq 2$, each $\mathrm{LP_{lm}}$ mode comprises of an $\mathrm{HE}_{l+1,m}$ and an $\mathrm{EH}_{l-1,m}$ mode. Note that within each LP mode either the electric or magnetic field is significant. Furthermore, each of these polarisations can be coupled with an azimuthal dependence of $\cos(j\phi)$ or $\sin(j\phi)$, resulting in the four degenerate modes of an $\mathrm{LP_{lm}}$ mode, denoted by an additional subscript a or b.

The field intensity profiles of LP modes can be represented in a single graph, where the two colours represent the positive and negative amplitudes of the fields. The mode profiles of the first 15 LP modes are given in Fig. 2.5. The shape of each profile can be derived from the indices l and m. The first index equals the number of sign changes of the amplitude along the azimuthal axis. The other index corresponds to the number of sign changes in the radial direction. The mode profiles of graded-index profiles have a similar profile and can be grouped in sets of quasi degenerate modes. The n modes within the nth group have a similar group velocity, resulting in stronger coupling compared to modes between different groups. In an ideal fibre, the mode groups are distributed equally over the graded-index profile and have therefore a lower differential group delay (DGD) compared to step-index fibres.

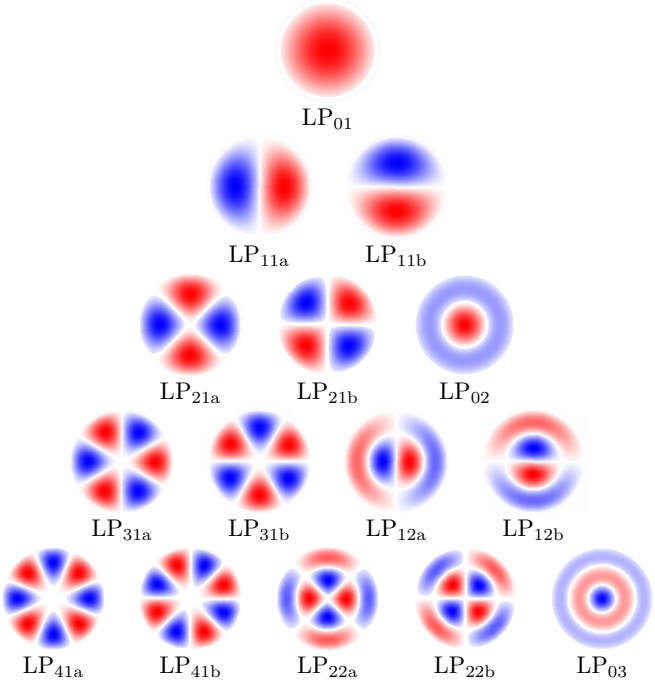

Figure 2.5: Mode profiles of the first 15 LP modes, where red and blue correspond to the positive and negative phase, respectively. The modes are grouped according the mode groups in graded-index fibres.

Table 2.1: V-number and composition of waveguide modes for LP modes

Group	LP mode	V cut-off (SI)	Degenerate modes	Waveguide modes
1	LP_{01}	-	2	HE_{11}
2	LP_{11}	2.4	4	$TE_{01}, TM_{01}, HE_{21}$
3	LP_{21}	3.8	2	EH_{11}, HE_{31}
	LP_{02}	3.9	4	HE_{12}
4	LP_{31}	5.1	4	EH_{21}, HE_{41}
	LP_{12}	5.5	4	$TE_{02}, TM_{02}, HE_{22}$
5	LP_{41}	6.4	4	EH_{31}, HE_{51}
	LP_{22}	7.0	4	EH_{12}, HE_{32}
	LP_{03}	7.1	2	HE_{13}

2.3 Pulse propagation

In the previous section, expressions for the electromagnetic field propagating through an optical fibre were derived under ideal material properties to simplify the equations, including the assumption of a medium without polarisation. However, in the presence of an electrical field, the molecules in the material gain an electric dipole moment. The induced electric dipole moment of a material, given by vector $\mathbf{P}$, is included in the constitutional relation of the electrical field as $\mathbf{D} = \epsilon\mathbf{E} + \mathbf{P}$. Since the optical fibre is a non-magnetic medium, there is no induced magnetic field. Hence the constitutional relation for the magnetic field of Eq. (2.11b) still holds. Consequently, the updated wave equation Eq. (2.18) becomes:

$$\nabla \times (\nabla \times \mathbf{E}) = \epsilon_0 \mu_0 n^2 \omega^2 \mathbf{E} + \mu\omega^2 \mathbf{P} \tag{2.36}$$

The total polarization $\mathbf{P}$ in the optical fibre medium can be expressed in a linear and nonlinear component [47]:

$$\mathbf{P} = \epsilon_0 \left(\chi^{(1)} \cdot \mathbf{E} + \chi^{(3)} \vdots \mathbf{EEE} \right), \tag{2.37}$$

where $\chi^{(j)}$ is the jth order susceptibility. Since SiO_2 is a symmetric molecule, silica fibres generally do not exhibit second-order nonlinear effects. Hence it is not included in Eq. (2.37). The third order susceptibility introduces the generation of third order harmonics, four-wave mixing and nonlinear refraction, as will be covered in more detail later in this section. The solution of Eq. (2.36) is given by the generalized GNSE, which take the form of [47]:

$$\frac{\partial \mathbf{E}}{\partial z} = \overbrace{-\underbrace{\frac{\alpha}{2}\mathbf{E}}_{\text{attenuation}} - \underbrace{\beta_1 \frac{\partial \mathbf{E}}{\partial t}}_{\substack{\text{group}\\\text{velocity}}} - \underbrace{\frac{j\beta_2}{2}\frac{\partial^2 \mathbf{E}}{\partial t^2}}_{\substack{\text{group velocity}\\\text{dispersion}}} + \underbrace{\frac{\beta_3}{6}\frac{\partial^3 \mathbf{E}}{\partial t^3}}_{\substack{\text{dispersion}\\\text{slope}}}}^{\text{linear}} + \overbrace{\underbrace{j\gamma|\mathbf{E}|^2\mathbf{E}}_{\substack{\text{Kerr}\\\text{nonlinearity}}}}^{\text{nonlinear}} \tag{2.38}$$

where γ is the nonlinear parameter in $\left[\mathrm{W}^{-1}\,\mathrm{m}\right]$ defined as:

$$\gamma = \frac{\bar{n}_2 \omega}{c A_{\text{eff}}} \tag{2.39}$$

In Eq. (2.39), $\bar{n}_2$ is the nonlinear Kerr parameter with units $\left[\mathrm{m}^2/\mathrm{W}\right]$ and A_{eff} is the effective mode area of the fibre. The effective area is introduced as a normalization factor such that $|\mathbf{E}|^2$ represent the optical power. By doing so the effective area can be expressed in terms of the lateral modal distribution as:

$$A_{\text{eff}} = \frac{\left(\int\int_{-\infty}^{\infty} |F(x,y)|^2 \, dxdy \right)^2}{\int\int_{-\infty}^{\infty} |F(x,y)|^4 \, dxdy} \tag{2.40}$$

Note that the electrical field evolution of each LP mode in a fibre is governed by its own propagation vector $\beta_{l,m}$, and experiences a different effective area due to the various mode field distributions. Hence, Eq. (2.38) describes only the propagation of a single polarisation mode. In order to describe the interactions between polarisations and modes, the individual GNSE is extended to the coupled nonlinear Schröding equations (NLSEs) [48] in Section 2.3.5. However, the physical effects related to the components of Eq. (2.38) are discussed first in Sections 2.3.1 to 2.3.4.

2.3.1 Attenuation

The first term Eq. (2.38) represents the attenuation of the electrical field. In this subsection, the impact on attenuation on the signal, and components contributing to the fibre attenuation are discussed. The importance of attenuation as a design parameter for optical communication systems is related to the maximum achievable transmission distance between the transmitter, intermediate amplifiers, and receiver.

Let P_{in} be the optical power at the input of the fibre. After propagating through a fibre of length L, the output power P_{out} is given by:

$$P_{out} = P_{in} e^{-\alpha L}, \tag{2.41}$$

where α is the attenuation coefficient, typically expressed in units of dB/km. Several phenomena contribute to the attenuation, of which the most import are: material absorption, Rayleigh scattering, and radiative losses as a result of fibre bending.

Rayleigh scattering

Rayleigh scattering arises from local microscopic variations in the material density resulting in fluctuations of refractive index on a scale smaller than the wavelength of the signal [49]. These defects can originate from compositional fluctuations, structural inhomogeneities or defects during the manufacturing process of the glass. An interesting side note, this phenomenon is also responsible for the blue sky, as the sunlight scatters in the atmosphere. Signal power degradation caused by Rayleigh scattering is mainly dominant for shorter wavelengths and rapidly diminishes for longer wavelengths because of its λ^{-4} scaling. Around 1600 nm, Rayleigh scattering is superseded by material absorption as the dominant source of losses.

Absorption

Material absorption can be divided into losses corresponding to the absorption of the fibre material itself, and impurities of the silica [50]. The first category, called intrinsic absorption, is related to electron absorption and atomic resonances of silica and dopants in the optical fibre medium. Electron absorption occurs when

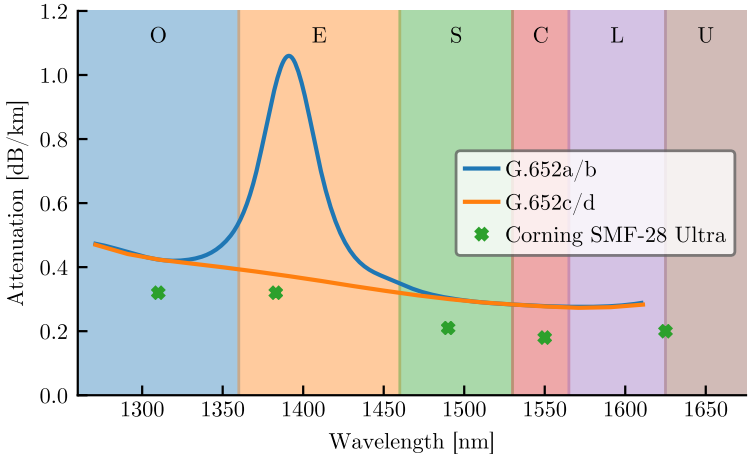

Figure 2.6: Maximum attenuation of single mode mode fibre (G.652a/b) and dry-fibre (G.652c/d) as specified by the ITU [52]. Example of specified attenuation of modern commercially available single-mode fibre. The shaded areas correspond to the transmission windows specified by the ITU-T.

photon-electron interaction results in the excitation of a higher energy level of the electron in the valance band. The associated absorption coefficient decreases exponentially with photon energy, and since the wavelength is inverse proportional to the photon energy, this type of attenuation increases with wavelength.

Extrinsic absorption is caused by impurities introduced in the fibre material and the presence of water. Concentrations of transition metals, such as iron, copper, chromium, and vanadium introduce several absorption peaks at different wavelengths because of electron energy band transitions. The concentration of these metal ions in fibres manufactured using modern production processes is significantly low, such that this type of attenuation becomes negligible. Furthermore, dehydration techniques in the manufacturing process have practically removed the OH^- absorption peaks [51]. OH ions have a fundamental vibrational peak around 2.73 µm, but has overtones at 950 nm, 1240 nm and 1390 nm. Dry fibres have been available for around two decades, but many telecommunication systems still rely on legacy fibres.

Transmission bands

The combined contributions of the afore-mentioned sources yields the attenuation profile of single-mode fibre as specified in the G.652 standards, as is depicted in Fig. 2.6. Note that this figure represents the maximum attenuation defined in these standards and typical values for modern fibres are lower, as can be seen from the specified attenuation of Corning SMF28-Ultra fibre [53]. Within this

broad spectral range, the International Telecommunications Union (ITU) assigned six spectral bands, as can be seen in the figure [54]. The original band (O-band: 1260 nm-1360 nm), was the first region used for single-mode fibre transmission links. Nowadays, the O-band is often used for upstream channels in passive-optical networks (PONs), because of the availability of cheap laser diodes and a negligible amount of chromatic dispersion in this window. Since transmission distances are short, the slightly higher attenuation is not important.

A significant increase in system capacity was realised by multiplexing wavelength channels. The main driver behind wavelength-division multiplexing (WDM) is the erbium doped fibre amplifier (EDFA), capable of amplifying multiple wavelength channels simultaneously. Its gain spectrum defines the conventional (C-band) and long bands (L-band), ranging from 1530 nm to 1565 nm, and 1565 nm to 1625 nm, respectively. The C-band is widely used for the majority of metro, long-haul and submarine transmission links. Although amplification in the L-band is less efficient, hybrid C+L band systems are employed to provide a larger bandwidth.

The S-band (short-wavelength band: 1460 nm-1530 nm), is generally employed for downstream channels in PON. The E-band is the least used transmission window as it overlaps with the water absorption peak of legacy optical fibres. Finally, the ultra-long band (U-band: 1625 nm-1675 nm), is employed for network monitoring purposes. Not included in the figure is the 850 nm band, which is primarily used for multi-mode communication inside data-centres and in-building or campus networks. Equipment is typically less expensive compared to single-mode, but distance and capacity are limited due to modal dispersion. Although this band is not of interest to the telecommunication systems discussed in this thesis, prototype multi-mode fibres for space-division multiplexing (SDM) can benefit from the optimized production process for OM fibres used in this window.

Bending losses

Another source of loss, not included in the attenuation profile is radiative losses related to fibre bending. These bending losses can be divided between macrobending and microbending. The first, often generalized as bending losses, occurs when the bending radius is large compared to the dimensions of the fibre [55–57]. In a curved fibre section, one side is compressed whereas the other side is stretched. As a result, a pulse must propagate at different speeds to maintain its shape. For a critical radius, parts of the pulse must propagate faster than the speed of light. Since this is not possible, the energy starts radiating away from the fibre. The susceptibility to bending losses of higher-order modes is exploited for modal cut-off in the design of few-mode fibres.

Microbends are small fluctuation in the radius of the curvature of the fibre caused by local pressure points or nonuniformities [58]. Microbends results in repetitive coupling of light between modes, and if coupled to a leaky mode, it will result in loss.

2.3.2 Group delay

The linear contributions in Eq. (2.38), originate from a Taylor expansion of the propagation constant for mode lm around an angular frequency of interest ω_0. This expansion up to the third order yields:

$$\beta_{lm}(\omega) = \beta_{lm}^{(0)} + \beta_{lm}^{(1)}(\omega - w_0) + \frac{\beta_{lm}^{(2)}}{2}(\omega - \omega_0)^2 + \frac{\beta_{lm}^{(3)}}{6}(\omega - \omega_0)^3, \tag{2.42}$$

with

$$\beta_{lm}^{(i)} = \frac{\partial^i \beta(\omega)}{\partial \omega^i}$$

The expansion terms in this mathematical expression of the propagation constant have physical meaning. The first term, $\beta_{lm}^{(0)}$, is related to the phase velocity ν_p of the propagating field as:

$$\nu_p = \frac{\omega}{\beta_{lm}^{(0)}}. \tag{2.43}$$

Two modes with similar phase velocities can couple during propagation. This coupling takes place over a length that is inverse proportional to the difference in ν_p. The beat length for modes a and b with a different phase velocity couple is given as:

$$L = \frac{2\pi}{\left|\beta_a^{(0)} - \beta_b^{(0)}\right|} \tag{2.44}$$

The second term in Eq. (2.42) is related to the group velocity of transmitted pulse over a mode. It is denoted by $\nu_{g(lm)}$ and relates to the propagation constant as:

$$\frac{1}{\nu_{g(lm)}} = \frac{\mathrm{d}\beta_{lm}(\omega)}{\mathrm{d}\omega} \tag{2.45}$$

Since the group velocity might differ between modes, the arrival time of pulses transmitted over modes with different group delays will result in differential group delay (DGD). The accumulated DGD between modes a and b after transmission over an ideal fibre of length L is:

$$\mathrm{DGD} = L\left|\frac{\beta_a^{(1)}}{\nu_{p,a}} - \frac{\beta_b^{(1)}}{\nu_{p,b}}\right| \tag{2.46}$$

DGD is the general term for group velocity difference between any two propagating fields. Often, a more specific term is used to specify whether the DGD is related to modes (DMD), mode groups (DMGD) or polarisation (PMD).

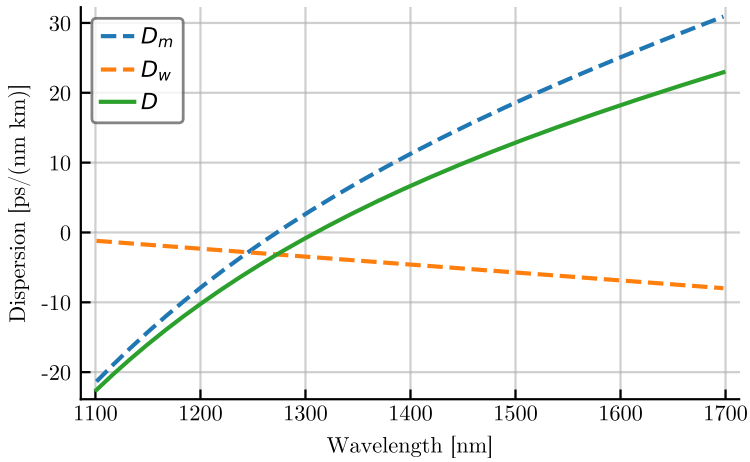

Figure 2.7: Dispersion map of standard single-mode fibre. The total dispersion is the sum of waveguide and material dispersion, resulting in zero dispersion at 1310 nm [62].

2.3.3 Dispersion

The third component of Eq. (2.42) describes a varying group velocity of spectral components, which result in pulse broadening during propagation. This phenomenon, known as group velocity dispersion (GVD) or chromatic dispersion (CD) is the result of material dispersion and waveguide dispersion [59]. The first type is caused by the wavelength dependence of the refractive index. Since the group velocity is a function of the refractive index, spectral components propagate with different group velocities. The second type of CD arises from the wavelength varying group velocity induced by the geometric properties of the fibre. The material dispersion D_m and waveguide dispersion D_w add up to a total dispersion parameter D, which relates the propagation constant as:

$$D = D_m + D_w = -\frac{2\pi c}{\lambda^2}\beta_{lm}^{(2)} \quad [\text{ps}/(\text{nm}\cdot\text{km})] \tag{2.47}$$

The dispersion map for standard single-mode fibre is depicted in Fig. 2.7, which shows both the contribution of material and waveguide dispersion. Since the waveguide dispersion depends on the core radius and index difference, fibres can be designed with a zero-dispersion wavelength other than 1310 nm. Fibres with the zero-dispersion around 1550 nm are known as dispersion-shifted fibre [60]. Similarly, dispersion compensated fibre (DCF) can be made with large negative amounts of dispersion to compensate dispersion of a transmission link [61]. Nowadays, digital dispersion compensation at the receiver is used in coherent transmission links, as will be explained in more detail in Section 4.3.

The last component of Eq. (2.42) describes the change of GVD to angular frequency. Its contribution towards the pulse broadening is limited compared to

the GVD itself for C-band transmission. However, in the wavelength range where $\beta_n^{(2)} \approx 0$, it can not be neglected.

2.3.4 Non-linear impairments

Nonlinear effects in optical fibres are complicated effects depending on the length and effective area of the fibre, as well as the optical power. The strength of these effects scale with fibre length and are proportional to the optical power. Therefore, modelling can be simplified by operating on an effective length, that takes this interaction into account. This parameter is given by:

$$L_{\text{eff}} = \frac{1 - e^{-\alpha L}}{\alpha}, \tag{2.48}$$

where α is the attenuation coefficient of the fibre in [dB/km], and the actual fibre length is given by L. Equation (2.48) can be interpreted as the length over which the optical power is approximately constant. Due to the attenuation, most nonlinear effects will occur in the first L_{eff} of a fibre span with length L.

Scattering related nonlinear effects

Nonlinearities can be categorized in two ways. The first one classifies the effects based on whether they are introduced by refractive index changes or result from scattering. The other type of categorization separates inter-channel effects from intra-channel effects [40]. Stimulated Brillouin scattering (SBS) and stimulated Raman scattering (SRS) are the intra- and inter-channel scattering effects. Both relate to interactions of the electromagnetic field and vibrational modes of the silica atoms. During this interaction, energy from incident photons is partially absorbed and stored in vibrational modes. These vibrations can be associated with both optical and acoustic phonons, and their effects are called stimulated Raman or Brillioun scattering, respectively. Due to the low speed of acoustical phonons, stimulated Brillouin scattering (SBS) is considered an intra-channel effect. The backscattered photon experiences a Doppler shift and a gain from the forward propagating signals, which lead to transmission performance degradation [47, 63]. However, SBS only becomes troublesome when the energy of the reflected wave is comparable to that of the signal, reflected by the SBS threshold value.

Increasing the launch power while below this threshold will result in an approximately linear increase in signal power. However, beyond this threshold, increasing the total launch power has diminishing returns on the signal power. At values far larger than the threshold, all additional optical power launched into the fibre will be backscattered. Hence, SBS limits the maximum launch power into optical fibres. Several options are available to reduce the impact of SBS, such as installing optical isolators to limit backscattering to a single amplifier span and reduce the signal power within each span, which most likely implies a reduction in amplifier spacing. Furthermore, a broader linewidth of the transmitter laser or adding a

small frequency dithering will increase the SBS threshold. Moreover, the threshold power scales proportional to A_{eff}, therefore the inherently larger effective area multi-mode fibres are less susceptible to SBS, which allows for improved launch powers.

The other scattering type of nonlinear effects is Raman scattering [64]. As this effect is associated with optical phonons that propagate at significantly larger speeds through the material compared to their acoustic counterparts, the bandwidth of stimulated Raman scattering (SRS) can cover multiple wavelength channels. Since photon energy is absorbed by the material, this nonlinear effect could be interpreted as an impairment. However, Raman scattering can be exploited to provide distributed amplification along the transmission link. Therefore, Raman amplifiers can be employed to reduce the overall nonlinear effects in transmission systems. The operational principles of this amplifier type will be discussed in Section 3.5.2.

Self-phase modulation

The other type of nonlinear effects is related to changes in the refractive index introduced by high-intensity optical signals. This nonlinear change in the refractive index of the medium is the result of nonlinear susceptibility caused by the anharmonic response of electrons to optical fields [62]. Consequently, a nonlinear term is added to the expressions for the refractive index of both core and cladding:

$$n_i = n_i + \bar{n}_2 \frac{P}{A_{\text{eff}}}, \quad i = 1, 2, \tag{2.49}$$

where n_1 and n_2 represent the previously defined refractive index of core and cladding respectively. The optical power of the pulse is given by P, and A_{eff} is the effective index from Eq. (2.40). For typical fibres, $\bar{n}_2$ is relatively small value, in the order of $10^{-20}\,\text{m}^2/\text{W}$. Therefore, a linear approximation of the optical fibre medium is still applicable for low signal powers, but it is not accurate for high signal powers.

It can be shown with first-order perturbation theory [47], that the nonlinear contribution in Eq. (2.49) manifests itself as spurious phase changes proportional to the optical signal power. This nonlinear phase shift is given by:

$$\phi^{\text{NL}} = \gamma P_{\text{in}} L_{\text{eff}}, \tag{2.50}$$

where γ is the nonlinear parameter given by Eq. (2.39), and P_{in} is the power inserted into the fibre. The self-induced nonlinear phase modulation is known as self-phase modulation (SPM). SPM manifests mainly as a time varying frequency of optical pules. This effect is known as chirp and is proportional to the time-derivative of the signal power. Therefore, the rising flank of a pulse, where the optical power increases, the pulse experiences a red frequency shift. When the signal power decreases, the frequency reduces, and a blue shift is observed. The frequency chirp

affects the pulse shape through GVD, which in general results in additional pulse broadening. However, in fibres designed with negative dispersion coefficients, SPM can be beneficial as it mitigates the pulse broadening from chromatic dispersion.

Cross-phase modulation

In the case of SPM, the alteration of the optical pulse shape is the result of its optical power. However, also pulses of neighbouring wavelength channels contribute to the nonlinear phase change. This interaction can occur between pulses within the same wavelength channel, or with pulses in other channels. Therefore cross-phase modulation (XPM), is both an intra- and inter-channel nonlinear effect. However, in general, only the latter is considered cross-phase modulation (XPM) and the first is referred to as SPM. The total nonlinear phase noise introduced by SPM and XPM is given by:

$$\phi_i^{NL} = \gamma L_{\text{eff}} \left(P_i + 2 \sum_{i \neq j} P_j \right), \tag{2.51}$$

Note that the contribution of XPM is twice as strong as SPM at the same intensity, which originates from the triple product of the electric fields in the expression for the polarisation in Eq. (2.37). XPM affects the pulse shape in a similar way as SPM, however, it only builds up when pulses overlap in both space and time. When the pulses overlap due to GVD, the nonlinear phase noise is added to the signal, which remains as timing jitter after CD compensation [65]. By increasing the channel spacing, the overlap between pulses can be reduced, thereby minimizing the impact of XPM. However, this comes at the cost of reduced spectral efficiency.

Both SPM and XPM scale inverse proportional to the effective area. The potentially larger effective area of multi-mode fibre (MMF), can lead to reduced signal distortion due to nonlinear phase noise at the same signal intensities. Alternatively, for the same level of nonlinear distortions, the system can be operated at higher signal powers, which can improve signal-to-noise ratio (SNR) and capacity. However, the larger number of modes in MMF can introduce additional XPM.

Four-wave mixing

The third-order nonlinear susceptibility does not only introduce power-dependency of the refractive index but also results in four-wave mixing (FWM). This nonlinear phenomenon is the generation of a fourth frequency ω_4 as a result of three co-propagating optical fields, with carrier frequencies ω_1 ω_2 and ω_3 [47, 66]. The relation between these four frequencies is given as $\omega_4 = \omega_1 \pm \omega_2 \pm \omega_3$. This relation suggests the generation of more than a single tone, but only phase-matched components will build up. The phase-matching requirement follows from the conservation of energy and momentum between the destroyed and generated photons.

The mixing products are related to the scattering process where two photons with energies $\hbar\omega_1$ and $\hbar\omega_2$ are destroyed and two new photons with energies $\hbar\omega_3$ and $\hbar\omega_4$ are created. In particular, the degenerate case where $\omega_1 = \omega_2$ can be detrimental to transmission system performance, as only a single pump wavelength is required to generate mixing products. The frequencies of the two mixing products are given by $\omega_3 = \omega_1 - \Omega$ and $\omega_4 = \omega_1 + \Omega$, with Ω representing the channel spacing. As all waves are co-propagating, the corresponding phase mismatch is given as:

$$\begin{aligned} \Delta &= \beta(\omega_3) + \beta(\omega_4) - \beta(\omega_1) - \beta(\omega_2) \\ \Delta &= \beta(\omega_1 - \Omega) + \beta(\omega_1 + \Omega) - \beta(\omega_1) - \beta(\omega_1) \end{aligned} \tag{2.52}$$

After inserting the second order Taylor approximation of the propagation constant of Eq. (2.42), the terms related to the phase and group velocity cancel, resulting in $\Delta = \beta^{(2)}\Omega^2$. From this expression it can be seen that the phase is matched in the absence of GVD. Since typical wavelength spacing is less than 100 GHz, a small dispersion coefficient will result in crosstalk between wavelength channels. Therefore, in order to minimize four-wave mixing (FWM), a high GVD during propagation followed by digital CD compensation is preferred. Although it can be considered a harmful effect in dense WDM light-wave systems, FWM has some practical applications, among which are wavelength conversion and optical phase conjugation.

2.3.5 Spatial channel interactions

The impairments discussed in the previous subsections were derived from the GNSE, which do not include any interaction between spatial channels. A set of two coupled GNSE has been derived to include the coupling between the two polarisations in single-mode fibre [47]. This procedure can be extended to include spatial mode interactions. To obtain this set of equations, the $\mathrm{LP}_{\mathrm{l,m}}$ modes are ordered by increasing magnitude of the propagation constant. The subscript n is used to refer to the nth mode in this ordered list. Subsequently, the total electrical field in the fibre is given as the sum of the individual mode fields as [67]:

$$\mathbf{E}(x, y, z, t) = \mathrm{Re}\left[\sum_{n=1}^{2N} \frac{\mathbf{F}_n(x, y, \omega_0)}{\mathcal{N}_n(\omega_0)} E_n(z, t) e^{-j\omega_0 t}\right], \tag{2.53}$$

where $\mathcal{N}_n(\omega_0)$ is a normalization coefficient such that the power of the nth mode is given by $|E_n(z,t)|^2$ [67]. Furthermore, the frequency dependent mode field distribution and normalization coefficients are presumed to be independent of the longitudinal position and can be approximated by a constant value ω_0 within the signal bandwidth. Within the approximations of the WGA, the mode orthogonality condition takes the simplified form of [67]:

$$\frac{n_n}{2Z_n}\left\{\int dxdy \mathbf{F}_n \cdot \mathbf{F}_m^*\right\} = \delta_{n,m}\mathcal{N}_n^2, \tag{2.54}$$

where $n_n = \beta_n c/\omega_0$ is the effective index and Z_n represents the impedance of the nth mode. Before extending the GNSE to the coupled NLSEs, a hyper-polarization vector $|E(z,t)\rangle$ is introduced to represent the $2N$ complex envelopes $E_n(z,t)$ as a column vector [67]. The corresponding frequency domain vector is denoted $|E(z,\omega)\rangle$. Recall that the tilde is dropped for simplicity of notation and frequency dependence is implicitly understood. A graphical representation of the hyper-polarization vector of the electric field in a 3-mode fibre is shown in Fig. 2.8a. Since fibre modes can be grouped in sets of quasi-degenerate modes, the hyper-polarisation vector can also be interpreted as the stacking of smaller vectors corresponding to the mode groups, which is represented by the differentially coloured elements. The linear components of the single channel GNSE (Eq. (2.38)) can now be described by

$$\frac{\partial \left|\mathbf{E}\right\rangle}{\partial z} = j\mathbf{B}\left|\mathbf{E}\right\rangle - \mathbf{A}\left|\mathbf{E}\right\rangle, \tag{2.55}$$

where $\mathbf{A}(z,\omega)$ and $\mathbf{B}(z,\omega)$ are $2N \times 2N$ Hermitian matrices, describing the mode dependent loss (MDL) and the unitary evolution of the electric field. MDL is defined as the optical field gain ratio between the strongest and weakest channels, as will be explained in more detail in Section 4.1. Note that $\mathbf{B}(z,\omega)$ in this section does not refer to the magnetic field. In the absence of MDL, $\mathbf{A}$ reduces to an identity matrix, with the conventional loss coefficients $\alpha/2$ on its diagonal. Matrix $\mathbf{B}$ describes the rotation of the hyper-polarization vector in a $2N$ complex vector space, which is the generalized case of polarization rotation in single-mode fibre. Similar to the expansion of the propagation constant at the beginning of this section, the matrix $\mathbf{B}$ can be approximated with a Taylor expansion as

$$\mathbf{B}(z,\omega) \simeq \mathbf{B}^{(0)} + \omega\mathbf{B}^{(1)} + \frac{\omega^2}{2}\mathbf{B}^{(2)} \tag{2.56}$$

In a fibre with ideal properties and in the absence of mode mixing, $\mathbf{B}$ is a diagonal matrix with the fibre propagation modes as basis. Along the diagonals of $\mathbf{B}^{(j)}$, the propagation constants of modes β_n and their derivatives describing the group velocities and group velocity dispersion are found. In practice, interaction between the modes occurs, e.g. due to material and structural imperfections or mechanical stress. The impact of modal interactions on the expanded propagation matrices $\mathbf{B}^{(j)}$ decreases with j, which can be explained by the fact that phase changes of the optical field are easier to realise compared to a change in group velocity or GVD. Therefore, structural imperfections mainly result in a random rotation of the hyper polarisation signal vector. A graphical representation of $\mathbf{B}^{(0)}$ for the 3-mode fibre is given in Fig. 2.8b.

Similar to the expression for the electric field, a hyperpolarisation vector $\left|L^{(NL)}\right\rangle$ can be constructed from the elements $L_n^{(NL)}$ and appended to Eq. (2.56) to include the nonlinear effects. The elements of this vector are given by:

$$L_n^{(NL)} = j\gamma \sum_{h,k,m} C_{nhkm} E_h^* E_k E_m \hat{e}_n, \tag{2.57}$$

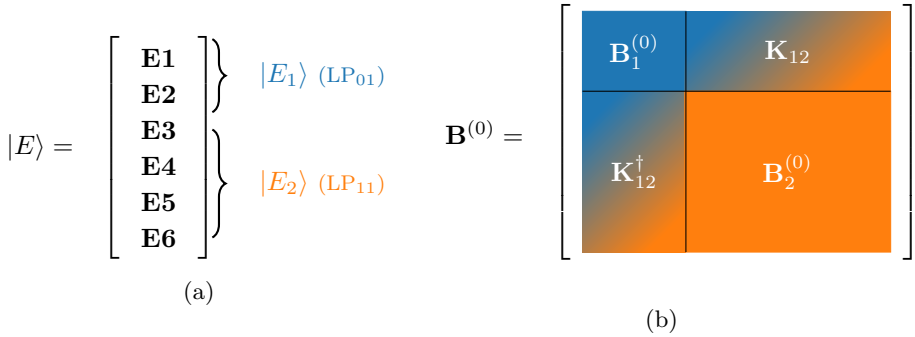

Figure 2.8: (a) Hyperpolarisation vector $|E\rangle$ of a 3 mode system, consisting of the two vectors $|E_1\rangle$ and $|E_2\rangle$, which correspond to the LP$_{01}$ and LP$_{11}$ modes respectively. Due to degeneracy of the LP$_{11}$ modes, the second sub-vector has 4 elements. (b) Corresponding $\mathbf{B}^{(0)}$ matrix, where the matrices on the diagonal represent the mode coupling between quasi degenerate modes within mode groups. The off-diagonal matrices are each other complex conjugate and represent the inter-mode group coupling.

where C_{nhkm} are dimensional constants describing the contribution of the electrical field of one mode towards the total nonlinearity in a given mode. As pulses require spatial overlap to couple, these coefficients depend on the spatial mode profiles. For the dual-polarization single-mode fibre, the coefficients are found to be $C_{1111} = C_{2222} = 1$, $C_{1221} = C_{2112} = 2/3$ [47]. This implies that the polarisations affect each other by a factor of $2/3$. More details on the derivation of the coupling coefficients and nonlinear effects can be found in [48, 67–69].

Summary

In this chapter, the concept of total internal reflection is applied to the circular structure of optical fibres. It has been shown that only light entering the fibre under discrete angles within its numerical aperture will propagate. If only a single angle is accepted, the fibre is known to be single-mode. In case more rays are accepted by the fibre, it is referred to as multi-mode. The field distribution of the modes is obtained by solving Maxwell's equations in the transverse direction of the optical fibre. The solutions take shape in the form of Bessel functions and are dependent on the refractive index profile of the fibre. As a result of the relative small refractive index difference between core and cladding, the waveguide modes can be approximated by linearly polarised modes. It was noted that for graded-index fibres, these LP modes exist in mode groups, where the quasi-degenerate modes have a similar propagation constant.

From the propagation constant, linear propagation effects, such as differential group delay and group velocity dispersion are derived. The first is a difference

in the propagation speed of two modes, which in combination with cross-talk introduces pulse broadening. The group velocity dispersion is also responsible for pulse broadening and originates from the different propagation speeds of spectral components. These effects are all linear, therefore, they can be compensated by employing digital signal processing as will be discussed in detail in Chapter 4.

Since the fibre is a nonlinear medium, certain types of distortion are dependent on the power of the transmitted signals. The impact of these effects increases with the optical power but decreases with the effective area of the fibre. Generally, the larger core size of multi-mode fibres have a larger effective area and is therefore expected to have increased tolerance to nonlinear impairments. Both linear and nonlinear effects are described by the generalized nonlinear Schrödinger equation, which is commonly used to model pulse propagation in optical fibres. This differential equation also includes the attenuation, introduced by the scattering and absorption of photons during propagation. A great endeavour has been made to obtain the less than 0.2 dB/km attenuation of modern optical fibres. The wavelength dependent attenuation gave rise to the designation of multiple bands, which are used for different applications in optical networks. Finally, it is shown that the generalized nonlinear Schrödinger equation (GNSE) for each mode can be coupled for the two polarisations of single-mode fibre as well as to the modes in multi-mode fibre. From this coupled set of equations, the concept of mode mixing is derived. The exploitation of modes in optical fibres for communication in an SDM transmission system will be explained in the next chapter.

Chapter 3

Space-division multiplexed transmission systems

In the previous chapter, the propagation of light in optical fibres and the concept of modes were introduced. In this chapter, the optical fibre medium will be employed for optical communications. This chapter focusses on the system aspect of optical fibre communications and introduces the components found in a space-division multiplexing (SDM) transmission systems. Such a system shares components with deployed single-mode fibre based transmission systems. However, the introduction of multiple spatial channels requires the development of new fibres and components, as well as the adaptation of existing ones.

A functional diagram of an SDM transmission system is depicted in Fig. 3.1. Here, the outputs of N transmitters are spatially multiplexed and transmitted over an optical fibre link. Each transmitter submodule in Fig. 3.1 composes of multiple transmitters, each modulating an optical carrier at different frequencies. Since the spatial channels are orthogonal, the same frequencies can be re-used among the SDM transmitters. Therefore, wavelength-division multiplexing (WDM) components found in currently deployed single-mode transmission systems can be employed for the multiplexing and demultiplexing of the wavelength channels (insets of Fig. 3.1).

Spatial multiplexers are required to connect the N single-mode transmitters to the N or more channels supported by the SDM fibre. An overview and comparison of multiplexing technologies will be presented later in this chapter. The same multiplexing technologies can be employed to convert the spatial channels back to the single-mode domain, because of reciprocity. In a reciprocal optical device, changes in the properties of light passing through the device are reversed when the light passes through in the opposite direction. Generally, some level of crosstalk between the spatial channels occurs in these multiplexers, which add up to the mode mixing that occurs during transmission over SDM fibres, or is introduced at splices or other system components. To unravel this mixing as well as compensate

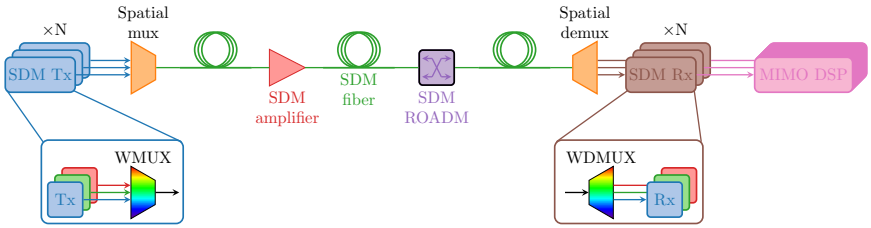

Figure 3.1: Functional diagram of an SDM transmission system, including reconfigurable optical add-drop multiplexer (ROADM) for channel routing. The insets show the compatibility with WDM technology.

linear transmission impairments, multiple-input multiple-output (MIMO) digital signal processing (DSP) is employed, which will be treated in Chapter 4.

This chapter is structured as follows: In Section 3.1, the signal generation and modulation of the optical carrier at the transmitter will be discussed. The different approaches to increase the spatial multiplicity in optical fibres is covered in Section 3.2. This includes the pure mode-division multiplexing (MDM) few-mode fibre (FMF) and multi-mode fibre (MMF), the single-mode multi-core fibre (MCF) as well the hybrid core/mode multiplexed few-mode multi-core fibre (FM-MCF). The coupling between the single-mode transmitters and SDM fibre performed by the spatial multiplexer is described in Section 3.3. This section mainly focusses on the transition from single-mode to multi-mode, as core multiplexing can be performed using similar or simpler technologies. Each output of the spatial demultiplexer is detected by a receiver. Three receiver architectures are presented in Section 3.6. The direct detection (DD) receiver capable of detecting only the amplitude of the optical field is included to introduce the concept of optical signal detection before the more complex coherent detection scheme is explained. The latter requires a more complex setup but is capable of recovering the full optical field. The third architecture covers the intermediate ground between the other schemes as digital signal processing can be applied to recover the full optical field with similar hardware of the DD scheme. The digital signal processing module will be treated in the next chapter.

3.1 Transmitter

At the transmitter, the data in the form of bits are modulated onto an optical carrier. Generally, the bits are mapped to symbols to enhance spectral efficiency (SE). The digital symbols are then converted to an analogue electrical waveform used to influence the amplitude or phase of the continuous wave (CW) laser source. The electrical current can be used to directly drive a laser source (Fig. 3.2a). This method, known as direct-modulation, produces large amounts of chirp; a time-

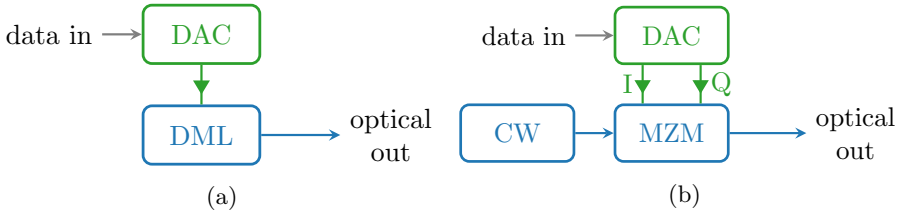

Figure 3.2: (a) Direct modulation: signal is modulation on the driver current of a directly-modulated laser (DML). (b) External modulation: the in-phase (I) and quadrature (Q) signal are modulated on the output of a CW laser source by a Mach-Zehnder modulator (MZM).

varying change of instantaneous optical frequency that has a dispersive effect on pulses.

The amount of chirp can be reduced by splitting the laser source and modulator, as is the case for externally-modulated laser sources. Both structures are still integrated into the same module, but the electrical waveform is employed to drive the modulator. Although this method has reduced chirp, it is also more expensive than direct-modulated lasers.

The best performance can be achieved by employing an external Mach-Zehnder modulator (MZM) with a separate laser source, that offers the flexibility to optimize the individual components (Fig. 3.2b). Furthermore, the MZM can be operated without any frequency chirp, as will be explained later in this section. Moreover, nested MZMs can be integrated into a single structure capable of modulating the in-phase and quadrature components of both polarisations of the light. This allows for higher-dimensional modulation formats, which can improve SE. Since this method offers the best performance, it is used in the transmission experiments of Chapters 6 and 7.

The next subsections cover the generation of the digital test sequences and optimisation of the electrical waveform. The actual modulation will be discussed at the end of this section.

3.1.1 Modulation formats

The spectrum for optical communications is divided into multiple transmission bands (Section 2.3.1), which requires efficient use of the limited available spectrum. To increase the spectral efficiency in [bit/s/Hz], multiple bits are mapped to a single symbol at the transmitter.

The simplest modulation formats contain only a single bit within each symbol. This symbol is either modulated on the amplitude or the phase of the carrier. The constellation diagrams of these modulation formats, known as on-off keying (OOK) and binary phase-shift keying (BPSK), are depicted in Figs. 3.3a and 3.3d. A

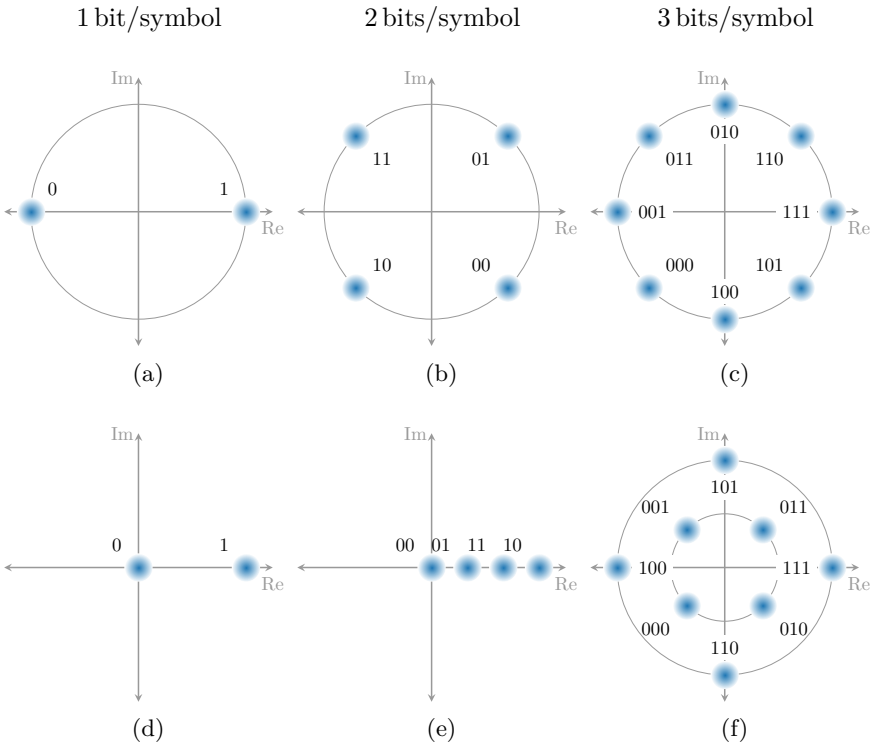

Figure 3.3: Examples of amplitude and phase modulated signals with a proposed bit mapping. (a) BPSK, (b) QPSK, (c) 8-PSK, (d) OOK, (e) PAM-4, (f) 2-ASK-4-PSK.

constellation diagram is a frequently used method to visualize two-dimensional modulation formats in the complex plane, where the real and imaginary axis represent the in-phase and quadrature components of the light. In the presence of noise, the diameter of constellation points increases, and will at some point overlap with neighbouring points, which leads to incorrect detection of the symbols.

Mapping additional bits to a symbol to enhance spectral-efficiency requires more points in the same constellation space. In the case of amplitude-shift keying (ASK), this can be realised by adding intermediate power levels, as is done for the 4-ary pulse-amplitude modulation (PAM) format depicted in Fig. 3.3e. Note that the Euclidean distance is reduced from the large spacing of the on-off keying (OOK) format. Consequently, less noise can be tolerated before the constellation points start to overlap, hence, a higher signal-to-noise ratio (SNR) is required for reliable communication. The proposed bit mapping in Fig. 3.3e follows a Gray coding, which minimises the number of bit-errors as neighbouring points differ in only one bit [70].

Similarly, higher-order phase modulation can be realized by including additional

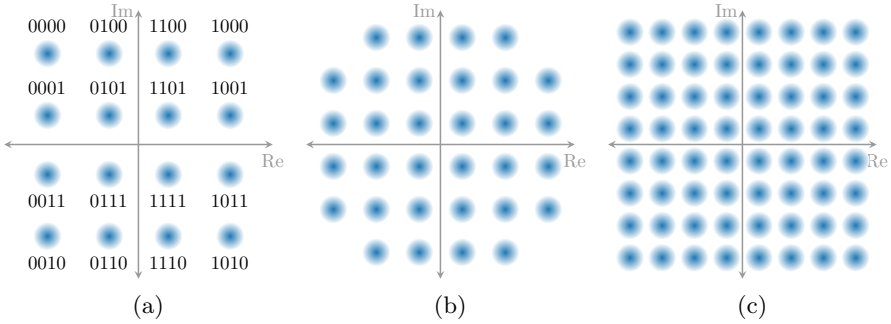

Figure 3.4: Examples of quadrature amplitude modulation (QAM) constellations. (a) 16-QAM (4 bits/symbol), (b) 32-QAM (5 bits/symbol), (c) 64-QAM (6 bits/symbol).

phase states, as is the case for quadrature phase shift keying (QPSK) (Fig. 3.3b) and 8-ary phase-shift keying (PSK) (Fig. 3.3c). Furthermore, both amplitude and phase modulation can be combined to a hybrid modulation format, of which 2-ASK-4-PSK is given as an example in Fig. 3.3f.

A cost-effective method to modulate higher-order constellations onto an optical carrier is by driving an IQ-modulator (IQ-MOD) with two analogue PAM signals. Each of the sequences modulates either the in-phase or quadrature component of the light, as will be explained in more detail in Section 3.1.4. Some examples of two-dimensional quadrature amplitude modulation (QAM) constellations are illustrated in Fig. 3.4. The number of bits transmitted in each symbol is equal to $\log_2 M$, with M equal to the number of constellation points in the M-ary quadrature amplitude modulation (QAM) format. Even values of M produce a square constellation (Figs. 3.4a and 3.4c), where bits can be Gray-coded to the symbols, whereas this is not the case for the non-square odd-numbered QAM constellations (Fig. 3.4b).

3.1.2 Random data generation

For the performance evaluation of optical transmission systems in laboratories, test patterns are designed to match the statistical properties of real data. Replicating a real transmission system where each transmitter generates independent data sequences, is costly as it requires a large amount of hardware. Therefore, a technique called signal decorrelation is applied, where independent data streams between polarisation, modes, cores, or wavelength channels are emulated by employing delay lines. In the optical domain, the modulated signal is split into multiple copies, followed by a delay line with an unique time-delay. The delays have to be chosen such that the signals do not overlap during propagation under the influence of dispersive effects and as such do not overlap within the equaliser window [71]. Due to the fast nature of polarisation dispersion, a relatively small delay suffices,

whereas the larger pulse spreading of chromatic dispersion (CD) requires longer delays or is preferably avoided by employing additional transmitters.

For the transmission experiments in this thesis, two types of random data generators are used to create the test sequences. The first method generates a pseudorandom bit sequence (PRBS) generated by a linear-feedback shift register (LFSR) that can be described by monic polynomials. A LFSR of length n will produce a bit sequence of length 2^{n-1}, that is commonly denoted as PRBSn. Note that for longer PRBS multiple polynomials exist, that are required to ensure the sequences are not correlated with itself when multiple bit sequences are combined to form higher-order constellations.

The other type of random data generator directly produces a sequence of symbols. Within this cyclic sequence, every possible substring of length n occurs exactly once. This type of sequence is known as a De Bruijn sequence and is denoted by $B(k, n)$, where k is the number of constellation points [72]. Several approaches are available to generate De Bruijn sequences of length k^n, which are generally more difficult than the LFSR approach of PRBS [73–75]. As the symbols in De Bruijn sequence are directly generated and are not a combination of multiple bitstreams, the autocorrelation requirement is automatically fulfilled. However, for equaliser windows longer than the order of the De Bruijn sequence, the desirable correlation properties can no longer be guaranteed.

Due to the memory constraints of the digital-to-analog converter (DAC), typical sequence lengths are in the order of 2^{15} to 2^{18}, which is also the case for the experiments described in Chapters 6 and 7. Note that an additional 0 is added to the PRBS pattern to obtain a sequence of length 2^n.

3.1.3 Digital-to-analogue conversion

The digital sequences are converted by a DAC to an analogue electrical signal to drive the optical modulator. Typical symbol rates of optical transmission are in the order of GHz, which requires high-speed DAC. Generally, the number of quantization levels or the resolution of such a fast sampling DAC is limited [76, 77]. On top of that, noise and distortions further lower the effective number of bits (ENOB). Furthermore, the electrical output power is often not sufficient to drive the MZM directly, and ultra-linear amplifiers are employed.

Ideally, the transformation from the electrical output to the optically modulated signal is linear. However, the transfer function of the modulator is described by a sine function, as will be shown in the next subsection. On top of that, bandwidth limitations of the DAC and electrical cables further decrease the electrical signal quality. The resulting low-pass filter response of the transmitter is shown in Fig. 3.5a. To compensate for this response, digital pre-compensation filters can be applied to enhance the signal quality. Such a pre-emphasis filter is designed to be the inverse of the transfer function of the electrical system. Several methods for measuring the transfer function and designing the pre-emphasis filters are

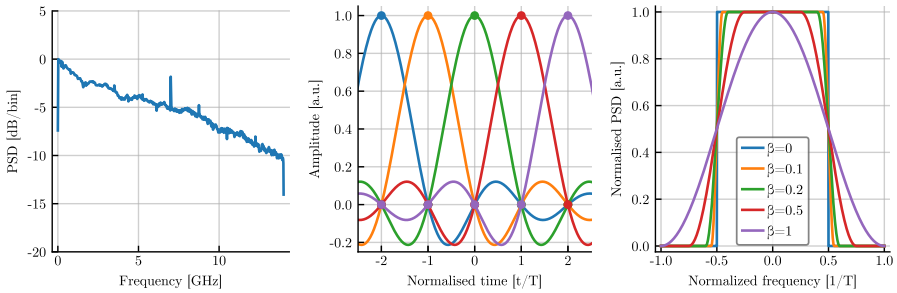

(a) (b) (c)

Figure 3.5: (a) Frequency response of the transmitter including DAC, driver amplifiers, and, cables. (b) Trains of raised cosine pulses with 0.1 roll-off. (b) Spectrum of raised cosine pulses for various roll-off factors.

available [78, 79]. Additionally, nonlinear pre-compensation techniques can be employed to include the nonlinear response of driver amplifiers or MZM [80].

Additionally, pulse shaping is applied to minimise intersymbol interference (ISI), and increase the SE by shaping the signal spectrum. Without any pulse shaping, the bandwidth occupied by a sequence of non-return-to-zero (NRZ) pulses transmitted at a symbol rate R_s, is approximately $2R_s$. The bandwidth can be reduced by applying a raised-cosine filter [81], which spectrum is described as:

$$S(f) = \begin{cases} 1, & |f| \leq \frac{1-\beta}{2T} \\ \frac{1}{2}\left[1+\cos\left(\frac{\pi T}{\beta}\left[|f| - \frac{1-\beta}{2T}\right]\right)\right], & \frac{1-\beta}{2T} < |f| \leq \frac{1+\beta}{2T} \\ 0, & \text{otherwise} \end{cases} \tag{3.1}$$

where f is the frequency, β is the roll-off factor, and T is the symbol period. Figure 3.5c shows the spectrum for various roll-off factors. Note that the bandwidth can be controlled via the roll-off parameter, resulting in an occupied bandwidth of $R_s(1+\beta)$ for a symbolrate R_s. The minimum bandwidth is achieved by transmitting Nyquist pulses, for $\beta = 0$. However, at such sharp roll-off, imperfect sampling will result in ISI. Therefore, roll-off factors of 0.01 to 0.2 are typically chosen to minimize ISI at the cost of a small bandwidth increase. The zero-ISI property of perfectly sampled raised cosine pulses can be seen in Fig. 3.5b, as at each sampling point all pulses except one are equal to zero. Generally, the raised cosine filtering is divided between transmitter and receiver to filter white Gaussian noise (WGN) by employing matched filtering [82]. The root-raised-cosine (RRC) filter shape is obtained by taking the square root of Eq. (3.1).

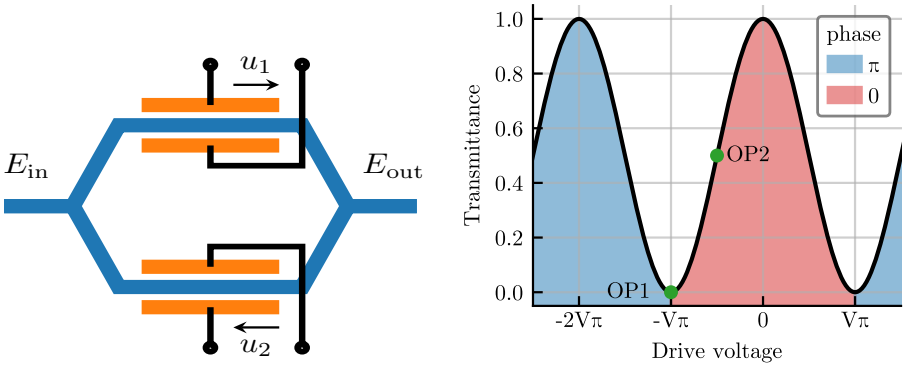

Figure 3.6: (a) Integrated optical Mach-Zehnder modulator. (b) Transfer function of a MZM.

3.1.4 Optical modulation

The electrical waveform generated by the DAC is modulated onto the amplitude and phase of a CW signal generated by an external optical source by an optical modulator. In the transmission experiments described in later chapters, IQ-modulators (IQ-MODs) are employed, which are integrated modulators containing nested MZM. The schematic of a single MZM, depicted in Fig. 3.6a, consists of a single Mach-Zehnder interferometer (MZI) with tunable phase modulators in each arm. The refractive index of these waveguide sections can be influenced by an electric field, according to an electro-optical phenomenon known as Pockels effect [83]. These sections are commonly made from Lithium niobate ($LiNbO_3$) as it has high electro-optic coefficients and is transparent for wavelengths used in telecommunications [84, 85].

The phase of the incoming CW source is changed in the two arms of the interferometer, yielding an output field described by the following expression:

$$\begin{aligned} E_{\text{out}}(t) &= \frac{1}{2} E_{\text{in}}(t) \left[\exp\left(j\pi \frac{u_1(t)}{V_\pi} \right) + \exp\left(j\pi \frac{u_2(t)}{V_\pi} \right) \right] \\ &= E_{\text{in}}(t) \underbrace{\exp\left(j\pi \frac{u_1(t) + u_2(t)}{2V_\pi} \right)}_{\text{phase modulation}} \underbrace{\cos\left(\pi \frac{u_1(t) - u_2(t)}{2V_\pi} \right)}_{\text{amplitude modulation}}, \end{aligned} \tag{3.2}$$

where the factor 2 stems from an ideal splitter, and parameters u_1 and u_2 are the driving voltage of the top and bottom arm of the MZM respectively (Fig. 3.6a). The driving voltage required to apply π phase shift is denoted by V_π, which is assumed to be equal for both phase modulators. Observe that the modulation described in Eq. (3.2) is a combination of phase and amplitude modulation. Hence, a MZM

can be employed for both types of modulation formats. To obtain a pure phase modulated signal, both modulators are driven by the same drive signal, resulting in the same phase shift in both arms. Note that the amplitude modulation term reduces to zero only in the case of perfect beam splitting. When the second driving signal is equal to the first, but with opposite sign ($u_1(t) = -u_2(t)$), the introduced phase shift in the bottom arm is the opposite of the shift in the top arm, i.e. $\phi_2 = -\phi_1$. Therefore, the phase modulated part of Eq. (3.2) yields zero, resulting in a chirp-free amplitude modulated signal. This mode of operation is referred to as push-pull mode.

The power transfer function of the MZM is obtained by squaring Eq. (3.2), and is shown in Fig. 3.6b. The two operating points, OP1 and OP2 are also shown. Operating at the first point, known as the quadrature point, requires a bias voltage of $-V_\pi/2$ and allows for a peak-to-peak modulation of V_π. The fluctuation in the drive voltage is translated to an amplitude modulated signal. The second operating point is found at the minimum transmission point, which requires a bias voltage of $-V_\pi$. At this operating point, a π phase shift occurs in the transfer function. Therefore the phase of the light can be modulated with a maximum peak-to-peak modulation of $2V_\pi$.

IQ modulator

The MZM is capable of modulating only a single dimension of the optical carrier, which is sufficient for formats such as OOK or BPSK. However, to modulate QAM constellations, both in-phase and quadrature components of the carrier have to be modulated. This can be achieved by combining two MZMs, of which one has its output shifted by $\pi/2$, as is depicted in Fig. 3.7. In this structure the two MZMs are operated in push-pull mode with a driving voltage given by $u_I(t)$ and $u_Q(t)$. The phase modulator in the bottom arm is excited with a DC voltage u_ϕ such that it introduces $\pi/2$ phase shift. Consequently, the output of the subsequent MZM can be expressed as an imaginary contribution to the total output field, which is given as:

$$E_{\text{out}}(t) = \frac{E_{\text{in}}(t)}{2}\left[\cos\left(\pi\frac{u_I(t)}{2V_\pi}\right) + j\cos\left(\pi\frac{u_Q(t)}{2V_\pi}\right)\right] \tag{3.3}$$

Modulators that modulate the in-phase and quadrature of both polarisations of the light are also available as integrated modules. The polarisation of the incoming CW signal is split by a polarisation beam splitter (PBS) and each output is guided through an IQ-MOD. This enables transmission of 4D symbols, which can be designed to be more resilient to effects such as polarisation mode dispersion (PMD) and polarisation dependent loss (PDL) [86–89].

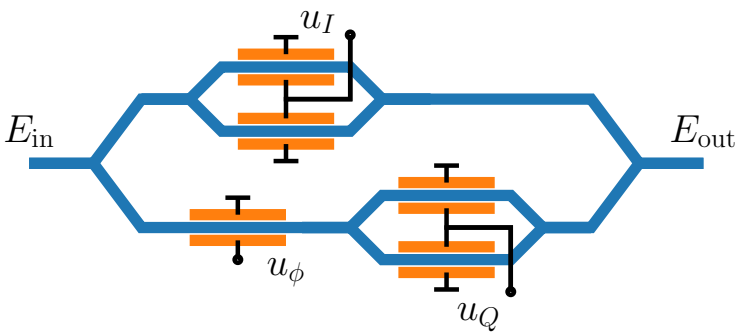

Figure 3.7: Integrated IQ-modulator containing two nested Mach-Zehnder modulators and a phase modulator.

3.2 Fibres for space-division multiplexing

The single-mode fibre (SMF) gained interest for optical communication due to favourable properties, such as low attenuation over a wide bandwidth, the lack of modal dispersion, and low production costs as a result of the simpler step-index profile. However, the nonlinear properties of the material limit the capacity [13]. As has been outlined in Chapter 1, demand for bandwidth is rapidly approaching this limit. Therefore, spatially multiplexing of signals is proposed as a method to increase system capacity. A straight forward implementation of SDM is operating multiple SMF links in parallel, offering a linear scaling in capacity but also an approximately linear increase in costs, as each link requires its own set of components. Cost reduction could be achieved by small levels of integration, such as CW sources and sharing pump lasers in optical amplifiers [90]. However, to further reduce costs more integration is required, therefore, multi-mode and multi-core fibres are proposed to increase fibre capacity. The five fibre types discussed in this section are shown in Fig. 3.8.

3.2.1 Multi-mode fibres

Multi-mode fibres are widely deployed in combination with low-cost optical sources in the 850 nm range for short communication links. Since all guided modes carry the same data, pulse broadening due to the large differential mode group delay (DMGD) limits the reach of such links to datacentre, in-building or campus networks. All guided modes are in principle orthogonal to each other, and could thus be exploited as individual data channels. This is the concept of mode-division multiplexing (MDM) over multi-mode fibres. However, managing the coupling, differential losses and dispersion between the possible hundred modes is challenging.

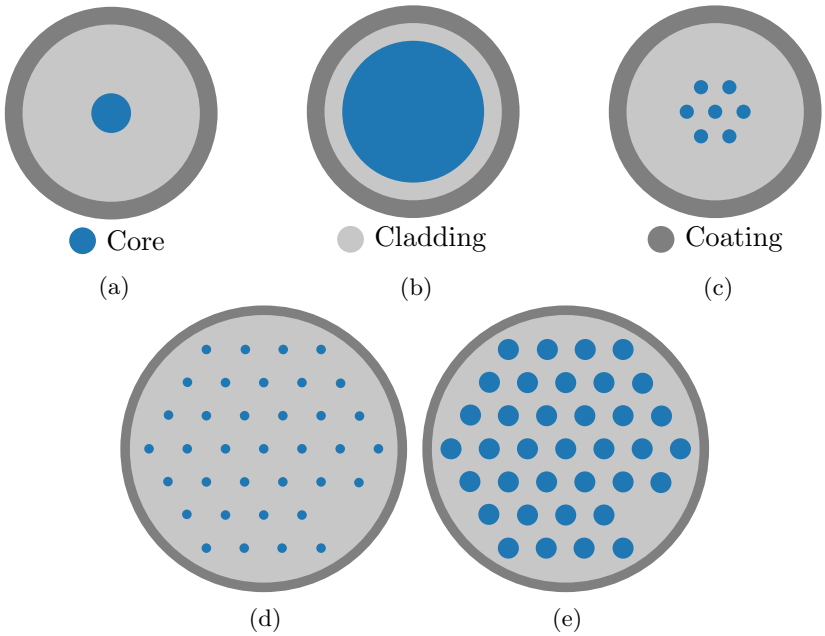

Figure 3.8: (a) Few-mode fibre, (b) 50 µm core diameter multi-mode fibre, (c) coupled-core fibre. (d) (uncoupled) multi-core fibre, (e) few-mode multi-core fibre.

Few-mode fibres

To simplify these challenges, multi-mode fibres supporting only a limited number of modes were proposed. These few-mode fibre (FMF) typically support 3, 6, 10, or 15 linearly polarised (LP) modes [91–95]. Therefore, managing the properties of the guided modes and addressing the challenges of coupling, losses, and differential mode delay (DMD) is less challenging. Especially for a 3-mode fibre, as only a single DMGD value has to be managed due to the mode degeneracy of the LP_{11} mode. Therefore, this could be realised by designing a depressed cladding step-index fibre [27]. However, the lower modal dispersion of the graded-index profile is a more suitable candidate for scaling towards higher spatial multiplicity.

The design procedure [96] for low DMGD graded-index FMF with m-modes starts by choosing the highest possible V parameter that supports m modes. Subsequently, the core radius a and numerical aperture (NA) are optimised to achieve the designed V number. Next, a low refractive index trench is added to the cladding to increase the index difference between the higher-order modes and cladding. Increasing the trench volume decreases the bend losses of bend-sensitive supported modes. However, increasing the volume also decreases the losses of undesired leaky LP modes. Consequently, the volume is optimised to ensure macro bending losses

below 10 dB/turn for all m modes, while ensuring sufficient losses for the leak higher-order modes. Finally, the α-parameter (2.8), determining the curvature of the graded-index profile is optimised to minimize the DMGD. Generally, $\alpha \approx 2$, which results in a parabolic index profile. By applying this design strategy to few-mode fibres, a maximum |DMGD| between any two modes less than 10 ps/km is theoretically possible for a 10 mode fibre. However, due to variations in the refractive index profile introduced during the manufacturing process, the DMGD of few-mode fibres is significantly larger, e.g. from a designed 8.6 ps/km, to a measured 80 ps/km for a 10-mode fibre [94]. Therefore, scalability of low DMGD FMF is challenging.

50µm core diameter multi-mode fibres

A closer match to the designed profile can be realised by utilising the matured manufacturing process for 50 µm core diameter multi-mode fibres. Consequently, the number of modes guided by the larger core size is 55-LP modes [97]. The design procedure towards low DMGD MMF is similar to FMF design, although the core size is fixed. Compared to the FMF, the DMGD between the first 3 mode-groups is larger. However, if the fourth and fifth mode-groups are also taken into account, the DMGD of the MMF is lower than for 6-, or 9-LP fibre [97].

The n quasi-degenerate modes inside mode-group n experience stronger coupling compared to inter-group coupling, due to similar propagation constants. When the transmitted signals spread over modes due to this coupling, the complete impulse response is required to recover the data at the receiver. Hence, low DMGD is preferable to minimize low computational complexity.

Alternatively, lower computational complexity can be achieved by reducing the crosstalk, which allows for multiple smaller MIMO equalisers. This can be realised by breaking the degeneracy of the modes. To decrease the beat length (Eq. (2.44)), the difference in phase velocity between any two modes has to be enlarged. Increasing the small phase velocity difference between degenerate mode is the most challenging. However, it can be realized by moving away from circular core fibres. In an elliptical few-mode core fibre, the degenerate LP modes have different propagation constants because of the birefringence introduced by the core asymmetry [98]. This allows for mode division multiplexed transmission with standard 2×2 MIMO processing to undo polarisation mixing, as has been demonstrated [99, 100]. MIMO DSP could be completely avoided, when also the degeneracy of the polarisation is broken [101]. Other core designs, such as ring-core fibres [102] and rectangular core fibres [103] could also be used to decrease the mode coupling during transmission. The latter is of interest since the core profile matches with planar waveguides in photonic integrated circuits. Even though fibres can be designed to have low modal crosstalk, it can add up during transmission as a result of fibre imperfections and Rayleigh scattering. Furthermore, fusion splices, connectors, amplifiers, and switches can introduce spatial channel cross-

talk. Therefore, low cross-talk fibres are mainly of interest for passive short-distance optical communication links.

3.2.2 Multi-core fibres

The SDM variant closest to the parallel single-mode fibre solution is the multi-core fibre (MCF), which hosts multiple cores in a single cladding (Fig. 3.8d). For a design with sufficient spacing between the cores, the cores act as independent waveguides and the inter-core crosstalk can be calculated using coupled-power theory [104, 105]. This theory implies that crosstalk can be reduced by increasing the core pitch or employing heterogeneous core designs resulting in a larger difference of propagation constants of neighbouring cores. Furthermore, low refractive index trenches or holes around each core improves the light confinement, thus also reducing inter-core crosstalk.

Increasing the spatial multiplicity of MCFs by adding additional cores results in large cladding diameter fibres, which will impact the mechanical strength of the fibre. Next to the more difficult manufacturing and handling of fragile fibres, deviating from the standardized 125 µm cladding diameter means incompatibility with cabling processes and fibre processing instruments. Furthermore, rotational alignment has to be taken into account when connecting two fibre sections. Advanced fusion splicers with end-facet view are capable of automatic alignment of MCFs based on visual feedback. Generally, a visual reference marker is added to remove any ambiguity due to symmetry. However, the alignment accuracy is generally lower compared to conventional centric single-core fibres, resulting in slightly higher splicing losses. Multi-core fibres have been reported with over 30 single-mode cores in various transmission experiments [106, 107].

Coupled-core fibres

Instead of minimizing the crosstalk between cores by increasing the core pitch, a coupled waveguide structure is obtained by reducing the core pitch. Light in the coupled cores propagates in so-called super modes, which are mode field distributions that span over multiple cores [108, 109]. As the propagation of super modes is comparable to modes in multi-mode fibre, the MCF behaves as a MMF. The strongest coupling is achieved when the difference in propagation constant between super modes is comparable to variations introduced by perturbations. In this strongly-coupled regime, the super modes mix continuously during propagation, resulting in a low DMGD. Coupled-core fibre (CCF) with 4, 7, or 12 cores with significant shorter impulse responses compared to graded-index multi-mode fibres have been demonstrated [110–113].

Few-mode multi-core fibres

Multi-mode and multi-core fibre technology can be combined to achieve the highest spatial multiplicity [33, 114–116]. For this type of fibre, both inter- and intra-core

crosstalk has to be taken into account. Since in any practical transmission link, mode interaction will occur as a result of perturbations of the fibre, fusion splices, and other multi-mode components, suppressing inter-core crosstalk is key in the design of FM-MCF. This can be realised using the same design approaches as applied to the single-mode MCF. Maintaining a consistent core profile for all cores over a long length of MCF is challenging, therefore the behaviour of the few-mode cores can differ significantly, as will be demonstrated for a 39-core 3-mode fibre in Section 5.6.

3.3 Spatial multiplexers

Connecting the single-mode transmitters and receivers to an SDM fibre requires a spatial multiplexer and demultiplexer. Since the transmission experiments are focussed on mode-division multiplexing, this section is mainly discussing different types of mode-multiplexers. Due to the reciprocal properties of these solutions, they can also be employed as demultiplexers.

3.3.1 Phase plates based solutions

One of the first implementations of mode-multiplexers was based on optical phase plates [27, 118, 119], of which a 3-mode version is depicted in Fig. 3.9a. The light from each single-mode fibre is collimated and converted by a phase plate to one of the higher-order LP modes. By employing conventional beam-combiners the inputs are multiplexed and coupled into the few-mode fibre. As the required number of beam-combiners scale linearly with the number of modes, also the insertion losses increase with 3 dB per mode. Therefore, this solution is not scalable to a large number of modes. Other disadvantages of this type of multiplexer are the bulky

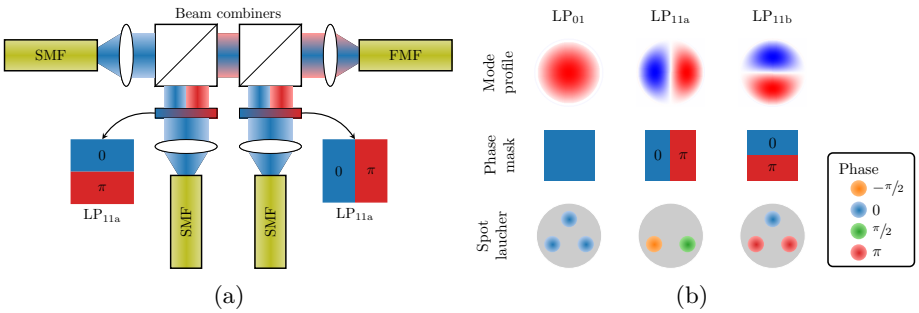

Figure 3.9: (a) 3-Mode multiplexer based on optical phase plates. All blue beams represent LP_{01} modes, that are converted by phase masks to LP_{11} modes (red/blue). (b) The relationship between the LP modes, phase masks, and the phase and position of the spot launcher [117].

size and temporal instability. The high mode selectivity, on the other hand, is a major advantage. Alternatively, the phase masks can be generated using an liquid crystal on Silicon (LCoS) based spatial light modulator (SLM) [25, 120, 121]. As a result of the dynamic control of the phase mask, each hologram can be optimized for the individual modes, and misalignments can be corrected by applying beam steering. The downside of this solution is the polarisation dependence of the SLM and higher insertion losses.

3.3.2 Spot launching

The second-generation spatial-multiplexers were based on a technique called spot-launching, which samples the optical field of the FMF with multiple single-mode spots. This field is a superposition of the N mode fields supported by the fibre. By sampling this optical field in amplitude, phase, and polarisation with $N/2$ spots, an approximation of the optical field is obtained [117]. The factor of 2 accounts for the 2 polarisations of an SMF. The position and relative phase of the single-mode beams incident on the few-mode fibre is shown in Fig. 3.9b. The mode profiles, and corresponding phase plates required to convert a fundamental mode to an LP mode are included for reference. This solution does not require beam-combiners, hence a lower insertion loss (IL) can be achieved. However, the alignment of single-mode fibres to the right position on the fibre can become challenging for a larger number of modes.

3.3.3 Fibre based photonic lanterns

Due to excessive losses and the large footprint of the other two multiplexing techniques, fibre-based solutions were proposed. The photonic lantern (PL) exploit the same principles of spot launching but are an all-fibre solution [122–125]. Therefore, they can be easily fusion spliced to both single-mode and few-mode fibres, reducing the excess losses of the multiplexer. Photonic lanterns have a background in astronomy, where they are applied to increase the system numerical aperture while maintaining the processing in the single-mode domain [126].

Photonic lanterns are fabricated by positioning N single-mode fibres in a low refractive capillary according to a geometric structure that matches with the mode profile [124, 125]. This is the same geometry as employed in the spot launching multiplexer. The structure is then tapered by heating and stretching the assembly. After a certain tapering length, the single-mode cores cease to be effective waveguides for the optical field. The fused claddings of those fibres will become the core of a few-mode waveguide, with the lower refractive index capillary as a new cladding. For a perfect adiabatic tapering, the transition from single-mode to few-mode is unitary and thus lossless. However, in practice, IL of less than 1 dB can be achieved for 3-mode multiplexers, with slightly higher values as the number of modes increase. Photonic lanterns for SDM up to 15 modes have been repor-

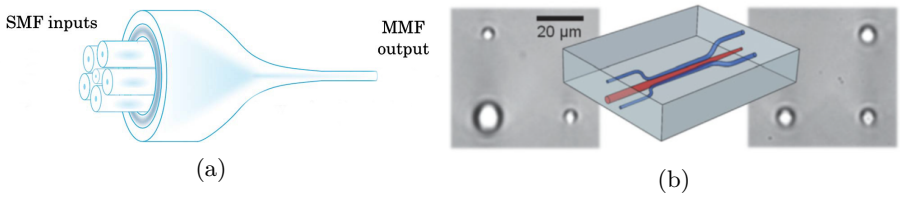

Figure 3.10: (a) Artist impression of a 6-port photonic lantern. (b) Schematic of a 3-mode 3D-waveguide spatial multiplexer and its facets.

ted [127, 128]. For a larger number of modes, matching the required geometry and minimising the mode dependent loss (MDL) becomes challenging.

The first-generation PLs for SDM applications was manufactured with similar single-mode fibres. Since the propagation constant is equal between all inputs, a fully mixed combination of the input signals is obtained at the few-mode facet of the multiplexer. To improve the mode selectivity and obtain a direct mapping between the single-mode ports and LP modes, the degeneracy of the modes has to be broken. Employing dissimilar single-mode fibres in the fabrication result in different modal evolutions of each fibre among the tapered section, and thus improving mode selectivity [129–131].

3.3.4 Glass inscribed waveguide

To achieve mode coupling, it is not strictly required to diminish the cores of the single-mode fibres. Positioning them closer together would also result in a larger multi-mode core. Since this approach is impractical to realise with optical fibres, the structure is inscribed in a glass substrate. The waveguides are created by locally changing the refractive index of the material by exciting it with focussed femtosecond pulses [132–134]. This glass inscribed variant has numerous advantages over the fibre-based photonic lantern. Firstly, a larger versatility of the geometric layout can be realized. For example, manufacturing a fibre-based PL for a few-mode multi-core is significantly more challenging compared to the glass inscribed variant [33, 135–137]. Furthermore, the inscribed waveguide index profile can be close to a step-index fibre, resulting in a high mode-selectivity. The largest disadvantage of this solution over the fibre-based variant is the high propagation losses of the material. Also, the coupling to the fibre is an additional source of loss.

3.3.5 Multi plane light converter

A mode-multiplexer can be mathematically described as a conversion between two sets of orthogonal optical fields. The transformation from N single modes to N orthogonal modes can be expressed as a single continuous unitary transformation.

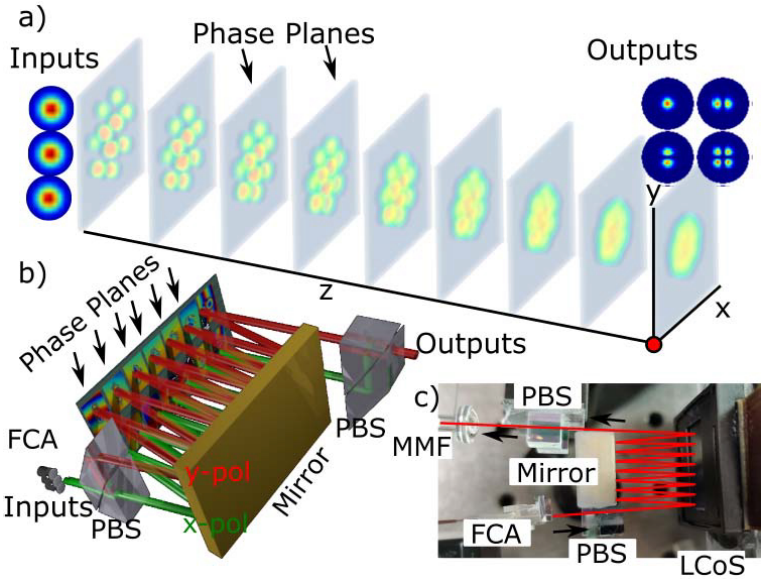

Figure 3.11: Programmable MPLC based on LCoS SLM. (a) Spatial transformation described by cascaded phase planes. (b) Dual-polarisation folded implementation. (c) Experimental realisation. [J15]

In [138] it was demonstrated that any unitary spatial transform can be approximated by a succession of phase profiles, separated by optical Fourier transforms, which is visualised in Fig. 3.11a. From the mathematical model follows that each mode can be generated with two masks [138]. However, it does not specify a minimum number of masks required to generate the simultaneous transformation of multiple modes.

An objective-first design approach is generally applied to calculate the phase profiles of the individual masks. In this optimisation process, the design objective is prioritised, even if it results in not satisfying the underlying physics [139]. More specifically, the design is optimised subject to a boundary value formulation applied to the difference of input and output electromagnetic fields. As a result of the reciprocal property of light, an input can only excite a given output, when the forward propagating wave matches with the backward propagating wave at every spatial position. The residual phase error at each coordinate can be computed and applied as a correction to the phase mask. For a multi-plane light conversion (MPLC) this optimization is performed iteratively for each phase mask. Individual masks can be designed by a sequence of optimisations applied to each phase mask for a forward and backward propagating wave. For mode selective devices, the overlap integral matrix describing the coupling efficiency of modal inputs to outputs at the phase plates is maximized. For non-mode selective devices, the MDL and

IL are minimized. Additional constraints to favour broadband adiabatic solutions are added to reduce the probability of converging towards a local minimum [140].

The designed phase masks can be fabricated on silica using lithography, or projected by a programmable SLM. A high-reflective mirror is positioned in parallel to the phase planes to reflect the beams towards the next phase mask section (Fig. 3.11b and c). Employing this type of multiplexer, 45 LP modes in a 50 µm core diameter multi-mode fibre [97] have been excited [140]. The converged solution requires 14 masks to convert all 45 inputs to the 45 modes of the fibre, which is the same number of plates required for commercial 10-mode MPLC [141]. Note that the most efficient basis to represent the modes might not be the LP modes.

3.4 Optical switching and routing

Reconfigurable optical add-drop multiplexers (ROADMs) are reconfigurable optical multiplexers that allow wavelength channels to be added or dropped at a node in the network. It can also be employed to reroute wavelength channels without adding or dropping them. Due to the reconfigurability, this component is a signature difference between flexible optical networks and point-to-point links.

Key component of a ROADM is the wavelength selective switch (WSS) that can redirect wavelength channels from an input port to a different output port. Modern ROADMs employs multiple of these switches to provide colourless, directionless and contentionless operation [142]. This allows an input signal on any wavelength channel to be switched to any direction without the potential issue of colliding with another channel at the same wavelength inside the ROADM.

Each of the WSS inside a ROADM consists of a diffraction grating, beam shaping optics, and a switching engine. Light entering from one of the inputs is collimated and guided through beam shaping optics before it encounters a diffraction grating. Upon reflecting on the grating, the wavelength channels are spatially separated. Consequently, each wavelength channel hits a different element of the switching engine. Subsequently, each wavelength channel is redirected to one of the output fibres via the diffractive grating and beam shaping optics.

Two commonly employed switching technologies are micro-electro-mechanical systems (MEMS) and liquid crystal on Silicon (LCoS) [143]. MEMS are micro-mirrors, that can be tilted by applying an electrical signal. The latter is the same technology as employed in displays and the MPLC spatial multiplexer. Each pixel of the LCoS can be programmed to introduce a phase shift, thereby steering the beams. As the number of pixels exceeds the number of channels, this technology allows flexible grid allocation, by grouping multiple pixels [144].

For channel routing in WDM-SDM optical networks, two cases can be distinguished based on the spatial channel crosstalk. Coupled spatial channels have to be switched together for MIMO equalisation at the receiver, whereas uncoupled channels can be routed individually. For the first, a single-mode WSS can be adapted to switch multiple spatial channels simultaneously, which has been demonstrated for

3-modes [145]. However, the difference in the mode profiles led to mode-dependent passbands and spectrally dependent mode mixing [146]. Alternatively, spatial multiplexers could be employed at the inputs and outputs of the WSS, which allows for more conventional single-mode switching [147].

Uncoupled spatial channels allow for full space and wavelength granularity for switching. However, it requires a large number of switches with a large port count WSS to fully exploit this flexibility. Therefore joint switching of spatial or wavelength channels to some extent is suggested to reduce the complexity scaling of SDM-WDM ROADMs [142]. The experiments in this thesis focus on point-to-point links and thus do not include ROADMs.

3.5 Optical amplification

Even though the attenuation in optical fibres have been reduced significantly, from the 1000 dB/km in the early designs in the 1960s, to typical values below 0.2 dB/km for standard single-mode fibre (SSMF) [34]. This value is close to current attenuation limit, which is reflected in the relative small difference with the lowest reported fibre attenuation of 0.1419 dB/km [39]. Therefore, signal amplification is required for long-haul communication.

Long-haul optical fibre connections up to the early 1990s relied on 3R signal regeneration to overcome the degradation of signal power. The 3R scheme requires expensive optical-electrical-optical (OEO) conversion to apply reamplification, reshaping, and retiming of data pulses [148]. Moreover, the OEO conversion has to be applied on an individual wavelength channel. Therefore, it is not a (cost) efficient method for wavelength-division multiplexed transmission systems. A more promising solution was found in the optical amplification of erbium doped fibre amplifier (EDFA), capable of amplifying all channels in the 35 nm wide spectrum of the C-band [6].

3.5.1 Erbium doped fibre amplifiers

Optical amplifiers, such as the erbium doped fibre amplifier (EDFA), have an active medium which is doped with a rare-earth material. The operating wavelength region of each type of amplifier is dependent on both host material and dopant. Optical amplifiers rely on population inversion and stimulated emission to amplify optical signals. These phenomena will be explained for the EDFA, since this type will be employed in the transmission experiments in Chapters 6 and 7.

The energy level diagram and the transitions for Erbium ions (Er^{3+}) in silica are shown in Fig. 3.12. The energy levels of the three depicted bands correspond to wavelengths of 980 nm, 1530 nm and 1600 nm, and all transition types in the figure are numbered. The first type of transition occurs when the active medium is pumped with an optical laser operating at 980 nm and electrons from the ground-state band are excited to the pump-band (1). Subsequently, a fast decay ($\sim 1\,\mu s$) to a meta-stable band occurs by the release of energy in the form of phonons

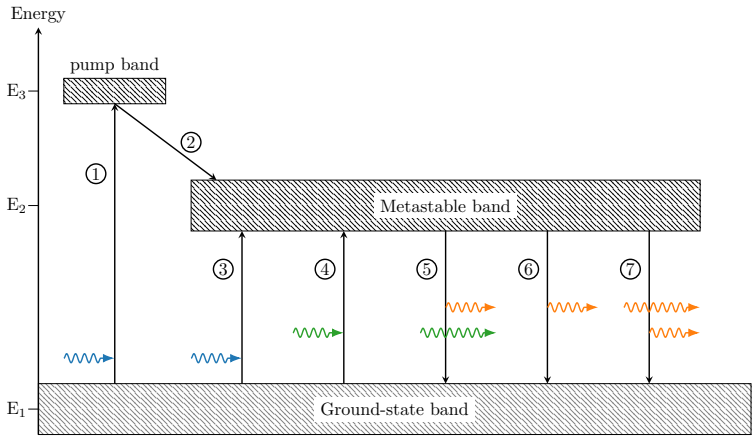

Figure 3.12: Energy level diagram and transitions of Er^{3+} ions in silica. Photons can be categorized in three types: pump photons (blue), signal photons (green), and emitted photons (orange). The numbers correspond to the following transitions: 1) absorption of 980 nm pump light, 2) fast non radiative decay of excited ions, 3) absorption of 1480 nm pump light, 4) spontaneous absorption, 5) stimulated emission, 6) spontaneous emission, and 7) amplified spontaneous emission.)

(2). Alternatively, in-band pumping at 1480 nm can be applied to directly move electrons from ground-state to the metastable band (3). As the photon energy is inversely proportional to its wavelength, pumping at 1480 has a higher optical power conversion efficiency compared to 980 nm pumps. However, stimulated emission of the pump photons results in a higher noise figure. Next to excitation of erbium ions by pumping the active medium, also photons of the signal in the transmission band can be absorbed, which is represented by transition (4). Due to this spontaneous absorption, sufficient pump power is required to avoid high signal losses. The process of exciting ions to a higher energy state is referred to as population inversion.

An external photon flux can trigger the transition from the metastable back to the ground-state band. During this transition, a photon is emitted with the same frequency, phase, and direction as the photon that triggered the process of stimulated emission (5). Both original and generated photons can trigger stimulate emission, thereby amplifying the signal. However, when an excited ion is not stimulated within its approximate 10 ms lifetime, it will fall back to the lower energy state. The emitted photon, with an arbitrary frequency, phase, and direction (6) can also trigger a chain reaction of stimulated emission (7). This phenomenon is known as amplified spontaneous emission (ASE), and is the dominant noise source in EDFAs.

The total amount of noise added by an optical amplifier is reflected in its noise

figure (NF), which is defined as the ratio between the SNR at the input and output:

$$\mathrm{NF} = \frac{SNR_{\mathrm{in}}}{SNR_{\mathrm{out}}} = \frac{1 + 2n_{sp}(G-1)}{G}, \tag{3.4}$$

where G is the amplifier gain, given as the ratio between optical output and input powers. The spontaneous emissions factor n_{sp} denotes the completeness of population inversion, and is equal to 1 for a completely inverted population. Note that for an infinite large gain, the noise figure converges to 3 dB, which is the quantum limit for phase insensitive amplifiers.

The pump signal can be provided such that it co-propagates with the signal, resulting in high population inversion at the beginning of the active fibre. Alternatively, a counter-propagating pump signal can be provided at the end of the active medium. The latter provides a higher output power at the cost of a higher noise figure and is commonly deployed as a booster amplifier at the transmitter. The lower noise figure and output power forward pumping strategy is typically deployed as a pre-amplifier to ensure the minimum power requirements of the receiver is satisfied. Instinctively, a combination of both pumping schemes can be employed for more uniform population inversion along the active medium resulting in balanced gain and noise figure at a higher economic cost.

To further improve the efficiency of optical amplifiers the material is co-doped with Ytterbium (Yb), which absorbs the pump light around 976 nm. The excited Yb^{3+} ions transfer their energy to Er^{3+}-ions, thus improving the gain around 1550 nm [149, 150]. This is of interest for the high pump power requirements of SDM amplifiers as will be shown later in this chapter.

3.5.2 Raman amplifier

The lumped amplification of cascaded EDFAs results in large variations between the maximum and minimum signal power along the link, which potentially results in nonlinear signal distortions. Distributed amplification, where the gain is spread out over the transmission medium, can be realized by employing Raman amplifiers. This amplifier type relies on the nonlinear stimulated Raman scattering (SRS) effect.

Raman scattering is an interaction between photons and molecular vibrations [64, 151]. When a photon is scattered by the material, part of its energy can be absorbed by the molecule in the form of vibrational energy. According to the conservation of energy, the frequency and energy of the scattered photon is reduced. This frequency is referred to as Stokes shift, and the resulting photon a Stokes photon. For silica, the Stokes shift in the C-band is in the range of 80 nm to 100 nm. It is also possible for the material to lose energy and increase the photon energy. This generation of anti-stoke photons is less likely in silica and is thus not efficient for amplification.

If the Raman scattering is triggered by a signal photon, the generated stokes photon has the same frequency, phase, and polarization state. Hence, it can

be applied for signal amplification. Generally, this is realized by pumping the transmission fibre with multiple pump lasers in the 1400 nm to 1500 nm range. Besides a broader gain spectrum, the spectrum can be flattened by controlling the relative powers of each pump. Both forward and backward pumping could technically be applied to distributed Raman amplifier (DRA). However, the first would result in high optical signal power in the first part of the span, which could lead to detrimental performance due to other nonlinear transmission impairments.

DRA is often employed in combination with EDFAs in a hybrid amplification scheme [152]. The DRA compensates partly for the attenuation of the fibre span, and the EDFA mitigates the residual signal power loss. Raman amplification can also be applied to few-mode fibre-links [153, 154], by distributing the pump light over the spatial modes.

3.5.3 Amplifiers for space-division multiplexing

Important for the performance of optical amplifiers is a balanced performance of all channels. For single-mode amplifiers, this is limited to controlling the spectrum gain tilt to ensure a flat transmission spectrum. Additionally, SDM amplifiers have to be designed to also ensure an uniform amplification among all spatial channels. The difference in gain between spatial channels is referred to as differential modal gain (DMG) or mode dependent gain (MDG), and has a similar impact on transmission capacity as MDL. Hence, both DMG and MDL are collectively referred to as MDL. Since MDL is a fundamentally performance-limiting factor [155], design of SDM amplifiers with DMG is key for the actual deployment of SDM in long-haul optical transmission systems.

Gain equalisation in single-mode multi-core fibre amplifiers can be realised by gain flattening filters operating on the individual cores [156, 157]. Due to the mixing of modes, such a device is not compatible with few-mode fibres. Therefore, the overlap of dopant distribution, signal mode profile, and pump mode profile, which govern the amplification efficiency has to be optimized [158]. Maximizing the overlap integral for single-mode amplifiers is relatively simple since the signal has only a single mode-profile, namely the Gaussian distribution of the LP_{01} mode. However, in MDM systems, the optical field is given as the sum of modal field distributions, each with distinct profiles. When providing a single-mode pump to a few-mode fibre core, the transmitted fundamental mode will experience a larger gain compared to the higher-order modes, as it has a large overlap with the pump distribution. One way to increase the gain for higher-order modes is by offset launching the pump signal. However, matching the radial symmetry of a mode profile is challenging with only a single pump. Alternatively, the single-mode pump profile can be modified using optical phase plates to closer match the signal mode distribution. Core pumped amplifiers supporting up to 10 modes in a few-mode fibre [159, 160], up to 19 cores in a multi-core fibre [161, 162] have been reported. Also FM-MCF amplifiers can be realised by employing core pumping [163].

Generating the high optical pump power required to amplify multiple modes simultaneously can generally not be delivered by a single pump diode, especially for a large number of modes such as in multi-mode fibres. It is possible to combine the outputs of multiple single-mode pumps, but this is not an efficient method to pump such an amplifier. Cladding pumping the active fibre with a multi-mode pump is a more efficient method to provides high optical pump powers compared to single-mode core-pumping. Due to the larger beam size, multi-mode pump diodes can generate high optical powers at low brightness levels. Furthermore, the large number of spatial pump modes supported by the cladding provide a more equal energy distribution among the guided modes, thereby reducing the DMG. Moreover, cladding pumping can be realised in a fibre only solution, where the pump fibre is tapered and twisted around the active fibre [164]. The coating of both fibres has been removed and a new low refractive polymer is applied to the structure, enhancing coupling of the pump to the cladding. Any residual pump power can be dumped by applying a high refractive polymer near the end of the active fibre section, increasing the radiant losses of pump energy. This side-coupling approach allows for conveniently splicing active and transmission medium. Whereas the low brightness allows for coupling of high optical power, it also limits the maximum level of population inversion and results in a higher noise figure (typically an additional 1 dB [4]) compared to core pumping. Amplification in FMF up to 10 modes [164, 165], and even 36 LP modes in multi-mode fibre [166] has been reported using cladding-pumped amplifiers. Cladding pumping can also be applied to multi-core fibres to provide a homogenous gain among the cores [167–169]. Furthermore, it does not require pump couplers to excite individual cores.

The second design strategy to minimize DMG is tailoring the dopant distribution in the active medium. As a result of the close to uniform pump field distribution of cladding pump amplifiers, controlling the dopant distribution is an efficient way to minimize MDG in few-mode amplifiers. For core-pumped schemes, the pump field and dopant distribution are generally co-optimised to achieve low mode differential gain. As can be seen in Fig. 3.13a, an uniform doping distribution results in a large preferential gain for the fundamental mode. To equalise the gain for this 3-mode step-index example, the erbium dopant concentration is reduced in the centre, resulting in a centre-depressed or raised-edge dopant profile. In the most extreme implementation, all dopants reside on the edges of the profile, with a close to zero concentration at the centre. A schematic representation of such a ring-doped fibre core is depicted in Fig. 3.13b. This design principle can be extended to a multi-ring doping structure for large-mode-count few-mode amplifiers [170]. Other doping distributions include cladding doping [171], or oversized core fibres [165] However, manufacturing complex doping distributions requires high accuracy chemical vapour deposition processes and is limited by inevitable dopant diffusion.

Finally, the modal distribution of the signal can be optimised to increase the overlap with pump and dopant distribution by changing the refractive index of the fibre. A common adjustment is a dip in the refractive index section around the

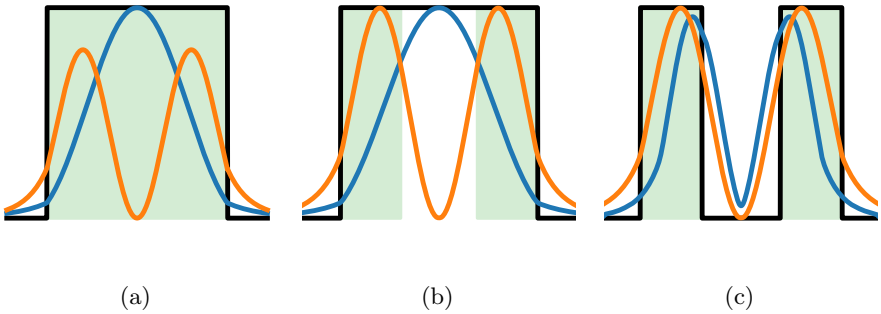

Figure 3.13: Three different doping distributions applied to a 3-mode amplifier. The LP_{01} mode and LP_{11} modes are represented by the blue and orange lines, respectively. The doped area is colour shaded. (a) Uniformly doped fibre core, (b) ring-doped core, and (c) ring-core fibre.

centre. By decreasing the refractive index, the mode profile of the fundamental mode transforms slowly to a more LP_{11}-like profile. When the refractive index in the centre is reduced to the same level at the cladding, the fibre becomes a ring-core fibre as depicted in Fig. 3.13c. Due to the similar overlap factors of each mode with the erbium doped area, this type of fibre amplifier is a suitable candidate for low DMG operation [170]. However, the transition between active and passive fibre requires mode field adapters to bridge the large difference in refractive index profiles.

3.6 Receiver

At the receiver, one of the spatial multiplexers is employed reciprocally to demultiplex the N spatial channels of the SDM fibre to N single-mode channels. As a result of spatial channel mixing during propagation, each output might contain a combination of the originally transmitted data. For the MIMO equaliser to unravel the spatial channel crosstalk, all channels must be available digitally. Therefore each of the transmission system outputs is detected by a polarisation-diverse coherent receiver (PD-CRX) and converted to an electrical signal. Subsequently, an analog-to-digital converter (ADC) is employed to convert it to the digital domain after which the DSP of Chapter 4 is applied.

The remainder of this section is structured as follows: First, the principle of detecting optical signals is explained at the hand of the direct detection scheme. Next, the coherent receiver and its polarisation-diverse variant are introduced. Finally, the novel Kramers-Kronig receiver (KKRX) is touched upon as it recently received extensive interest from the community because it covers the intermediate ground of the other two detection methods.

3.6.1 Direct-detection

A direct-detection receiver employs square-law detectors to directly convert the intensity of the optical field to an electrical current. An incident optical field $\mathbf{E}$ on an ideal detector results in the following photo current [62]:

$$I(t) = \mathcal{R}\mathbf{E}\mathbf{E}^* = \mathcal{R}\left|\mathbf{E}\right|^2, \tag{3.5}$$

where $\mathcal{R}$ is the receiver responsivity in [A/W] given by:

$$\mathcal{R} = \frac{q\eta}{h\nu}, \tag{3.6}$$

where q is the electron charge, h denotes Planck's constant, and η is the quantum efficiency of the photodiode. The latter describes the number of electron-hole pairs generated per incident photon with energy $h\nu$. In practice, the photocurrent includes contributions from several noise sources. The most influential sources are shot noise and dark currents. The first type originates from the discreteness of photons and electrons. Since fluctuations in the number of generated photoelectrons are fundamental to photodetection, shot noise is the fundamental or quantum limit of receiver sensitivity. Dark currents are electrical currents generated in the detector without any incident photons.

As can be seen from Eq. (3.5), the phase information of the optical field is lost due to the square operation. Therefore, this type of detection is generally combined with the intensity modulation of a laser source, hence the name of the intensity-modulation and direct-detection (IM-DD) scheme. It is possible to detect phase-modulated signals using direct-detection by including additional hardware. The constant amplitude of phase-modulated signals produces a constant photocurrent, except at symbol transitions. Therefore, an interferometer with exactly one symbol delay between the arms is placed in front of the receiver. Consecutive symbols with the same phase will constructively interfere, whereas a phase difference will destructively interfere. Therefore, the resulting photocurrent describes the differential phases of the signal. Obviously, the bit-encoding at the transmitter must be adapted accordingly.

IM-DD is widely deployed in optical fibre communication systems, mainly of its low costs and complexity. Furthermore, the receiver sensitivity is independent of the carrier phase and the state of polarisation. However, digital compensation of transmission impairments such as chromatic dispersion is challenging since the phase information of the optical field is not recovered. To mitigate pulse broadening introduced by CD, fibre modules with high negative dispersion are included to compress the optical pulses [61]. However, these modules typically have a low effective area and are lossy. Therefore, they are susceptible to nonlinear impairments that might degrade system performance. Alternatively, the more complex coherent detection scheme can be applied.

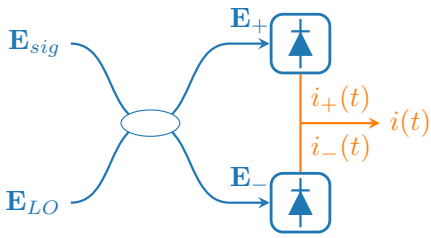

Figure 3.14: Schematic representation of coherent detection using balanced detection.

3.6.2 Coherent detection

Typical to coherent detection is the interference of the optical signal with a CW local oscillator (LO). From this beating product the complete optical field, i.e. both amplitude and phase, can be recovered and is thus available for DSP algorithms.

The basic operation principle of coherent detection will be explained at the hand of Fig. 3.14. In this figure two complex electrical fields $\mathbf{E}_{sig}$ and $\mathbf{E}_{LO}$ are combined using a symmetric coupler. These electric fields can be described by the phasor $\mathbf{E}(t) = A(t)e^{j\omega t}$, where A is the complex field amplitude and ω is the angular frequency. Subscripts sig and LO indicate whether the parameter relates to the signal or local oscillator (LO). Furthermore, the optical power of the two electrical fields is proportional to the complex amplitude squared, subject to a constant scaling factor, and is given by $P = k|A|^2$. If both fields are combined in the coupler, all cross-connections undergo a 90° phase shift, which can be translated to a 180° phase shift to the LO field between the two outputs. If perfect polarisation alignment between the signals is assumed, the output fields of the coupler are given by:

$$\mathbf{E}_{\pm} = \frac{1}{\sqrt{2}}(\mathbf{E}_{sig} \pm \mathbf{E}_{LO}) \tag{3.7}$$

and the photo currents generated by the square-law detectors with responsivity $\mathcal{R}$ is given as:

$$\begin{aligned} I_{\pm}(t) = {}^1\!/\!_2\mathcal{R}\Big[&P_s(t) + P_l(t) \\ &\pm 2\sqrt{P_{sig}(t)P_{LO}(t)}\cos\left[\omega_{IF}t + \theta_{sig}(t) - \theta_{LO}(t)\right]\Big], \end{aligned} \tag{3.8}$$

where $\omega_{IF} = |\omega_{sig} - \omega_{LO}|$ is the intermediate frequency (IF) as result of mixing the optical signals, θ_{sig} and θ_{LO} denote the phase of the signal and LO respectively. The additional mixing product $\omega_{sig} + \omega_{LO}$ is assumed to be outside the detectable bandwidth of the photodiodes, and is therefore not included in Eq. (3.8). The output of the balanced detector is the difference between the two photocurrents,

and is thus given by:

$$\begin{aligned} I(t) &= i_+(t) - i_-(t) \\ &= 2\mathcal{R}\sqrt{P_{sig}(t)P_{LO}}\cos\left[\omega_{IF}t + \theta_{sig}(t) - \theta_{LO}(t)\right] \end{aligned} \tag{3.9}$$

Note that time dependence of the LO power is dropped, because it is implemented as a constant power CW signal. For homodyne detection, where the optical frequencies of LO and signal are exactly matched, the intermediate frequency (IF) is zero, and the detector output is given as:

$$I(t) = 2\mathcal{R}\sqrt{P_{sig}(t)P_{LO}}\cos\left[\theta_{sig}(t) - \theta_{LO}(t)\right] \tag{3.10}$$

Equation (3.10) indicates that both amplitude and phase modulated signals can be recovered, either by directly observing P_{sig} in case of amplitude modulated signals, or θ_{sig} for phase modulated signals. However, it requires an optical phase-locked loop (OPLL) controlled LO to track the transmitter phase noise. Implementing such a loop is not straight forward and adds additional complexity to the receiver. Also, the exact matching of both laser frequencies imposes stringent requirements for linewidth and tunability of components.

Alternatively, when the LO frequency is chosen with an offset to the transmitter laser for heterodyne detection, no OPLL is needed. This offset must be at least larger than the electrical bandwidth to avoid spectrum folding. Consequently, the bandwidth of the detector is doubled with respect to homodyne detection. Just as for homodyne detection, this scheme can be employed for the detection of pure amplitude or phase-modulated signals. Furthermore, both types of detection benefit from increased sensitivity with respect to direct detection which results in an improvement of SNR. Note that Eq. (3.10) scales equally for P_{sig} and P_{LO}. Since the LO is generated locally at the receiver, it can be easily set to high optical powers, such that $P_{LO} + P_{sig} \approx P_{LO}$. Consequently, the shot noise becomes the dominating noise factor in the received current, even for thermal noise limited detectors. Due to the non-zero ω_{IF}, and the quadratic relation between current and power, heterodyne detection suffers from a 3 dB sensitivity penalty compared to homodyne detection. However, the design is significantly simplified because the OPLL can be replaced by a phase-locked loop (PLL) at the IF to track phase noise. Nevertheless, both implementations are incapable of capturing the complete complex optical field.

Homodyne and heterodyne detectors only extract the in-phase component, as can be seen from the cosine term in Eq. (3.8). To also detect the quadrature component, the LO is split and a phase shift of 90° is applied to one of the branches before combining it with the signal. This functionality is implemented in a 90° optical hybrid, of which two are shown in Fig. 3.15. Each of these modules operates on one of the polarisations of signal and LO, which are obtained by the PBSs. The four balanced photodetector outputs are obtained in a similar method as Eq. (3.9),

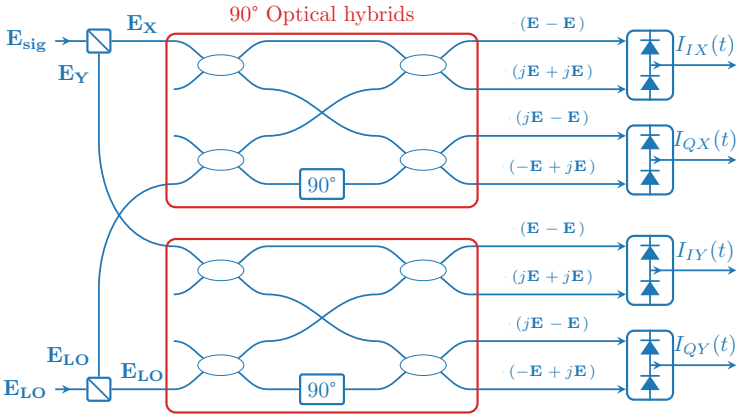

Figure 3.15: Functional diagram of a polarisation-diverse coherent detector.

and are given by:

$$I_{IX}(t) = \mathcal{R}\sqrt{P_X(t)P_{LO}}\cos\left[\theta_X(t) - \theta_{LO}(t)\right] \tag{3.11a}$$

$$I_{QX}(t) = \mathcal{R}\sqrt{P_X(t)P_{LO}}\sin\left[\theta_X(t) - \theta_{LO}(t)\right] \tag{3.11b}$$

$$I_{IY}(t) = \mathcal{R}\sqrt{P_Y(t)P_{LO}}\cos\left[\theta_Y(t) - \theta_{LO}(t)\right] \tag{3.11c}$$

$$I_{QY}(t) = \mathcal{R}\sqrt{P_Y(t)P_{LO}}\sin\left[\theta_Y(t) - \theta_{LO}(t)\right], \tag{3.11d}$$

where P_X and P_Y denote the signal power of the two polarisations. From this set of equations the complex amplitude of the field of each polarisation is obtained by combining an in-phase and quadrature component:

$$I_X(t) = I_{IX}(t) + jI_{QX}(t) = \mathcal{R}\sqrt{P_X(t)P_{LO}}\exp\{j\left[\theta_Y(t) - \theta_{LO}(t)\right]\} \tag{3.12a}$$

$$I_Y(t) = I_{IY}(t) + jI_{QY}(t) = \mathcal{R}\sqrt{P_Y(t)P_{LO}}\exp\{j\left[\theta_X(t) - \theta_{LO}(t)\right]\} \tag{3.12b}$$

The spectrum of the complex quantities in Eq. (3.12) contains both the in-phase and quadrature components. Although this detector could be operated as phase-diversity homodyne receiver with $\omega_{IF} = 0$, it is typically operated with a minimum offset between transmitter and LO, such that $\omega_{IF} \approx 0$. This type of receiver is referred to as intradyne detection, which relies on DSP to compensate frequency and phase offsets between transmitter laser and LO. Therefore, it requires the same electrical bandwidth as homodyne detection, but does not require an OPLL. Hence, it is the most practical type of detector and is thus employed in the transmission experiments of Chapters 6 and 7.

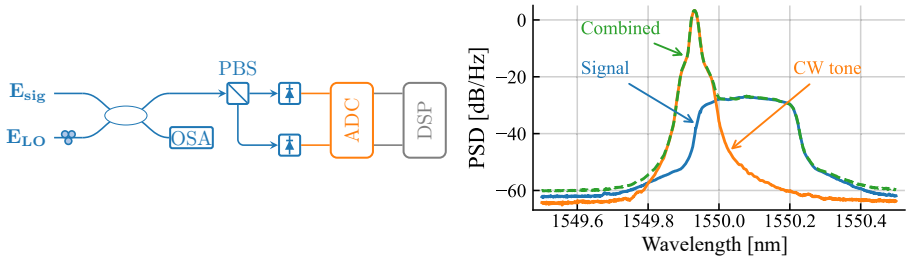

(a) (b)

Figure 3.16: (a) Polarisation-diverse KK-receiver. (b) Optical spectrum measured by the optical spectrum analyser (OSA).

3.6.3 Self-coherent Kramers-Kronig receiver

Recently a new type of receiver has gained attention as it combines the advantage of obtaining the complex field of coherent detection with the smaller hardware complexity of direct-detection. This receiver type requires a CW signal at the edge of the signal spectrum that operates as an LO at the receiver. After square law detection, the modulated signal is found on an electrical carrier related to the CW tone. If the LO has sufficient power, the detected photocurrent satisfies the minimum phase requirement needed to extract unique phase values from its intensity [172]. The reconstruction is performed digitally based on the Kramers-Kronig (KK) relations. Hence, the name of the receiver architecture. The retrieved complex field can be processed using conventional coherent DSP, allowing compensation of linear impairments such as CD and PMD.

The LO signal can be generated digitally at the transmitter, electrically before driving the modulator, or optically. Due to the minimum phase requirement, generating the high-intensity LO signal digitally results in reduced DAC resolution for the modulated frequencies that carry data. Alternatively, the LO is generated separately and electrically mixed before driving the modulator. However, this method requires sharp electrical filters and suffers from the 6 dB mixing losses. Optical generation shows high similarity to the LO in conventional coherent detection. However, tuning a second laser to exactly the edge of the signal spectrum requires precise tuning and accurate control. Furthermore, both transmitter and LO are susceptible to frequency drifts. To avoid spectral folding, an offset between the two lasers is introduced. The optical spectrum is shown in Fig. 3.16b. Consequently, the electrical carrier is shifted with the same offset. Hence, a larger bandwidth for photodiode and ADC is required.

The KK principle can also be applied to detect polarisation multiplexed signals by adding a PBS after the LO is combined with the signal [172, 173]. Note that the polarisation of the LO must be aligned such that the power is split equally over the two PBS outputs. Each of these outputs is detected by a single KKRX, after which

the complex fields are recovered independently. A standard 2×2 MIMO equaliser is employed to recover the polarisation-division multiplexed signals. Similar to detecting mode-division multiplexed signals using polarisation-diverse coherent receivers at each single-mode output of the spatial demultiplexer, a KKRX can be used instead. A functional diagram of the employed polarisation-diverse KKRX is depicted in Fig. 3.16a. The second output port of the coupler is monitored by an OSA, which spectra are shown in Fig. 3.16b [J13]. After digitisation the KK algorithm operates on all inputs independently, before it is fed to the MIMO DSP described in the next chapter.

The hardware complexity of the KKRX is comparable to the IM-DD scheme. However, the reconstruction of the complex field allows for more advanced DSP to compensate CD, PMD or even DMD. This makes the KKRX an interesting candidate for short-reach interconnects.

Summary

In this chapter five fibre types have been proposed for employment in future SDM transmission systems. The low inter-core crosstalk of uncoupled SMF shows the highest compatibility with conventional polarization multiplexed systems, as each core can be used as an independent channel. However, the multi-core structure is more challenging to fabricate and handle. This does not hold for the FMF because of its geometric structure is similar to that of SMF. This is even more true for the 50 µm core diameter graded-index MMF, which greatly benefits from the well-developed production process of OM fibres. Consequently, the DMGD of MMF is closer to its designed value with respect to FMF, which is important for the computational complexity of the DSP. Another approach towards low DMGD is decreasing the core pitch of MCF to increase the coupling between spatial channels. The DMGD of strongly coupled modes in these coupled-core fibres, develops with the square root of the transmission system instead of linear. However, the number of spatial channels is still limited to 12. Combining multi-core and multi-mode technology can achieve the highest spatial multiplicity, especially when not limited by standard cladding dimensions. However, the fabrication and fusion splicing of FM-MCFs is even more challenging as any misalignment could result in MDL.

As MDL is a fundamentally capacity limiting effect that is challenging to compensate by digital techniques it has to be minimized in the components. The MDL is mainly introduced by spatial multiplexers, switches, and optical amplifiers. For optical amplifiers, this is achieved by optimizing the distributions of dopants, signal, and pump. The latter can be provided by pumping the core of erbium-doped fibre, similar to its single-mode equivalent. The erbium ions absorb the pump energy and generate copies of the signal photons by the stimulated emission. Alternatively, the pump can be injected to the cladding from the side of the fibre. This method can provide a more uniform gain between modes, but it is less efficient.

To connect the single-mode transmitters and receivers with the SDM fibres,

spatial multiplexers are required. The evolution of different approaches for mode-multiplexers is presented. The first phase plate solution had a high mode selectivity but is bulky, not scalable due to its insertion losses. The discovery of sampling the multi-mode field with multiple single-mode fibres or spot launching quickly resulted in the development of photonic lantern. In this all fibre device, single-mode fibres are tapered to form a multi-mode facet that can be spliced to the transmission fibre. This transition is in theory lossless, and thus these devices are known for their low loss. A similar structure can be realised by inscribing waveguides into a piece of glass, to reduce the footprint at the cost of higher losses due to the material. The scalability of photonic lanterns prevents this multiplexer type to be employed in combination with MMF for now. Therefore, the multi-plane light converter is proposed. Light traversing through the phase plates in this device are stepwise converted to the desired spatial distribution of the MMF.

Depending on the spatial channel crosstalk, the outputs of the spatial demultiplexer carry combinations of the modulated signals from the transmitters. To recover the transmitted symbols, each output is detected by a receiver. As the full optical field is required in the digital domain to apply the DSP algorithm of the next chapter, either a conventional polarisation diverse detector or the novel Kramers-Kronig receiver can be employed.

Chapter 4

Digital signal processing for SDM transmission systems

The introduction of digital signal processing (DSP) to the field of optical communications enabled compensation of transmission impairments and as such boosted the capacity of these systems. Especially for coherent links as both amplitude and phase information are retrieved at the receiver. With the complex field digitally available, chromatic dispersion (CD) can be compensated digitally, avoiding the nonlinear noise related to dispersion compensated fibre (DCF) and dispersion-shifted fibre (DSF). Furthermore, the addition of 2×2 multiple-input multiple-output (MIMO) equalisation enabled data transmission over both polarisations of the optical field, thereby approximately doubling the capacity of single-mode fibre (SMF) based systems. Due to its complexity and power consumption, DSP is mainly found in the long-distance links of optical networks.

Many algorithms used in optical communications today originate from the field of wireless transmission systems. However, differences between the two domains have to be taken into account. A key difference is the rate at which symbols are transmitted. For a wireless system, this is in the order of tens of MBaud, whereas optical systems transmit at tens of GBaud. Therefore fast electronics are required for conversion between digital and analogue domains, which generally have a lower resolution compared to lower sampling speed models. Consequently, the electrical signal is of lower quality in optical systems. The high-symbol rate signals also occupy a larger bandwidth, and as such require a high-frequency carrier. For optical systems, these carriers are generated using lasers, which have a non-zero linewidth resulting in the addition of phase noise. Furthermore, the frequency of lasers tends to drift over time. The other key difference between optical and wireless communication is the channel. Fibres are known to be a nonlinear medium, which restricts the signal power and in turn also capacity. Despite differences between the two domains, the algorithms can be adapted for fibre communications.

The DSP modules implemented to extract the transmitted symbols from the

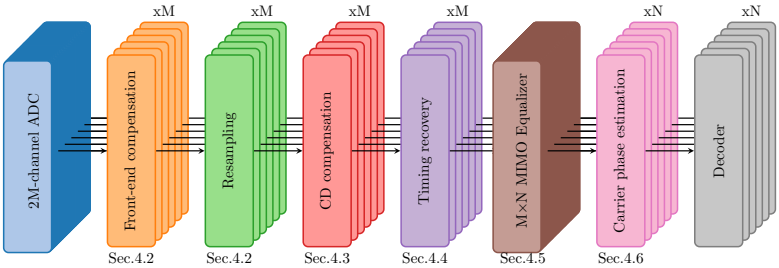

Figure 4.1: DSP flowchart

received signals of the space-division multiplexing (SDM) transmission system from the previous chapter are depicted in Fig. 4.1. The photocurrents digitized by the analog-to-digital converter (ADC) are arranged to M streams of complex numbers, representing the in-phase and quadrature of a spatial channel. For this representation to hold, any quadrature error and other front-end impairments have to be compensated. Subsequently, the channels are resampled to twice the symbol rate, followed by the removal of chromatic dispersion. Due to the independent sampling clocks at the transmitter and receiver, the samples have to be aligned with the transmitted symbols, which is performed by the timing recovery module. Next, a $M \times N$ MIMO equaliser is employed to recover the N transmitted sequences from the M received ones, as well as mitigating any dispersion introduced by differential mode delay (DMD). Carrier phase estimation is applied to each of the MIMO outputs to compensate any frequency offset between transmitter and receiver lasers, and compensating the phase noise. The equalised symbols are fed to the decoder which uses this information to decide which symbol was detected. Finally, the symbols are demapped to bits for bit error counting.

In the next section, the linear MIMO model is introduced to describe the SDM transmission system and explain the concepts of channel estimation and equalisation. The other sections of this chapter each cover one of the modules of Fig. 4.1.

4.1 Multiple-input multiple-output system model

Regardless of the number of components in an SDM transmission link, it can be represented by the linear multiple-input multiple-output model, which is visualised in Fig. 4.2. Note that in this model the transmission system is presumed to be operating in the linear regime, thus neglecting any nonlinear effects. In the fully coupled system model, the signals generated by the T transmitters are multiplexed onto n spatial channels. After transmission, m spatial channels are received and detected by R transmitters. Since a linear channel is presumed, the noise is

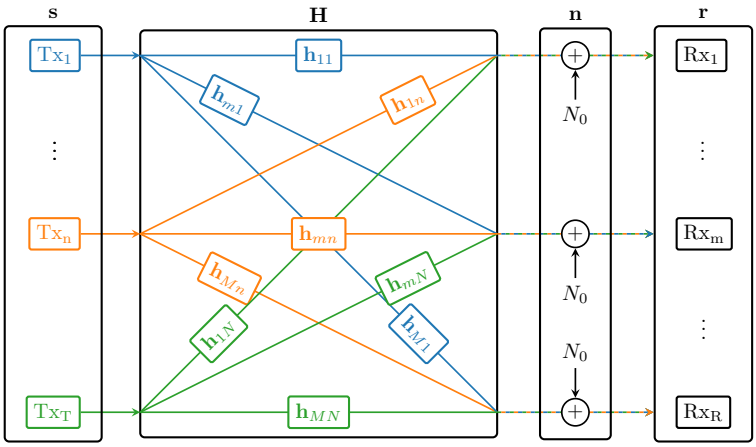

Figure 4.2: Linear multiple-input multiple-output system model.

modelled as additive white Gaussian noise (AWGN) sources with the same power spectral density N_0 for each channel.

First, consider a non-coupled system, i.e. receiver $\mathrm{Rx_m}$ detects the signal r_m, which is fully determined by transmitted signal s_n originating from transmitter $\mathrm{Tx_n}$. In that case, the signal evolution along the channel is given by:

$$r_m(t) = h_{mn}(t) \circledast s_n(t) + n(t), \tag{4.1}$$

where h_{mn} represents the linear impulse response of the system, and $\circledast$ denotes the convolution operation. Note that all signals are continuous functions of time t. However, in optical communication, quantized bits of digital information are transmitted. Therefore, all signals can be represented by their discrete-time variants, where the notation $[k]$ is used to denote the kth symbol. Expanding the convolution operation for the discretised variables in Eq. (4.1) yields:

$$r_m[k] = \sum_l \left(h_{mn}[k-l]s_n[l]\right) + n[k] \tag{4.2}$$

By limiting the summation operation to the duration of the impulse response the following vectorized expression of Eq. (4.2) is obtained:

$$r_m[k] = \mathbf{h}_{mn}[k]\mathbf{s}_n[k] + n[k]. \tag{4.3}$$

The newly defined vectors for the transmitted signal and impulse response are given by Eq. (4.4) and (4.5). The vector length is determined by the impulse response duration T_h, which can be described by $2L+1$ symbols. The vector transpose operator is denoted by $^\intercal$.

$$\mathbf{s}_n[k] = \begin{bmatrix} s_n[k+L] & \dots & s_n[k] & \dots & s_T[k-L] \end{bmatrix}^\intercal \tag{4.4}$$

$$\mathbf{h}_{mn}[k] = \begin{bmatrix} h_{mn}[k+L] & \dots & h_{mn}[k] & \dots & h_{mn}[k-L] \end{bmatrix}, \tag{4.5}$$

Equation (4.3) represents the 1×1 linear transmission model for the AWGN channel. Next, this equation is expanded to describe a sequence of received symbols, and include the multiple inputs and outputs of the SDM transmission system. Therefore, the following matrix is defined to describe the set of received signals:

$$\mathbf{R} = \begin{bmatrix} \mathbf{r}_1[k] & \dots & \mathbf{r}_m[k] & \dots & \mathbf{r}_R[k] \end{bmatrix}^{\mathsf{T}}, \tag{4.6}$$

with

$$\mathbf{r}_m[k] = \begin{bmatrix} r_m[k+L] & \dots & r_m[k] & \dots & r_m[k-L] \end{bmatrix} \tag{4.7}$$

Where $\mathbf{r}_m[k]$ is the concatenation of the signals detected by each of the R receivers. The signal detected by receiver m at time instance k is given by Eq. (4.3). Similar to Eq. (4.6), the transmitted sequences and noise vectors can be stacked to obtain a concatenation of Toeplitz matrices:

$$\mathbf{S} = \begin{bmatrix} \mathbf{s}_1[k] & \dots & \mathbf{s}_n[k] & \dots & \mathbf{s}_T[k] \end{bmatrix}^{\mathsf{T}}, \tag{4.8}$$

and a matrix expressing the AWGN for the received channels:

$$\mathbf{N} = \begin{bmatrix} \mathbf{n}_1[k] & \dots & \mathbf{n}_m[k] & \dots & \mathbf{n}_R[k] \end{bmatrix}^{\mathsf{T}}. \tag{4.9}$$

Finally, the linear MIMO transmission model can be described by:

$$\mathbf{R} = \mathbf{HS} + \mathbf{N}, \tag{4.10}$$

where the system impulse response matrix $\mathbf{H}$ has dimensions $R \times T \times (2L+1)$, and is given as:

$$\mathbf{H} = \begin{bmatrix} \mathbf{h}_{11} & \dots & \mathbf{h}_{1n} & \dots & \mathbf{h}_{1T} \\ \vdots & \ddots & \vdots & \iddots & \vdots \\ \mathbf{h}_{m1} & \dots & \mathbf{h}_{mn} & \dots & \mathbf{h}_{mT} \\ \vdots & \iddots & \vdots & \ddots & \vdots \\ \mathbf{h}_{R1} & \dots & \mathbf{h}_{Rn} & \dots & \mathbf{h}_{RT} \end{bmatrix} \tag{4.11}$$

Since the complete transmission system is described by $\mathbf{H}$, measuring it directly is key to characterisation of SDM transmission systems and understanding its limitations. If the transmitted data is known at the receiver, the channel state information can be obtained from a least squares estimation:

$$\hat{\mathbf{H}} = \mathbf{RS}^{\dagger} = \mathbf{RS}^{\mathrm{H}} \left(\mathbf{SS}^{\mathrm{H}}\right)^{-1}, \tag{4.12}$$

where † denotes the Moore-Penrose inverse. By performing an singular value decomposition (SVD) as defined in Eq. (4.13) on the channel estimation matrix, a diagonal matrix $\mathbf{\Sigma}$ and two unitary matrices $\mathbf{U}$ and $\mathbf{V}$ describing the spatial channel coupling at both sides of the transmission system are obtained.

$$\hat{\mathbf{H}} = \mathbf{U\Sigma V}^{*} \tag{4.13}$$

Along the diagonal of $\mathbf{\Sigma}$, the singular values λ_i are found in decreasing order. The singular values are associated with the electrical field gains, whereas the singular values squared represent the optical field gains of the spatial channels in the system [174]. The latter are used to define the system averaged mode dependent loss (MDL) as:

$$\mathrm{MDL[dB]} = 10 \cdot \log_{10} \left(\frac{\max \lambda_i^2}{\min \lambda_i^2} \right) \tag{4.14}$$

In the absence of mode dependent loss (MDL), all singular value would be equal to 1, and could thus be employed to transmit at their maximum capacities. As MDL increases, the optical field gains and therefore also system capacity decreases. In the case of severe MDL, λ_i can reduce to zero, resulting in channel outage [175]. Since MDL is a fundamental capacity limiting impairment, it is one of the key design parameters for SDM transmission systems and its components.

As the channel estimation matrix is extracted from a sampled time-model, the derived average system MDL yields a single value for each modulated carrier. In practice, the MDL varies for each frequency component in the spectrum, and a frequency-resolved MDL is required to accurately describe the distribution of spatial channel gains. Therefore, it is useful to use an alternative representation of the MIMO channel. By taking the Fourier transform of Eq. (4.10), the transfer function matrix in the frequency domain is obtained. To differentiate between the two domains, the notations $\mathbf{h}(t)$ and $\mathbf{H}(\omega)$ will be used for the time domain impulse response and transfer function matrix in the frequency domain, respectively. Analogue to the previous derivation of MDL, performing a SVD on $\mathbf{H}(\omega)$ yields the frequency-resolved singular values. Finally, a similar expression to Eq. (4.14) is derived for the frequency-dependent MDL:

$$\mathrm{MDL}(\omega)\mathrm{[dB]} = 10 \cdot \log_{10} \left(\frac{\max \lambda_i^2(\omega)}{\min \lambda_i^2(\omega)} \right) \tag{4.15}$$

The frequency-resolved MDL is of particular interest to the characterisation of individual components, as their bandwidth exceeds that of a single modulated carrier. Extracting the transfer function matrix of individual components from the estimated channel matrix is challenging and other methods are required to directly measure the transfer function matrix of components. To address this challenge, an optical vector network analyser (OVNA) is developed, which will be discussed in detail in Chapter 5.

4.2 Front-end impairment compensation

Impairments arising from the imperfect behaviour of optical and electrical components of the receiver are addressed by the front-end compensation module. One of these impairments is caused by an imbalance of the photodiodes inside the balanced detectors, which manifests itself as a DC offset in the detected real-valued signals, and a translation of the constellation diagram, as can be seen in Fig. 4.3a.

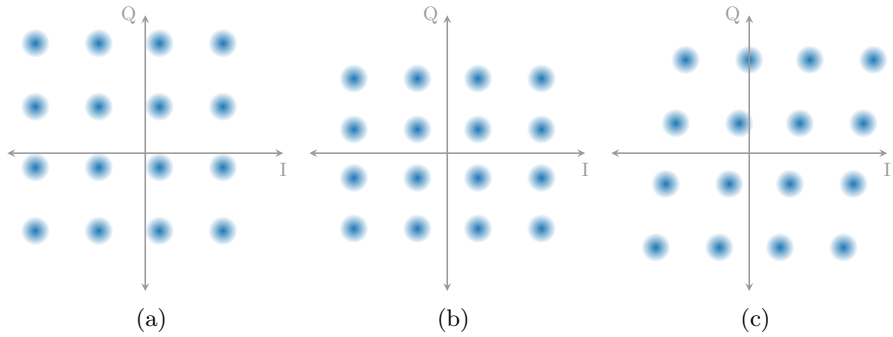

Figure 4.3: IQ imbalance effects on a 16-QAM constellation: (a) Offset (b) Gain error (c) Quadrature error.

By subtracting the mean of the detected signal, these impairments are relatively straightforward to compensate. Note that this only holds for transmitted signals that have zero mean, which is the case for the quadrature phase shift keying (QPSK) and quadrature amplitude modulation (QAM) modulation formats used in this thesis.

When representing the real values of the detected waveforms for I and Q as a complex value, both vectors have to be orthogonal. Gain and phase mismatch between I and Q, or IQ imbalance, can result in performance degradation when not accounted for. Different path lengths and losses in the optical receiver or electrical lines, as well as bias-drifts at the transmitter attribute to the IQ imbalance. In the constellation diagrams, these differential losses can be recognized as a compression along one of the axis of the constellation (Fig. 4.3b), whereas path length difference translates to a skew of the diagram (Fig. 4.3c).

In the presence of these errors, the relation between the detected complex signal $I'(t) + jQ'(t)$ and the ideal signal $I(t) + jQ(t)$ can be expressed as [176]:

$$I'(t) + jQ'(t) = \left[g_I I\left(t - \frac{\tau_{IQ}}{2}\right)\right] + \left[g_Q Q\left(t - \frac{\tau_{IQ}}{2}\right)\right] \exp\{j\,(\pi/2 + \phi_{IQ})\} \quad (4.16)$$

Where g_I and g_Q are the gains of I and Q, τ_{IQ} is the timing skew, and ϕ_{IQ} is the quadrature phase error. To compensate the IQ imbalances a orthogonalisation procedure is applied, of which the Gram-Schmidt [177] and Löwdin orthogonalisations [178] are the most commonly applied methods in coherent optical communications. The first method selects $I'(t)$ as a basis vector. Next an orthogonal vector is calculated by projecting the second detected vector $Q'(t)$ onto the first vector. This two-step transformation can be expressed by the following matrix representation:

$$\begin{bmatrix} I(t) \\ Q(t) \end{bmatrix} = \begin{bmatrix} 1 & 0 \\ -p & 1 \end{bmatrix} \begin{bmatrix} I'(t) \\ Q'(t) \end{bmatrix}, \quad (4.17)$$

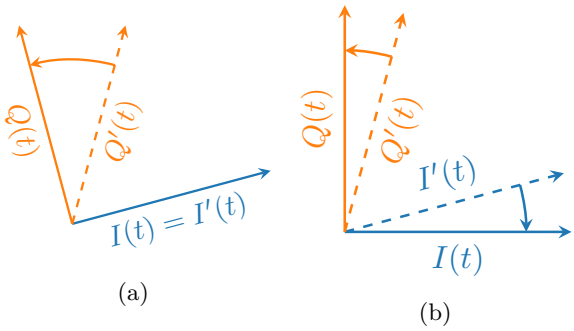

Figure 4.4: Graphical representation of two orthogonalisation procedures. (a) Gram-Schmidt and (b) Löwdin.

where p denotes the normalised projection of the second vector onto the first given as the inner product $\langle Q'(t)|I(t)\rangle$.

Note that due to the rotation of $Q'(t)$, this vector is more prone to ADC quantization noise [179]. Therefore, Löwdin orthogonalisation is proposed to offer a symmetric alternative where both vectors are rotated equally. This transformation is given as:

$$\begin{bmatrix} I(t) \\ Q(t) \end{bmatrix} = \frac{1}{2} \begin{bmatrix} \frac{1}{\sqrt{1+p}} + \frac{1}{\sqrt{1-p}} & \frac{1}{\sqrt{1+p}} - \frac{1}{\sqrt{1-p}} \\ \frac{1}{\sqrt{1+p}} - \frac{1}{\sqrt{1-p}} & \frac{1}{\sqrt{1+p}} + \frac{1}{\sqrt{1-p}} \end{bmatrix} \begin{bmatrix} I'(t) \\ Q'(t) \end{bmatrix} \tag{4.18}$$

As can be seen from Fig. 4.4, both procedures result in an orthogonal basis, thereby mitigating the quadrature error. The gain imbalance is compensated by normalizing the new orthogonal vector basis, leaving only the timing skew of Eq. (4.16) as error that needs to be addressed. This error can be compensated by applying a time shift in the form of interpolation. Generally a low degree La Grange polynomial implemented as a finite-impulse response (FIR) filter suffices [180]. The secondary objective of the interpolator is adapting the sample rate to Nyquist rate sampling at two samples per symbol. This two-fold oversampling is required for DSP modules such as CD compensation and MIMO equalisation. Although some algorithm require a higher oversampling rate, such as a minimum 4-fold oversampling for timing recovery or a 3-fold oversampling required for complex field reconstruction in Kramers-Kronig (KK) receivers (Section 3.6.3).

4.3 Chromatic dispersion compensation

For long-reach transmission systems, CD is a main contributor towards the broadening of the impulse response. Fortunately, CD is a linear effect that can be

described by an all pass transfer function [181]:

$$H(z,\omega) = \exp\left(-j\frac{D\lambda_0^2}{4\pi c\omega^2}\right), \tag{4.19}$$

where D is the accumulated dispersion after transmission, λ_0 is the centre wavelength of the channel, and ω is the angular frequency. When D is known, an inverse filter can be designed to compensate for CD. Both time-domain or frequency-domain implementations of this filter can be applied. For long dispersion unmanaged links the required number of taps increases, which makes the frequency-domain implementation favourable as its complexity scales with $\mathcal{O}(\log N)$ compared to the $\mathcal{O}(N)$ scaling of the time-domain variant [182].

In case the accumulated dispersion is known, it can be directly inserted in Eq. (4.19) to generate the appropriate filter. If this is not the case, the accumulated CD has to be estimated. In this thesis, a best-match search method is applied to find the best matching filter in a specified solution space [183]. Multiple filters, each with a different amount of CD are designed and applied to copies of the received signals. Subsequently, the autocorrelation is calculated. For a correctly compensated amount of dispersion a sharp peak, related to the clock is to be expected in the spectrum. Therefore, the filter resulting in the sharpest spectral peak is selected. Note that computational complexity increases with the number of dispersion values to validate. Since the MIMO equaliser is capable of compensating small amounts of residual CD, a coarser step size can be used, to save computation time and power. Furthermore, for mode-division multiplexing (MDM) transmission, the group velocity dispersion (GVD) parameter of each spatial mode might vary. In combination with the mixing of the channels, residual CD is inevitable when applying bulk CD compensation. Although it is possible to mitigate all CD by the MIMO equalizer, it would increase its complexity as larger filter sizes are required.

4.4 Timing recovery

The front-end compensation module outputs a two-fold oversampled signal, but the sampling points do not necessarily match with the transmitted symbols. This is a result of the independent sampling clocks at the transmitter and receiver, which differ in both frequency and phase. Several algorithms are available to compensate this timing phase error, of which the Gardner algorithm [184] is widely deployed due to its simplicity and independence of the carrier phase. A timing error detector calculates the error at each sample, which is generally averaged over a block of symbols for noise suppression. The tracked error is fed to a digital interpolator which applies the correction to the signal. Whereas this method works well for classical non-return-to-zero (NRZ) and return-to-zero (RZ) signals, it fails for Nyquist shaped pulses with sharp roll-off. Also, the mixing of the spatial channels contributes to the loss of pulse shape. Therefore, the digital square timing recovery procedure [185] is commonly applied in the presence of polarisation mode

dispersion (PMD) or in the case of MDM, differential mode group delay (DMGD). This algorithm is more complex compared to the Gardner algorithm as it requires 4 samples per symbol and a fast Fourier transform (FFT). By taking the fourth power of the incoming signal, the phase modulation is removed, resulting in a periodic waveform with a frequency corresponding to the symbol rate. The phase of this clock tone represents the timing phase error, which can be directly extracted from the spectrum. Note that a four times oversampling is required, as the clock tones would appear at the edges of the spectrum in case of a twofold oversampled signal. Furthermore, for clear clock tones, bulk CD compensation has to be performed first. Since the CD equalisation is generally performed in the frequency domain, no additional computation extensive FFT is required.

4.5 MIMO equalisation

The purpose of the multiple-input multiple-output (MIMO) equaliser is twofold. First it has to unravel the spatial channel mixing and secondly it is employed to compensate intersymbol interference (ISI) as result of DMD and CD. Recall the expression for the linear MIMO channel given by Eq. (4.10) as:

$$\mathbf{R} = \mathbf{HS} + \mathbf{N}. \tag{4.20}$$

An estimation of the transmitted signals, denoted as $\hat{\mathbf{S}}$ can be obtained by multiplying the received signals by a weight matrix $\mathbf{W}$ as:

$$\hat{\mathbf{S}} = \mathbf{WR} = \mathbf{W}\left(\mathbf{HS} + \mathbf{N}\right), \tag{4.21}$$

A stochastic gradient algorithm is employed to find the minimum mean squared error (MMSE) weight matrix $\mathbf{W}$, as will be explained later in the section. The weight matrix can be implemented as a network of FIR filters for each element in $\mathbf{W}$, as depicted in Fig. 4.5 [186]. For an accurate estimation of transmitted sequence, the FIR filters must be sufficiently long to accommodate the complete impulse response which is broadened by dispersive effects such as DMD and residual CD. As such, DMD increases the computational complexity of the equaliser, and thus low DMD transmission links are desirable for mixed spatial channels.

Generally, the channel transfer function matrix is not known and might vary over time. Therefore, after each equalisation step, an error is calculated which is subsequently used to update the weight matrix. This error is multiplied with step-size parameter μ to control the adaptation speed of the algorithm. A larger step-size means a larger contribution of the calculated error signal on changes of the weight matrix, whereas a small step-size result in a more slowly updating equaliser. To achieve fast initial convergence, followed by a more stable equaliser, a variable step size is introduced for the transmission experiments in Chapter 6 [187]. Figure 4.6 shows a functional diagram of the adaptive equaliser with feedback loops that include the next DSP modules in the chain: carrier phase estimation (CPE),

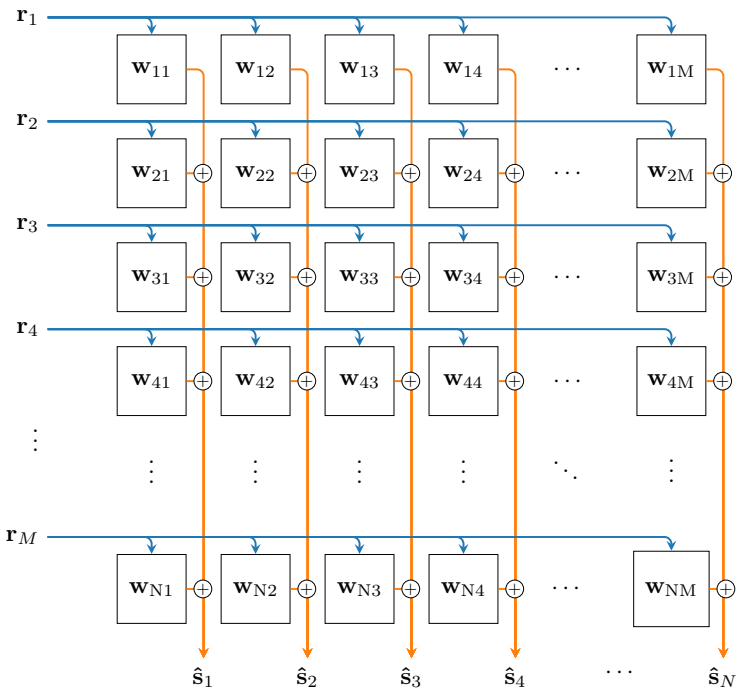

Figure 4.5: MIMO equalizer with N inputs and M outputs.

and the decoder. The equalisation step is represented by a multiplication of the incoming signals with weight matrix $\mathbf{W}$, which is implemented as Fig. 4.5. The equalised symbols are fed to the CPE to compensate the frequency offset between transmitter and receiver laser. The CPE module will be discussed in more detail in the next section. Finally, the symbols are decoded and demapped back to bits. The three colours in Fig. 4.6 represent the feedback loops of the constant modulus algorithm (CMA), least means square (LMS), and decision-directed least mean square (DD-LMS) algorithms used to estimate the gradient of the weight matrix.

Constant modulus algorithm

The constant modulus algorithm (CMA) algorithm, indicated by the green feedback loop in Fig. 4.6, exploits the constant modulus property of phase-modulated signals such as the QPSK format. The algorithm forces the received inputs to a known constant power R_2 by taking the distance of the equalised symbol to this value as an error. Therefore, the update rule for the weight elements of $\mathbf{W}$ is given as [188]:

$$\mathbf{w}_{mn}[k+1] = \mathbf{w}_{mn}[k] - \mu \mathbf{r}[k]^{\mathrm{H}}[k]\hat{s}_m[k]\left(|\hat{s}_m[k]|^2 - R_2\right), \tag{4.22}$$

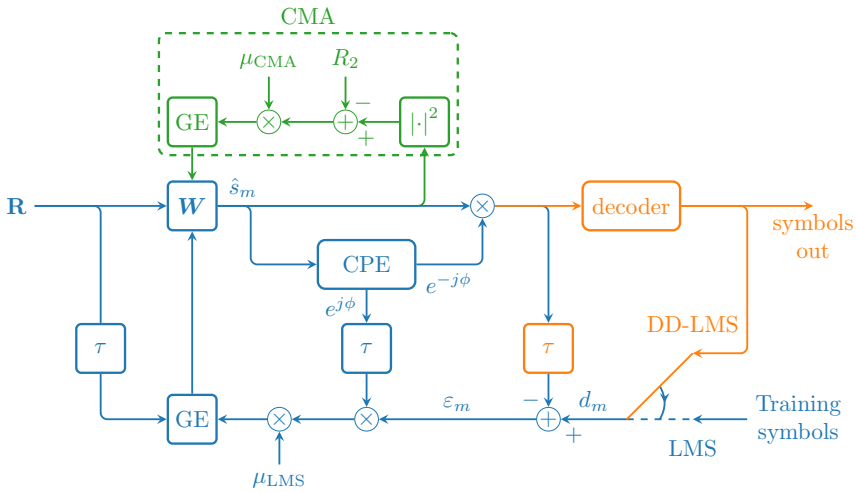

Figure 4.6: Functional diagram of an adaptive MIMO equaliser. The weight matrix is heuristically updated according to either CMA (green), LMS (blue) or DD-LMS (orange) algorithms. Subsequent DSP modules, carrier phase estimation (CPE) and decoder are included in the feedback loop for LMS. **W** is updated by one of the two gradient estimators (GE).

As can be seen from Eq. (4.22) and Fig. 4.6, CMA does not require any knowledge on the transmitted data other than the modulation format. This type of blind equalisation favours a short feedback loop, independent of subsequent modules, enabling a low latency implementation. Note that weight elements are updated independent of each other, and can converge towards the same output. To address this issue, blind source separation algorithms have been proposed [189, 190].

CMA can be directly applied to higher-order modulation formats with multiple power levels, such as QAM. By taking the average constellation power as value for R_2 the algorithm can still unravel the channel mixing, but its steady-state error can never reach zero. Alternatively, the radius directed or multi-modulus algorithms that take the multiple power levels into account can be applied [191, 192].

Least mean square algorithm

Opposite to blind equalisation, the least means square (LMS) algorithm [193] requires a sequence of known symbols proceeding the transmitted data to train the weight matrix. After training, the equaliser switches to decision-directed least mean square (DD-LMS), where the decoded symbols are used for updating the weight matrix. In Fig. 4.6, the extended feedback path for DD-LMS is shown in orange. To decode the symbols correctly, the frequency offset between the transmitter and

the receiver laser has to be removed. Therefore, the CPE module is integrated into the feedback loop. To ensure the MIMO equaliser only unravels the spatial channel mixing, the phase error estimation is removed before calculating the equalisation error. Furthermore, to accommodate for the processing time of the CPE module, time delays denoted by τ are included to synchronise the feedback loops. Hence, the latency of LMS is higher compared to that of CMA.

Although training sequences enable convergence towards the desired output without the issue of source separation, it reduces the system throughput. Furthermore, the pattern has to be detected within the received signals, which requires frame synchronization techniques [194].

Frequency domain equalisation

Recall that the equalisation in Fig. 4.6 is performed using the FIR filter structure depicted in Fig. 4.5. From the latter figure, it can be seen that this implementation requires $M \times N \times L$ complex multiplication and $(M-1) \times N \times L$ complex additions, where L is the number of $T/2$ spaced taps. Consequently, the complexity of this method increases rapidly for an increasing number of spatial channels and longer impulse responses.

Alternatively, the complex convolution in the time-domain can be replaced by a multiplication operation in the frequency domain, thereby reducing the computational complexity [28]. However, as the gradient estimation is still performed in the time domain, frequent conversions between the two domains is required. Nonetheless, the relative complexity attributed to the FFT and inverse fast Fourier transform (IFFT) operations diminishes as the number of taps increase. Due to the blockwise nature of the frequency domain equaliser (FDE), its convergence is slower compared to the time domain equaliser (TDE).

In the transmission experiments of Chapters 6 and 7, both TDE and FDE are employed using combinations of CMA and LMS. For MDM transmission the impulse response broadening introduced by DMD scales linearly, or at its best with the square root of the transmission distance. Therefore, the lower complexity FDE is used for the long-distance transmission experiments in Chapter 7. It uses LMS for convergence and a multi-modulus variant of CMA during transmission. The smaller number of taps used in the short-reach experiments of Chapter 6, do not require FDE. Furthermore, the employed TDM-SDM measurement technique to reduce the number of receivers by time multiplexing the outputs of a transmission system limits the number of symbols taken within each capture. Therefore, a TDE based on LMS for training and DD-LMS for transmission is used for those experiments.

4.6 Carrier phase estimation

For coherent detection, the local oscillator (LO) is tuned to the same frequency as the laser employed at the transmitter. Besides a possible mismatch between the

two frequencies, the non-zero linewidth of both lasers results in phase noise. The CPE module compensates for both impairments and is the last module before the detector.

Frequency recovery

A frequency offset between the transmitter and receiver laser results in a fast developing phase noise that is challenging to track by phase recovery methods in the case of large offsets. Therefore, this frequency offset is removed first. This is achieved by multiplying the input of the module with a range of frequency offsets. Subsequently, the correlation with the transmitted signal for all test frequencies is compared, and the highest correlation value is selected. For the transmission experiments in Chapter 6, a search range of 500 MHz and a step size of 25 MHz is used. Any remaining frequency offset is presumed to be small enough to be tracked by the phase recovery.

Phase recovery

The fast sampling rates of optical communication systems enable phase noise tracking using a phase estimator. The phase estimator proposed by Viterbi and Viterbi is a well-known algorithm to recover the carrier phase of phase-modulated signals [195]. To estimate the carrier phase offset the phase modulation of the symbols is removed by taking the Mth power, where M is equal to the number of phases in the constellation, i.e. 4 of QPSK. Subsequently, a windowing function is applied to calculate and estimate phase error over a block of symbols. Finally, the estimated phase offset is applied as a correction to all the symbols in the block. The choice of block length heavily depends on the dominant noise type in the system. In the linear regime, averaging over a larger number of samples averages out the Gaussian noise. Whereas a small block length allows for faster tracking of phase noise introduced by cross-phase modulation (XPM) or broad linewidth laser sources.

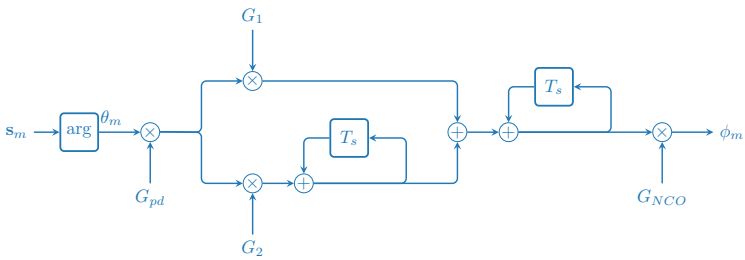

Figure 4.7: Functional diagram of a second-order phase-locked-loop for carrier phase estimation (Costas loop).

Another well-known phase tracker, and the method used in Chapter 6, is the digital phase-locked loop (DPLL). In particular, the 2th order digital phase-locked loop (DPLL) depicted in Fig. 4.7 which is better known as Costas loop [196]. In this figure, G_{pd}, G_1, G_2, and G_{NCO} represent the gains of the phase detector, first, second, and numerically controlled oscillator.

The third method for CPE is a blind phase search (BPS) algorithm, which employs a brute force approach [197]. Within the search space $-\pi$ to π, several possible phase rotations are selected. Note that symmetry in the constellation can be exploited to reduce the search range. For the QPSK and square QAM modulation formats, the range reduces to a single quadrant, which is depicted in Fig. 4.8. In this figure, the blue point represents one of the constellation points of the QPSK format, and the orange point is the received point after equalisation. Subsequently, N phase rotations (θ_n) are applied to the received symbol, resulting in the red and green points in the figure. Note that in practice 128 or more phase offsets are explored to obtain sub-degree resolution. However, for readability purposes, the number of angles has been reduced to 8 in the figure. The Euclidean distance for each rotated point to the constellation point is calculated and compared. Finally, the nearest point (green) is selected.

Generally, BPS is applied to a block of symbols. Therefore, the Euclidean distances for each θ_n are averaged. Subsequently, the phase offset with the lowest distance is selected. Note that by feeding the training sequence as an input to the distance calculation instead of the nearest point, the CPE can be trained. Furthermore, this method is relatively simple to scale towards higher-dimensional modulation formats, such as 4D constellations [89].

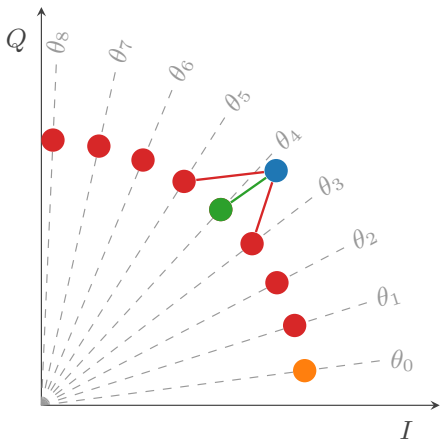

Figure 4.8: Simplified example of blind phase search applied to a QPSK modulation format.

Summary

The DSP required to recover the transmitted data after transmission over the system illustrated in Chapter 3 is given in this chapter. Due to crosstalk, the received channels contain a combination of the transmitted sequences that can be recovered by employing a MIMO equaliser in the case of low MDL. Before the signals are presented to the MIMO, the orthogonality between in-phase and quadrature components is restored by the front-end compensation module. Followed by resampling to twice the symbol rate using digital interpolation techniques. Next, the CD is removed by a static FIR filter designed with the opposite amount of CD of the transmission system. This module is not required to mitigate all CD, as any residual dispersion will be removed by the MIMO equaliser. The MIMO equaliser is a structure of FIR filters, that is heuristically updated to track changes of the channel while unravelling the transmitted channels. Two families of adaptive algorithms are suggested: constant modulus algorithm (CMA) and least means square (LMS). The first is a blind algorithm that does not require training using a header sequence. However, its convergence towards the right output cannot be guaranteed without blind source separating algorithms. This is not an issue for the LMS algorithm as it is trained using a sequence of known symbols to the right output. To do so, the carrier phase needs to be estimated. This is performed by the digital phase-locked loop or maximum likelihood phase estimator of the carrier phase estimation module. The compensation of the frequency offset between transmitter and local oscillator laser, and removal of phase noise is required for the symbol detections in the decoder. As this module is integrated into the feedback loop of LMS, it has a higher latency compared to CMA. The latency further increases during transmission as the symbols have to be decoded first before updating the equaliser. The equaliser requires the complete impulse response of the system for the best performance. Consequently, the computational complexity increases with the number of taps. Alternatively, the filtering operation can be performed in the frequency-domain, which replaces the time-domain convolution by a multiplication in the frequency-domain. Finally, carrier phase estimation is applied to remove frequency and phase offsets between the transmitter and receiver laser. The MIMO equaliser can be exploited for channel estimation, as its weights converge to the inverse of the channels transfer function matrix. This transfer function matrix is vital information in the design and optimisation of transmission systems and components. However, the transfer function matrices of individual optical system components cannot be extracted from the system matrix. Therefore, an instrument to directly measure these matrices at a component level is discussed in the next chapter.

Chapter 5

Spatially-diverse optical vector network analyser

Key to unlocking the full potential of optical fibre transmission systems is to gain a more in-depth understanding of the impact of any performance limitation at every level from component, sub-system, to end-to-end transmission systems. Therefore, characterisation at these levels is crucial. Single-mode components have the advantage of having off-the-shelf instrumentation available, which can enable characterisation at the component level. However, space-division multiplexing (SDM) components are still quite premature in this aspect.

The amplitude and phase response of any component or system can be represented by a complex transfer function, which when applied to an incoming optical field produces a given outgoing field. Due to the polarisation diversity of single-mode devices, it is not possible to describe a component with a single transfer function. The complete linear response, given by a complex 2×2 transfer function matrix, contains information on all linear device parameters, such as losses, dispersion, and polarisation dependence. For the coupled spatial channels of SDM components, the dimensionality of this transfer function matrix increases to $2N \times 2N$, where N is the number of single-mode inputs and outputs of the device. The factor of two represents the polarisation diversity of each input and output. Two device parameters key to SDM component characterisation can be extracted from this transfer matrix, namely mode dependent loss (MDL) and differential mode group delay (DMGD). The first, represents fluctuations in spatial channel gains, which limits system capacity or can result in an outage for severe cases. The latter introduces pulse broadening, resulting in increased digital memory requirements of the receiver. Furthermore, it decreases system performance in the presence of phase noise [198].

The transfer function matrix of a complete space division multiplexed transmission system can be obtained from channel estimation digital signal processing (DSP) algorithms (Section 4.5). However, isolating transfer matrices of individual

components from the obtained result is not possible, hence this method is suitable for system characterisation only. Furthermore, a transmission setup requires numerous and costly components, such as high-speed digital-to-analog converters (DACs) and analog-to-digital converters (ADCs). Moreover, the analysed frequency range is limited to the electronic bandwidth of the transmitter and receiver, which is orders lower compared to the supported optical bandwidth of the device under test (DUT).

An alternative method for direct measurement of the transfer function matrix is optical vector network analysis. This technology, based on swept wavelength interferometry (SWI), employs an interferometric setup with a single-mode DUT in one arm excited by a swept optical source. Enabled by DSP, the transfer function matrix can be extracted from the produced fringe pattern [199, 200]. However, commercially available optical vector network analysers do not support the larger transfer matrices of multi-port SDM components. Hence, a spatially-diverse variant is required to fully capture the linear response of SDM components [201, 202, J3].

In the next section, the fundamentals of optical vector network analysis are given, followed by the extension towards spatial diversity in Section 5.2. To extract the transfer function matrix and derive linear parameters from it, several digital signal processing steps are required, which are presented in Section 5.3. In Section 5.4, design constraints and limitations of optical vector network analysis are explained. Furthermore, specifications of the developed optical vector network analyser (OVNA) system are presented as well. One key advantage of OVNA, is the ability to characterise a single spatial multiplexer. Section 5.5 describes the characterisation of a photonic lantern (PL), by employing a reflective OVNA configuration. Finally, the developed OVNA is utilized for characterisation of large-core count few-mode multi-core fibres. In Section 5.6, a 39-core 3-mode fibre is analysed, particularly focussing on dispersion effects. Finally, a detailed analysis of inter-mode-group cross-talk under the influence of fibre bending and twisting is performed on a 36-core 3-mode fibre in Section 5.7[1]

5.1 Basics of optical vector network analysis

The simplest SWI system consists of an optical source, an interferometric structure with fixed path lengths, and the means to detect the optical signal, as illustrated in Fig. 5.1. The coherent optical source must be capable of producing a linear time-frequency sweep, resulting in an optical field given by:

$$\mathbf{E}_0(t) = A_0 \mathrm{e}^{-j\omega(t)t} \rho_0, \tag{5.1}$$

where A_0 is the complex amplitude, ρ_0 is the polarisation vector at the output of the source, and $\omega(t) = 2\pi(\nu_0 + \gamma t)$ is the angular frequency produced by linear

[1]This chapter incorporates results published in [J3, J10, J2]. Parts of these experiments were conducted in collaboration or at the Photonic Network System Laboratory of the National Institute of Information and Communications Technology (NICT) in Tokyo, Japan.

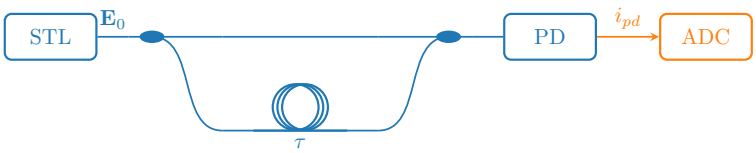

Figure 5.1: Swept wavelength interferometer based on linear frequency sweep produced by the swept tunable laser (STL), and detected by the photodetector (PD) and analog-to-digital converter (ADC). The group delay of the fibre is denoted with τ.

time-frequency sweep with tuning rate γ, starting at ν_0. The source signal is split and sent over two single-mode fibres of different lengths, introducing a phase difference between the fields arriving at the photodetector. For now, splitting losses are ignored, and all fibre lengths not annotated with τ are considered to have zero length to simplify the equations. In the schematic, the introduced phase difference is represented by a single-mode fibre in one of the arms. The group delay of this fibre, which is linearly proportional to the fibre length, is denoted by τ. Assuming square law detection, the incident field on the detector produces a current:

$$i_{pd}(t) = \mathcal{R}A^2 \left[1 + \cos(2\pi\gamma\tau t + \varphi)\right], \tag{5.2}$$

where $\mathcal{R}$ is the sensitivity of the photodetector, $A = A_0$ is the complex field amplitude of the incident field, which is equal to the field of the source in a lossless scenario, and φ is a constant phase factor. For now, perfect polarisation alignment between both arms is assumed. The power fading due to polarisation mixing will be addressed in a later section of this chapter. From Eq. (5.2), it is clear that the spectrum of i_{pd} contains one single frequency component, which follows from the product of the tuning rate (γ) and the path length difference between the arms (τ). This property will be used later to separate and identify the transfer functions of components in OVNA measurements.

Note that, a perfect linear time-frequency sweep requires accurate tunable laser sources. Depending on the laser type and tuning rate, generating a perfect linear sweep is difficult or even impossible [203, 204]. Moreover, most swept tunable lasers (STLs) only support wavelength sweeps, which are inherently not linear in frequency. The time-varying behaviour of the tuning rate is included in the expression for angular frequency as: $\omega(t) = 2\pi(\nu_0 + \nu(t))$ within Eq. (5.1). Since the system is no longer linear in time, the photocurrent is now given as a function of the linear, instantaneous optical frequency $\nu(t)$:

$$i_{pd}(\nu(t)) = \mathcal{R}A_{pd}(t)^2 \left[1 + \cos(2\pi\nu(t)\tau + \varphi - 2\pi\nu_0\tau)\right], \tag{5.3}$$

The last term of the cosine argument is independent of t, thus producing a constant phase shift, which can be omitted for the remainder of this analysis. Whereas the fringe pattern described by Eq. (5.2) is both linear in time and optical frequency, the

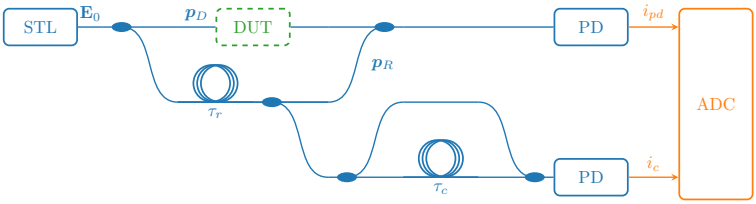

Figure 5.2: Swept wavelength interferometer including auxiliary clock interferometer for sweep linearisation. The system is capable of measuring fibre lengths or a single complex transfer function of a device under test (DUT).

spectrum could be obtained by performing a fast Fourier transform (FFT) directly on the time-sampled waveform. The fringe pattern of Eq. (5.3) is no longer periodic in time, but only in optical frequency. Therefore, the detected signal needs to be resampled with fixed optical frequency intervals before an FFT can be applied. For this linearisation process, an additional interferometric structure is added to the system, as is shown in Fig. 5.2. Both interferometers experience the same non-linear sweep produced by the source. Consequently, the fringe pattern generated by the auxiliary interferometer can be used to resample the equal time interval signal to equal frequency intervals [205–207]. The new sampling rate is given by $1/\tau_c$, where τ_c is the differential group delay of the clock interferometer. With an accurate estimation of τ_c and thus the optical frequency interval $\delta\nu$, this setup can be employed to measure single-mode fibre lengths. Adding additional single-mode fibre (SMF) in one of the interferometer arms will result in a frequency shift of the fringe pattern. For a known tuning-rate, this frequency shift can be directly translated to the group delay difference between the measurements. Since group delay scales linearly with length, and its value is well known for standard single-mode fibre (SSMF), the fibre length can be calculated.

Scalar transfer function measurement

Besides measuring fibre lengths, the amplitude and phase response of single-mode components can be measured with the setup of Fig. 5.2, when a DUT is inserted in the top arm of the interferometer. This device will change both the amplitude and phase of the optical field produced by the swept tunable laser (STL) according to its transfer function. With DSP, this transfer function can be extracted from the produced fringe pattern. One single transfer function is limited to describing only a single polarisation state. To take polarisation effects into account, a 2×2 transfer function matrix $\mathbf{H}(\omega)$ is required to completely describe a single-mode component. When a DUT is placed in the top interferometer arm of Fig. 5.2, it will project its transfer matrix $\mathbf{H}(\omega)$ on the incoming polarisation vector ρ_D. When this signal beats with the reference arm, which also has an arbitrary polarisation vector ρ_R,

the incident field produces a photocurrent:

$$i_{pd}(\nu) = \mathcal{R}A^2 \left[1 + |\mathbf{H}(\omega)\rho_D|^2 + 2\Re\mathfrak{e}\{\rho_R \cdot \mathbf{H}(\omega)\rho_D\} \cos(\nu\tau + \varphi)\right], \tag{5.4}$$

In the digital domain, the scalar quantity $H(\omega) = \rho_R \cdot \mathbf{H}(\omega)\rho_D$ can be extracted from Eq. (5.4) using a windowing function to select the response around $\nu\tau$. This scalar value can be interpreted as the coupling from one input polarisation vector to the reference arm vector, which does not necessarily match with one of the four transfer functions of the matrix. To measure the complete transfer function matrix in a single sweep, polarisation diverse detection and multiplexing are added to the setup.

Polarisation-diversity

In Fig. 5.3, an interferometric structure is added in front of the DUT, which effectively changes the differential group delay of one of the polarisation states with τ_p. Polarisation controllers are employed to align the signals with the orthogonal polarisation vectors of the polarisation beam combiner (PBC). Assuming perfect polarisation alignment, the optical field at the output of the PBC is given by:

$$\mathbf{E}_P = \sqrt{\frac{\kappa_1}{2}} A \mathrm{e}^{-j\omega(t)t} \left[\rho_{P,s} + \mathrm{e}^{j(\omega(t)\tau_p)}\rho_{P,p}\right], \tag{5.5}$$

where $\rho_{P,s} = \mathbf{R}_{P,s}\rho_0$ and $\rho_{p,p} = \mathbf{R}_{P,p}\rho_0$ are the input polarisation states of the PBC, which are related to the polarisation state of the source via 2×2 unitary matrices $\mathbf{R}_P$. The factor $\sqrt{\kappa_1/2}$ follows from beam splitting between measurement and reference arm. An asymmetrical splitter is employed to boost the signal power in the measurement arm, which will experience more losses in the spatial-diverse setup. The input polarisation vectors of the PBC are considered as the set of

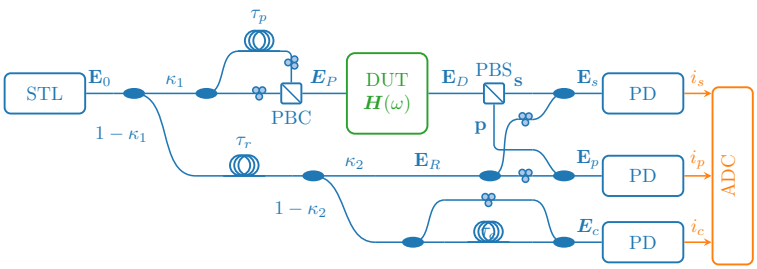

Figure 5.3: Polarisation-diverse optical vector network analyser for characterisation of a single-mode device under test (DUT). **p** and **s** denote the output polarisation states of the polarisation beam splitter (PBS). The splitting ratios of the beam splitters are denoted by κ.

orthogonal basis vectors, which simplifies expression Eq. (5.5) to:

$$\begin{aligned}
\mathbf{E}_P &= \sqrt{\frac{\kappa_1}{2}} A \mathrm{e}^{-j\omega(t)t} \left[\begin{pmatrix} 1 \\ 0 \end{pmatrix} + \mathrm{e}^{j\omega(t)\tau_p} \begin{pmatrix} 0 \\ 1 \end{pmatrix} \right] \\
\mathbf{E}_P &= \sqrt{\frac{\kappa_1}{2}} A(t) \begin{pmatrix} \mathrm{e}^{-j\omega(t)t} \\ \mathrm{e}^{-j\omega(t)(t-\tau_p)} \end{pmatrix} \\
\mathbf{E}_P &= \sqrt{\frac{\kappa_1}{2}} A \mathbf{E}_{2p}
\end{aligned} \tag{5.6}$$

The polarisation axes of the DUT are most likely not aligned to the newly defined basis vectors and additional rotation matrices are needed to express the field after propagation through DUT, right at the input of the polarisation beam splitter (PBS) of the receiver:

$$\mathbf{E}_D = \frac{\sqrt{\kappa_1}}{\sqrt{2}} A \mathbf{R}_{out} \mathbf{H}(\omega) \mathbf{R}_{in} \mathbf{E}_{2P} \tag{5.7}$$

The reference signal experiences a polarisation rotation, a delay τ_r, and power loss from the coupler with the reference clock interferometer. The resulting optical field at the input of the polarisation diverse detector is given by:

$$\mathbf{E}_R = \frac{\sqrt{\kappa_2}\sqrt{1-\kappa_1}}{2} A \mathrm{e}^{-j\omega(t)(t-\tau_r)} \mathbf{R}_R \rho_0 \tag{5.8}$$

To recover information on both polarisation states, a polarisation diverse detection scheme is required. Therefore, the signal of the top arm is split into two orthogonal polarisation vectors $\mathbf{p}$ and $\mathbf{s}$, which produce the following fields that are combined with reference signal $\mathbf{E}_R$:

$$\mathbf{E}_{D,s} = (\mathbf{E}_D \cdot \mathbf{s})\mathbf{s} \quad \text{and} \quad \mathbf{E}_{D,p} = (\mathbf{E}_D \cdot \mathbf{p})\mathbf{p} \tag{5.9}$$

A symmetric beam-splitter is employed to divide the reference signal over the two detectors. The incident fields on these photodetectors is given by:

$$\mathbf{E}_s = \frac{1}{\sqrt{2}} \mathbf{E}_{D,s} + \frac{1}{2} \mathbf{E}_R \mathbf{R}_{R,s} = \sqrt{2} \mathbf{E}_D \cdot \mathbf{s} + \frac{\sqrt{\kappa_2}\sqrt{1-\kappa_1}}{2} A \mathrm{e}^{-j\omega(t)(t-\tau_r)}, \tag{5.10}$$

$$\mathbf{E}_p = \frac{1}{\sqrt{2}} \mathbf{E}_{D,p} + \frac{1}{2} \mathbf{E}_R \mathbf{R}_{R,p} = \sqrt{2} \mathbf{E}_D \cdot \mathbf{p} + \frac{\sqrt{\kappa_2}\sqrt{1-\kappa_1}}{2} A \mathrm{e}^{-j\omega(t)(t-\tau_R)}, \tag{5.11}$$

where $\mathbf{E}_{D,s}$ and $\mathbf{E}_{D,p}$ are the output fields of the PBS, and $\mathbf{R}_{R,s}$ and $\mathbf{R}_{R,p}$ represent the polarisation rotation of the reference arm to ρ_s and ρ_p. Under assumption of square law detection, with sensitivity $\mathcal{R}$, the photo-currents flowing in to the ADC are given by:

$$\begin{aligned}
i_s(\nu) = \mathcal{R}|A|^2 \frac{\sqrt{\kappa_1\kappa_2}\sqrt{1-\kappa_1}}{2} \mathfrak{Re} \Big[& s_1 \hat{H}^*_{1,1} s_2 \hat{H}_{1,2} \mathrm{e}^{2j\pi\nu\tau_p} + \\
& s_1 \hat{H}_{1,1} \mathrm{e}^{2j\pi\nu\tau_r} + s_2 \hat{H}_{1,2} \mathrm{e}^{2j\pi\nu(\tau_r-\tau_p)} \Big],
\end{aligned} \tag{5.12}$$

$$i_p(\nu) = \mathcal{R}|A|^2 \frac{\sqrt{\kappa_1\kappa_2}\sqrt{1-\kappa_1}}{2} \mathfrak{Re}\left[p_1 \hat{H}^*_{2,1} p_2 \hat{H}_{2,2} \mathrm{e}^{2j\pi\nu\tau_p} + p_1 \hat{H}_{2,1} \mathrm{e}^{2j\pi\nu\tau_r} + p_2 \hat{H}_{2,2} \mathrm{e}^{2j\pi\nu(\tau_r-\tau_p)}\right], \tag{5.13}$$

where $\mathbf{s}_i$ and $\mathbf{p}_i$ are the components of the unit vectors $\mathbf{s}$ and $\mathbf{p}$ in Eq. (5.9). In the spectra of these photo-currents, three peaks appear at positions τ_r, $|\tau_r - \tau_p|$, and τ_p. The latter corresponds to the frequency introduced by the polarisation multiplexer. As this component does not carry any information on the DUT, it is not of interest for component characterisation. The other two peaks, contain one impulse response matrix element each, which can be extracted using digital filtering. The details of this process will be discussed in Section 5.3, after the system is extended to the spatially-diverse variant.

5.2 Spatially-diverse optical vector network analyser

The setup in Fig. 5.3 allowed direct measurement of the polarisation-diverse 2×2 transfer function matrix of single-mode components. With the introduction of space-division multiplexing (SDM), transfer function matrix dimensionality increases to $2M \times 2N$, where M is the number of single-mode inputs, and N the number of outputs. The factor two originates from the polarisation diversity of each spatial channel. For devices with low spatial channel crosstalk, e.g. single-mode multi-core fibres, the setup from the previous section can be employed to measure each single-mode channel sequentially. For coupled spatial channels, such as modes in few-mode and multi-mode fibres, all spatial channels must be analysed simultaneously to obtain $\mathbf{H}(\omega)$, which require spatial-diversity of the OVNA. Similar to polarisation multiplexing, support for multi-port devices can be realized by adding additional delays to the setup [208]. In Fig. 5.4, a $1 \times M$ splitter and M delay fibres τ_{in} are positioned between the polarisation multiplexer and DUT. At

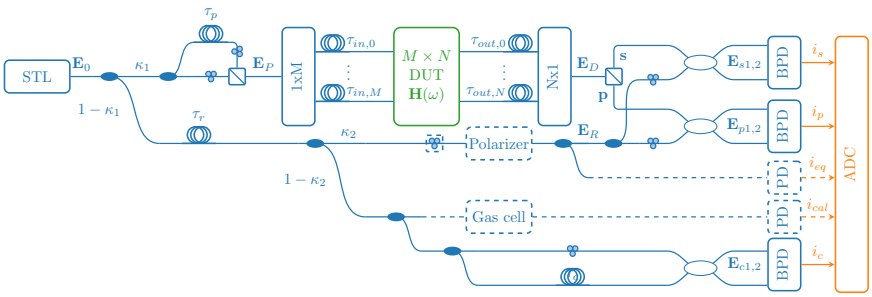

Figure 5.4: Spatially-diverse optical vector network analyser for $2M \times 2N$ SDM components employing balanced photo-detectors (BPDs). Detection of two optional signals i_{eq} and i_{cal} are included for performance enhancement.

the output of each fibre, the optical field is a delayed copy of $\mathbf{E}_{2P}$ (Eq. (5.6)) with an arbitrary polarisation rotation. The new expression for the optical field at the input of the DUT is:

$$\mathbf{E}_{in} = \sqrt{\frac{\kappa_1}{2M}} \underbrace{\begin{bmatrix} \mathbf{R}_{in,1} & \cdots & 0 \\ \vdots & \ddots & \vdots \\ 0 & \cdots & \mathbf{R}_{in,M} \end{bmatrix}}_{\mathbf{R}_{in}} \mathbf{D_{in}} \underbrace{\begin{bmatrix} \mathrm{e}^{-j\omega(t)t} \\ \mathrm{e}^{-j\omega(t)(t-\tau_p)} \\ \vdots \\ \mathrm{e}^{-j\omega(t)t} \\ \mathrm{e}^{-j\omega(t)(t-\tau_p)} \end{bmatrix}}_{\mathbf{E}_{2NP}}, \tag{5.14}$$

with

$$\mathbf{D}_{in} = \begin{bmatrix} \mathrm{e}^{j\omega(t)\tau_{in,1}} & 0 & \cdots & 0 & 0 \\ 0 & \mathrm{e}^{j\omega(t)\tau_{in,1}} & \cdots & 0 & 0 \\ \vdots & \vdots & \ddots & \vdots & \vdots \\ 0 & 0 & \cdots & \mathrm{e}^{j\omega(t)\tau_{in,M}} & 0 \\ 0 & 0 & \cdots & 0 & \mathrm{e}^{j\omega(t)\tau_{in,M}} \end{bmatrix} \tag{5.15}$$

Each DUT output port is guided through another fibre delay τ_{out}, which can be described by similar rotation and delay matrices. For the majority of components, the number of input and output delays is the same, but it is possible to measure asymmetric transfer matrices. Including all fibre delays, the signal at the input of the receiver is now given by:

$$\mathbf{E}_D = \frac{\sqrt{\kappa_1}}{\sqrt{2MN}} A \sum_{2\times 1} \mathbf{D}_{out}\mathbf{R}_{out}\mathbf{H}(\omega)\mathbf{R}_{in}\mathbf{D}_{in}\mathbf{E}_{2NP} \tag{5.16}$$

Compared to Eq. (5.7), not only the dimensions of all rotational matrices $\mathbf{R}$ increased, transfer function matrix $\mathbf{H}(\omega)$ now contains $2M \times 2N$ transfer functions $H_{k,l}(\omega)$, with $k \in [1, 2N]$ and $l \in [1, 2M]$. The reference arm is not changed in this setup and the signal is still described by Eq. (5.8). Also the equations for the incident fields on the photodetectors, given by equations Eq. (5.10) and Eq. (5.11) still hold, although the expression for $\mathbf{E_D}$ has been updated to Eq. (5.16). Detection using single photodiodes becomes impractical, as the photo-currents will contain numerous spectral components not usable for optical vector network analysis. Similar to the third spectral component in the polarisation-diverse system, originating from the interferometric polarisation multiplexing structure, multiple spectral components are introduced by interferometers created by the input and output delays. None of the undesired spectral components is a beating product of the reference signal. Therefore, when detected by the two photo-diodes of a balanced detector, they appear with equal parts in both photo-currents. Consequently, they are cancelled out in the differential photo-current, which is given by:

$$
\begin{aligned}
i_s = \mathcal{R}|A|^2 \frac{\sqrt{\kappa_1}}{\sqrt{MN}} \frac{\sqrt{\kappa_2}\sqrt{1-\kappa_1}}{2} \sum_{k=1}^{N}\sum_{l=1}^{M} \\
\mathfrak{Re}\Big[(s_1\hat{H}_{2k-1,2l-1} + s_2\hat{H}_{2k,2l-1})\mathrm{e}^{-j\omega(t)(\tau_r-\tau_{out,k}-\tau_{in,l})} \\
+(s_1\hat{H}_{2k-1,2l} + s_2\hat{H}_{2k,2l})\mathrm{e}^{-j\omega(t)(\tau_r-\tau_{out,k}-\tau_{in.l}-\tau_p)} \Big]
\end{aligned}
\tag{5.17}
$$

$$
\begin{aligned}
i_p = \mathcal{R}|A|^2 \frac{\sqrt{\kappa_1}}{\sqrt{MN}} \frac{\sqrt{\kappa_2}\sqrt{1-\kappa_1}}{2} \sum_{k=1}^{N}\sum_{l=1}^{M} \\
\mathfrak{Re}\Big[(p_1\hat{H}_{2k-1,2l-1} + p_2\hat{H}_{2k,2l-1})\mathrm{e}^{-j\omega(t)(\tau_r-\tau_{out,k}-\tau_{in,l})} \\
+(p_1\hat{H}_{2k-1,2l} + p_2\hat{H}_{2k,2l})\mathrm{e}^{-j\omega(t)(\tau_r-\tau_{out,k}-\tau_{in.l}-\tau_p)} \Big]
\end{aligned}
\tag{5.18}
$$

The setup diagram of Fig. 5.4 includes optional components that are denoted by dashed lines, used to detect two additional signals. One of them is used to track the wavelength-dependent polarisation state of the reference arm, by polarising the light before combining it with the measurement data signals. A fraction of the polarised reference signal is detected by a single-ended photodiode, and digitised using the fourth ADC channel. Alternatively, this last available digitiser port can be used to calibrate the optical sampling frequency and the start point of the sweep. To obtain i_{cal}, a fraction of the reference arm is guided through a pressurised gas cell. The absorption spectrum of this cell contains several narrow linewidth absorption peaks at accurately specified wavelengths described in NIST standards, e.g. SRM2517a. In the digital domain, the positions of detected absorption peaks are compared with the specifications of the standard, resulting in an accurate estimation of the optical sampling frequency (and its inverse τ_c), as well as the actual starting point of the sweep. Note that the ADC has only four ports, of which three are reserved for digitizing the mandatory dual polarisation data and clock signals, and thus only one of the before mentioned additional signals can be detected for each measurement.

Up to now, only the group delay τ, introduced by the delay fibres is considered, leading to frequency shifts of the fringe pattern. This assumption is based on the first-order expansion of the propagation constant β. While this is an accurate assumption for OVNA configurations with short delays and slow tuning speed, it is no longer valid for faster sweep rates, with long fibre delays. For large port-count and highly dispersive SDM components, long fibre delays are unavoidable. Consequently, higher-order propagation effects, defined within the propagation constant have to be taken into account. Consider the field generated by the STL (Eq. (5.1)) to propagate over a single-mode fibre of length z. The field at the output of this fibre is given by:

$$
\mathbf{E}(z,t) = A(z,t)\mathrm{e}^{j(\beta z-\omega(t)t)}\rho_z, \tag{5.19}
$$

where $\beta(\omega)$ is the frequency-dependent propagation constant. This propagation constant can be approximated by the Taylor expansion given by Eq. (2.42). The first expansion term relates to the phase velocity, which can be ignored in this analysis as it is independent of the angular frequency, and thus produces a constant phase factor. The second term describes group velocity, which is related to the group delay τ. The third term of the expansion describes the change in group delay with wavelength, named group velocity dispersion (GVD) or chromatic dispersion (CD). All higher-order terms are considered small for the applications discussed in this thesis and are thus neglected. Whereas the group delays introduced by the fibre is critical for separation of transfer function elements, the accompanying CD results in additional dispersion. Note that due to the change of DUT and corresponding reference arm this cannot be calibrated out. To accurately determine the linear device parameters of the DUT, this additional CD needs to be removed, which is done using digital filters. When the third-order term of the approximation of Eq. (2.42) is included the detected photocurrents are given by:

$$\begin{aligned} i_s = \mathcal{R}|A|^2 \frac{\sqrt{\kappa_1}}{\sqrt{MN}} \frac{\sqrt{\kappa_2}\sqrt{1-\kappa_1}}{2} \sum_{k=1}^{N}\sum_{l=1}^{M} \\ \mathfrak{Re}\Big[(s_1\hat{H}_{2k-1,2l-1} + s_2\hat{H}_{2k,2l-1})\mathrm{e}^{-j[\beta(z_{out,k}+z_{in,l}-z_r)+\omega(t)t]} \\ +(s_1\hat{H}_{2k-1,2l} + s_2\hat{H}_{2k,2l})\mathrm{e}^{-j[\beta(z_{out,k}+z_{in,l}+z_P-z_r)+\omega(t)t]} \Big] \end{aligned} \tag{5.20}$$

$$\begin{aligned} i_p = \mathcal{R}|A|^2 \frac{\sqrt{\kappa_1}}{\sqrt{MN}} \frac{\sqrt{\kappa_2}\sqrt{1-\kappa_1}}{2} \sum_{k=1}^{N}\sum_{l=1}^{M} \\ \mathfrak{Re}\Big[(p_1\hat{H}_{2k-1,2l-1} + p_2\hat{H}_{2k,2l-1})\mathrm{e}^{-j[\beta(z_{out,k}+z_{in,l}-z_r)+\omega(t)t]} \\ +(p_1\hat{H}_{2k-1,2l} + p_2\hat{H}_{2k,2l})\mathrm{e}^{-j[\beta(z_{out,k}+z_{in,l}+z_P-z_r)+\omega(t)t]} \Big] \end{aligned} \tag{5.21}$$

It can be seen that each of the fibre delays introduce additional dispersion, which is proportional to its length. As a result of the large bandwidth of the sweep, even small lengths of single-mode fibre can result in large amounts of dispersion. Since it is challenging to distinguish sources of dispersion, i.e. modal or chromatic dispersion, in time domain impulse response graphs, compensating CD can improve the accuracy of DMGD estimations. Therefore, digital CD compensation is included as one of the digital signal processing steps discussed in the next section.

5.3 Digital signal processing for OVNA

Extracting the desired transfer function and impulse response matrices from the sampled photocurrents Eq. (5.20) and Eq. (5.21) require several DSP steps, as shown in Fig. 5.5. Firstly, the non-flat frequency response of the ADC and power

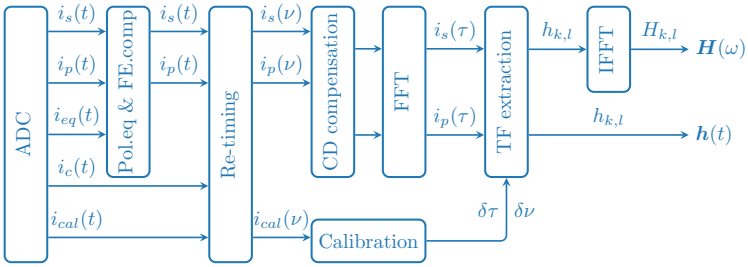

Figure 5.5: Sequence of digital signal processing steps and their signal flows.

fading introduced by polarisation rotations are compensated. Secondly, the dual-polarisation measurement is resampled to a linear frequency sweep using the fringe pattern of the reference clock interferometer. After an FFT, the transfer function matrix is extracted using windowing. Finally, linear device parameters as insertion loss (IL), mode dependent loss (MDL), group delay (GD), chromatic dispersion (CD), and differential mode delay (DMD) are calculated. These processes are explained in more detail in the next subsections.

5.3.1 Polarisation equalisation and front-end compensation

The first DSP module compensates two impairments, namely polarisation fading [J2] and any non-flatness of the digitiser's frequency response. The first algorithm requires both data signals, and polarisation tracker signal as input. The latter is a power measurement of the polarised reference arm that beats with the measurement signal in the polarisation-diverse receiver. As can be seen in Fig. 5.6a, a fluctuation of power over time is noticeable in the digitised polarisation tracker signal. This power fading originates from wavelength-dependent polarisation rotation effects, which emerges as a time-varying effect in swept wavelength interferometry. Similar power fluctuations are observed in both data channels, of which one is shown in Fig. 5.6b [209]. Without compensation, the same wavelength-dependent power fading would affect the transfer function matrix and parameters derived from it, as can be seen in Fig. 5.7a. To compensate this fading, the polarisation tracker data is averaged using a moving average window to obtain the orange curve in Fig. 5.6a. Next, the signal is normalized to yield unitary gain at its maximum. Thereby, assuming the reference polarisation is aligned at least once during a sweep. Finally, its inverse is subtracted from the measurement data to obtain the signal shown in Fig. 5.6c. It can be seen, that the power fading is significantly reduced. Consequently, the standard deviation of the obtained insertion loss (IL) reduces from 1.48 to 0.70 with polarisation equalisation enables, as can be seen in Fig. 5.7b. More details on the characterisation of this fibre will be given in Section 5.6.

Another impairment addressed in this module is the non-ideal frequency response of the ADC and receivers. By injecting a wide-band optical signal with a

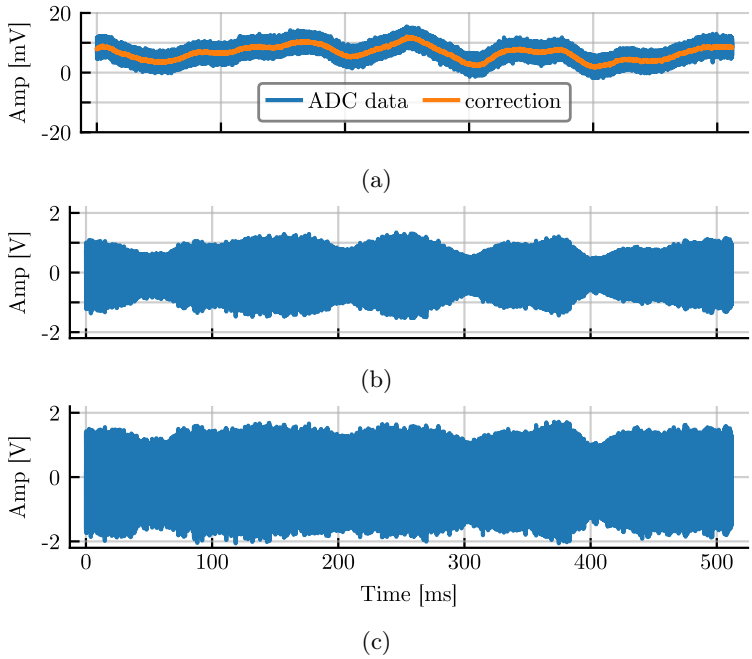

Figure 5.6: (a) Polarisation tracker and its time averaged signal used to compensate power fading effects on the measurement data shown in (b), resulting in signal (c) after compensation.

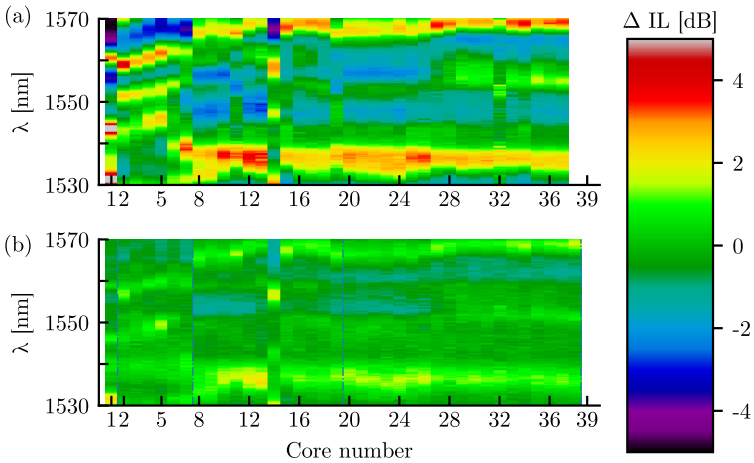

Figure 5.7: (a) Wavelength-varying insertion loss for the 3-mode cores of a few-mode multi-core fibre (FM-MCF) obtained without reference arm polarisation equalisation. (b) The same insertion loss measurement with polarisation equalisation enabled.

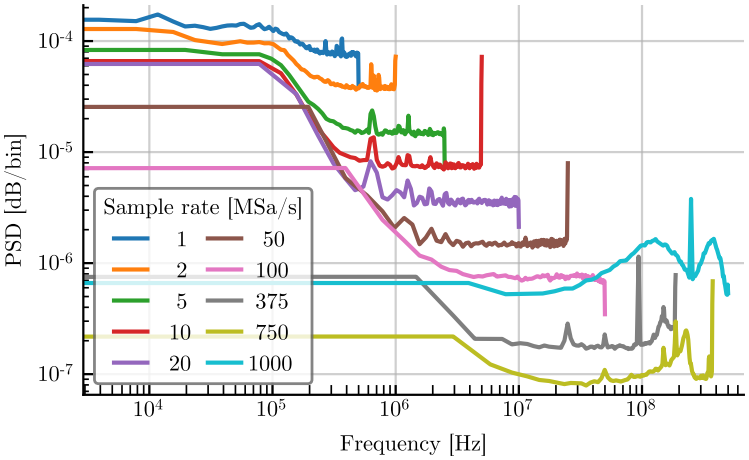

Figure 5.8: Frequency response measurements of receiver at different sampling rates.

flat spectrum, generated by shaping amplified spontaneous emission (ASE), into the photodetectors a frequency response estimation of the receiver is obtained. Figure 5.8 shows the frequency response estimation of the receiver at different sampling rates. Observe the non-flat response at higher frequencies for fast sampling speeds. The frequency responses for sampling rates below 100 MSa/s are very similar; a slow roll-off after a flat response, followed by some small spikes. For typical delay lines lengths and sweep rate of OVNA systems, these peaks will overlap with the spectral components containing the transfer functions of the DUT. Therefore, a digital filter designed to be the inverse of the measured frequency response is applied to all received signals.

5.3.2 Sweep linearisation

The captured signals, periodic in optical frequency, are sampled by the time-linear sampling clock of the ADC. As the clock interferometer experiences the same non-linear sweep, its output signal can be used to convert the measurement data to a linear frequency grid. If supported by the ADC, the photodetector output can be used as an irregular clock signal for the digitiser, with sample spacing $\delta\nu = 1/\tau_c$ [205, 210, 211]. Consequently, the measurable device length is limited to $\tau_c/2$ for Nyquist sampling. Furthermore, this method is susceptible to sampling errors introduced by the propagation time difference between channels. For accurate sampling, the light generated by the STL should arrive at the same time at all detectors. Note that, closely matching the measurement and clock interferometer lengths for accurate time alignment is challenging. Therefore, the fringe pattern of the clock interferometer is sampled by the same ADC, and re-sampling is performed digitally. This alleviates the hardware restrictions imposed

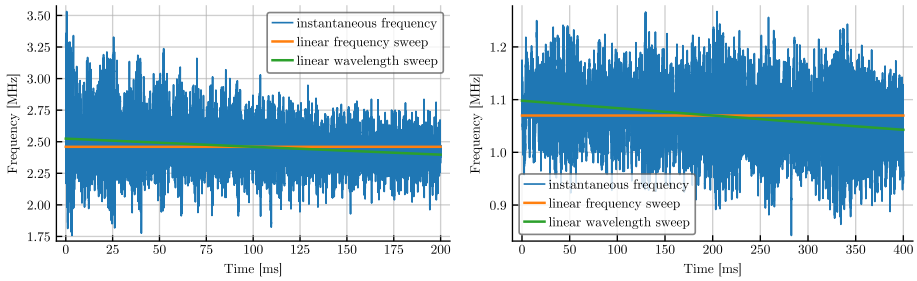

Figure 5.9: Instantaneous optical frequency $\nu(t)$ of the fringe pattern generated by the auxiliary interferometer for (a) Keysight 81960 tunable laser swept at 200 nm/s and (b) Santec-TSL510 swept at 100 nm/s. Ideal tuning rates for sweeps linear in frequency and wavelength are included for reference purposes.

by the previous linearisation solution. Firstly, a standard digitiser with a linear sampling clock can be employed. Secondly, the sampling rate of the digitiser is independent of τ_c, allowing characterisation of components longer than $\tau_c/2$, by digital upsampling of the clock. Consequently, the same interferometer can be used for all measurements, and calibration of the clock interferometer only needs to be performed once. Lastly, resolving timing misalignment between signals is significantly easier to achieve digitally, thereby reducing sampling errors.

The importance of sweep-linearisation can easily be understood from Fig. 5.9, which shows the instantaneous optical frequency $\nu(t)$ of the fringe pattern generated by the auxiliary interferometer for two different tunable laser models, swept are the maximum rates. In Fig. 5.9a, the laser is swept from 1530 nm to 1570 nm at a rate of 200 nm/s and is guided through a clock interferometer with differential group delay $\tau_c \approx 98.6$ ns. To obtain the instantaneous frequency, a Hilbert transform is applied to the digitized fringe pattern. From the analytic signal, the instantaneous phase and frequency are calculated [212]. A 2 µs long moving average filter is applied to the data shown in Fig. 5.9a. The orange line shows the instantaneous optical frequency for a perfect linear sweep with tuning rate γ in Hz/s, which would be constant at $\tau_c\gamma$. The green line shows the instantaneous optical frequency in case the configured wavelength sweep would be perfectly linear. Such a sweep would produce a slow but predictable decreasing instantaneous optical frequency over time. A similar slope can also be seen in the measured instantaneous optical frequency. From this slope and the fast fluctuations it can be seen that the sweep is non-linear and therefore tracking of the sweep rate for re-sampling is required. Figure 5.9b, shows the same three curves for a Santec TSL-510 laser source, swept at a rate of 100 nm/s, through an interferometer with differential group delay $\tau_c = 85.7$ ns. The actual frequency fluctuates by approximately $\pm 10\,\%$ from the perfect linear wavelength sweep. A similar deviation of $\pm 8\,\%$ is observed close to

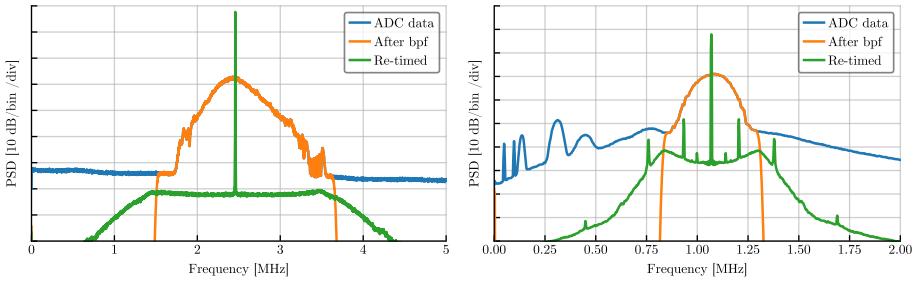

(a) (b)

Figure 5.10: Power spectral density of clock interferometer signal directly after digitization, after band-pass filtering, and after re-timing for (a) Keysight 81960 and (b) Santec-TSL510.

the end of the sweep for the other laser model. However, at the start of the sweep, the fluctuation is almost doubled to $\pm 16\,\%$. It is presumed this can be attributed to the ramping up phase of the laser. If the clock signal is accurately sampled, such that fast and large fluctuations in instantaneous optical frequency can be tracked accurately, it should not affect the sweep-linearisation process. Alternatively, the start wavelength of the sweep is lowered and the digitiser trigger is delayed, such that this part of the sweep is neglected.

Figure 5.10, shows the power spectral density of the time-linear sampled clock interferometer signal of the aforementioned laser models. In both sub-figures, the spectrum of the linear-sampled waveform is given by the blue curve. The fluctuations in instantaneous optical frequency can also be seen in Fig. 5.10 by the width of the main lobe. Note that the spectrum in Fig. 5.10a, does not contain any other spectral components besides the reference clock signal. The spectrum in Fig. 5.10b, on the other hand, shows the presence of lower frequency signals next to the main lobe of the clock signal. These frequencies, attributed to reflections in the system, are well separated from the frequencies of interest. Therefore, a digital bandpass filter is applied to remove any unwanted frequencies, as can be seen by the orange curve in Fig. 5.10b. After filtering, the signal is resampled using one of the following two methods. The first method approximates the time-domain waveform by a cubic spline, followed by a root-finding algorithm to locate all zero crossings. The second method searches for rising and falling flanks by thresholding the signal. Since the fringe pattern is a sinusoidal signal, the local area around each zero-crossing can be approximated by a linear function. Consequently, the zero points can be estimated via linear interpolation of consecutive rising and falling edges. Alternatively, a first or third-order approximation of a sine function can be used to improve the interpolation accuracy at the cost of slightly increased computation complexity. One advantage of sampling the reference clock is the ability of digital clock rate upsampling, required to sample the higher frequencies

of the measurement data. Since the interval between consecutive sample points is generally small, linear interpolation is applied to calculate the intermediate sample points. The green curves in Fig. 5.10 shows the spectra of the re-timed clock signal after digital upsampling. In Fig. 5.10a, the clock is a narrow single frequency, but in Fig. 5.10b harmonics of the main frequency are observed. These harmonics are at least 36 dB below the main frequency of interest, with minimum impact on further signal processing steps.

The calculated set of sampling points is used to re-time the two data signals from the polarisation diverse detector, using one of the previously mentioned interpolation methods. The resampled signals, now periodic in optical frequency, are spaced at interval $\delta\nu = \frac{N_R}{2N_S\tau_c}$, where N_R is the number of detected zero crossings, and N_S is the number of sample points after digital upsampling. Due to the detection of both rising and falling edges, a factor of two is added to the expression. Any time-offset between the two data channels or the reference clock, originating from unmatched path lengths, is simply negated by a linear offset of the sampling points for each channel before resampling. The spectra, of the now periodically spaced measurement signals, can be obtained via an FFT. Computing the FFT for a large number of samples is computationally intensive. Since most implementations of the FFT algorithm are efficient for signal lengths that can be factorized by prime numbers 2, 3, 5 and 7, computation time can be reduced by a possible factor of 100 [213]. The number of sampling points is therefore reduced to satisfy the following definition: $N_s = 2^i \cdot 3^j \cdot 5^k \cdot 7^l$. This step effectively reduces the sweep range to $\Delta\nu = \delta\nu N_S$, most often a small insignificant reduction at the cost of significant speed-up.

Optionally, chromatic dispersion compensation can be included in this processing step. From Eq. (5.20) and Eq. (5.21), it can be seen that a differential CD originating from the various interferometer path lengths still remains in the detected signals. For most OVNA configurations, the majority of the accumulated differential CD between two interferometer arms is introduced by the delay fibre

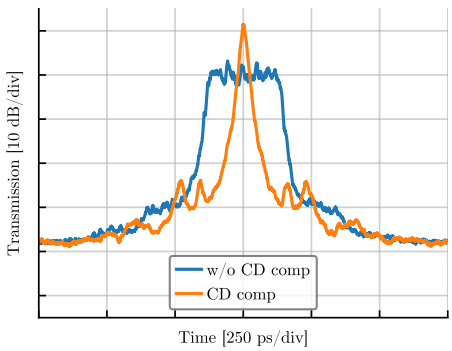

Figure 5.11: Impulse response of SMF before and after digital CD compensation.

in the reference arm, τ_r. The amount of differential CD introduced is given by:

$$H_{CD}(\omega, z) = \exp\left\{\left(-\frac{j\omega^2\beta^{(2)}z}{2}\right)\right\}, \tag{5.22}$$

where β is the propagation constant, and z the propagation distance. To compensate for this dispersion, a digital filter is designed with a complementary amount of dispersion [181]. It is common to express the chromatic dispersion D of the filter in ps/(nm · km), resulting in:

$$H_{CD}(\omega, z) = \exp\left\{\left(-\frac{4j\pi\omega\lambda_0^2 Dz}{c}\right)\right\}, \tag{5.23}$$

where λ_0 is the centre wavelength of the sweep, and $D \cdot z$ is the accumulated differential chromatic dispersions of the system. The latter quantity can be measured by the OVNA, as will be explained in Section 5.3.5 or directly estimated from the fibre lengths employed in the system in case the dispersion coefficient is known.

An example of the beneficial effect of CD compensation on impulse response measurements with OVNA is shown in Fig. 5.11, where the averaged impulse response matrix of a single-mode fibre core is shown. The reference arm length was closely, but not exactly matched to the 13.6 km long DUT. From OVNA measurements, the differential CD between the two arms was found to be 16.4 nm/ps, which corresponds to a SMF length difference of approximately 46 m. Both length and dispersion values were verified by measuring both arms independently with a fibre analyser based on optical time-domain reflectometry (OTDR). As can be seen in Fig. 5.11, the impulse response duration is significantly reduced by applying a filter designed with −16.4 nm/ps dispersion.

5.3.3 Wavelength calibration

If the pressurised gas cell is employed in the setup, the resulting signal can be used to calibrate the clock interferometer, and calculate the actual sweep range. The calibration signal i_{cal} is re-sampled at the sampling points found by the methods described in Section 5.3.2. Subsequently, a peak searching algorithm is applied to select N_p absorption lines above a certain threshold in the resampled calibration signal spectrum. Next, for each consecutive N_p lines of the reference, the sampling rate and start point are calculated using a least-squares solver. Subsequently, the solution with the smallest error is chosen, and the values for $\delta\nu$, ν_0, and $\delta\tau$, are updated. From the latter, the differential delay of the clock interferometer, τ_c, is derived and stored for future measurements. Note, that it is technically possible to compare the detected spectrum to all combinations of N_p absorption lines, but this would greatly increase computation time for large values of N_p. By ensuring a minimum distance between detected peaks, limiting the maximum number of detected peaks not to exceed the 54 lines of the gas cell, and adaptively adjusting the threshold, the algorithm generally finds an accurate estimation of the optical sampling frequency.

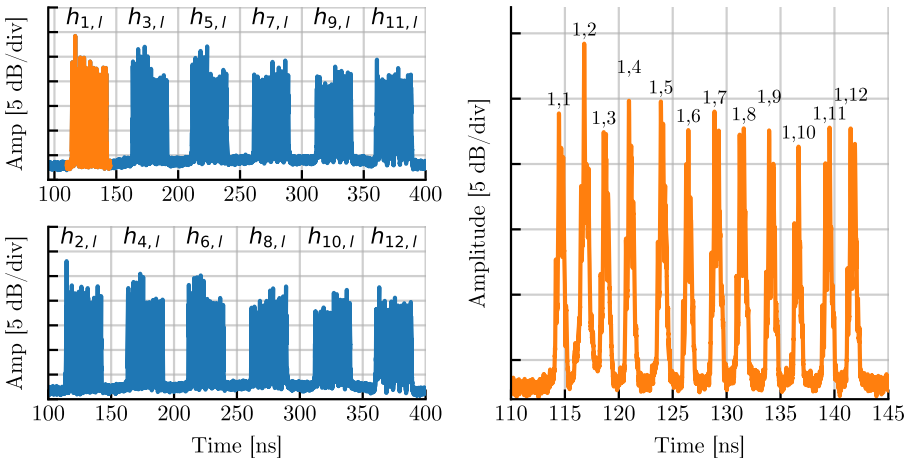

(a) (b)

Figure 5.12: (a) Spectra of re-timed signals for characterization of a 6-port mode-selective photonic lanterns spliced to a couple meters of multi-mode fibre (MMF). (b) Enlarged view of the coloured section of the first receiver, containing 12 impulse response elements.

5.3.4 Transfer function extraction

After sweep linearisation, each of the impulse response matrix elements appear at known delay values τ_p, $\tau_{in,l}$, and $\tau_{out,k}$ in the spectra of i_s and i_p. To extract each of these elements, and construct the impulse response matrix, digital windows are applied to the signals. Figure 5.12a, shows the spectra of both measurements channels for the characterisation of a 6-mode photonic lantern spliced to approximately 4.5 km of multi-mode fibre. Both spectra contain 6 groups, each with 12 impulse responses, resulting in a total of 144 matrix elements of the 12×12 transfer function matrix. Figure 5.12b is an enlarged view of the first group in the spectrum of i_s, which describes the transmission of all 12 excited spatial channels to one polarisation state of the first output port. The first element $h_{1,1}$ is found at the differential group delay between reference and measurement arm, given as $\tau_r = 114$ ns. It describes the transmission of the non-delayed polarisation to receiver s of the fundamental mode of the DUT. The other transmitted polarisation, can be found after its delay $\tau_p = 2.4$ ns. Five more sets of 2 consecutive responses, delayed by τ_{in} =4.2 ns, 9.4 ns, 14.4 ns, 19.5 ns and 24.7 ns, can be seen in Fig. 5.12b, representing the transmission of the other dual polarisation inputs to one polarisation of the first output port. Windowing at the same positions in the other spectrum returns the transmission of all input spatial channels to the other polarisation. The coupling of all input channels to all other output ports is found by adding one of the output delays, τ_{out} =48.8 ns, 96.7 ns, 147.0 ns, 197.6 ns and 245.2 ns to the positions of the first 12 elements. All odd rows of the transfer

matrix are found in the spectrum of the first detector, and the other 6 even row numbers in the second spectrum.

After labelling each element according to its position in the transfer matrix, windows are placed at the specified delay values τ. In principle, a straight-forward box car function can be applied. However, this windows shape is susceptible to ringing due to edge effects, which can be reduced by selecting a window with smooth edges. In this example, a 2 ns wide Tukey window, with a flat top and sharp cosine edges, is applied to select each of the elements. Note that, by selecting a portion of data in the time domain, the optical frequency spacing has been reduced from $\delta\nu$ to $1/\tau_w$, where τ_w is the window duration. Finally, the complex transfer function matrix is calculated via an inverse fast Fourier transform (IFFT) on all impulse response elements. It is important to highlight, that the extracted transfer function matrix is not the actual transfer matrix of the DUT, because it is rotated by arbitrary polarisation rotations. From the photo-currents of Eq. (5.20) and Eq. (5.21), the expression from input l to output k of the calculated transfer matrix $\hat{\mathbf{H}}(\omega)$ is given by:

$$\begin{aligned}
\tilde{\mathbf{H}}_{k,l}(\omega) &= \begin{bmatrix} s_1\hat{H}_{2k-1,2l-1} + s_2\hat{H}_{2k,2l-1} & s_1\hat{H}_{2k-1,2l} + s_2\hat{H}_{2k,2l} \\ p_1\hat{H}_{2k-1,2l-1} + p_2\hat{H}_{2k,2l-1} & p_1\hat{H}_{2k-1,2l} + p_2\hat{H}_{2k,2l} \end{bmatrix} \\
&= \begin{bmatrix} s_1 & s_2 \\ p_1 & s_1 \end{bmatrix} \cdot \begin{bmatrix} \hat{H}_{2k-1,2l-1} + \hat{H}_{2k,2l-1} & \hat{H}_{2k-1,2l} + \hat{H}_{2k,2l} \\ \hat{H}_{2k-1,2l-1} + \hat{H}_{2k,2l-1} & \hat{H}_{2k-1,2l} + \hat{H}_{2k,2l} \end{bmatrix} \\
&= \mathbf{R}_{s,p} \begin{bmatrix} \hat{H}_{2k-1,2l-1} + \hat{H}_{2k,2l-1} & \hat{H}_{2k-1,2l} + \hat{H}_{2k,2l} \\ \hat{H}_{2k-1,2l-1} + \hat{H}_{2k,2l-1} & \hat{H}_{2k-1,2l} + \hat{H}_{2k,2l} \end{bmatrix}
\end{aligned} \tag{5.24}$$

Combining these 2×2 sub-matrices with the polarisation rotations of all input and output delays, result in the following expression for the calculated transfer function matrix:

$$\begin{aligned}
\tilde{\mathbf{H}}(\omega) &= \begin{bmatrix} \mathbf{R}_{s,p}\tilde{\mathbf{H}}_{1,1} & \cdots & \mathbf{R}_{s,p}\tilde{\mathbf{H}}_{1,M} \\ \vdots & \ddots & \vdots \\ \mathbf{R}_{s,p}\tilde{\mathbf{H}}_{N,1} & \cdots & \mathbf{R}_{s,p}\tilde{\mathbf{H}}_{N,M} \end{bmatrix} \\
\tilde{\mathbf{H}}(\omega) &= \underbrace{\begin{bmatrix} \mathbf{R}_{s,p} & \cdots & 0 \\ \vdots & \ddots & \vdots \\ 0 & \cdots & \mathbf{R}_{s,p} \end{bmatrix}}_{\mathbf{R}_{rx}} \begin{bmatrix} \tilde{\mathbf{H}}_{1,1} & \cdots & \tilde{\mathbf{H}}_{1,M} \\ \vdots & \ddots & \vdots \\ \tilde{\mathbf{H}}_{N,1} & \cdots & \tilde{\mathbf{H}}_{N,M} \end{bmatrix} \\
\tilde{\mathbf{H}}(\omega) &= \mathbf{R}_{rx}\mathbf{R}_{out}\mathbf{H}(\omega)\mathbf{R}_{in}
\end{aligned} \tag{5.25}$$

Equation (5.25) shows that the calculated matrix differs from the actual transfer matrix of the DUT by multiple polarisation rotations, which are expressed by unitary rotation matrices. Stated in another way, the polarisation rotation does not affect the amplitude or phase response of the device and thus does not impact the linear device parameters calculated in the next section.

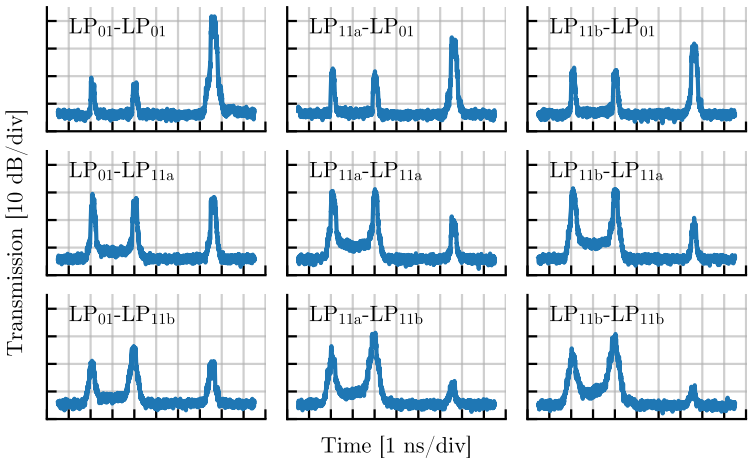

Figure 5.13: Polarisation averaged impulse response matrix of elliptical core 3-mode fibre. The labels are formatted as output port - input port.

5.3.5 Linear device parameters

Without any further processing steps, both the time and frequency response of the DUT can be directly observed from the extracted matrices of the previous section. To highlight recognisable features in the impulse response matrix, the polarisation averaged impulse response matrix of a 3-mode elliptical core fibre and mode-selective 3-port photonic lanterns is shown in Fig. 5.13. As a result of the core ellipticity, mode degeneracy between LP_{11a} and LP_{11b} is broken, which results in three distinct peaks in the impulse response graphs [100]. In Fig. 5.13, the two peaks on the left correspond to the LP_{11} modes. Peaks in impulse response represent strong mode mixing at discrete points, such as spatial multiplexers. Whereas, distributed modal crosstalk of fibres appears as plateaus between peaks. From the spacing between peaks, differential mode delay (DMD) or differential mode group delay (DMGD) can be estimated. Finally, an indication of mode selectivity of spatial multiplexers can be obtained from the impulse response strengths of peaks. For example, in Fig. 5.13, approximately 20 dB selectivity between LP_{01} and LP_{11ab} can be seen in the top left response (LP_{01} to LP_{01}).

Although a lot of information can be retrieved directly from the impulse response, it does not include any wavelength-dependent characteristics, e.g. any filtering behaviour or chromatic dispersion. The latter will produce additional impulse response spreading, thus affecting any estimations of DMGD, as discussed in Section 5.2. The transfer function matrix, on the other hand, shows wavelength varying attenuation but lacks temporal information, and thus cannot visualize pulse broadening. By combining both spectral and temporal information in one spectrogram, a comprehensive visual representation of DUT behaviour can be obtained.

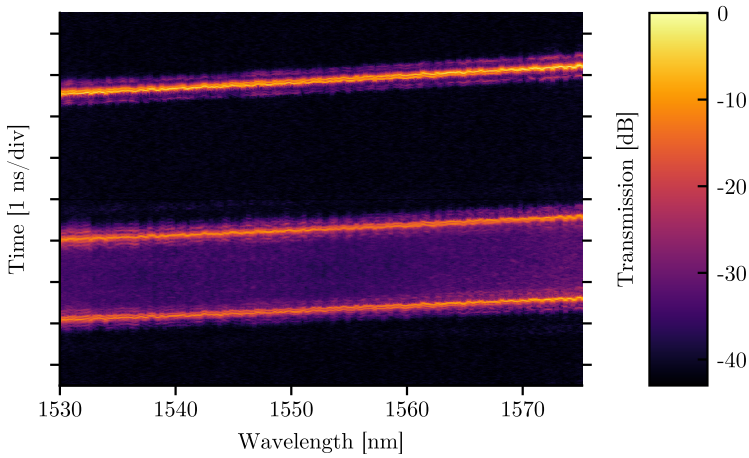

Figure 5.14: Spectro-gram of elliptical 3-mode fibre.

As an example, the fibre averaged spectrogram of the same 3-mode elliptical core fibre is shown in Fig. 5.14. In this figure, three temporal lines corresponding to the three impulse response peaks are observed. Based on the stronger modal cross-talk between the LP_{11}-modes, it can be presumed the bottom lines represent the LP_{11a} and LP_{11b} modes. Furthermore, all lines have a non-zero slope, indicating there is a wavelength-dependent change in group delay. The impulse response, as shown in Fig. 5.13, can be interpreted as the sum of all vertical slices of the spectrogram. The pulse broadening shown in the impulse response would be larger than the actual pulse width at a single wavelength in the spectrogram. Consequently, any estimate on DMGD from the pulse width would be overestimated.

While spectrograms provide a quick impression of the behaviour of the DUT by combining both transfer function matrix and impulse response matrix, quantifying linear device parameters from it is not practical. However, it is possible to extract parameters such as mode dependent loss (MDL), insertion loss (IL), group delay (GD), chromatic dispersion (CD), and differential group delay (DGD) from the transfer matrix. The first two parameters can be obtained via a singular value decomposition (SVD) [174]. An SVD factorizes an $m \times n$ complex matrix $\mathbf{M}$, to $\mathbf{U\Sigma V}^*$, where $\mathbf{U}$ is an $m \times m$ unitary matrix, $\mathbf{\Sigma}$ is an $m \times n$ diagonal matrix, and $\mathbf{V}$ is an $n \times n$ unitary matrix [214]. The values on the diagonal of $\mathbf{\Sigma}$ are the non-negative real singular values of $\mathbf{M}$. This factorisation can be interpreted as multiple transformations, starting with a rotation $\mathbf{V}^*$, followed by a scaling $\mathbf{\Sigma}$, and a final rotation $\mathbf{U}$. A singular value decomposition (SVD) factorises the transfer matrix into:

$$\tilde{\mathbf{H}}(\omega) = \mathbf{U}(\omega)\mathbf{\Sigma}(\omega)\mathbf{V}^*(\omega), \tag{5.26}$$

where the unitary matrices $\mathbf{U}(\omega)$ and $\mathbf{V}^*(\omega)$ represent the modal coupling or mixing

at the input and output of the DUT. The modal propagation is represented by the singular values in descending order, along the diagonal of $\mathbf{\Sigma}(\omega)$. The singular values $\lambda_i(\omega)$ of $\tilde{\mathbf{H}}(\omega)$ are associated with the electrical field gains, whereas MDL and IL are commonly expressed in terms of optical field gains. Insertion loss is defined as the mean of the singular values squared, and mode dependent loss is the ratio between the largest and smallest singular value:

$$\mathrm{IL} = \overline{\lambda_i^2(\omega)} \tag{5.27}$$

$$\mathrm{MDL} = \frac{\max \lambda_i^2(\omega)}{\min \lambda_i^2(\omega)} \tag{5.28}$$

The optical field gains $\lambda_i^2(\omega)$ correspond to the mathematically equal, eigenvalues of phase-conjugate round-trip propagation matrix $\tilde{\mathbf{H}}(\omega)\tilde{\mathbf{H}}^*(\omega)$ [174]. An SVD at each frequency, results not only in IL and MDL for each frequency, but also their frequency resolved IL and MDL.

Another parameter of interest for SDM components is associated with propagation speed difference between spatial channels. The differential mode (group) delay is obtained via principal mode analysis on $\tilde{\mathbf{H}}(\omega)$. Principal modes are an extension on the principal states of polarisation (PSP), which describe a pair of input states which, under a fixed input state of polarisation and small change in optical frequency, produce a pair of output vectors invariant to the first order of ω [215]. The group delays associated with these principal states describe the polarisation mode dispersion (PMD) for single-mode components or differential mode delay (DMD) for multi-mode components. The principle modes are obtained from the transfer function via differentiation:

$$\mathbf{G}(\omega) = j\frac{\mathrm{d}\tilde{\mathbf{H}}^*(\omega)}{\mathrm{d}\omega}\tilde{\mathbf{H}}(\omega), \tag{5.29}$$

with the eigenvalues of $\mathbf{G}(\omega)$ representing the group delays of the different principal modes. Chromatic dispersion can be defined as the derivative of the group delay with respect to frequency or wavelength. Since the latter is more common, the CD of the principal modes are obtained by taking the derivative of the group delays with respect to wavelength.

5.4 Specifications and design considerations

In the previous sections, a comprehensive overview of the required hardware and signal processing steps were presented, without going into system specifications and limitations. In this subsection, an overview of design considerations is presented for the development of spatially-diverse optical vector network analysers.

Consider a DUT, with N input and N output ports, insertion losses IL_D, and a total dispersion resulting in an impulse response width of T_w. The maximum number of ports supported by the OVNA is mainly determined by the power budget

available for the $1 \times N$ splitter and coupler. To fully utilise the dynamic gain of the digitiser, the minimum received optical power should cover the full input range V_{pp} of the ADC. Therefore, the minimum received power can be expressed as:

$$P_{Rx,min}[\text{dBm}] = 10 \cdot \log_{10}\left(10^3 \cdot \frac{V_{pp}}{G_{TIA}\mathcal{R}Z_{ADC}}\right), \tag{5.30}$$

where G_{TIA} is the trans-impedance gain of the photo-receiver, and Z_{ADC} is the impedance of the digitiser port. After subtracting the minimum received power and splitting losses introduced by the mandatory splitters, i.e. polarisation multiplexing and splitting the reference and clock signals, from the maximum source output power, the remaining budget is equally split between the N-port splitter and combiner for the spatial channels.

Besides optical power, the signal frequency is another design constraint, which is imposed by the delay lines and the tuning rate of the laser source. To accommodate the total impulse response, the digital window must be at least T_w wide. For the windowing process to succeed, impulse response elements are not allowed to overlap, Defining the polarisation multiplexing delay τ_p as the shortest delay, leads to input delays $\tau_{in,l} = 2l \cdot T_w$, and output delays $\tau_{out,k} = 2kN \cdot T_w$. Note that it is possible to swap input, output, and polarisation fibre delays. Finally, the reference arm is closely, but not perfectly matched to the DUT length, resulting in a differential delay of τ_r.

Next, the minimum sampling rate required to digitize the highest frequency is calculated as the product of the tuning rate and the longest fibre: $f_s = (\tau_r + 4N^2T_w)\gamma$. A faster sweeping rate is preferred because it minimises the influence of temporal distortions during the measurement. Since the clock interferometer is sampled by the same digitiser, the maximum differential interferometer must satisfy the following condition: $f_s \geq \tau_c^{-1}$. Obviously, the bandwidth of all photodetectors, including trans-impedance amplifiers must be sufficient as well. Depending on the number of spatial channels of the DUT, a high gain trans-impedance amplifier (TIA) is required, which typically is limited in bandwidth. However, this limited bandwidth is often sufficient for most OVNA configurations.

The maximum dynamic range of the signal is determined by the resolution of the digitiser, thus a high resolution ADC is favoured. Generally, digitisers are available either with high resolution or sampling speed. However, with typical signal frequencies in the order of MHz, cutting edge fast sampling technology is not required. The achievable dynamic range is calculated from the effective number of bits (ENOB), which also takes noise sources within the ADC in to account. Since digital upsampling of the clock signal is applied, temporal resolution can be digitally enhanced. The spectral resolution, on the other hand, is completely determined by the window duration T_w. Table 5.1 gives an overview of the operating range and typical values of the developed OVNA during this PhD project.

Table 5.1: Specifications of developed OVNA.

Parameter	symbol	unit	Min	Max	Typical
Sweep range		nm	1510	1625	1530-1570
Sweep rate	γ	nm/s	.1	200	200
Source power		dBm	6	10	
DUT port count	N		1	16	
Dynamic range		dB		60.2	
Temporal resolution	$\delta\tau$	fs			≈ 500
Spectral resolution					
before windowing	$\delta\nu$	MHz			≈ 1
after windowing	$\delta\nu$	MHz			≈ 100

5.5 Characterisation of spatial multiplexers

The optical vector network analyser described in the previous section and illustrated in Fig. 5.4 employs Mach-Zehnder interferometric structures. Consequently, the transmission of optical components can be measured. A major limitation of this configuration is that it cannot be applied for characterisation of a single spatial multiplexer, because the multi-mode facet is incompatible with the single-mode optical source and detectors. Therefore, spatial multiplexers are often characterised as a pair. Consequently, within the obtained transfer matrix, the matrices of individual components is not accessible.

To characterise a single spatial multiplexer, the interferometers of the OVNA are replaced with Michelson-interferometers to obtain the setup depicted in Fig. 5.15. This setup captures the reflection of cleaved fibre at the multi-mode facet of the spatial multiplexer [201, 216, 217]. Note that this reflection is typically small, ($\approx 4\,\%$), which aggravates the already stringent power budget requirements of the

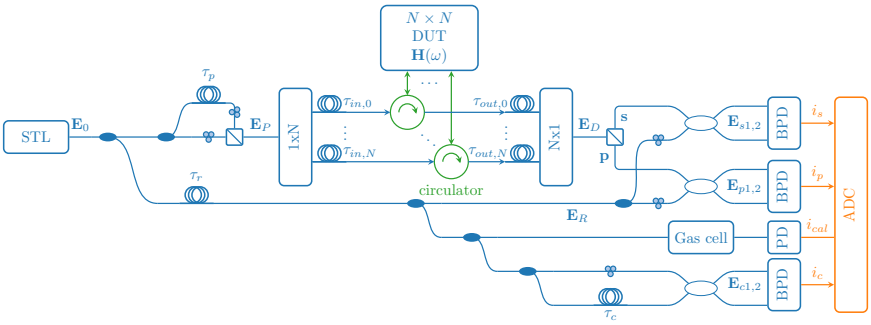

Figure 5.15: Spatially-diverse optical vector network analyser configured to measure the reflection of a $2N \times 2N$ component.

system. Optical circulators are positioned at each single-mode fibre of the DUT, redirecting the reflection towards the polarisation diverse receiver. The digital signal processing steps remain unchanged for this type of measurements.

One of the 6-port mode-selective lanterns employed in the experiment described in Section 6.3, is characterised using the reflective OVNA setup depicted in Fig. 5.15. The six-port configuration employs fibre delays at the inputs in steps of 1 m, and 10 m at the outputs of the 6 optical circulators. The polarisation delay is realised using a 50 cm long SMF patch cord. Since the DUT length is negligible, no additional fibre delay is placed in the reference arm. The source is swept at 200 nm/s, starting at 1530 nm. Using the wavelength calibration method described in Section 5.3.3, the auxiliary clock interferometer delay is found to be 87.6 ns, resulting in an optical sampling rate of approximately 2.45 MHz. Since this rate is too low for sampling the highest signal frequency of approximately 10 MHz, the clock is digitally upsampled.

In the transmission experiment, the 6-mode PL needs will be fusion spliced to MMF. However, the multi-mode facet was designed to match the dimensions of 4-linearly polarised (LP) mode fibre. To reduce the large change from the 29 µm core diameter lantern output, to 50 µm core graded-index MMF, a short length of graded-index 6-LP is used as intermediate fibre. In Fig. 5.16, the MDL and IL obtained from the singular values of the measured transfer matrix of the DUT are shown. Note that this result is the concatenation of the DUT transfer function matrix in both directions and reflection at the cleaved fibre:

$$\tilde{\mathbf{H}}(\omega) = \mathbf{H}_{DUT,out}\mathbf{H}_r\mathbf{H}_{DUT,in} \tag{5.31}$$

The transfer function matrix $\mathbf{H}_{DUT}$ can be decomposed into matrices for each of different fibre sections. However, since the DUT will be used as such for transmission experiments, the individual matrices are not of interest. Based on the reciprocal behaviour of the spatial multiplexer, it can be assumed that $\mathbf{H}_{DUT,out} = \mathbf{H}_{DUT,in}$. Furthermore, the contribution of $\mathbf{H}_r$ can be minimised by subtracting a calibration measurement of the reflection at the optical circulator ports. Therefore, the IL and MDL for a single propagation through the lantern is estimated to be half of the values shown in Fig. 5.16a.

Figure 5.16b is a visual representation of the transfer function matrix, which is obtained by integrating the impulse response matrix elements and sum over polarisations. From this figure, the mode selective property of the DUT can be observed from intensity differences on the diagonal compared to the off-diagonal elements. The first represents intra-mode-group coupling, and the latter is the coupling between mode-groups.

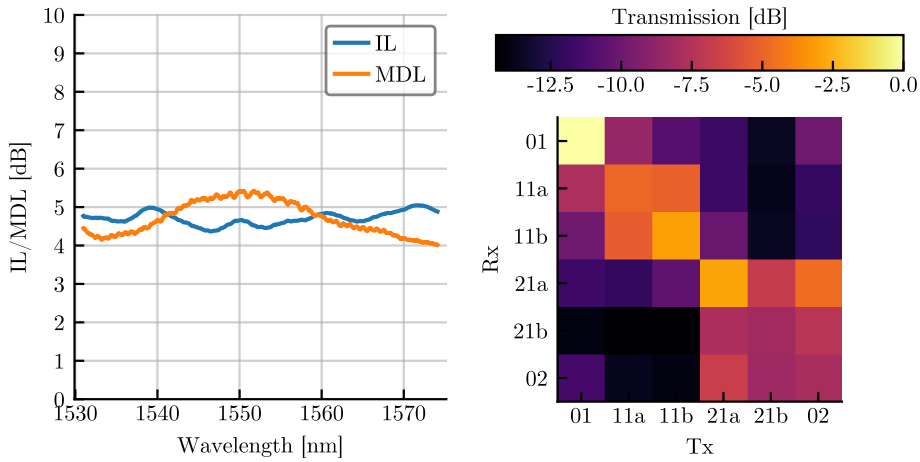

(a) (b)

Figure 5.16: Insertion and mode dependent losses (a) and transfer matrix (b) of 6-port mode-selective lantern spliced to multi-mode fibre.

5.6 Analysis of a 39-core few-mode fibre

By combining multi-core fibre technology with few-mode cores, spatial multiplicity beyond 100 channels can be realized [218]. When the inter-core cross-talk of a FM-MCF is negligibly small, each core can be measured sequentially, and the high splitting losses to support a large port count DUT can be avoided. The maximum inter-core cross-talk of the fibre employed in this experiment was found the 50 dB [114]. Therefore, the transfer function matrix of each few-mode core is measured independently. The focus of this experiment is the effect of CD on the impulse response duration, and DMGD estimations derived from it.

The analysed FM-MCF fibre has 38 3-mode cores and 1 single-mode core [114]. For simplicity, the fibre is referred to as a 39-core fibre. The single-mode core is added for transmission using self-coherent detection schemes [172, 173, J13, 219], or -as in this work- used as the reference arm of the OVNA. Furthermore, this single-mode core acts as a visual reference marker for rotational alignment and fusion splicing. The cores are positioned on a three-ring layout with radii $r_1 = 41\,\mu\text{m}$, $r_2 = 79\,\mu\text{m}$, and $r_3 = 127\,\mu\text{m}$, with a minimum core pitch of 40 µm, as can be seen in Fig. 5.17b. This figure also includes the designed relative refractive index profiles of both core types. The graded-index few-mode cores have a trench design to reduce inter-core cross-talk. Free-space core (de)multiplexers, with 3-mode SC/UPC connectors are employed to access the 39 cores of the 13.6 km long FM-MCF [114]. Single-core 3-mode laser inscribed glass mode-multiplexers are switched between the few-mode ports of the core multiplexers. These are placed at both sides of 13.6 km FM-MCF, with the few-mode facets connected to one of

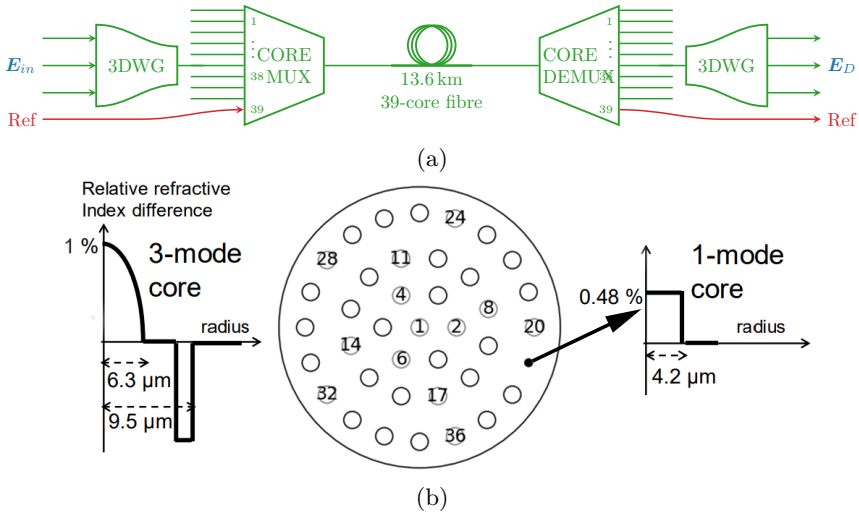

Figure 5.17: (a) DUT section of the OVNA. (b) Core mapping and index profiles of the FM-MCF (fig (b) after [114]).

the 3-mode cores in the fibre.

For each core, the 6×6 impulse response matrix $\mathbf{h}(t)$ and transfer function matrix $\mathbf{H}(\omega)$ are measured. Note that the employed PL were not mode-selective, hence, each core can be represented by a single spectrogram, as shown in Fig. 5.18. Observe that the temporal lines can be grouped into two sets based on their slope for all figures. One set is a more confined group of two lines, corresponding to the two polarisation states of the fundamental mode. The four lines in the other set represent the four degenerate modes within the LP_{11} group, which have a larger spread between them. Even though the same set of lines can be found in all spectrograms, their position and slopes vary strongly between the cores.

In the spectrogram of core 5, both mode groups overlap for the majority of the 40 nm swept wavelength range, indicating a stronger mode coupling between the 6 modes in both mode-groups. Consequently, the impulse response duration is one of the shortest for all cores. As both lines have a dispersion slope in the opposite direction, the impulse response duration increases with wavelength. Cores 11 and 12 show similar overlapping lines, with low DMGD behaviour. A longer temporal response is observed for core 22, which contains 3 sets of temporal lines. Based on the dispersion slope of all lines, it is presumed that the middle group represents the LP_{01} mode, surrounded by the degenerate LP_{11} modes. Furthermore, the intensity of the area between the outer lines is of similar magnitude as the intra-mode-group cross-talk in other spectrograms. Since the fundamental mode resides between the other lines, the impulse response duration is completely determined by the other mode group. Consequently, there is no wavelength-dependent impulse response

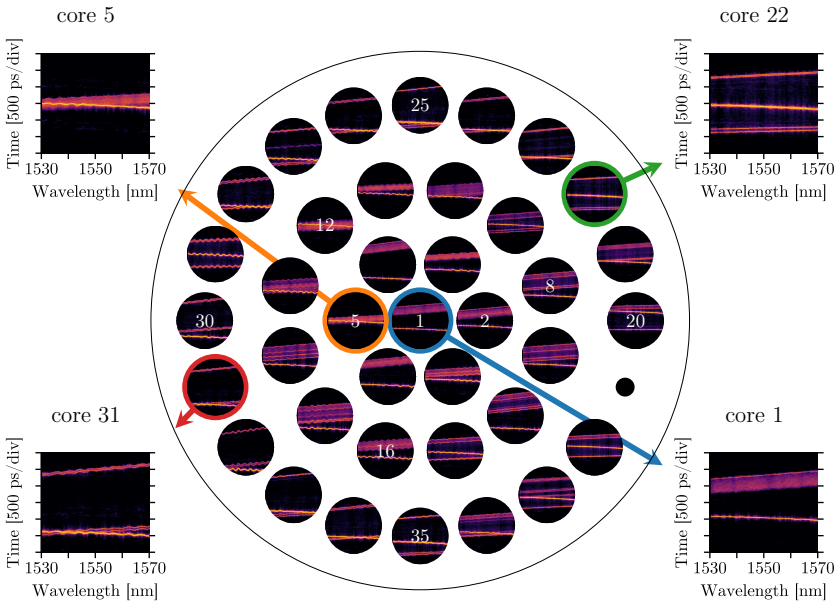

Figure 5.18: Spectrograms for all 38 few-mode fibre cores, and enlarged views for cores 5, 22, and 31

broadening as the outer lines have the same wavelength-dependent behaviour. Almost half of the cores on the outer ring show these features, the other half resembles more closely to the spectrogram of core 31. In this figure, the first mode group overlaps with one of the LP_{11} modes. The last type of spectrogram is illustrated by core 1, in which a clean separation between the two mode-groups can be observed. The LP_{11} modes show a wide spread of energy, approximately 10 dB above the inter-mode-group cross-talk, suggesting there is a significant amount of mode dispersion between the degenerate modes.

All spectrograms show a wavelength-dependent slope of the temporal lines with opposite signs. For each core, the slope of both lines is estimated and shown in Fig. 5.19a. On the left axis, the differential chromatic dispersion with respect to single-mode core 39 is shown. Next to opposite signs, it can be seen that the variance of differential CD for the LP_{11} mode group is larger compared to the well-confined values for the fundamental mode. The mean differential CD is estimated to be -2.3 ps/nm and 3.8 ps/nm for the LP_{01} mode, and the LP_{11} mode respectively. To translate the differential CD to absolute values, the single-mode core is analysed with the OVNA. A SSMF of similar length is placed in the reference arm. Since the dispersion coefficient of the reference fibre is known, the differential CD can be translated to an absolute value on the right axis.

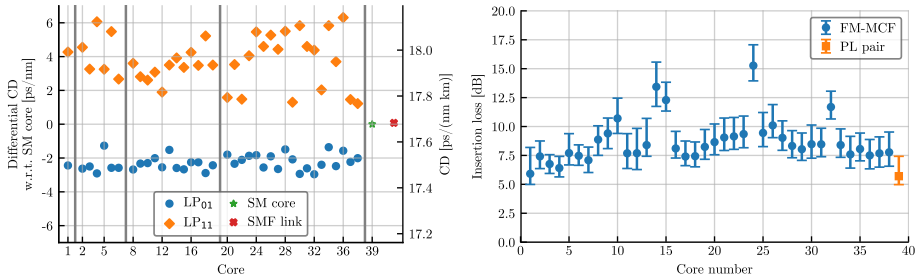

(a) (b)

Figure 5.19: (a) Differential chromatic dispersion for each of the mode-group of the 38 3-mode cores. Differential values are translated to absolute values based on CD measurement of the single-mode reference arm, which is included as a reference. (b) Insertion loss for each core and a pair of photonic lanterns. The error bars indicate the spread over the 40 nm sweep range.

The measured CD values are mapped to the core-layout in Fig. 5.20a, where each half of the circle represents one of the mode groups. This measurement is compared to the previously analysed impulse response duration, shown in Fig. 5.20b [209]. A strong correlation between the colour intensities of both graphs can be seen, linking the longer impulse response duration to a larger differential CD value. For cores on the left side of the outer ring (core 25-35), the highest differential CD and longest impulse response duration is observed.

A SVD is performed on the transfer function matrix of each core at each measured frequency. Subsequently the IL is calculated at a 50 GHz resolution. In Fig. 5.19b, the markers represent the average IL over the 1530 nm to 1570 nm scanned range. The error bars around each marker correspond to the minimum and maximum IL. For reference sake, the IL of a back-to-back measurement of the photonic-lantern pair is included. The average insertion loss over all cores is found to be 8.7 dB. Significantly higher losses are observed for cores 10, 14, 15, 25 and 32, which is in agreement with the reported transmission experiments [114].

Besides IL, also MDL can be calculated from the singular values. The largest contribution of MDL is to be expected from the spatial multiplexers. Hence, the performance of the pair of photonic lanterns is characterised first, without the core multiplexer and FM-MCF. An average MDL of 20.1 dB was found within the 40 nm of analysed bandwidth. For the complete system, including 13.6 km FM-MCF and both mode- and core-multiplexers, the MDL for each core was found to be below 25 dB. Since this result is dominated by the large MDL of the photonic lanterns and the total MDL of concatenated elements of weakly coupled modes strongly depends on the relative alignment of their respective principle modes, no statement of the MDL is made.

The skew between the single-mode core and few-mode cores is of interest as this

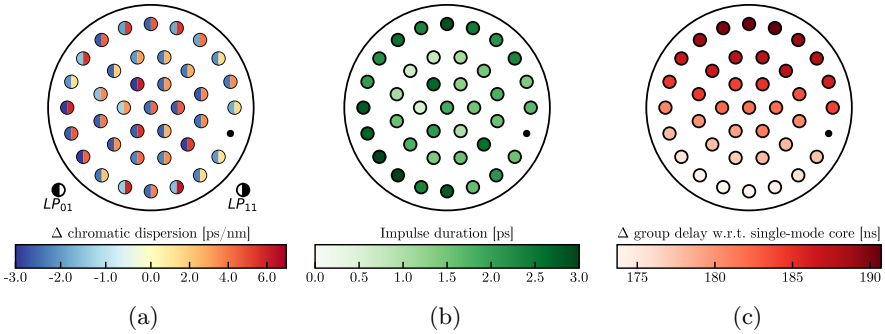

Figure 5.20: (a) Differential chromatic dispersions for both mode groups. The left half of the coloured area represents the differential CD for LP_{01} mode, the right side for LP_{11} mode-group. (b) Total impulse response duration mapped to the core layout of the fibre. (c) Group delay differences between few-mode and single-mode core.

fibre was designed with self-coherent applications in mind. Figure 5.20c shows the group delay difference of each few-mode mode with respect to the single-mode core. The obtained skew ranged from 173.3 ns to 190.7 ns, with an average of 182.2 ns. Note that the lowest and highest skew values are found at opposite sides of the fibre. This gradient is likely attributed to the compression of the inner cores and stretching of the outer cores of the spooled fibre.

CD compensation using the estimated values shown in Fig. 5.19a is applied to the measurements of core 9. As can be observed by the flat temporal line in Figs. 5.21b and 5.21c, CD compensation for one of the mode groups can be realized. Figure 5.21a shows the spectrogram without any CD compensating, the other two figures are compensated by applying receptively -2.3 ps/nm and 2.8 ps/nm dispersion compensation. Alternatively, an intermediate value can be chosen for partial compensation of both mode groups. By removing the wavelength-dependent dispersion, the summed impulse responses are narrower and give a better indication of the modal dispersion.

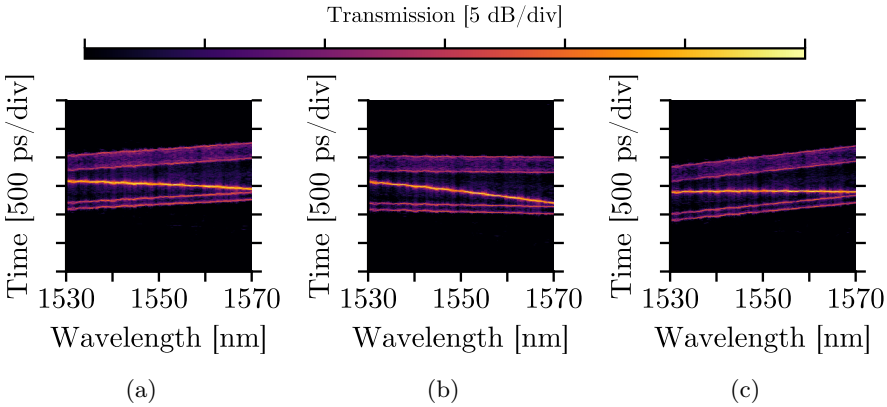

Figure 5.21: (a) Spectrogram for core 9 without chromatic dispersion compensation, (b) with −2.3 ps/nm CD compensation and (c) with 2.8 ps/nm CD compensation applied.

5.7 Impact of fibre bending and twisting on FM-MCF

In this experiment, the OVNA is employed to observe the inter-mode-group cross-talk of bent and twisted FM-MCF. Stronger mode-coupling can be beneficial for transmission, as one of the main performance-limiting impairments, MDL, would scale with only the square-root of distance, compared to linear growth in weaker coupled systems [174]. On the other hand, if the inter-mode-group cross-talk is insensitive to bending and twisting, the fibre is interesting for short reach interconnects employing partial multiple-input multiple-output (MIMO) equalisers for systems in environments where fibre bending is unavoidable. Partial MIMO is proposed to reduce the computational complexity of the equalizer by employing multiple smaller MIMO equalisers, one for each mode group, to unravel the intra-mode-group mixing [99, 220, 221]. Since these equalisers can operate independently and in parallel, the latency can be reduced. However, for partial MIMO to work, the inter-mode-group cross-talk must be sufficiently low, and high mode-selective spatial multiplexers are required [222].

The DUT evaluated in this experiment is a set of 3DWGs and a heterogeneous 36-core 3-mode fibre, of various lengths and spooled at different bending radii. The core arrangement and refractive index profiles of the 3 different core types are depicted in Fig. 5.22. The first digit of the core labels is the row number when the fibre is aligned with the marker on top, the second digit is the core number within that row. The three different colours represent the core types and match with the colours of the index profiles in Fig. 5.22c. The refractive index difference between core and outer cladding is 0.74, 0.64 and 0.54 for type A,B, and C, respectively. The relative refractive index to the trench is kept constant at 0.94 for all core types [223]. Combined with a core pitch of 34 µm, the heterogeneous cores minimizes the inter-core cross-talk to −86 dB between the fundamental mode

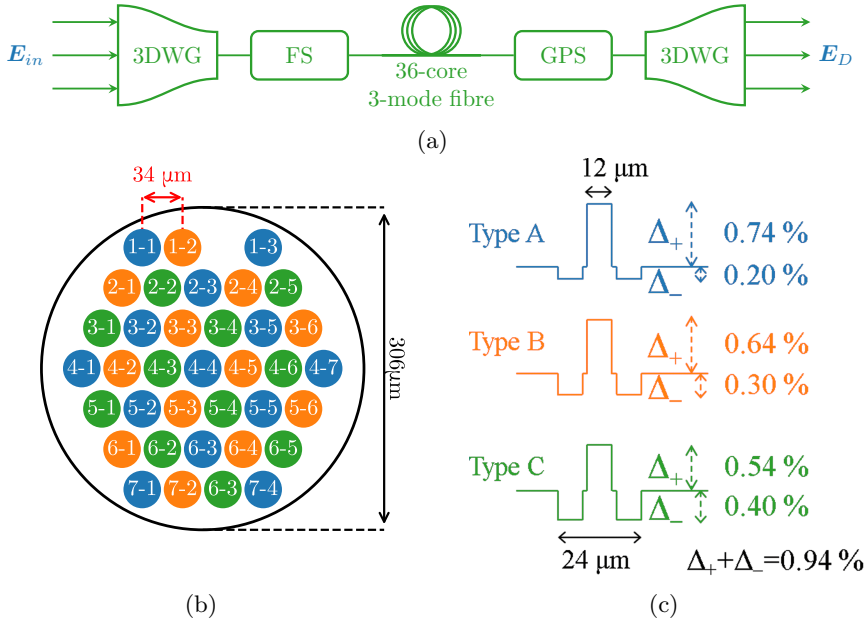

Figure 5.22: (a) Schematic of the DUT evaluated with the OVNA, including 36-core 3-mode fibre sections spooled at different radii, 3D-waveguide (3DWG) mode-multiplexer. Core-alignment is done by the fusion splicer (FS) and glass processing system (GPS) with end-facet view. (b) Core layout of the heterogeneous 36 core FM-MCF and (c) the index profiles of the three core types.

and -31 dB between two LP_{11} modes of adjacent cores. All cores have a step-index profile, designed to support only the fundamental and first LP modes. The main motivation for selecting this fibre for this experiment is the large DMGD between the two-mode groups. A large dispersion results in a clear separation of the impulse response peaks originating from the spatial multiplexers, even after a short transmission distance that can easily be spooled with different bending radii. The mode-group dispersion is designed to be 7.4 ps/m, 7.1 ps/m and 6.3 ps/m, for core type A, B, and C respectively.

Alignment of the single-core 3-mode multiplexers is done using the fibre positioning and rotation mechanisms of a Fujikura ARCMaster FSM-100P fusion splicer and Vytran GPX-3000 glass processing system. A visible light source is injected into one of the single-mode inputs of the demultiplexer. Using the end-facet view of the Vytran machine, this light source can be detected when it is aligned to one of the cores. This alignment step aligns the spatial demultiplexer to the core of interest. Subsequently, with only the LP_{01} input connected, the output of the STL is enabled with the coherence control switched off. This increases the laser linewidth to 40 MHz, which decreases power fluctuations when only a single

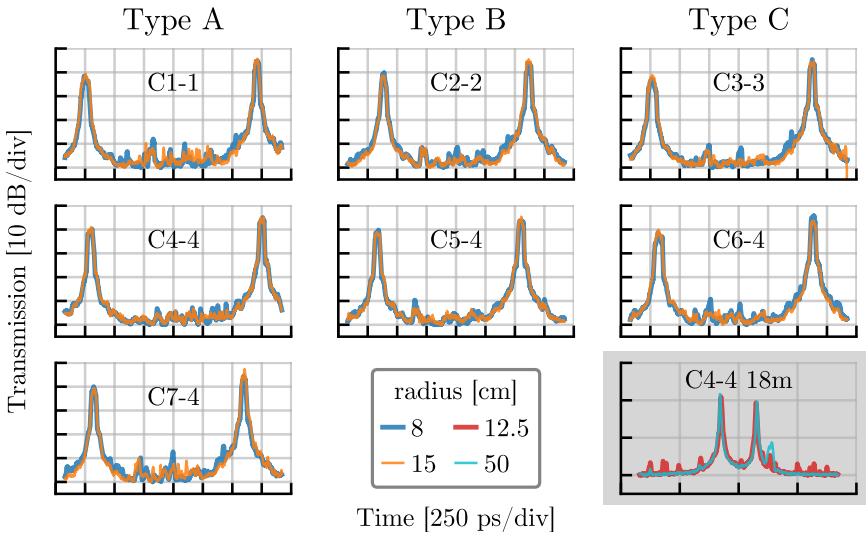

Figure 5.23: Summed impulse response matrix for cores 1-1, 2-2, 3-3, 4-4, 5-4, 6-4, and 7-4 of 195 m FM-MCF with bending radii of 8 cm and 15 cm. Bottom right: impulse response of centre core (4-4) for 18 m FM-MCF with bending radii of 12.5 cm and 50 cm.

3DWG output port is observed. By maximising the power transfer, the alignment of the multiplexer is improved.

The OVNA is configured with a polarisation multiplexing delay of 0.4 m, and delay lines of 3.2 m and 6.4 m at the input and 1 m and 2 m at the output. As a result, the measurable impulse response duration is limited to 1.9 ns, which translates to a maximum fibre length of approximately 265 m. For each evaluated piece of FM-MCF, the delay in the reference arm is matched within approximately 10 m to keep the signal frequencies and required sampling frequency low. The STL is swept from 1530 nm to 1570 nm with a rate of 100 nm/s.

At first, two short pieces of FM-MCF of approximately 18 m are spooled with a bending radius of 12.5 cm and 50 cm. The first radius is chosen to represent fibre spooled on a drum, and the latter a link without any (tight) bends. As can be seen in the bottom right graph of Fig. 5.23, the impulse responses are very similar. Therefore, an attempt to increase the influence on fibre bending is made by decreasing the bending radius and increasing the fibre length. A 195 m long section of FM-MCF is spooled on a fibre drums with 8 cm radius, and re-spooled on a 15 cm radius drum. The impulse response matrix of seven cores along the diagonal (1-1, 2-2, 3-3, 4-4, 5-4, 6-4, and 7-4) are measured sequentially using the OVNA. The sum of all 36 elements squared is shown for each core in Fig. 5.23. Again, no significant change in impulse response is notable between the two bending radii. From the separation of the two peaks, the DMGD is estimated to be 1.45 ns, 1.22 ns,

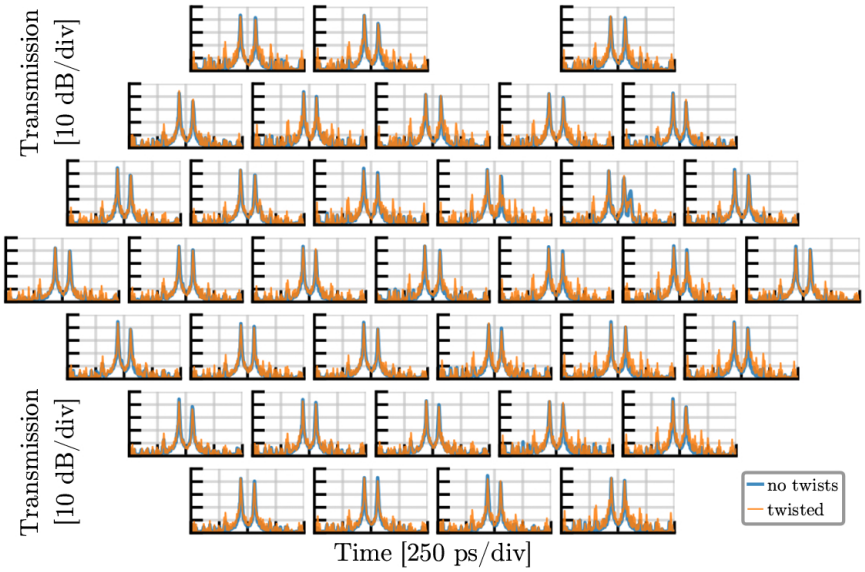

Figure 5.24: Summed impulse response matrix for each core of twisted and untwisted fibre with a bending radius of 8 cm.

1.37 ns, 1.45 ns, 1.20 ns, 1.32 ns and 1.27 ns for cores ascending in numbering. After dividing these values by the expected DMGD of each core type, the fibre length is found to be 195 m. The estimations for cores 1-1, 2-2, 3-3, 4-4, and 5-5 are in close agreement, but from the impulse responses of cores 6-4 and 7-4, a slightly shorter estimate is found. For all impulse responses the distributed inter-mode-group crosstalk, represented by the plateau between both peaks, is found to be at least −28.1 dB.

On top of bending the fibre by spooling on a small drum, the fibre is also twisted as this might be an additional source of increased modal-crosstalk. First, multiple pieces of fibre are twisted to determine the maximum number of twists before it breaks. Almost all fibre sections broke after approximately 4 twists per metre. Therefore, 50 twists along the propagation axis are applied over a length of 15 m, which are held in place by fibre clamps. Short fibre lengths of approximately 1 m bridge the gap between clamps and alignment stages, resulting in a total DUT length of 17.4 m. For each core, the impulse response is measured with the OVNA, which is illustrated by the orange curves in Fig. 5.24. Next, the tension introduced by the twists is removed, and the fibre is re-spooled to the same drum for a second set of impulse response measurements. In Fig. 5.24, it can be seen that the blue curves, representing the untwisted fibre, overlaps with the twisted fibre for all cores.

In Figure 5.25, the estimated DMGD of each core for both twisted and untwisted fibre, and their targeted design value are shown. Minimal differences between

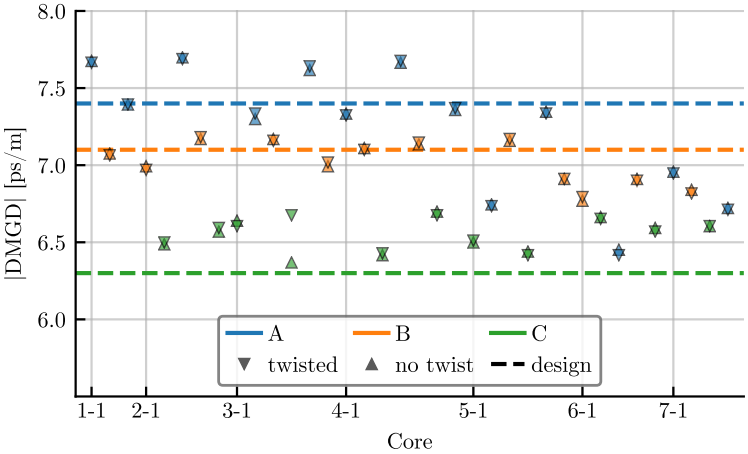

Figure 5.25: Estimated and designed DMGD values for each core of twisted and untwisted fibre.

twisted and untwisted fibre are observed from the impulse responses. Note, that core type B matches the closest to its designed value. For core type C, the measured DMGD is above the targeted value, which matches with earlier observations [223]. From the impulse response measurements of 195 m fibre (Fig. 5.23), a larger than designed DMGD was observed for core 6-4 and 7-4. Similar behaviour is observed for almost all cores on the 6th and 7th row in this smaller section of fibre. Since this deviation from designed DMGD values is observed for different fibre sections, which are re-spooled in-between measurement, the influence of bending seems unlikely. Manufacturing imperfections are a more probable origin for this effect. Nevertheless, the maximum inter-mode-group cross-talk of -29.4 dB, observed for core 2-5, will have a minimum impact on the optical signal-to-noise ratio (OSNR).

With a minimum mode-group cross-talk of -28.1 dB and large DMGD, this FM-MCF is a suitable candidate for 3-mode partial MIMO transmission over short distances where fibre bending with is unavoidable. Note that the smallest bending radius exceeds that of bend-insensitive single-mode fibre, as the FM-MCF will break at these small radii.

5.8 Conclusions

In this chapter, a comprehensive overview of optical vector network analysis is given, starting from the fundamentals of swept wavelength interferometry, to the spatial-diverse variant capable of direct measurement of the $2M \times 2N$ transfer function matrices of SDM components. Next to the required DSP steps required to extract the transfer function matrix from measurement data, and derive linear

parameters, additional performance enhancing steps are proposed.

A big advantage of optical vector network analysis is its ability to characterise a single spatial multiplexer, whereas generally multiplexers are characterised as a set of multiplexer and demultiplexer. By exploiting the reflection of cleaved fibre, a 6-port photonic lantern is characterised. Key parameters as IL, MDL, and mode-selectivity are extracted from the obtained transfer function matrix.

Inherent to the large optical bandwidth property of spatial diverse optical vector network analysers is pulse broadening due to chromatic dispersion. From the analysis of a 39-core 3-mode fibre, a correlation between chromatic dispersion and impulse response duration is observed. Furthermore, it is shown that partial CD compensation can improve DMGD estimations based on impulse response measurements.

The impact of fibre bending and twisting on the impulse response matrix, in particular, inter-mode-group cross-talk, is investigated in a FM-MCF utilizing optical vector network analysis. No significant changes in the impulse response were observed by reducing the bending radius of the fibre or twisting the fibre along the propagation axis. Consequently, no increase in inter-mode-group cross-talk was observed.

Enabled by optical vector network analysis, the complete linear response of individual transmission system components can be obtained. Therefore, an insight of component-specific contributions towards transmission system impairments can be gained. This knowledge can be utilised to operate transmission systems at their optimum, and thereby improving capacity as is the objective of the transmission experiments in the next chapter.

Chapter 6

Short-reach space division multiplexed transmission

The wide interest of the telecommunication research community towards space-division multiplexing (SDM) culminated in numerous publications on mode multiplexing using three modes [27, 224, 225]. Driven by the ambition to increase the number of modes, extensive development of few-mode fibres, multiplexers and digital signal processing (DSP) algorithms, rapidly resulted in mode-division multiplexing exploiting six modes [30]. Scaling to a higher number of modes has its challenges. Key to unravelling spatial channel mixing is managing the mode dependent loss (MDL) and differential mode group delay (DMGD), caused by the different modal gains and propagation constants of the spatial modes. Transmission systems employing large DMGD fibres, generally have a broad impulse response. To successfully unravel the spatial channel mixing, the memory of multiple-input multiple-output (MIMO) signal processing must be sufficiently long to accommodate the complete impulse response. Furthermore, the dimensions of the MIMO equaliser scale quadratically with the number of spatial channels. Whereas the challenge of managing DMGD is mainly addressed in the transmission fibre, spatial multiplexers greatly contribute to MDL. This impairment describes variations among the spatial channel gain and may degrade system performance. For large values, it can even result in channel outage for narrowband systems [155].

Enabled by low DMGD 6-LP few-mode fibre (FMF), low loss photonic lantern mode-multiplexers, and advanced DSP, the first-ever reported transmission exploiting 10 spatial modes is discussed in Section 6.1. A line rate of 400 Gbit/s per wavelength channel is achieved over 4.45 km few-mode fibre. A space-time code is proposed to mitigate performance differences between spatial channels. Furthermore, a ten-hour experiment is performed to demonstrate the system performance stability.

Scaling towards higher spatial multiplicity in few-mode fibres is challenging, as small manufacturing imperfections can result in large deviations from targeted

fibre parameters [97]. Therefore, the design of conventional 50 µm core diameter multi-mode fibre (MMF) is optimised for SDM transmission in the C-band. The produced fibre supports a total of 55 linearly polarised (LP) modes and is designed to minimize cross-talk to mode groups not excited at launch. Consequently, the capacity of transmission systems based on this MMF can be scaled by upgrading terminals when required. In Section 6.2, the first 10 modes of the MMF are exploited for transmission at similar line rates to the few-mode fibre over a distance of 40 km.

Generally, the first N modes, distributed over multiple mode-groups, within a few-mode or multi-mode fibre are selected for mode-division multiplexing. Compared to inter-mode-group coupling, modes within a mode-group exhibit strong mode coupling, which is beneficial for SDM transmission as it reduces the group delay spread and variations of losses from MDL [155]. This property is investigated by compared two transmission systems; a conventional system populating spatial channels over multiple mode-groups, and a proposed setup exciting the same number of modes in a single, higher-order mode-group. A shorter impulse response was reported, which allows for signal detection using smaller equaliser windows, and thus reducing computation complexity.[1]

6.1 10-Mode transmission over 6-LP fibre

In this section, key subsystems developed to demonstrate the first transmission exploiting 20 spatial channels (2 polarisations per 10 spatial modes) over 4.45 km 6-LP fibre. A line rate of 400 Gbit/s per wavelength channel was achieved by transmitting quadrature phase shift keying (QPSK) symbols at 10 GBaud. As large variations between spatial channel performance were observed, a round-robin space-time code, that allocates data across all channels in a round-robin fashion, is proposed. Accordingly, it minimises the performance variance between transmission channels. Finally, system stability is demonstrated by means of a ten-hour measurement. Over this period, the system bit error rate (BER) is below the presumed 20 % soft-decision forward error-correction (SD-FEC) limit of 2.4×10^{-2}, required for reliable communication. In Section 6.1.1 the 6-LP fibre is introduced. Followed by the design and characterisation of the employed 10-mode photonic lantern (PL) spatial multiplexer in Section 6.1.2. The transmission setup employed to evaluate transmission performance, including the required digital signal processing steps are covered in Section 6.1.3. Experimental results of the single wavelength channel transmission are presented in Section 6.1.4. In this section, also the round-robin encoder is introduced. Finally, the performance of the combined mode-division multiplexing (MDM)-wavelength-division multiplexing (WDM) transmission setup is discussed in Section 6.1.5.

[1] The experiments described in this chapter are based on the following publications: [J26, J8, J20, J22]

6.1.1 Low-DMGD 6-LP few-mode fibre

Key to mode-division multiplexing is a low DMGD characteristic of the fibre, as it limits the impulse response broadening. Consequently, the receiver memory requirements are relaxed. Therefore, the transmission fibre is designed according to the strategy described in [226]. First, the nominal frequency V is set to 9.65, and the core radius is fixed to 14 µm, and the trench volume is adjusted to 0.54 µm^2 to ensure low bending losses for guided LP modes. The trench volume is calculated as the integral of the trench index, relative to the cladding over its cross-section. The resulting index profile is depicted in Fig. 6.1a. Observe the four horizontal lines in the profile, representing the four guided mode-groups. Due to the two-fold degeneracy of the LP_{11}, LP_{21}, LP_{31}, and LP_{12} modes, a total of 10 LP modes are supported by this fibre. Hence, when accounted for the polarisation diversity of each LP mode, a total of 20 spatial channels are available for SDM transmission. To reduce the maximum |DMGD| between any combination of LP modes, the α-parameter, which describes the shape of refractive index arc for graded-index core profiles, is optimised to be 1.95 [94]. The resulting characteristics of the optimised 6-LP are given in Table 6.1.

Critical to the fabrication of low DMGD few-mode fibres, is its resilience to small variation of the refractive index and α-parameter. Manufacturing tolerances of 1 % variation in α are not uncommon for conventional fibre drawing processes. This relative small deviation can significantly increase the DMGD, from theoretical achievable minimum of 8.6 ps/km to 98.5 ps/km [96]. To closely match the designed profile, this fibre is fabricated using high accuracy plasma chemical vapor depostion (PCVD) fabrication process. It has standard glass (125 µm) and

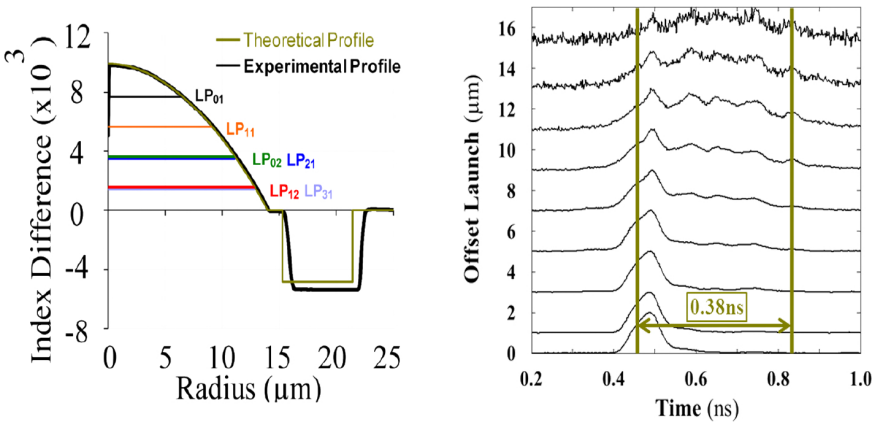

(a) (b)

Figure 6.1: (a) Theoretical and experimental index profile of the 6-LP mode fibre. (b) An estimated maximum |DMGD| of 0.38 ns based on offset launching measurements.

Table 6.1: Design characteristics of 6-LP fibre at 1550 nm

	LP_{01}	LP_{11}	LP_{21}	LP_{02}	LP_{31}	LP_{12}
n_{eff}-$n_{cladding}$ [10^{-3}]	7.71	5.62	3.54	3.55	1.46	1.48
Bend loss [dB/turn] (10mm radius)	$\ll 1$	$\ll 1$	$\ll 1$	$\ll 1$	1.6	7.3
DMGD(vs LP_{01}) [ps/km]	-	-7.6	-6.5	-7.8	0.8	-7.5
CD [ps/(nm · km)]	20.1	20.4	20.6	20.6	20.9	20.9
Effective area [μm^2]	126	169	227	256	273	274

coating (245 µm) dimensions. Fibre parameters are measured for the fundamental mode of the 4.45 km long fibre employed in the transmission setup of Section 6.1.3. The chromatic dispersion (CD), effective area, and attenuation were found to be 19 ps/(nm · km), 117 μm^2 and 0.236 dB/km at 1550 nm. Figure 6.1b, shows the pulse broadening of a short 50 ps pulse, offset launched into the few-mode fibre. Observe the increasing pulse broadening for large offset values, introduced by the DMGD between the excited higher-order modes. From this figure, a delay spread $\leq$ 0.357 ns after 4.45 , is observed [94]. The estimated |DMGD| of 80 ps/km, is roughly ten times larger than the targeted value, but given the manufacturing accuracy can still be considered low for FMF.

6.1.2 10-Mode photonic lanterns

To interface with the modes of the FMF, a set of fibre-based PLs is employed. Compared to the first spatial multiplexers based on optical phase plates (Section 3.3.1), all-fibre PLs have the advantage of low insertion loss (IL) and low MDL. Furthermore, both single-mode and few-mode facets can be fusion spliced to other fibre components, further reducing the losses and improving temporal stability.

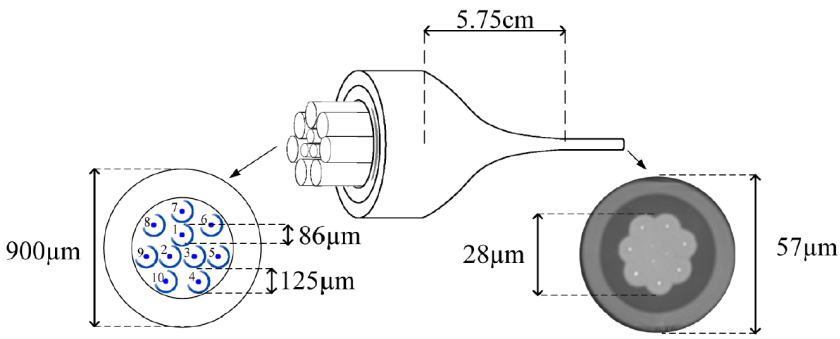

Figure 6.2: Schematic of a 10-port photonic lantern and cross-section of the capillary before tapering. A photo of the tapered facet is shown on the right.

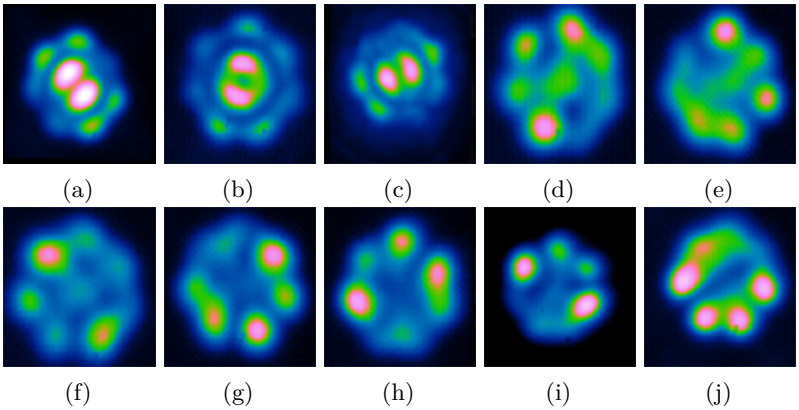

Figure 6.3: Mode profiles of the mode-selective 6-port photonic lantern for ports 1 (a) to 10 (j).

For these reasons, all-fibre photonics lanterns are investigated for this 10-mode transmission system.

The spatial multiplexers are manufactured by adiabatically tapering a bundle of single-mode fibres (SMFs). The 10 single-mode fibres, one for each mode, are placed in a low refractive index, fluorine-doped silica capillary. To prevent high losses, the fibre arrangement, depicted on the left-hand side in Fig. 6.2, matches with the modal symmetry [124]. To achieve the required geometry, 86 µm cladding diameter fibres are used for the 3 inner single-mode fibres. The SMFs on second ring have conventional 125 µm cladding diameters. The core diameter of all 10 fibres is 13 µm. Next, the assembly is adiabatically tapered down from 900 µm to 47 µm over a transition length of 5.75 cm. As can be seen in the tapered facet, depicted on the right-hand side of Fig. 6.2, the single-mode fibres have merged to one few-mode core. Note that the inner diameter of 28 µm matches with the 6-LP fibre dimensions.

Before employment in the 10-mode transmission system, the set of spatial multiplexers are characterised. First, the single-mode ports are consecutively excited by a 50 nm bandwidth light source around 1550 nm. By observing the tapered facet with an infrared camera (Xenics, XEVA-1.7-320), the near field intensity profiles are obtained. From the profiles depicted in Fig. 6.3, no discernable mode fields are visible in a single image due to the non-mode-selective property of the spatial multiplexer. Although, a hint of selectivity between ports on the inner and outer ring of the assembly (Fig. 6.2) can be observed.

Next, the excess losses of the devices are investigated by measuring the power transfer from each single-mode port to the few-mode facet. A distributed feedback (DFB) laser at 1540 nm generates the source signal of 0 dBm, which is detected by an integrating sphere detector. Figure 6.4 shows the obtained excess losses, measured directly at the output of the PL, and after butt-coupling to approximately

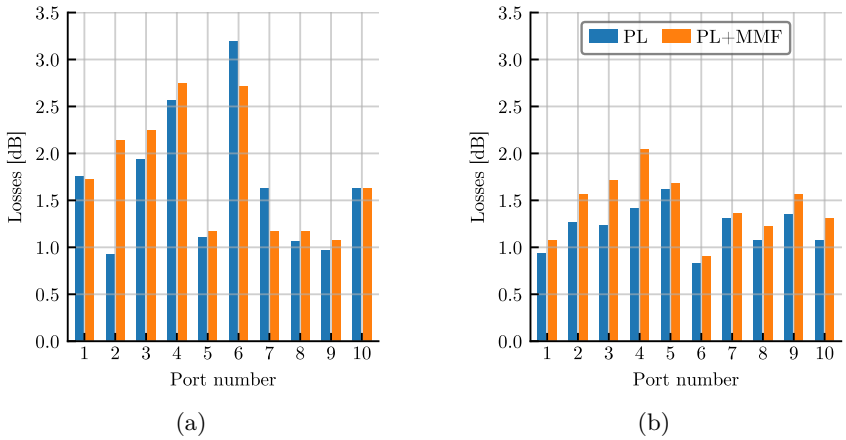

Figure 6.4: Insertion losses of the 10 mode photonic lanterns measured directly and after splicing to approximately 2 m of graded-index (GI)-MMF.

2 m of 50 µm core diameter MMF. The later measurement is of interest for the experiment discussed in Section 6.2. Observe the larger variation of losses between ports in Fig. 6.4a, compared to the other lantern (Fig. 6.4b), which is mainly attributed to the quality of the cleaved few-mode facets. To preserve the matched fibre dimensions, it was not possible to redo the few-mode cleave. The spatial multiplexer with the lowest IL is selected as a demultiplexer, because it results in higher signal power into the erbium-doped fibre amplifiers (EDFAs). The noise figure of these fibre amplifiers degrades for lower input powers. A higher IL at the transmitter can easily be mitigated by increasing the launch power.

6.1.3 Experimental setup

In the experimental setup, depicted in Fig. 6.5, external cavity lasers (ECLs) are tuned to generate 5 wavelength channels centred around 1547.72 nm, with a 100 GHz spacing. The output of one ECL is split to serve as local oscillator (LO) for homo-dyne detection, before it is combined with the other loading channels. The carriers are modulated with a 10 GBaud QPSK sequence of length 2^{15}, using an IQ-modulator driven by two synchronised digital-to-analog converters (DACs).

The output of the modulator is guided through a polarisation multiplexing stage, where the signal carried by one of the polarisations is delayed by 485 ns. Polarisation controllers are employed to align the polarisation of both arms with the orthogonal inputs of the polarisation beam combiner (PBC). Subsequently, wavelength decorrelation is applied by delaying the odd-numbered channels with 985 ns, after splitting the grid using a wavelength selective switch (WSS). Finally, mode decorrelation using the following delay lines 49 ns, 85 ns, 134 ns, 193 ns, 237 ns, 281 ns, 322 ns, 397 ns and 442 ns is performed to generate the 10 decorrelated signal

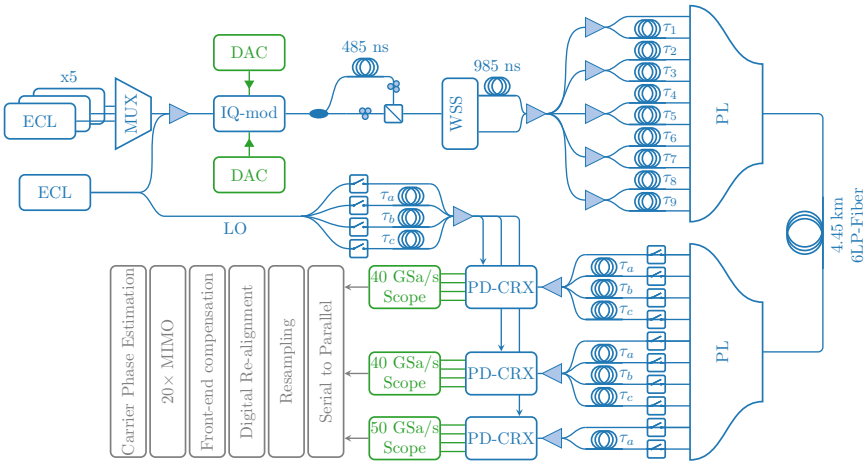

Figure 6.5: 10 mode transmission setup including 10-port photonic lantern (PL) and 6LP FMF. External cavity laser (ECL), wavelength selective switch (WSS), digital-to-analog converter (DAC), polarisation-diverse coherent receiver (PD-CRX), EDFAs are denoted by triangles. Mode decorrelation delays τ_i are 49 ns, 85 ns, 134 ns, 193 ns, 237 ns, 281 ns, 322 ns, 397 ns and 422 ns. Delay lines of the time-domain multiplexed space-division multiplexing (TDM-SDM) are τ_a=3 km, τ_b=6 km, and τ_c=9 km.

copies that are fed to the single-mode inputs of the spatial multiplexer. EDFAs are employed per two inputs, to compensate for splitting losses and control the launch powers.

The photonic lanterns from Section 6.1.2 are butt-coupled to 4.45 km of 6-LP few-mode fibre described in Section 6.1.1, using multi-axis alignment stages. A first rough alignment is performed on visual feedback using a microscope objective. Next, the alignment is optimised based on the output powers of all 10 output ports of the demultiplexer. Note that each of the single-mode outputs of the demultiplexer contains a combination of the 10 transmitted signals, as a result of the mode mixing of the spatial multiplexers and fibre. Unravelling the mode mixing is performed in the digital domain, for which the full optical field of all 10 dual-polarisation outputs is required. Employing a polarisation-diverse coherent receiver (PD-CRX) and analog-to-digital converter (ADC) for each channel would be a costly endeavour. Hence, a TDM-SDM sub-system, which allows the detection of multiple spatial channels with a single coherent receiver and ADC by time multiplexing the signal, is employed [227]. Note that the TDM-SDM is a measurement technique and for any real application of MDM, one receiver per channel is still required. In this sub-system, the 10 single-mode outputs of the transmission link are gated by acousto-optic modulators (AOMs). Subsequently, the signals are guided through delay lines of 0 km, 3 km, 6 km and 9 km before recombination, realised by an 1×4 optical fibre coupler. Finally, the signals are amplified and fed to 3 PD-CRXs. The

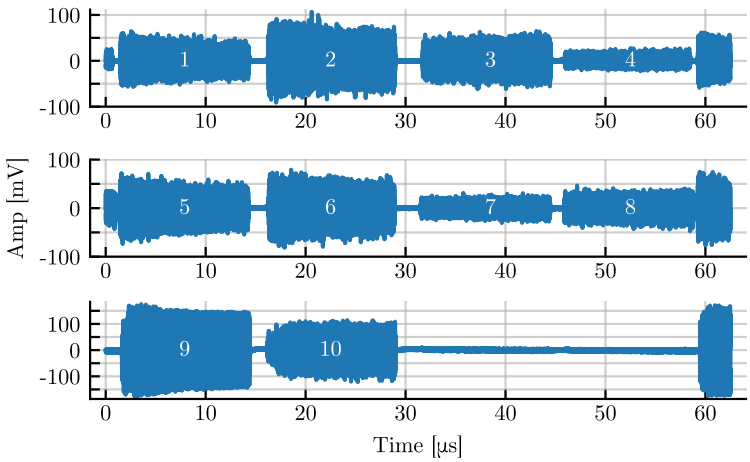

Figure 6.6: One of the four waveforms detected by each of the 3 ADCs after TDM-SDM.

to base-band converted signals are digitised at 40 GSa/s or 50 GSa/s by synchronous triggered real-time oscilloscopes with a minimum channel bandwidth of 20 GHz. The detected waveforms for a 10-mode transmission are depicted in Fig. 6.6. Note that only one of the four channels of each ADC is shown. Blocks 5 to 10, are detected by integrated coherent receivers with trans-impedance amplifiers (TIAs), which introduce transients at the start of each block. As the duration of each block is approximately 12.5 µs, and the 2^{15} symbols long sequence is repeated every 3.3 µs, the unwanted transient can be simply discarded, while enough symbols remain for accurate BER estimations. It is critical to phase match the LO signal for all delayed signals to apply accurate carrier-phase recovery. Therefore, the LO is guided through a similar delay lined structure.

All digital signal processing is performed offline, starting with the serial to parallel conversion of the serialised data blocks of the TDM-SDM. As the other DSP processing steps require $T/2$ sample spacing, the 20 complex signals (10 modes, 2 polarisations) are resampled to two-fold oversampling. Mandatory for MIMO processing is the correct time alignment between all received modes. This is realised by calculating the cross-correlation with the transmitted sequence and applying shifts accordingly. Next, front-end impairments, including IQ-orthonormalization are compensated. Unravelling the 20 transmitted data channels is achieved by a 20×20 minimum mean squared error (MMSE) time domain equaliser (TDE). The weight matrix is updated according to the least means square (LMS) algorithm for convergence, and is switched to decision-directed least mean square (DD-LMS) after 40 000 symbols. Both algorithms include variable step-size error updating rules [187]. To corroborate the impact of impulse response changes during the change from data-aided to decision-directed, a capture is reprocessed without

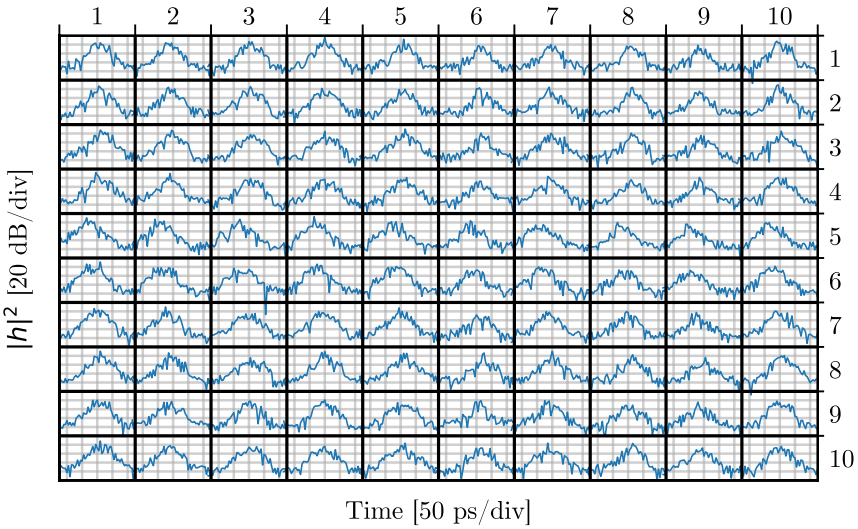

Figure 6.7: Polarisation averaged equaliser weights of 20×20 MIMO. Input and output spatial modes correspond to the port numbers of the spatial multiplexers.

any updates after the 40 000 symbols used for convergence. No change in the impulse response and stable BER estimations over multiple captures were observed. Therefore, a stable impulse response can be assumed within the capture length. Frequency domain equaliser (FDE) can reduce the computational complexity with respect to TDE [228]. However, due to the lower adaptation gain, FDE is too slow for stable convergence in the relative short capture window, while still maintaining enough symbols for accurate BER calculations. The capture window is time constraint by the delay fibres of the TDM-SDM.

Subsequently, the minimal frequency offset between transmitter and LO is removed by applying carrier phase estimation (CPE) based on digital phase-locked loops (PLLs) [229]. Next, the symbols are de-mapped to bits for performance evaluation. Note that symbols used for convergence are not taken into account, and the BER is calculated over the remaining 100 000 symbols per channel. The system averaged BER is obtained by averaging over the 4 million bits in all channels: polarisation, mode, in-phase and quadrature.

6.1.4 Single channel performance

At first, the low DMGD property of the fibre is investigated by observing the impulse response of the system in single-wavelength operation. It is not possible to visualise all 400 weight elements of the 20×20 MIMO equaliser without losing detail. Therefore, a polarisation averaged response for each LP mode is depicted in Fig. 6.7. Note that no direct relation between LP mode and input could be made because of the non-mode selective spatial multiplexer. Hence, the inputs and outputs are numbered according to the single-mode fibre arrangement of Fig. 6.2. From these elements an impulse response spread of ≤ 0.2 ns after 4.45 km can be observed, which in agreement with the DMGD values obtained by offset launching Fig. 6.1b. Due to the low temporal resolution of the equaliser and small accumulated DMGD, it is challenging to distinguish the mode groups in Fig. 6.7.

Furthermore, the equaliser convergence of the 10-mode transmission is compared to the single-mode optical back-to-back configuration in Fig. 6.8. Both measurements used 39 T-half spaced taps with a fixed adaptation gain of $\mu = 10^{-4}$. For the sake of comparison, both errors are normalised such that the initial error is 1 and the final error is 0. System convergence is assumed when the error is within 5 % of the final error value. From Fig. 6.8 it can be seen that all spatial channels converge at the same rate, and reach the convergence threshold after 0.58 µs. This is roughly 11 times slower compared to the SMF transmission, which takes only 0.05 µs to converge. This result matches with the theoretical expected linear scaling of convergence time with the number of mixed channels [230]. The small discrepancy is attributed to the eigenvalue spread of the transmission system.

Transmission performance is evaluated based on the pre-FEC BER for each spatial channel. As can be seen in Fig. 6.9b, a strong fluctuations in BER between

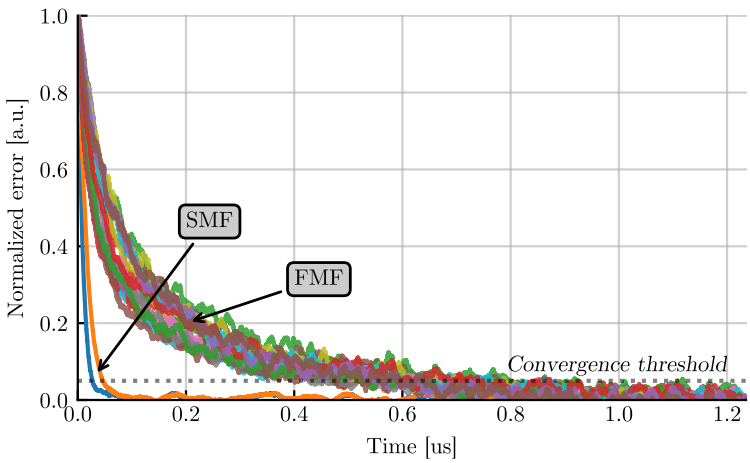

Figure 6.8: TDE convergence for 10-mode transmission and single-mode back-to-back.

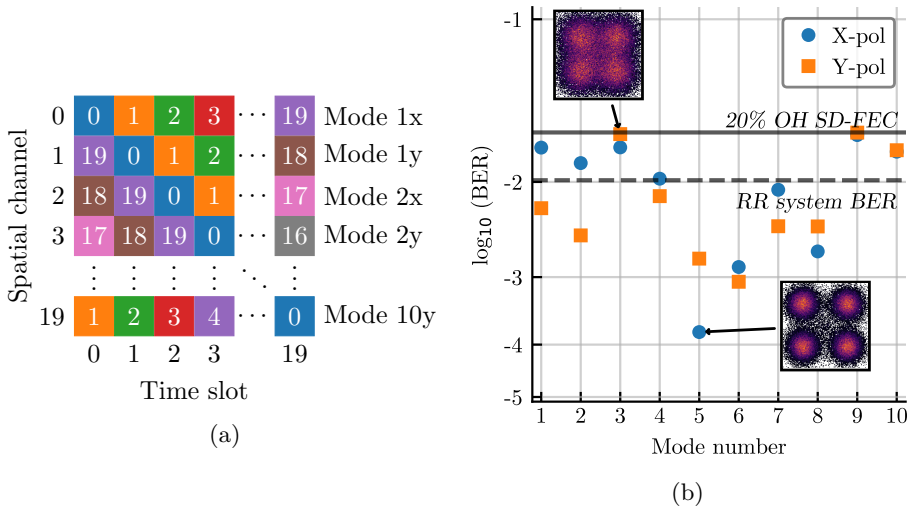

Figure 6.9: (a) Graphical representation of the round-robin space-time encoder. (b) BER for all 20 spatial channels, and the system averaged result with the applied round-robin coding. Constellations of the best and worst performing channels are shown in the insets.

the spatial channels can be observed. This large difference is also visible in the insets of that figure, showing the constellations for the best and worst-performing channel. Without any channel coding applied, the system performance would be determined by the worst-performing channel. For this measurement, it prevents successful transmission, when a standard 20 % overhead SD-FEC is applied, as the BER of some channels is above the threshold. To balance the performance of individual channels, a round-robin space-time coding, which allocates the time-slotted data channels over the available spatial channels, is applied to the sequences. For this 10-mode system, data channel $0 \leq m \leq 19$ is allocated to transmission channel $0 \leq n \leq 19$ at time slot $0 \leq k \leq \infty$ as $n = mod_{20}(m + k)$, where mod_{20} is the modulus after division by 20. A graphical representation of this code is given in Fig. 6.9a. It is important to note that the theoretical implication of this coding scheme is small, however, the hardware considerations for potential implementation are challenging due to timing implications. Critical timing alignment is required at the transmitter and receiver for decoding the channels in DSP. With the proposed round-robin coding applied, the performance of the channels is averaged to the dashed line in Fig. 6.9b, which is below the before-mentioned threshold, enabling transmission at a data rate of 320 Gbit/s.

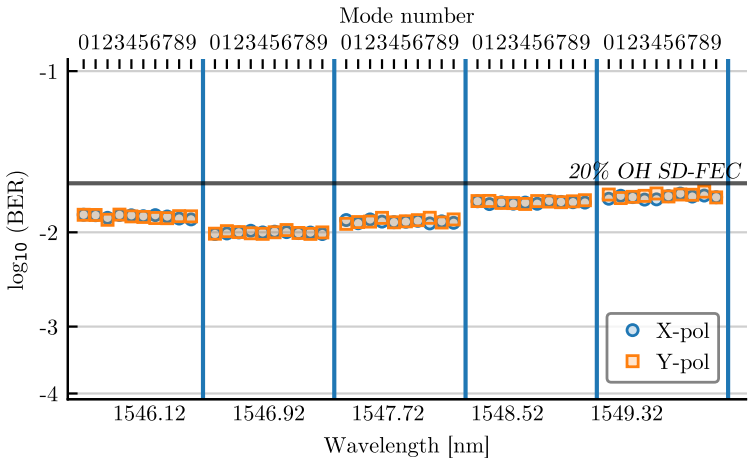

Figure 6.10: BER for all spatial channels for wavelength channels ranging from 1546.12 nm to 1549.32 nm.

6.1.5 Temporal stability of combined WDM/SDM transmission

The transmission rate of the previous experiment is increased by applying WDM over 5 channels on top of the 10-mode multiplexed signal. These wavelength channels are spaced at 100 GHz, centred around 1547.72 nm. The ECL used for both channel under test (CUT) and LO is tuned to one of the 5 channels, and combined with the other 4 loading channels. It can be seen in Fig. 6.10, that all channels perform below the assumed SD-FEC threshold, resulting in a data rate of 1.6 Tbit/s. Note that the variation in spatial channel performance is small because of the included round-robin coding. For each wavelength channel, the MDL is calculated as the ratio between the strongest and weakest singular value of the equaliser weights. The observed MDL of 8.7 dB, 9.3 dB, 9.0 dB, 9.4 dB and 9.5 dB shows a similar trend as the BER in Fig. 6.10.

Key for transmission systems is reliability, which is investigated by performing a 10 hours measurement with 5 wavelength and 20 spatial channels. The system BER and MDL versus time for the centre channel (1547.72 nm) is shown in Fig. 6.11. Over 10 hours a small variation of 1.1×10^{-2} in BER is observed, demonstrating the temporal stability of the transmission setup. An average of 8.5 dB MDL with a maximum variation of 1.7 dB is measured over this interval.

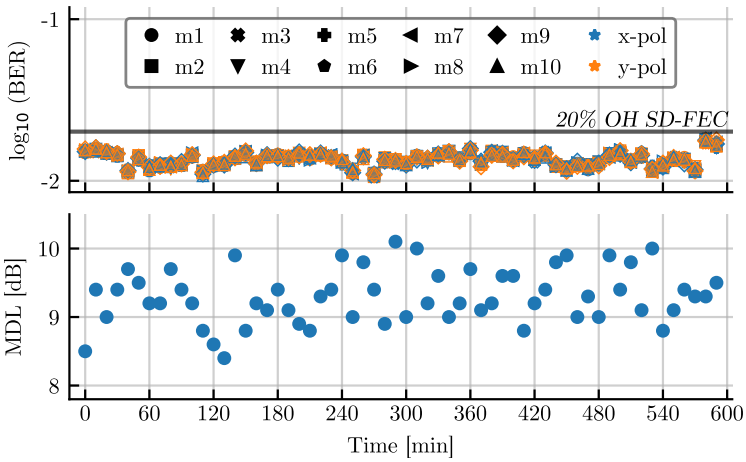

Figure 6.11: BER and MDL of the centre wavelenght channel measured over a duration of 10 hours.

6.2 10-Mode transmission over 50 µm core diameter multi-mode fibre

The first multiple-input multiple-output (MIMO) mode-division multiplexing (MDM) transmission experiments were conducted using standard multi-mode fibre (MMF) [22, 23, 231–233] However, the cross-talk between the large number of modes supported by the fibre limited capacity increases with respect to SMF. To overcome this issue, few-mode fibres were designed to guide exactly the small number of modes exploited during transmission. In the previous section, 10-mode transmission over a few-mode fibre was demonstrated. Scaling, the number of spatial channels of few-mode fibres, while maintaining low differential mode group delay (DMGD) is challenging because it is highly susceptible to a small variation in the production process [97]. Alternatively, the design of standard MMF can be optimised for MDM transmission around 1550 nm. In this section, a 10-mode transmission over this optimised fibre is discussed. In Section 6.2.1, the fibre is introduced, followed by the transmission setup in Section 6.2.2. Finally, transmission results will be presented in Section 6.2.3.

6.2.1 50 µm core diameter multi-mode fibre for SDM applications

The index profile of the graded-index multi-mode fibre used in this experiment shown in Fig. 6.12a. The 50 µm core diameter fibre supports the first 30 LP modes or 55 spatial modes. However, the last two groups suffer from high bending losses ($\gg$10 dB/turn for 10 nm bending radius). Leaving the remaining 8 mode-groups

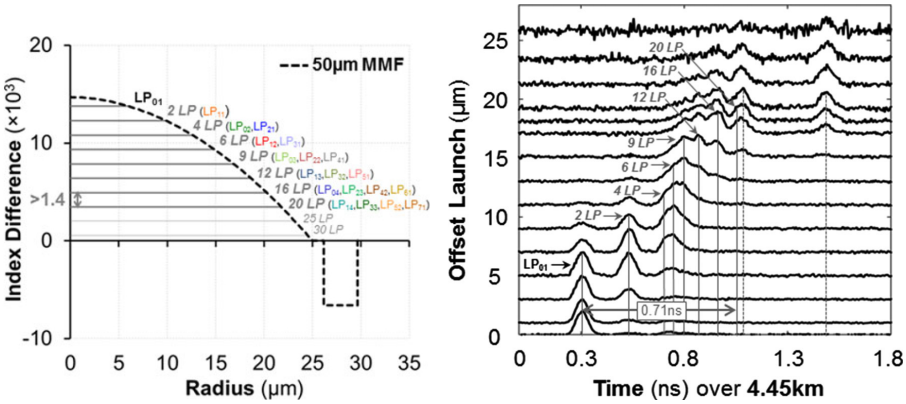

(a) (b)

Figure 6.12: (a) Theoretical and experimental index profile of the multi-mode fibre. (b) An estimated maximum |DMGD| of 0.71 ns based on offset launching measurements.

with 20 LP modes or 36 spatial modes available for MDM transmission. The relative large index difference of 1.4×10^{-3} between the mode-groups minimises coupling between the last mode-group used for transmission and the first group that is not excited at launch. This last property is key to an upgradeable transmission system from a single-mode equivalent to 36 spatial modes without replacing the fibre. By upgrading the spatial multiplexers and DSP accordingly, capacity can be increased when demand requires. The design is optimised for mode division multiplexing in the C-band following a procedure similar to few-mode fibre design. The maximum DMGD between any two modes is minimised by tuning the shape of the graded-index profile, described by the α-parameter. The optimum was found for $\alpha = 1.94$. Furthermore, the DMGD can be further reduced by optimising the trench volume.

The fibre with standard cladding (125 µm) and coating (245 µm) is fabricated using standardised multi-mode production process. From offset launching a 50 ps pulse, a DMGD of 0.71 ns after 4.45 km, or 160 ps/km, is observed between the first 20 LP modes (see Fig. 6.12b). For the 10-mode transmission experiment, a maximum |DMGD| around 100 ps/km is to be expected. Compared to the few-mode fibre, the observed dispersion values are closer to the minimal theoretical values, because of the higher accuracy of multi-mode fibre production process [97].

The attenuation of the fundamental mode is found to be 0.215 dB/km, with a modal variation below 0.020 dB/km for the guided 20 LP modes. The effective areas range from 175 µm^2 to 705 µm^2, increasing tolerance to non-linear propagation effects. The chromatic dispersion coefficients range from 19 ps/(nm · km) to 21 ps/(nm · km) [97].

6.2.2 Experimental setup

For evaluation of the MMF, the transmission setup illustrated in Fig. 6.13 is employed. The single wavelength transmitter is a $\leq$ 100 kHz line width ECL tuned to 1550.12 nm. The output of two synchronised DACs operating at 20 GSa/s is amplified by ultra-linear electrical amplifiers to provide the drive signals to an IQ-modulator. The modulated sequence is a combination of multiple 2^{16} pseudorandom bit sequence (PRBS) mapped to a QPSK constellation. The output of the modulator is guided through a polarisation multiplexer with a delay line of 485 ns for polarisation multiplexed emulation. A variable optical attenuator (VOA) controls the signal power into a conventional 3 dB fibre coupler, where it is combined with a noise signal. The latter is amplified spontaneous emission (ASE) generated by an EDFA with an open input. With control of both signal and noise power, the optical signal-to-noise ratio (OSNR) into the mode decorrelation section can be tuned. The second output of the fibre coupler is fed to an optical spectrum analyser (OSA) to measure the OSNR.

After mode decorrelation, the 10 signal copies needed for 10-mode transmission, are inserted into the 10 SMF inputs of the PL. The details of the PL spatial multiplexer are covered in Section 6.1.2. Note that the spatial multiplexers were designed to match the smaller 6LP few-mode fibre, which has a 14 µm core radius. The multiplexer is butt-coupled to the MMF transmission fibre, using three-axis alignment stages. The transmission span contains 3 spools of 4.45 km and 3 spools of 8.85 km, resulting in a 40 km link after fusion splicing each section. Both ends

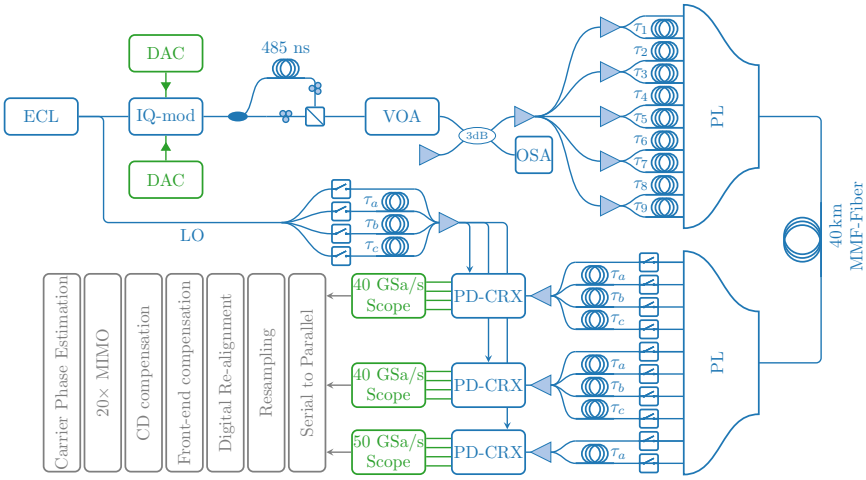

Figure 6.13: SDM over MMF transmission setup including noise loading stage consisting of a variable optical attenuator (VOA), an EDFA to generate amplified spontaneous emission (ASE) and an optical spectrum analyser (OSA).

of the MMF link contain a short tapered section that acts as a mode stripper for higher-order modes not used for transmission.

The 10 outputs of the spatial multiplexer are guided through the TDM-SDM setup described in Section 6.1.3, to reduce the required number of coherent receivers and ADCs from 10 to 3. Digital signal processing based on the same algorithms as described in Section 6.1.3 is performed offline. Since the transmission distance is increased to 40 km, digital CD compensation is included to reduce the residual CD needed to compensate by the MIMO equaliser. Furthermore, 175 double symbol rate taps are required to fit the broadened impulse response as a result of DMGD. The MIMO TDE based on the LMS updating rule, unravels the spatial channel mixing. Subsequently, CPE is applied to recover any small frequency offset between transmitter and LO. Finally, the BER is averaged over 4 million system bits.

6.2.3 Transmission results

System performance is evaluated based on BER calculation for an OSNR ranging from 10 dB/0.1nm to 30 dB/0.1nm. From Fig. 6.14, it can be seen that without any additional ASE, the system averaged BER is approaching the BER threshold for 7 % overhead hard-decision forward error-correction (HD-FEC) code. For degrading OSNR, a larger overhead SD-FEC is required to ensure reliable communication. Based on the assumed threshold of 2.4×10^{-2}, a minimum OSNR of 16 dB/0.1nm is required for reliable transmission. On the right axis in Fig. 6.14, the system MDL for the transmitted OSNRs values is shown. The MDL is calculated by taking the ratio between largest and smallest singular value of the TDE weight matrix. No accurate MDL calculation could be obtained for transmission at the three lowest

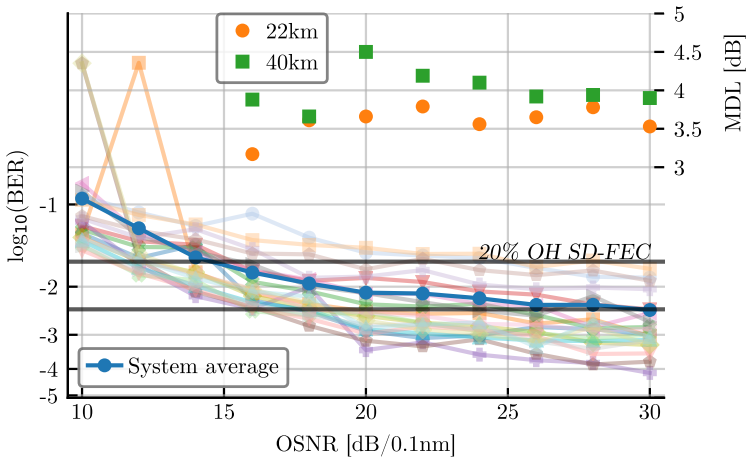

Figure 6.14: BER and MDL for the noise loaded signals at OSNR from 10 dB/0.1nm to 30 dB/0.1nm.

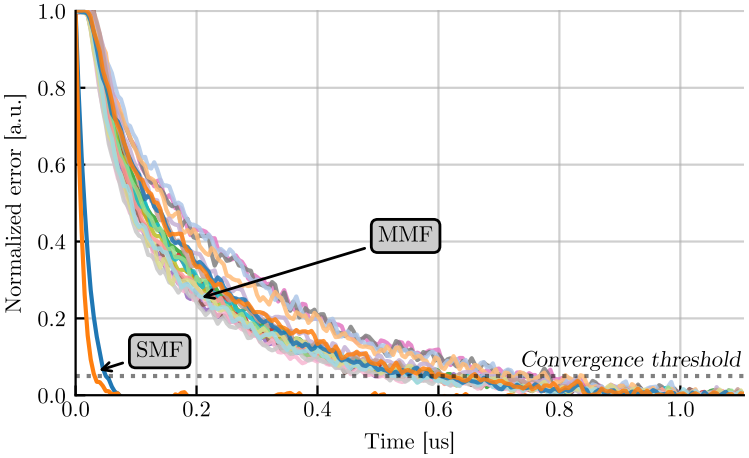

Figure 6.15: Normalized convergence of the equaliser comparison of transmission over MMF and SMF.

OSNR values. This can be attributed to instability of the DSP algorithms for noisy signals, which is also reflected by the high BER of some spatial channels.

In Section 6.1, the convergence of the TDE for FMF transmission is shown to scale linear with the number of spatial channels. The employed MMF supports more than the 10 modes used for MDM transmission, which might impact convergence speed. In Fig. 6.15, the convergence of each spatial channel in the MMF and SMF is shown. The errors are normalised, such that the initial error is 1 and the final error is 0. A convergence threshold of 5 % is assumed. Observe, that all but four spatial channels converge at similar rates. Since non-mode selective spatial multiplexers are employed in the experiment, these channels cannot be linked to spatial modes. However, it is presumed that cross-talk from the fifth mode-group to the last mode-group used for transmission contributes to the reduced convergence rate.

Finally, the equaliser weights are observed to estimate the DMGD. Due to size limitations, the polarisation averaged weight matrix is shown in Fig. 6.16. The elements are numbered according to the port labelling of the spatial multiplexer of Fig. 6.2. A maximum pulse broadening of 6.0 ns is observed after 40 km. This translates to 150 ps/km, which is higher than expected from offset launched measurements of Section 6.2.1. This can be partially attributed to the variance in CD coefficients between the spatial modes, since only bulk compensation is applied.

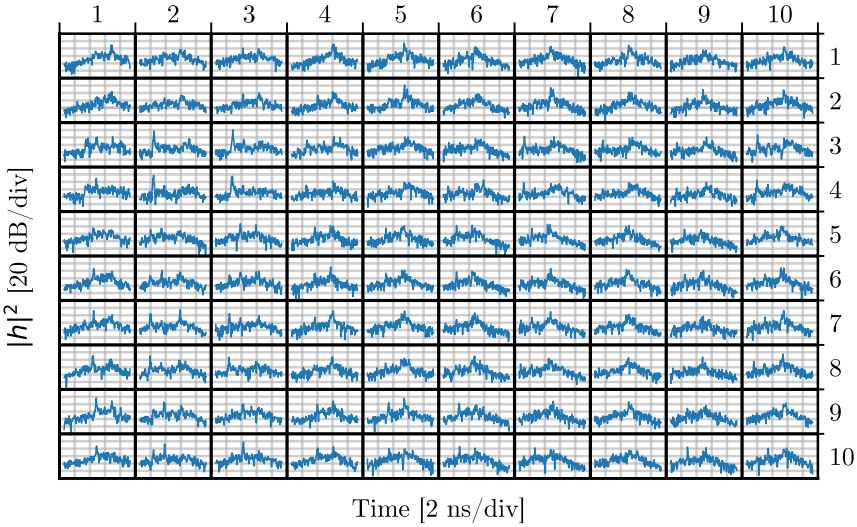

Figure 6.16: Polarisation averaged TDE weights after 40 km transmission showing a maximum pulse duration of 6.0 ns.

6.3 DMGD reduction by selective excitation of strongly coupled modes

The transmission of the previous section showed a potential 10-fold capacity increase by exploiting the first 4 mode-groups of a 50 µm core diameter MMF, optimised for MDM transmission. A total of 55 LP modes are supported by the fibre, divided over 10 mode-groups, with N modes in the Nth mode-group. The modes within a single-mode group experience significantly stronger coupling compared to the coupling with modes across groups. Furthermore, it is shown that stronger coupling between spatial channels can be beneficial, because it reduces the group delay spread from modal dispersion and variations in losses related to MDL [174]. In this section, the strong coupling of modes within a mode group is exploited to reduce the computational complexity of the DSP. A comparison between two 3-mode transmission systems is discussed. The first system employs the first two mode-groups, consisting of the fundamental and LP_{11} modes, for transmission. The second system uses the 3 LP modes (LP_{21} and LP_{02}) of the third mode group for transmission. To access the individual mode groups, a mode-selective spatial multiplexer is required. In Section 6.3.1, the design, fabrication and characterisation of a 6-port mode-selective photonic lantern are discussed. The experimental setup required to evaluate the two transmission systems is given in Section 6.3.2. Finally, the transmission results of both systems are compared in Section 6.3.3.

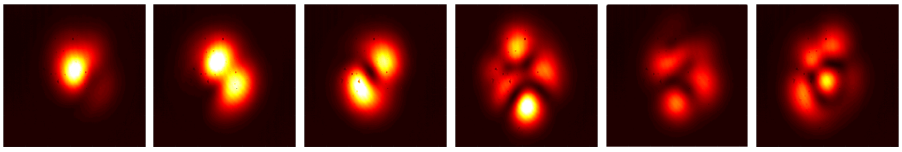

(a) (b) (c) (d) (e) (f)

Figure 6.17: Mode profiles of the mode-selective 6-port photonic lantern. (a) LP_{01} (b) LP_{11a} (c) LP_{11b} (d) LP_{21a} (e) LP_{21b} (f) LP_{02}.

6.3.1 Mode-selective photonic lantern

Along the tapered section of a PL, the light inserted into the single-mode inputs slowly evolves to a linear combination of modes. Typically, similar SMFs are employed for the fabrication of these spatial multiplexers, resulting in the same modal degeneracy for all single-mode ports [234]. Consequently, there is no distinct mapping between the single-mode ports and LP modes, as has been shown in Section 6.1.2 for the PL employed in the previous experiments. For mode-selective spatial multiplexers, the mode degeneracy must be broken. This can be achieved by employing dissimilar fibres in the fabrication of PLs. The different propagation constants of the single-mode fibres lead to different modal evolutions along the tapered section [130, 131].

The 6-port PL employed for this experiment was fabricated using step-index single-mode fibres with a core sizes 20 µm, 18 µm, 15 µm and 6 µm for LP_{01}, LP_{11}, LP_{21} and LP_{02}, respectively. The multi-mode facet of the tapered structure has an approximate core diameter of 29 µm. Note that this is smaller than the 50 µm core diameter of the MMF transmission fibre. Therefore, a short length of graded-index 6-LP few-mode fibre is fusion spliced to the lantern for a more gradual transition between core sizes. For the remainder of the section, all reference to the PL includes this transition fibre, unless noted otherwise.

First, the near-field intensity profiles of the PL are observed by consequently exciting the single-mode ports. Figure 6.17, shows the multi-mode facet observed with an infra-red (IR) camera. The mode-selective property of the multiplexer can be easily seen as the mode profiles depicted in Fig. 2.1 are clearly recognisable in Fig. 6.17. Especially when compared to the non-mode selective lanterns in Fig. 6.3. The component was also characterised using the optical vector network analyser (OVNA) of Chapter 5. A maximum IL of 2.5 dB, and MDL of 2.7 dB is observed for wavelength range 1530 nm to 1570 nm (Section 5.5).

6.3.2 Experimental setup

In this experiment, a six mode transmission setup is exploited for the comparison of two 3-mode transmission systems. The first setup transmits over 2 mode groups containing LP_{01}, LP_{11a}, and LP_{11b} modes. The second configuration excites 3

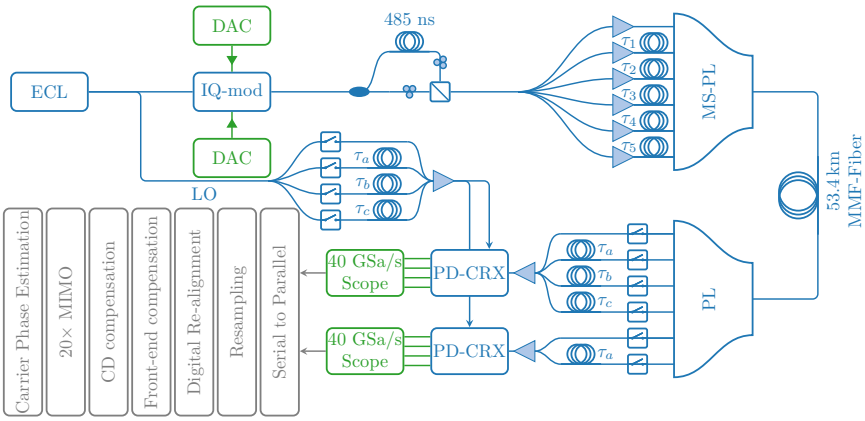

Figure 6.18: SDM over MMF transmission setup supporting 6 modes and 3 mode systems (LP_{01}+LP_{11} and LP_{21}+LP_{02}). A mode-selective photonic lantern (MS-PL) is employed at the transmitter.

modes in a single mode-group: LP_{21a}, LP_{21b}, and LP_{02}. In the transmission setup (Fig. 6.18), this is realized by connecting the 3 corresponding inputs of the photonic lantern at the transmitter.

The transmitter configuration described in more detail in the previous sections, is employed to generate a 10 GBaud QPSK signal, which is subsequently polarisation multiplexed with a 485 ns delay. One EDFA is employed for each single-mode input of the spatial multiplexer, allowing independent launch power control for all 6 modes. Consequently, the delays have been updated to 49 ns, 134 ns, 237 ns, 322 ns and 422 ns. The PL is butt-coupled to the transmission link of 53.4 km long 50 µm core diameter MMF. Details on the design are covered in Section 6.2.1, or can be found in [97].

The received spatial channels are demultiplexed by a 6-port PL, with low mode selectivity. Consequently, all 6 single-outputs must be received simultaneously for analysis. By employing a 6 to 2 TDM-SDM setup, all 6 channels are captured with only 2 PD-CRXs and corresponding ADCs. In the digital domain, the signal blocks are aligned in time, followed by front-end and chromatic dispersions compensation, before unravelling the modal cross-talk. Since the number of receivers is larger than the number of transmitters, an asymmetric 6×12 MIMO TDE is employed. After CPE, the symbols are demapped and the BER is calculated over 1.2 million bits.

6.3.3 Transmission results

First, the equaliser filter weights for both 3-mode systems are analysed. Figure 6.19 show one of the elements of each transmission systems. In Fig. 6.19a, two spikes

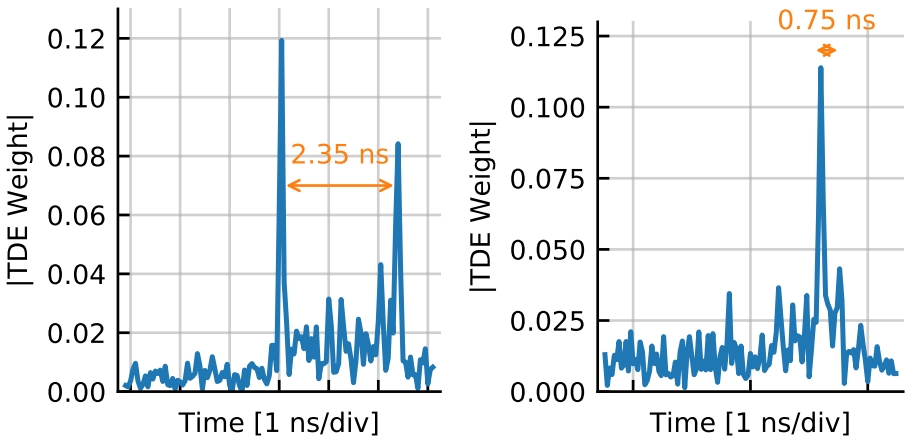

(a) (b)

Figure 6.19: (a) Impulse response of LP_{01}+LP_{11ab} transmission system after 53.4 km of MMF. (b) Impulse response of LP_{02}+LP_{21ab} transmission system after 53.4 km of MMF.

corresponding to the two mode-groups (LP_{01} and LP_{11}) are observed. The estimated DMGD of 2.35 ns (44 ps/km) is in agreement with the DMGD measurements of Fig. 6.12b. In the impulse response of the stronger coupled 3-mode system, depicted in Fig. 6.19b, a single but slightly broader peak can be seen. The width is approximately 3 times smaller, compared to the DMGD between the LP_{01} and LP_{11} modes.

The main interest of low DMGD fibres is the reduced amount of memory required for the MIMO processing. Therefore, the minimum equaliser window length needed to achieve a pre-forward error-correction (FEC) BER of 3.8×10^{-3} is found for both transmission systems. From Fig. 6.20a, it can be seen that for the evaluated wavelength channels, the strong coupling of the LP_{21} and LP_{02} translates to a maximum of 27 % reduction of equaliser taps. Furthermore, since the number of complex multiplications and additions for TDE scale linearly with the number of taps, an overall reduction in MIMO complexity is to be expected.

The system MDL for each wavelength channel of both systems is estimated from the singular values of the transfer function matrix. From Fig. 6.20b, the MDL of the LP_{01}+LP_{11} system is found to be between 1.4 dB to 3 dB, and 1.8 dB to 3.4 dB for the LP_{02}+LP_{21} system. These values are in agreement with the 2.7 dB observed with the OVNA. However, no benefit of the stronger mode coupling is to be observed in this aspect. This can be attributed to the limited contribution of the MMF towards the overall system MDL with respect to the spatial multiplexers.

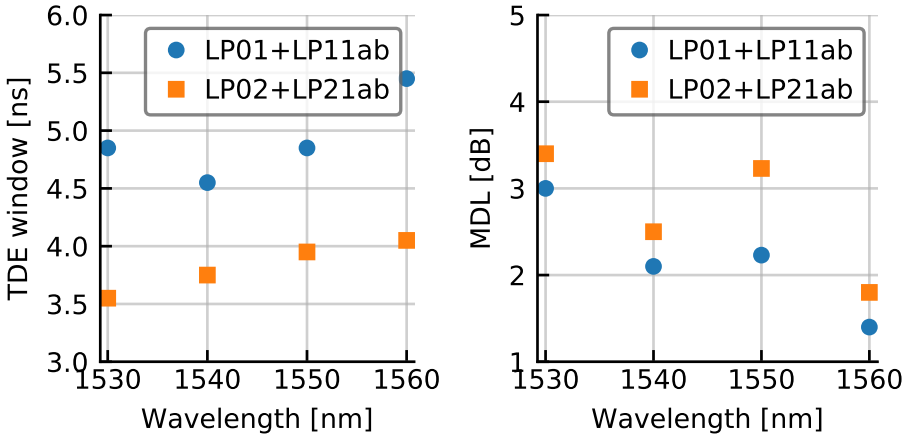

(a) (b)

Figure 6.20: Comparison of the equaliser window length (a) and mode dependent loss (b) of the two evaluated 3-mode transmission systems for various channels throughout the C-band.

6.4 Conclusions

In this chapter, the feasibility of increasing single fibre capacity with one order of magnitude by applying mode division multiplexing is demonstrated. First by transmitting 10-modes over 4.45 km span of 6-LP few-mode fibre. A maximum delay spread of 357 ps/km was obtained from DMGD measurements, resulting in a total system impulse response width of less than 2 ns after 4.45 km. The low DMGD property of the fibre offers potential scaling towards longer transmission distances with minimum impulse response broadening. Single wavelength channel transmission showed a large variation in BER between the spatial channels. By allocating time slots of data over all available channels using the proposed round-robin encoder, BER performance is equalised between the 20 spatial channels. Finally, the stability of the combined mode and wavelength multiplexed transmission system is verified over a 10-hour measurement. Scaling few-mode fibres beyond 6 and 9 LP modes, while maintaining the desirable low DMGD property, is challenging because of inaccuracies in the production process. Due to the widely deployed 50 µm core diameter MMF, their manufacturing is well developed. However, to cope with the mode mixing of the numerous modes supported by this fibre, the design must be optimised for mode-division-multiplexing in the C-band. This fibre, enabled reach extension to 40 km, within pre-FEC BER requirements for hard-decision error-correcting code. Amplified spontaneous emission was added to the signal to impair the OSNR from 30 dB/0.1nm to 16 dB/0.1nm, resulted in system BER below the assumed soft-decision FEC threshold of 2.4×10^{-2}. This suggests

that the transmission distance can be further increased. The relative large index difference between mode-groups limits the inter-mode-group talk. Hence, only a subset of the spatial channels can be used for mode-multiplexed transmission. This enables capacity scaling of the transmission link by replacing the terminals, without the costly deployment of new fibre. By exploiting this property in combination with the strong intra-mode-group coupling of modes, the impulse response broadening as a result of DMGD can be reduced. Two 3-mode transmission systems are compared, one based on conventional 3-mode transmission using LP_{01}, LP_{11a}, and LP_{11b} modes. The other system transmitting over LP_{21a}, LP_{21b}, and LP_{02}, which belong to the same mode group. A maximum of 27 % reduction of the MIMO equaliser window length is demonstrated. Due to the linear relation between the number of taps and complex additions and multiplication of TDE, a similar scaling in computation complexity can be expected. Unfortunately, this advantage scales badly with the number of modes as has been demonstrated in [235]. In the next chapter, mode division multiplexing will be applied to long-distance transmission.

Chapter 7

Long-distance space division multiplexed transmission

The experiments in the previous chapter applied mode-division multiplexing with a spatial multiplicity of 10, potentially increasing single-fibre capacity by one order of magnitude over short distance links. Due to the attenuation of the optical fibre medium, signal amplification or regeneration is required for long-distance transmission. For a space-division multiplexed transmission system, gain balancing between the spatial channels, thus minimising the differential modal gain (DMG) is key. DMG has the same effect on transmission capacity as mode dependent loss (MDL). In particular, low DMG multi-mode amplifiers are challenging to realise due to different overlaps of the modal fields with dopants distribution and pump profile. Transmission systems including few-mode amplifiers are therefore mainly limited by the performance of the amplifier itself. In this chapter, the focus is on evaluating the capabilities of space-division multiplexing (SDM) fibre technology. Hence, it includes long-distance transmission experiments employing single-mode amplifiers for each spatial channel.

One of the advantages of few-mode and multi-mode fibres is the increased tolerance to non-linear transmission impairments as a result of their potentially larger effective area. In Section 7.1, a large-effective area few-mode fibre is evaluated in a combined wavelength- and mode-division multiplexed transmission setup. It is demonstrated to outperform standard single-mode fibre (SSMF) up to distances 2400 km, at a spectral efficiency of 17.3 bit/s/Hz. The spectral efficiency is doubled for the experiment in Section 7.2, by multiplexing over 6 modes in a few-mode fibre. In combination with 120 wavelength-division multiplexing (WDM) channels, transmission at 138 Tbit/s over 590 km few-mode fibre (FMF) is reported.[1]

[1] The experiments described in this chapter were conducted at Nokia Bell Labs, Crawford Hill in New Jersey and culminated in the following publications: [J16, J14, J5]

7.1 Transmission over large-effective-area 3-mode fibre

In this experiment, the improved tolerance to non-linear transmission impairments for few-mode (and multi-mode fibres) is investigated by comparing a 3-mode transmission system to a conventional SSMF system. The 3-mode fibre has been specially designed with an even larger effective area compared to other 3-mode fibre designs. If this higher tolerance to fibre nonlinearities translates to a higher capacity is investigated by means of a transmission experiment. This section is structured as follows: First the transmission fibre is discussed in Section 7.1.1, followed by an introduction of the 3D-waveguide (3DWG) and photonic lantern (PL) spatial multiplexers in Section 7.1.2. In Section 7.1.3 the synchronised re-circulating few-mode transmission setup is explained. The results obtained with this setup are presented and discussed in Section 7.1.4.

7.1.1 Large-effective-area depressed-cladding 3-mode fibre

The transmission fibre employed in this experiment has a step-index depressed cladding profile. The index profile, designed with a normalised frequency $V \approx 5$, ensures stable propagation of the LP_{01}, LP_{11a}, and LP_{11b} modes, while any higher-order modes are cut-off. Furthermore, the design is optimised to minimise differential mode group delay (DMGD) across the C-band, thereby minimizing the number of equaliser taps required at the receiver. This DMGD is measured by observing a short pulse launched into the fibre while intentionally misaligning a phase plate spatial multiplexer [27]. The obtained DMGD measured over the wavelength range of 1530 nm to 1564 nm is found to be 27 ps/km. By means of optical time-domain reflectometry (OTDR) the fibre attenuation is estimated to be 0.205 dB/km for both mode groups. An unique feature of this few-mode fibre is the large effective area of 155 µm^2 for LP_{01} and 159 µm^2 for both LP_{11} modes. Typical values for 3-mode fibres range from approximately 65 µm^2 to 95 µm^2 [223, 236]. A larger effective area reduces the local optical power intensities for a given total signal power. As discussed in more detail in Section 2.3.4, Kerr nonlinearities are refractive index changes related to the signal intensity. Hence, increased tolerance to such effects is to be expected for a larger effective area. For comparison, the effective area of SSMF is 65 µm^2, which is less than half of the proposed few-mode fibre [27].

7.1.2 Spatial multiplexers

Interfacing with the few-mode fibre is done by the laser inscribed 3DWG depicted in Fig. 7.1 as multiplexer and a fibre-based PL as demultiplexer. Both components are reciprocal and could in principle be interchanged. However, high mode-selectivity at the transmitter side is beneficial, as this improves modal launch power control. For the 3DWG, the modal extinction ratio is specified as >20 dB [136]. This high mode selectivity follows from propagation constant matching of the

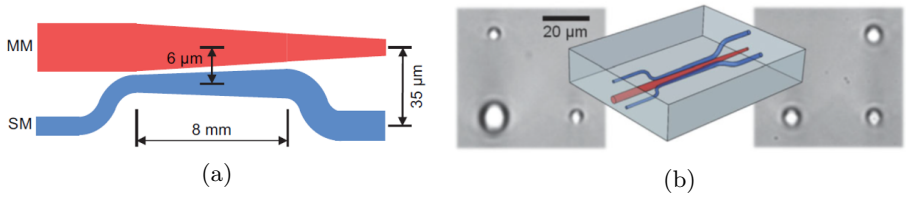

Figure 7.1: (a) Design of the tapered sections with in the 3D-waveguide. (b) 3D model and end-facets of the 3D-waveguide [136].

tapered single-mode waveguides to either the LP_{11a} or LP_{11b} mode, resulting in a zero overlap with the orthogonal variant. To couple into the other LP_{11} mode, the other single-mode waveguide is positioned perpendicular to the first, as is illustrated in Fig. 7.1b.

The photonic lantern, on the other hand, excels in having low insertion- as well as low mode dependent losses. This type of multiplexers has been discussed in Section 3.3 and in more detail for the models employed in the experiments of Chapter 6. Characterisation of both multiplexers was performed by exciting the single-mode inputs with amplified spontaneous emission (ASE) and observing the output power at the multi-mode facet. An average insertion loss (IL) of 1.1 dB with a 0.2 dB variation was observed for the three-port PL. The insertion losses of the 3DWG were slightly higher with an average of 1.7 dB and a 0.26 dB variation between the ports. An MDL of 1.75 dB was observed for both multiplexers fusion spliced to 96 km FMF.

7.1.3 Experimental setup

The experimental setup including the few-mode fibre and mode multiplexers is depicted in Fig. 7.2. The transmitter section of the setup consists of 5 distributed feedback (DFB) lasers, centred around 193.4 THz with a 100 GHz spacing aligned with the ITU grid. The multiplexed continuous wave (CW) signals are modulated with a 33.3 GHz tone to reduce the channel spacing and increase the number of WDM channels to 15. These channels are separated into odd and even channels by a wavelength selective switch (WSS) for modulation with independent data sequences. Each of these De Bruijn sequences contains 2^{16} symbols mapped to a 16-ary quadrature amplitude modulation (QAM) constellation. The digital signal is converted to an analogue driving voltage for the IQ-modulators by a four-channel digital-to-analog converter (DAC) running at 60 GSa/s. After recombination of the odd and even wavelength channels, polarisation multiplexing is realised by delaying one of the polarisation states with 50 ns. Subsequently, a gain flattening filter (GFF) is employed to balance the power between all wavelength channels. In parallel, an external cavity laser (ECL) is tuned to the wavelength of the channel under test (CUT). The lower linewidth of the ECL type laser produces less phase noise

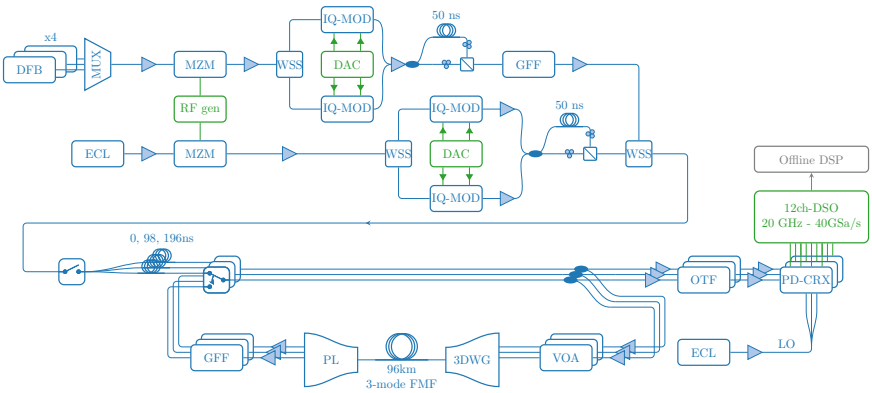

Figure 7.2: Long-haul transmission setup including 3-mode re-circulating loop with 96 km of 3-mode FMF, photonic lantern (PL) and 3DWG spatial multiplexers, variable optical attenuator (VOA) and gain flattening filter (GFF). Channel under test is generated by external cavity laser (ECL), loading channels by distributed feedback (DFB) lasers. Signal modulation by IQ-modulator (IQ-MOD) and digital-to-analog converter (DAC). Wavelength selective switch (WSS) and optical tunable filter (OTF) for adding or filtering channels. EDFAs are denoted by triangles.

compared to the DFB lasers and should thus perform better. This CW source is modulated with independent data sequences by a similar transmitter configuration as used for the loading channels. The outputs of both transmitters are combined in a WSS, which places the CUT on the grid and drops the overlapping loading channel.

The output of the WSS is fed to either a 3-fold re-circulating loop as included in Fig. 7.2, or a single-mode loop as depicted in Fig. 7.3. This subsystem allows for long-distance transmission using a limited number of components by propagating the signal multiple times through the same fibre span [237]. The loop has a cyclic behaviour, starting with a loading phase and followed by a re-circulating or transmission phase. In the first phase, the loop switch is positioned such that the signal generated by the transmitter fills up the loop. When at least a single round-trip time has expired the switch is flipped, blocking any new signals from the transmitter, and allowing the signal trapped inside the loop to start circulating. After each circulation, a fraction κ of the signal is tapped off and guided to a receiver for detection. By accurate triggering, the desired distance can be captured for further processing. Compared to the configuration described in [237], the 1×1 switch is replaced by a 2×1 variant, which allows the use of an asymmetric coupler. In this setup, only 10% signal power is tapped every circulation, thus reducing the losses of the circulating signal by 2 dB. A variable optical attenuator (VOA) inside the loop controls the launch power into the 78 km SSMF span. Amplification is realised by dual-stage erbium doped fibre amplifier s (EDFAs) which are configured

Figure 7.3: Single mode fibre recirculating loop, with gain flattening filter (GFF), loop-synchronised polarisation scrambler (LSPS), and variable optical attenuator (VOA).

to balance out the losses such that the loop has unity gain. Due to the non-flat gain spectrum of these amplifiers, a GFF is used to flatten the spectrum after each circulation. Furthermore, a loop-synchronised polarisation scrambler (LSPS), is included to change the polarisation state with each circulation, thereby minimising the penalties introduced by effects like polarisation dependent loss (PDL). The single-mode configuration of Fig. 7.3 is duplicated for each of the spatial modes of the 3-mode fibre, as can be seen in Fig. 7.2. These loops need to be synchronised and matched both in time and losses. The group delay of the three paths is measured using an optical vector network analyser (OVNA). Subsequently, the group delay differences between them are divided by the effective group index of the fibre, which was estimated to be around the typical value for fibres at 1.45. The obtained lengths were carefully cut-out, and the ends are fusion spliced back together. To further reduce losses in the system, all connectors between patch cords are removed and replaced by fusion splices. Any deviation in losses between the recirculating loops is balanced by tuning the VOAs accordingly. The internal power monitors of the EDFAs are used to measure the losses between sections of the setup.

The 3 outputs of the loop setups are amplified and fed to optical filters that select the CUT. The filtered signals are detected by conventional dual-polarisation coherent receivers where it beats with a local oscillator (LO) signal generated from an ECL with a specified $\leq 10\,\text{kHz}$ linewidth. The electrical signals are converted to the digital domain by a 12-channel, 20 GHz bandwidth digital sampling oscilloscope (DSO) sampling at 40 GSa/s. All signal processing is performed offline. First, the signals are aligned in time and resampled to 2-fold oversampling. Next, IQ-imbalance, chromatic dispersion (CD) and frequency offset between signal and LO are compensated. Subsequently, a multiple-input multiple-output (MIMO) frequency domain equaliser (FDE) is applied to unravel the spatial channels. For the 3-mode fibre, a 6×6 equaliser is employed, whereas a 2×2 is sufficient to recover the two polarisations of the single-mode fibre. Equalisation is based on the least means square (LMS) algorithm during convergence and multi-modulus algorithm (MMA) during transmission. Finally, carrier phase estimation (CPE) is performed before evaluating transmission performance.

The performance metric used in this chapter is the Q-factor in [dB], which is

a commonly used metric in the telecommunications industry to express the signal quality. Its definition follows from two Gaussian probability density functions belong that to two constellation points, surrounding a decision threshold [62]:

$$Q = \frac{\mu_1 - \mu_0}{\sigma_1 - \sigma_0}, \tag{7.1}$$

where μ and σ^2 are the mean and variance of these probability density functions. The subscripts refer to the intensity level related to the constellation points. The following direct mapping between Q-factor and bit error rate (BER) is applied to obtain the results presented in the following sections:

$$\mathrm{BER} = \frac{1}{2}\mathrm{erfc}\left(\frac{Q}{\sqrt{2}}\right), \tag{7.2}$$

where erfc is the complementary error function, defined as [46]:

$$\mathrm{erfc}(x) = \frac{2}{\sqrt{\pi}} \int_x^\infty \exp\left(-y^2\right) dy \tag{7.3}$$

7.1.4 Transmission results

To achieve the best system performance, the optimum launch power into the few-mode fibre has to be found. At first, any offset in power between the spatial channels is investigated by tuning the launch power of the individual spatial channels. As no significant difference in Q-factor could be observed, the same launch power was used for all spatial modes for the remainder of this section. Subsequently, the transmission power is swept from −5 dBm to 5 dBm for distances of 288 km, 768 km, 1440 km, 1920 km and 2400 km. The measured Q-factors for both FMF and SSMF transmission are shown in Fig. 7.4. From Fig. 7.4a, it can be seen that the best performance for the FMF system is achieved at a launch power of 2 dB, which is roughly 3 dB higher compared to the 78 km long SSMF system from Fig. 7.3, shown in Fig. 7.4b. The increased optimum power is mainly attributed to the more than doubled effective area of the few-mode fibre. For the remainder of this section, both systems are operated at their optimum launch powers. Compared to another 3-mode fibre long-haul transmission system that included a 70 km long 3-mode fibre span, with an effective area of 65 µm^2, the optimum is 5.5 dB higher [236].

From the observations based on the power sweep, the question arises if this higher transmission power leads to an improvement in capacity. Figure 7.5 shows the system average Q-factors versus transmission distance for both fibres under test. Q-factors above 6 dB were observed for transmission distances up to 2400 km, enabling transmission at a net spectral efficiency of 17.3 bit/s/Hz, when 20 % overhead for soft-decision forward error-correction (SD-FEC) is taken into account. Note that this FMF outperforms SSMF up to a reach of 4500 km, which is related to the 3 dB higher launch power. It is important to note that the effective area of FMF can potentially be larger than single-mode large effective area fibre (LEAF). When

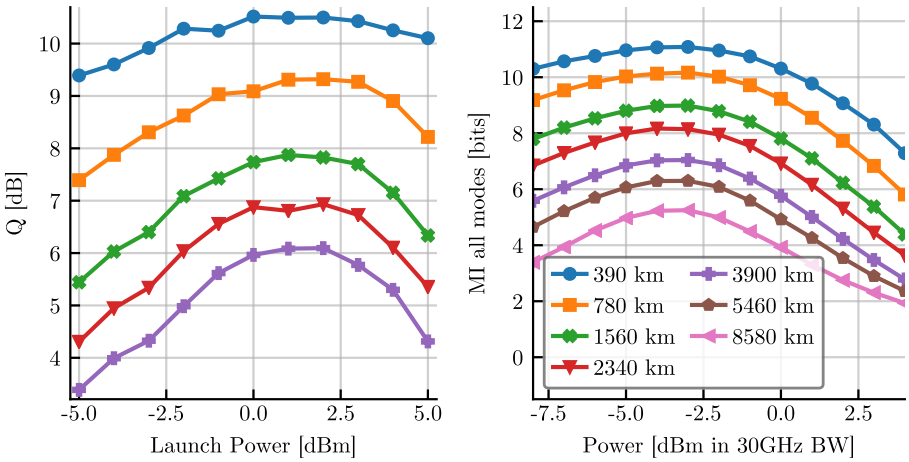

(a) (b)

Figure 7.4: (a) System averaged Q-factor for various launch powers and transmission distances over few-mode fibre. (b) System averaged Q-factor for various launch powers and transmission distances over standard single-mode fibre.

the Q-factor drops below the threshold for standardised SD-FEC after 2400 km of fibre, transmission can still be realised by increasing the coding overhead. Therefore, achievable rate (AR) for the FMF is calculated from mutual information (MI) using a binning method [238] and is given on the right axis in Fig. 7.5.

The mutual information $I(X;Y)$ is a quantity to express the amount of information between two random variables X and Y. For a memoryless channel with discrete complex input X and continuous out Y, the MI is given as:

$$I(X;Y) = \sum_{x \in \mathscr{X}} P_X(x) \int_{\mathbb{C}} p_{Y|X}(y|x) \log_2 \frac{p_{Y|X}(y|x)}{p_Y(y)} dy, \tag{7.4}$$

where P_X is the probability mass function expressing the distribution of symbols within the constellation $\mathscr{X}$. The term $p_{y|x}(y|x)$ denotes the channel transition probability expressed as a conditional probability. Since this quantity is unknown for the optical fibre channel, an additive white Gaussian noise (AWGN) channel is used as an auxiliary channel instead. Consequently, the MI becomes an upper bound of the optical channel capacity. The Gaussian transition probability of this auxiliary channel is expressed as:

$$q_{Y|X}(y|x) = \frac{1}{\sqrt{2\pi\sigma^2}} \exp\left(-\frac{(y-x)^2}{2\sigma^2}\right), \tag{7.5}$$

where the noise variance σ^2 is estimated from the received and transmitted symbols. Next, the conditional probability symbol x was transmitted for an observed symbol

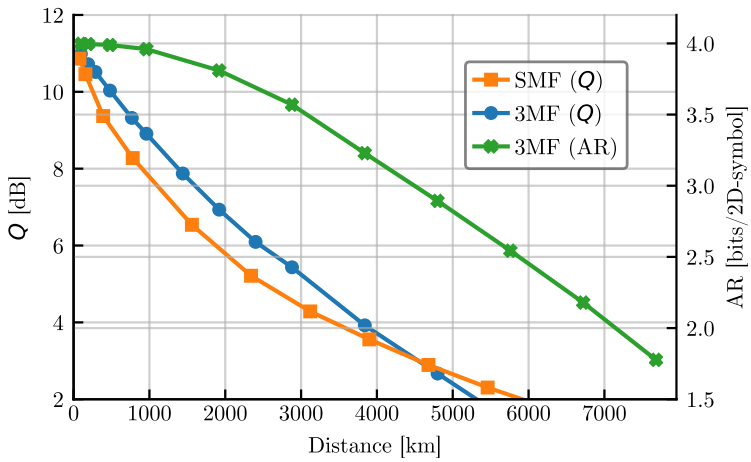

Figure 7.5: Q-factor versus distance for transmission over few-mode and single-mode fibre Achievable rate (AR) based on mutual information (MI) for FMF.

y_n can be obtained by combining Bayes theorem and the previous equation:

$$q_{X|Y}(x|y_n) = \frac{\exp\left(-\frac{(y_n-x)^2}{2\sigma^2}\right) P_X(x)}{\sum_{x'\in\mathscr{X}} \exp\left(-\frac{(y_n-x')^2}{2\sigma^2}\right) P_X(x')} \tag{7.6}$$

Calculating $q_{X|Y}(x|y_n)$ for all combinations of possible transmitted symbols x and received symbols y_n results in the following lower bound on MI:

$$R_{\mathrm{SD}} \approx -\sum_{x\in\mathscr{X}} P_X(x)\log_2 P_X(x) + \frac{1}{N}\sum_{n=1}^{N}\sum_{x\in\mathscr{X}} q_{X|Y}(x|y_n)\log_2 q_{X|Y}(x|y_n) \tag{7.7}$$

Note that the transmitted 16-QAM sequence is approximately uniformly distributed, hence, $P_X(x) \approx \frac{1}{M}$. Applying this assumption to Eq. (7.7) and inserting the expression for transition probability of the auxiliary channel of Eq. (7.6) yields the achievable rate of a soft decision encoder [238]:

$$R_{\mathrm{SD}} \approx m + \frac{1}{N}\sum_{n=1}^{N}\sum_{x\in\mathscr{X}} \frac{\exp\left(-\frac{(y_n-x)^2}{2\sigma^2}\right)}{\sum_{x'\in\mathscr{X}} \exp\left(-\frac{(y_n-x')^2}{2\sigma^2}\right)} \cdot \log_2 \frac{\exp\left(-\frac{(y_n-x)^2}{2\sigma^2}\right)}{\sum_{x'\in\mathscr{X}} \exp\left(-\frac{(y_n-x')^2}{2\sigma^2}\right)} \tag{7.8}$$

This expression has been used to calculate the AR shown in Fig. 7.5.

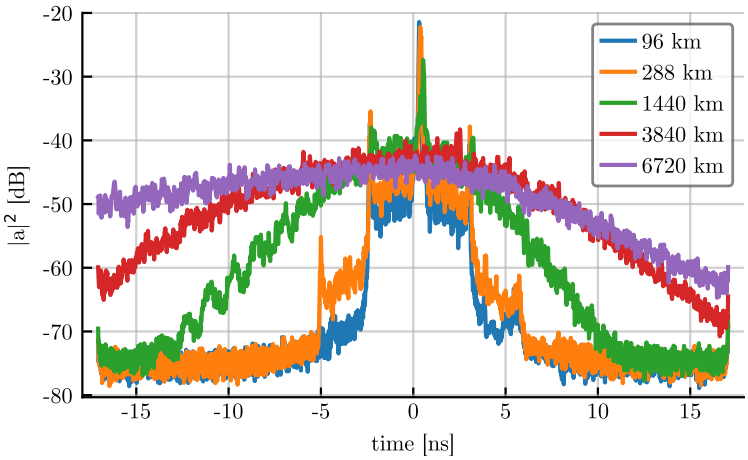

Figure 7.6: Few-mode fibre impulse response after 96 km, 228 km, 1440 km, 3840 km and 6720 km transmission.

The achievable rate predicts successful transmission distances up to 7000 km at an AR>2 bits/symbol, which is equivalent to the quadrature phase shift keying (QPSK) modulation format. However, at these distances, the system performance will be mainly limited by MDL, and impulse response broadening as a result of DMGD. This broadening effect, increasing with distance, can be seen in Fig. 7.6, which shows the sum of the squared 6×6 elements of the impulse response matrix. For short transmission distances (96 km and 288 km), each circulation can be recognised by the impulse response peaks corresponding to the strong discrete spatial mixing occurring in the mode-multiplexers, separated by the DMGD introduced in the 96 km FMF. This spacing of approximately 2.7 ns matches closely to the measured DMGD of 27 ps/km. With increasing distance, the impulse response broadens as DMGD accumulates, but also the shape changes because of the increased spatial channel mixing. After 2400 km transmission, the impulse response can no longer be captured within the configured 30 ns wide equaliser window.

The other reach limiting parameter, MDL, can be obtained by performing a singular value decomposition (SVD) on the estimated transfer matrix. The frequency resolved MDL, defined as the ratio between the largest and smallest singular value is given for each transmitted distance in Fig. 7.7. This curve starts at 1.7 dB, which matches the measured MDL of the 96 km FMF span and both spatial multiplexers. For the first couple of circulations, the MDL grows approximately linear, but for longer distances the growth-rate decreases to scale approximately with $\sqrt{L}$. This suggests an increased coupling between the spatial channels. Something that can also be observed from the bell shape impulse response in Fig. 7.6. Alternative to observing only the strongest and weakest singular value, all six values are taken into account in the standard deviation of the MDL, which is shown on the right

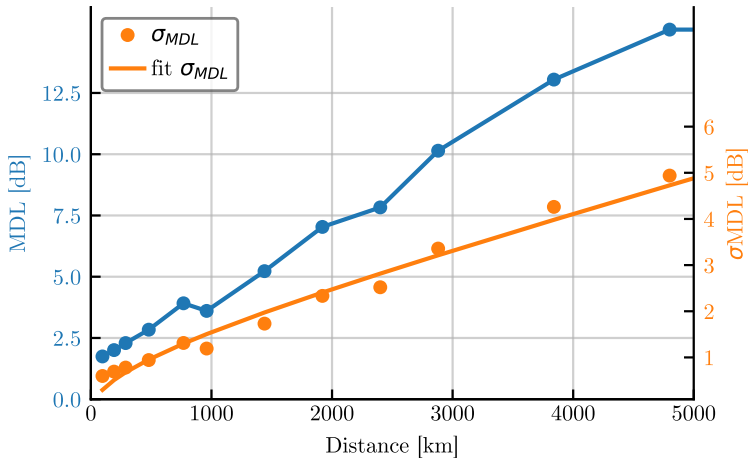

Figure 7.7: Mode dependent loss and its standard deviation for transmission distances up to 5000 km.

axis in Fig. 7.7. Because the signal propagates multiple times through the same fibre span in the re-circulating loop, the growth of σ_{MDL} can be described by:

$$\sigma_{\text{MDL}} = \xi\sqrt{1 + \frac{1}{12}\xi^2} \tag{7.9}$$

with $\xi = \sqrt{K}\sigma_g$, where K is the number of identical fibre sections or re-circulations in this scenario, and σ_g is the MDL standard deviation of a single section or circulation [155]. Fitting Eq. (7.9) to the calculated values leads to an estimate σ_g of 0.5 dB per 96 km span.

7.2 138-Tb/s combined wavelength and mode division multiplexed transmission

The previous experiment demonstrated the potential of SDM to outperform SSMF in transmission rate. In this section, the spectral efficiency is doubled as the number of modes is increased to six. On top of larger spatial multiplicity, the number of wavelength channels is increased to 120, resulting in a net transmission rate of 138 Tbit/s.

7.2.1 Dispersion matched few-mode fibre link

The transmission fibre employed in this experiment is designed to guide only the following linearly polarised modes, LP_{01}, LP_{11}, LP_{21}, and LP_{02}. Because of the two-fold degeneracy of the LP_{11} and LP_{21} modes, a total of six spatial modes

Table 7.1: Lengths and DMGDs of the spools in the few-mode link

		DMGD [ns]		
Spool	L [km]	LP_{01}-LP_{11}	LP_{01}-LP_{21}	LP_{01}-LP_{02}
1	3.0	-1.60	-3.19	-3.26
2	30.0	3.17	8.56	8.56
3	19.3	-0.70	-3.14	-3.31
4	6.5	-0.67	-1.88	-1.82
Total	58.8	0.20	0.35	0.16

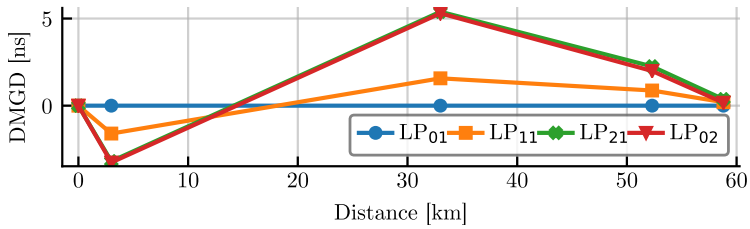

Figure 7.8: Evolution of differential mode group delay of the 58.8 km 6-mode fibre span.

are supported. Including both polarisation states of each modes, a total of 12 spatial channels are available for transmission. The attenuation of 0.2 dB/km for the supported modes as well as the CD of 18 ps/(nm · km) is slightly above typical values for SSMF. The effective area of the modes range from 90 µm^2 to 180 µm^2, which is not particularly large for few-mode fibre. However, it is still larger compared to SSMF.

Although the graded-index profile is optimised for low DMGD, the total mode dispersion can be further reduced by carefully selecting multiple fibre spools with positive and negative dispersion values. This technique shows high similarity to installation of dispersion compensated fibre (DCF) in transmission links limited by CD in cases digital compensation is unavailable [239, 240]. Building a nearly perfect compensated link becomes more challenging with an increasing number of modes, as the DMGD between any two mode groups must be matched. Therefore, a greater diversity of fibre spools may be required to achieve a close to zero DMGD span. The lengths and modal dispersion between the four fibre spools used to form the 58.8 km span in this section are given in Table 7.1. The development of DMGD can be seen in the dispersion map for this link in Fig. 7.8. Observe that even though the DMGD builds up to a maximum of 5 ns after 33 km, the accumulated dispersion at the end of the 58.8 km link is less than 0.35 ns. The propagation time difference between the slowest and fastest path is 10.8 ns. Note that for this analysis a linear growth of mode group dispersion is assumed, which

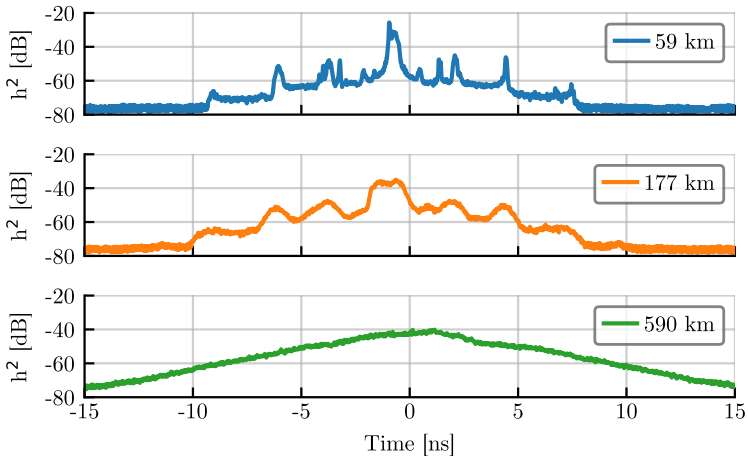

Figure 7.9: Estimated impulse response after 59 km, 177 km and 590 km transmission.

holds for weakly-coupled multi-mode transmission systems.

The effect of dispersion management can also be seen in the impulse response obtained from the MIMO equaliser. Figure 7.9, shows the sum of the 144 elements of the 12×12 MIMO equaliser obtained during the system optimisation process. It can be seen that the majority of the signal energy is concentrated within a 1 ns window around the centre. The other peaks in the graph are at least 20 dB suppressed and originate from the fusion splices within the fibre link. With increasing transmission distance the individual peaks disappear and a Gaussian-shaped response appears, indicating the stronger coupling between the modes. Note that, because of the DMGD optimised span, the total impulse response duration does not increase dramatically and can be still be fully captured with an equaliser window of 30 ns after 590 km. For this reason, it is not expected that this system is limited by modal dispersion for transmission distances up to 590 km.

7.2.2 Mode selective 6-mode photonic lanterns

For this setup, two fibre based PLs mode multiplexers are selected. As mentioned before, these all-fibre devices can be fabricated to have low mode-dependent and insertion losses and they can be conveniently fusion spliced to the transmission fibre to minimise coupling losses. In the production process for these multiplexers dissimilar single-mode fibres were used to enhance the mode selectivity [125]. The single-mode fibre (SMF) core diameters of 23 µm, 18 µm, 15 µm and 11 µm were used for LP_{01}, LP_{11}, LP_{21}, and LP_{02} respectively. The single-mode fibre coupling to the LP_{02} mode had a smaller cladding diameter of 86 μm^2 whereas the other SMFs had standardised 125 μm^2 cladding diameters.

Table 7.2: Insertion losses of the mode multiplexers and the 59 km FMF span

	Insertion loss [dB]			
Mode	MUX	DEMUX	59km FMF	Total
LP_{01}	0.59	1.93	12.99	15.51
LP_{11a}	0.76	0.80	12.84	14.40
LP_{11b}	0.38	3.20	13.17	17.34
LP_{21a}	2.30	0.87	13.30	17.06
LP_{21b}	0.79	0.91	13.54	15.83
LP_{02}	1.57	1.56	13.43	17.15

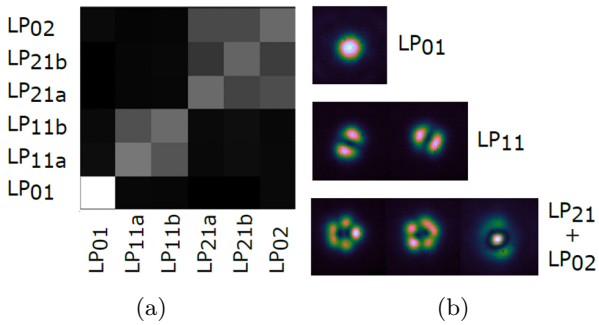

Figure 7.10: (a) Transfer matrix for a pair of mode multiplexers and (b) the mode profiles observed with a infra-red camera.

After fabrication, the set is characterised utilising an optical-vector network analyser, similar to the one described in Chapter 5. Figure 7.10 is a simplified representation of the transfer function matrix, which is obtained by integrating the signal power of all elements in the time domain impulse response matrix and subsequently average over polarisation. Observe that the modes within mode groups couple strongly, but the mixing with other mode groups is limited. From SVD analysis on the transfer function matrix, an MDL of 1.3 dB and 2.0 dB was found. An indication of the mode selectivity can also be obtained by observing the multi-mode output of the multiplexer with an infra-red camera while the single-mode inputs are excited sequentially. Figure 7.10 shows the pictures taken for one of the photonic lanterns. The linearly polarised (LP) mode profiles of the first 6 LP modes are clearly recognisable within these pictures.

A short length of 6-mode fibre, similar to the transmission fibre is fusion spliced to the PLs. The power transfer of ASE from each of the single-mode inputs to the few-mode output is measured for each of the multiplexers to verify the IL. After splicing both multiplexers to the transmission fibre, the power transfer from each

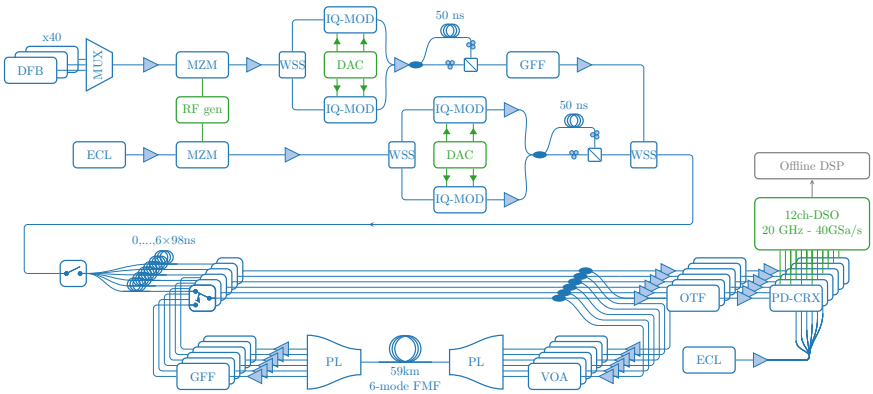

Figure 7.11: Long-haul transmission setup including 6-mode re-circulating loop consisting of 59 km 6-mode FMF span and two mode-selective photonic lanterns.

single-mode input to single-mode output is measured to determine the IL for the complete transmission link. Subsequently, the fibre attenuation in combination with the losses introduced at the fusion splices can be calculated. Assuming an attenuation of 0.2 dB/km, an additional 1 dB to 1.5 dB of losses is introduced in the 5 splice points. The maximum variation of 2 dB between the spatial channels, can be easily compensated during transmission by tuning the VOAs accordingly.

7.2.3 Experimental setup

The transmission setup required for evaluating the 6-mode fibre is an extended version of the setup used in the previous section. The updated schematic, giving in Fig. 7.11, has an additional 3 re-circulating loops, matched both in lengths and losses. Additional decorrelation delays of 294 ns, 392 ns and 490 ns are added to obtain the six decorrelated signal copies, one for each spatial mode. Furthermore, the wavelength grid is extended to contain 120 wavelength channels ranging 191.19 THz to 195.915 THz by increasing the number of lasers to 40 and modulating them with the same 33.3 GHz tone. Each De Bruijn sequence consists of 2^{16} symbols mapped to a 16-QAM constellation, resulting in a line rate of 240 Gbit/s. The 59 km dispersion managed fibre span and photonic lanterns are positioned between the two stages of the dual stage EDFAs, in a 6-fold re-circulating loop configuration. To detect all 12 spatial channels simultaneously, 6 polarisation-diverse coherent receiver (PD-CRX) in combination with a 24-channel DSO is employed. All digital signal processing (DSP) steps, including front-end and CD compensation, and MIMO equalisation are performed offline. The 12×12 MIMO FDE is based on the LMS algorithm during convergence and MMA during transmission. Finally, CPE is performed before evaluating transmission performance.

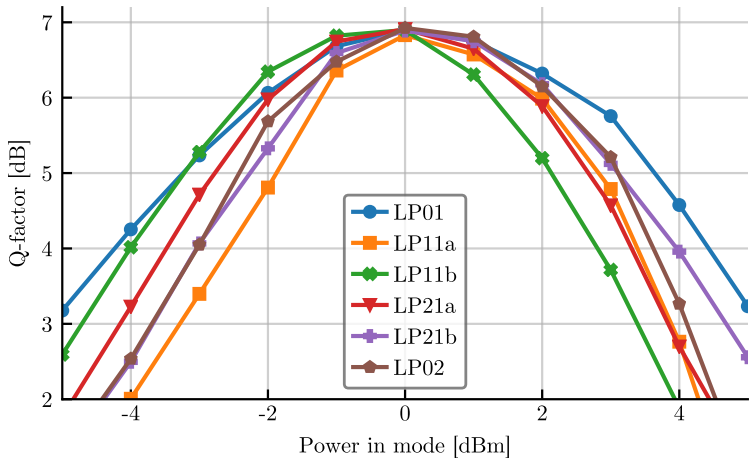

Figure 7.12: Q-factor for all spatial channels versus launch powers per mode. The lines represent the average over all 12 spatial channels, whereas the shaded areas indicate the highest and lowest values.

7.2.4 Transmission system optimisation

Key to achieving high capacity transmission results is understanding and optimisation of the setup. To reduce measurement and processing time this process is performed with only 15 of the 120 wavelength channels enabled. From the measured insertion losses of the transmission link (Table 7.2), a small variation between spatial channels was observed. As this could translate to an impact on the Q-factor performance, a launch power sweep is performed. In this sweep, the launch power in one of the single-mode inputs of the PL is changed. A 2 dB offset for one of the LP_{21} modes was observed, which matches with earlier IL measurement of the spatial multiplexer in Table 7.2. By tuning the corresponding VOA in the setup this offset is compensated and the highest Q-factor for all modes is obtained for a launch power of 0 dB per mode, as can be seen in Fig. 7.12.

With the performance balanced between modes, the transmission system performance is further evaluated by performing a launch power sweep at various transmission distances. The Q-factors after 118 km, 295 km, 590 km, 885 km, 1180 km and 1475 km transmission are shown in Fig. 7.13. A small Q-factor difference between the six transmitted modes was observed, which is visualised by the colour shaded areas around the solid line representing system average Q-factor. Note that after the longest shown transmission distance of 1475 km, a 6 dB Q-factor can be achieved at the optimum launch power. Assuming a SD-FEC with 20 % overhead this would result in a successful transmission at a net spectral efficiency of 34.8 bit/s/Hz. Since there is a trade-off between spectral efficiency (SE) and reach, it is useful to consider a metric that includes both, such as the spectral-

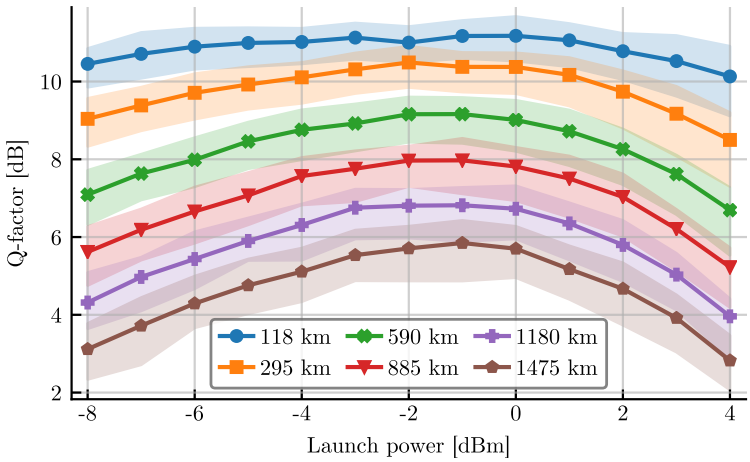

Figure 7.13: Q factors for various transmission distances versus launch power up to 1475 km transmission.

efficiency-distance product. After 1475 km transmission, the realised spectral-efficiency-distance product is 51 400 bit/s/Hz × km, which was a record at the time of publishing[J14]. Although individual spatial channels are performing on the edge of the assumed forward error-correction (FEC) threshold, a space-time coding scheme similar to the round-robin coding described in Section 6.1.4 can be applied to balance performance between the spatial channels and approach the system average.

For all evaluated transmission distances up to 5900 km, the MDL is calculated from the singular values of the 12 × 12 transfer matrix estimated by the MIMO equaliser. The MDL values shown in Fig. 7.14 are the ratio between the strongest and weakest eigenvalues within the 15 transmitted wavelength channels. An MDL of 3.9 dB after the first circulation is observed, which matches closely to the individual MDL values of the spatial multiplexers in Section 7.2.2 and a residual MDL of approximately 0.01 dB/km for the fibre.

Similar to the previous experiment, the standard deviation of MDL can be calculated as well using Eq. (7.9). In this recirculating loop configuration, the 59 km fibre link can be interpreted as identical fibre sections, allowing fitting the measured standard deviations to Eq. (7.9). As can be seen in, the fitted curve matches closely to the measured MDL values for σ_g of 0.62 dB.

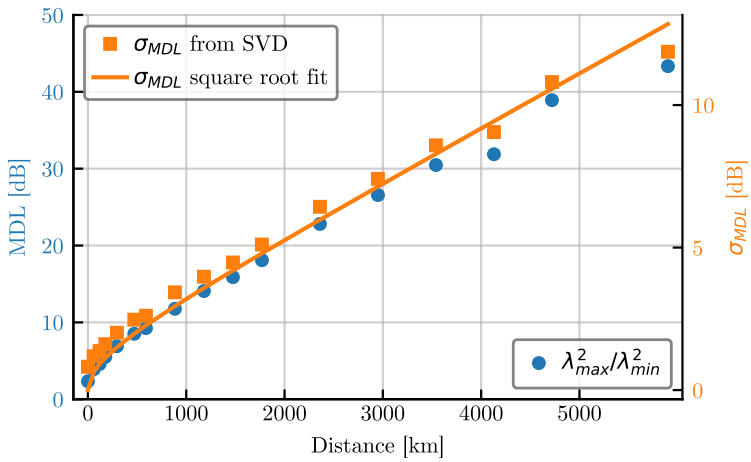

Figure 7.14: Mode dependent loss and its standard deviation for 15 wavelength channels.

7.2.5 High capacity transmission

After evaluating the transmission system using only 500 GHz of bandwidth, all 40 lasers are enabled. Because of the subtone modulation, this results in 120 channels within 4 THz of spectrum. No significant changes in the optimum launch power were observed for a second power sweep with all channels enabled. However, an approximately 1 dB Q-factor penalty for the previously investigated 15 wavelength channels was observed. These channels are highlighted with the grey area in Fig. 7.15. In the same figure, it can be seen that the overall system performance is limited by the shorter wavelength channels (lower channel numbers). Assuming a 20 % overhead SD-FEC, the lowest Q-factor of 6.3 dB limits the transmission distance of this system to 590 km.

This can be mainly attributed to the limited gain provided by the EDFA in the LO path for the shorter wavelengths in combination with a non-flat spectrum. These spectra, depicted in Fig. 7.17a, were obtained by observing one output of the recirculating loop. The optical spectrum analyser (OSA) needs to be synchronised with the recirculating loop to measure at the correct distance. Consequently, only a part of the spectrum can be observed with each trigger pulse. In combination with the time-varying behaviour of spatial channel mixing at a single output, the spectra in Fig. 7.17a do not represent the full multi-mode spectrum at a single moment in time. Nevertheless, a spectrum tilting effect, increasing with transmission distance, impairing the shorter wavelengths is visible.

Another observation taken from Fig. 7.15 is the larger spread in performance between the spatial channels, in particular at the shortest and longest wavelengths. A similar trend can be observed from the singular values and MDL derived from them in Fig. 7.16. Note that the singular values can only be calculated for mod-

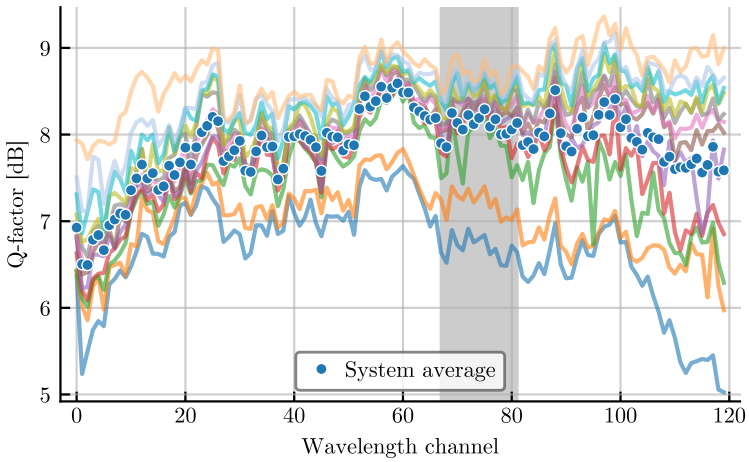

Figure 7.15: Q-factors for all 120 wavelength channels after 590 km transmission.

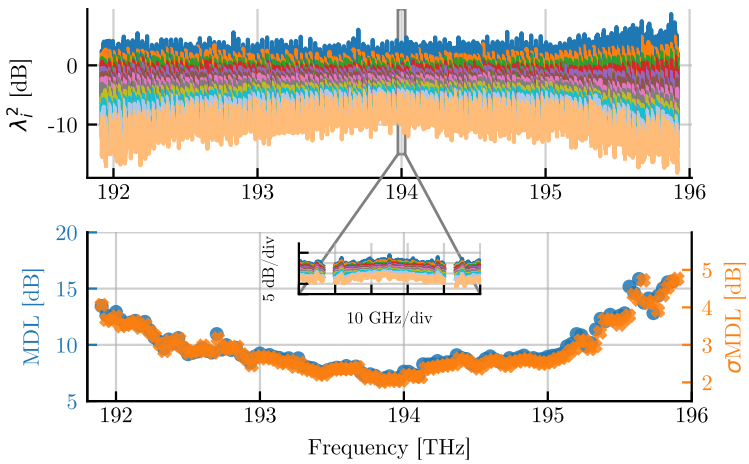

Figure 7.16: Singular values, mode dependent loss and the standard deviation σ_{MDL} for all modulated frequencies.

ulated frequencies, resulting in missing information at the small guard-bands of 3 GHz, as can be seen in the zoomed inset of Fig. 7.16. Furthermore, to obtain an unique solution, the singular values are ordered from largest to smallest and no direct relation with the spatial channel has to hold.

Inserting the previously determined standard deviation for a single circulation, σ_g of 0.62 dB/km in 7.9 would lead to an expected standard deviation of 2.9 dB. As can be seen in Fig. 7.16, this holds for the wavelengths in the centre of the C-band, including the previously investigated channels. Figure 7.17b shows the standard deviation of the MDL and Q-factor between the 12 spatial channels. Based on the similar trend of both curves for the higher wavelength channels, it can be assumed that performance in this regime is mainly determined by the mode-dependent loss of the system.

7.3 Conclusions

In this chapter, high-capacity mode-multiplexed transmission has been demonstrated. Long-haul distances up to 2400 km with a net spectral efficiency of 17.3 bit/s/Hz for 3-modes has shown to outperform SSMF due to its larger effective area allowing higher launch powers. An even larger spectral efficiency was achieved for a 6-mode fibre, resulting in a spectral-efficiency-distance product exceeding 50 000 bit/s/Hz × km by transmitting 120 Gbit/s 16-QAM modulated on 15 wavelength, and 12 spatial and polarisation channels over 1475 km few-mode fibre. By increasing the number of wavelength channels to 120, a net transmission rate of 138 Tbit/s over 590 km was achieved in a single fibre. These results demonstrate the potential of mode-division multiplexing to increase single fibre capacity in long-distance transmission links.

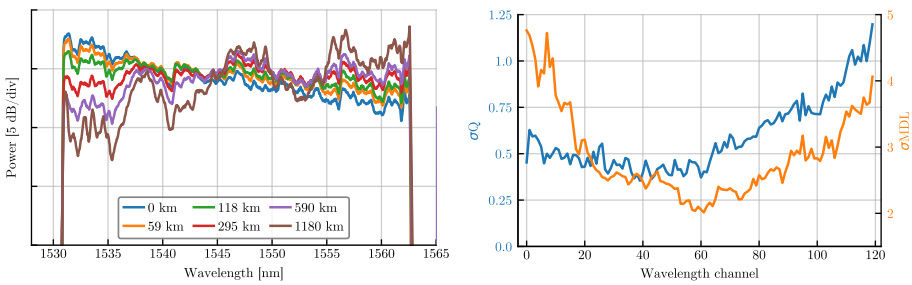

(a) (b)

Figure 7.17: (a) Optical spectra after various transmission distances. (b) Standard deviation of the mode dependent loss and Q-factor per wavelength channel.

Chapter 8

Conclusions and future outlook

8.1 Conclusions

In the introduction of this thesis, the rapid development of capacity in optical fibres was shown to approach the nonlinear Shannon limit for single-mode fibres. The nonlinear effects contributing to this limit were briefly explained in Chapter 2. Meanwhile, demand for bandwidth continues to grow with compound annual growth rate (CAGR) ranging from 25 % to 80 % depending on the applications and location in the network. Addressing this impending capacity crunch by improving single-channel spectral efficiency requires significant improvement of signal-to-noise ratio (SNR) due to their logarithmic relation in Shannon's theorem.

Introducing spatial parallelism to optical-fibre systems leads to linear scaling in spectral-efficiency. Space-division multiplexing (SDM) can be realised by employing multiple single-mode systems, multiple cores in a single cladding, or modes in a fibre. The latter offers the highest spatial density in the form of multi-mode fibre (MMF). However, the combined core and mode multiplexing in few-mode multi-core fibre (FM-MCF) can provide a larger spatial multiplicity in a single, but larger cladding diameter fibre. The large spatial overlap also introduces inter-channel crosstalk, which generally is resolved by employing multiple-input multiple-output (MIMO) digital signal processing (DSP) techniques, as discussed in Chapter 4. Although these algorithms are capable of unravelling spatial channels and compensating linear transmission impairments, their complexity has to be taken into account when considering real-time implementation and power consumption.

The advantage of spatially overlapping channels is integration on the component level, potentially leading to a cost reduction [241]. System components such as optical amplifiers and reconfigurable optical add-drop multiplexers (ROADMs) were introduced in Chapter 3. Other components such as signal generation and detection are still performed using single-mode technology. Hence, spatial multiplexers are required to convert between the two domains, of which multiple implementations were described in Chapter 3.

8.1.1 Optical vector network analysis

Key to the development of these novel components is characterisation on component level. For single-mode devices, a wide variety of off-the-shelve instruments is available to characterise at a component or subsystem level. However, measurement instruments for SDM components, and in particular multi-mode components, is still in its infancy. Furthermore, the introduction of spatial channels requires measurement of parameters that are irrelevant or non-existing for single-mode fibres, such as mode dependent loss (MDL) and differential mode group delay (DMGD). These impairments can be obtained from the transfer function matrix of components.

The optical vector network analyser (OVNA) developed for this PhD project allows the direct measurement of impulse response and complex transfer function matrices, thereby describing the complete linear device properties in both temporal and frequency domain. In a single measurement, the 11.5 THz of bandwidth in the C- and L- bands can be analysed in less than a second by sweeping a laser source at 200 nm, thereby minimizing the impact of temporal instabilities of the device. Furthermore, the low bandwidth interference pattern enables detection with high-gain low-bandwidth photodetectors and high-resolution analog-to-digital converter (ADC) to achieve a dynamic range over 60 dB. As accurate control over the laser sweep is difficult to realise, sweep linearisation is performed digitally be employing an auxiliary interferometer. In the digital domain, the complex impulse responses are extracted with a sub-picoseconds resolution. The spectral resolution of the complex transfer functions, obtained by performing a fast Fourier transform (FFT), is determined by the filtering width and is generally in the order of 100 MHz.

In this thesis, mode-multiplexers and fibres have been characterised using the OVNA, demonstrating the capabilities of measuring the transmission as well as the reflection of components. The latter allows characterisation of individual spatial multiplexers by exploiting the Fresnel reflection at the multi-mode facet of the component.

The FM-MCFs analysed in Chapter 5 have over 100 spatial channels each, which makes them the largest spatial multiplicity fibres to be analysed at the detailed level provided by the OVNA. This analysis showed a strongly varying temporal behaviour between cores designed to be homogeneous, which demonstrates the challenges in the fabrication of high core-count FM-MCFs. As a strong correlation between chromatic dispersion (CD) and impulse response duration is observed, digital CD compensation is proposed to improve DMGD estimations from impulse response measurements. Furthermore, up to 20 ns skew between the cores was observed for the 13.6 km long fibre, which is of importance as synchronisation of channels is required for the self-coherent applications for which this fibre was designed.

Lastly, the impact on fibre bending and twisting on FM-MCF is investigated. Radii ranging from 50 cm to the smallest radius achievable with the brittle fibre of 8 cm, no difference in impulse response and thus inter mode-group crosstalk was

observed. A similar observation could be made after twisting the fibre along its propagation axis. This suggests a potential application for high-capacity short-reach interconnects, where bending and twisting is generally unavoidable. Although it is important to note that the current designs of high-core count FM-MCF lack the mechanical strength to meet the small radii of tens of mm supported by single-mode bend-insensitive fibre.

8.1.2 Short-reach transmission

In Chapter 6, the feasibility of transmitting over more than 3 modes was investigated and demonstrated. First, by transmitting 10 modes over 4.45 km 6-linearly polarised (LP) few-mode fibre. As a large variation in bit error rate (BER) was observed between the spatial channels, a round-robin coding scheme is proposed to distribute the data uniformly along the spatial channels, thereby equalising the performance of the individual channels. By means of a 10-hour combined wavelength and mode division multiplexed transmission experiment, the temporal stability of the system is investigated, reporting small variations in BER and MDL. The observed impulse response duration of 2 ns, and DMGD measurements obtained by offset pulse launching (357 ps/km), show a strong deviation from the designed value of 8 ps/km. As this is mainly attributed to the inaccuracy of the production process, the well developed MMF process was used to manufacture a 50 µm core diameter MMF optimised for mode-division multiplexing (MDM) in the C-band.

The same line rate of 112 Gbit/s per spatial channel was achieved for 10-mode transmission over 40 km of MMF. The estimated impulse response duration of 6 ns after 40 km transmission confirms the lower DMGD compared to the few-mode fibre. As the MMF supports up to 55 spatial modes, crosstalk to non-excited mode-groups is controlled by maximising the index difference between groups. From the comparison of the equaliser error of both few-mode fibre (FMF) and MMF transmission, a larger spread of spatial channel convergence is observed for the MMF. As no direct relation to spatial channels can be made due to the non-mode-selective mode multiplexers, it is presumed this is caused by crosstalk from the fifth mode group that was not explicitly excited at launch. As the BER of the detected signal is well beyond the assumed threshold for soft-decision forward error-correction (SD-FEC), the signal is artificially impaired by noise loading to demonstrate a potentially larger transmission reach.

The intra-mode-group crosstalk of the MMF is significantly stronger than the inter mode-group crosstalk because of small effective index difference. As DMGD for strongly coupled channels evolve with the square root of the transmission distance instead of linear, selective excitation of modes in a single mode-group is proposed to limit the impulse response duration and thus also the equaliser window length. Therefore, the conventional 3-mode transmission over LP_{01} and LP_{11} is compared to LP_{21} and LP_{02}, where the latter comprised of three modes in a single mode-group. A maximum tap reduction of 27 % was observed for the single mode-group transmission while maintaining the same BER. Recently, it has been

shown that because of crosstalk the best performance is achieved by processing all 55 modes simultaneously [235].

8.1.3 Long-distance transmission

Two record long-distance transmission experiments were presented in Chapter 7. In the first, 16-ary quadrature amplitude modulation (QAM) was transmitted over 2400 km large-effective area index trench-assisted few mode fibre at a spectral efficiency of 17.3 bit/s/Hz by multiplexing 3 modes. The increased tolerance towards nonlinear effects because of the larger effective area allows for 3 dB higher launch power compared to standard single-mode fibre (SSMF), or 5.5 dB with respect to conventional 3-mode fibre [236]. Although the achievable information rate (AIR) derived from mutual information (MI) suggests towards longer distances by increasing the forward error-correction (FEC) overhead, it does not take the limitations imposed by DMGD and MDL into account.

By transmitting the same 16-QAM signal at 120 Gbit/s over the 6 modes of a graded-index FMF, spectral efficiency was doubled to 34.6 bit/s/Hz. This resulted in a spectral-efficiency-distance product exceeding 50 000 bit/s/Hz × km after the combined 12 spatial and 15 wavelength channels over 1475 km of FMF. At these distances, DMGD management is key to limiting impulse response broadening. Therefore, the transmission link consists of multiple spools of fibre, with both positive DMGD between the groups. However, perfectly matching DMGD becomes more difficult with an increasing number of modes. By fully loading the C-band with 120 wavelength channels a net transmission rate of 138 Tbit/s over 590 km was achieved in a single fibre.

8.2 Future outlook

It would be naive to expect the exponential growth in bandwidth demand will stagnate anywhere in the near future. Over the last decade, increased connectivity of the world population was driving up the capacity of communication systems. Even with decreasing population growth and saturating user connectivity, demand for bandwidth is likely to increase at similar rates because of machine-to-machine communications. The number of connected devices is already exceeding the global population, and is expected to triple in 2022 [10], following a CAGR of 19 %. The machine to machine (M2M) generated traffic is expected to grow even faster at a CAGR of 47 % as the increasing number of connections will be employed for higher-bandwidth applications, such as autonomous driving and the internet of things (IoT).

Nowadays user-generated traffic is dominated by high definition videos streaming, taking up nearly 58 % of the downstream bandwidth. Improved video quality at the cost of larger file sizes will ensure video streaming to maintain a major contributor to user-generated traffic in the near future. The emergence of augmented-, mixed-, and virtual reality can become an import factor in user-generated traffic.

However, it is proven to be difficult to predict the impact of emerging application that can decimate the dominant traffic sources of today.

8.2.1 Which SDM implementation

To keep up with demand, 1 Pbit/s optical systems with interfaces operating at 10 Tbit/s are required by 2024 [12]. As single-channel capacity is expected to grow annually with 20 %, spatial parallelism is unavoidable for future optical systems. For petabit/s systems, 6 to 80 spatial channels are required, depending on the actual development of single-channel capacity. Due to the exponential growth in 2037, 100 petabit/s systems with hundreds of spatial channels need to be available. Not only is capacity increase necessary, also the costs per bit has to come down. So the question arises, which SDM technology is the most viable?

1 Pbit/s systems

The most straightforward implementation of spatial parallelism is the deployment of multiple single-mode systems. The full compatibility with existing technology is obviously the main advantage of this approach. However, as component count and their related costs scale approximately linear, this might not be an economical solution in the long run. Therefore, some level of integration is required to realise this cost reduction. The most obvious and relatively easy to implement solution is sharing optical sources between spatial channels, thereby replacing N laser diodes by a single more powerful diode. Similarly, pump lasers can be shared between optical amplifiers. However, more integration is required at each component in the transmission link to provide the desired cost reduction. Conclusively, this approach is not the most feasible one for SDM systems with hundreds of spatial channels, but it might be sufficient to postpone the capacity crunch.

Employing fibres that host more than one single-mode core is a logical first step towards integration. If the inter-core crosstalk can be kept to a minimum by having sufficient spacing or high refractive barriers between them, each core can be used as an individual dual-polarisation single-mode channel and conventional coherent transceivers can still be used. This has been confirmed by various transmission experiments reporting an almost linear increase of capacity [31, 106]. However, due to their complex designs, it is unlikely the fibre manufacturing costs will be competitive to single-mode fibre (SMF) bundles.

Few-mode fibres, on the other hand, provide a potential 3 to 15 times increase of capacity with respect to single-mode fibres. Their centric, single solid-core design is highly similar to SMF and therefore relative simply to produce. However, the large spatial overlap of the modes is generally considered a disadvantage as it requires MIMO DSP to compensate for the linear mixing during propagation. This requires novel and more complex application-specific integrated circuits (ASICs), that can support a large number of high-speed input/output (IO) ports. Translating the offline DSP algorithms employed in experiments to real-time implementations

comes with it challenges. While the complexity of time domain equaliser (TDE) methods used in current products scale badly for an increasing number of spatial channels and taps, frequency domain equaliser (FDE) is a more scalable solution.

Note that in existing ASICs, the 2×2 MIMO equaliser only accounts for 10 % of the available power budget. The largest power consumption is attributed to the SD-FEC decoder and CD compensation [242]. A first, real-time demonstration of 6×6 MIMO DSP occupied about 80 % of the logical units available in a single field-programmable gate array (FPGA) [243]. Therefore it seems feasible to fit the complexity of larger MIMO equalisers in ASICs. However, the low bitrate of 2.5 Gbit/s indicates that the main challenge lies in the interface rates, which require integration of optical detection and DSP. As the IO is typically separated from the processing in FPGAs, this will be challenging. However, ASIC technology differs in this aspect as the IO can be integrated in the same chip, thereby alleviating this challenge. The coupling of spatial paths also introduces new opportunities for joint signal processing to reduce complexity. One example is the carrier phase estimation, which becomes a common impairment across modes when they share optical sources for the transmitter and local oscillator (LO) laser. Furthermore, the linear increase in convergence time with the number of coupled spatial channels has to be taken into account as well.

For optimal performance, the full impulse response must be available for the MIMO equaliser. Therefore, DMGD management is important to minimise computational complexity. As the manufacturing of low DMGD FMF becomes more difficult for an increasing number of modes due to deviations from their design, it is unlikely for FMF to provide more than 15 modes.

Towards 100 Pbit/s systems

MMF with a core diameter of 50 µm capitalise on the well-developed production process of OM multi-mode fibres. Consequently, fibres can be manufactured at relatively low costs while matching their designs closely, thereby achieving lower DMGD. Furthermore, the larger core size can support up to 55 spatial modes. Resolving the mode mixing requires powerful ASICs with a large number of high-speed IO ports. However, this fibre could be initially installed as part of a 3-mode system. When the required technology becomes available, the terminals can be upgraded to support a larger number of modes [J22, 235]. Therefore, MMF is a more promising solution compared to FMF.

For the excitation of modes in FMF, multiple solutions are available. The fibre-based photonic lantern (PL) offers low insertion loss (IL) and MDL and can be spliced to the other fibres in the system. However, it has a relatively large footprint and is not compatible with integrated photonics. For more compact and integrable solutions the 3D-waveguide (3DWG) or on-chip multiplexing [244] can be employed at the cost of higher losses. The excitation of all 55 modes of the MMF requires multi-plane light conversion (MPLC), of which support of 45 spatial modes has been demonstrated [245]. Although more optimization can result in lower IL and

MDL, targetting the differential modal gain (DMG) of optical amplifiers is more critical to system performance.

For a typical 80 km optical amplifier spacing, DMG can accumulate to significant values along long-distance links. Therefore it is key to develop optical amplifiers that can achieve population inversion in a cost-effective way, as well as accurate control of the gains of the individual modes. Additionally, channel coding can be employed to improve transmission performance, thereby alleviating the DMG requirements [J8, 246, 247].

Finally, FM-MCF provides over a hundred spatial channels, without excessive MIMO equalisers, as each few-mode core can be treated independently. However, it suffers from the same mechanical and production issues as multi-core fibre.

8.2.2 When will SDM become reality?

Before this question can be answered, one has to define SDM. In the research community SDM typically refers to the technology related to novel multi-mode and multi-core fibres, whereas the industry likes to advertise with SDM in the case of SMF fibre bundles. The question of when and which technology will be implemented has been the topic of discussion on numerous international conferences over the last years, with no clear winning technology or expected date for large-scale deployment. The direct answer is as soon as SDM technology becomes cheaper or at least comparable to conventional SMF systems. When this happens, SDM will most likely be introduced first in newly deployed green field optical systems. With a CAGR of 13 %, new hyperscale data centre are deployed. Similar to other parts of the network, their traffic shows exponential growth. Therefore, high-capacity interconnects are required, that can benefit from SDM technology. Inside the data centre, the use of 4 single-mode fibres is proposed in the multi-vendor PSM4 standard [248]. Although the latter is technically an implementation of SDM, it clearly differs from the SDM technology discussed in this thesis. Similarly, the deployment of the first subsea "SDM" cable between France and the USA by Google, is another example of the different interpretation of SDM within research and industry. This novel cable hosts twelve single-mode fibre pairs, instead of the six or eight of regular subsea cables. Along the 6400 km link, pump lasers and associated optics will be shared between the fibre pairs [249].

The deployment of the first multi-core fibre testbed in L'Aquila in Italy matches the interpretation of SDM discussed in this thesis. Over a length of 6.3 km, both coupled and uncoupled multi-core fibre (MCF) fibres were installed. The first results obtained from this testbed were recently presented [250].

Optical fibre communication is one of the fastest developing modern technologies, continuously driven by the exponential growth of data traffic generated by users and machines. Excess of bandwidth sparked new applications that could not have been predicted but shape our lives today. Space-division multiplexing has to potential to support this ever increasing demand for bandwidth. However, the implementation technology chosen for SDM is yet to be decided.

Bibliography

[1] T. H. Maiman. 'Stimulated Optical Radiation in Ruby'. In: *Nature* 187.4736 (Aug. 1960), pp. 493–494. ISSN: 0028-0836. DOI: 10.1038/187493a0.

[2] F. P. Kapron, D. B. Keck and R. D. Maurer. 'Radiation Losses in Glass Optical Waveguides'. In: *Applied Physics Letters* 17.10 (Nov. 1970), pp. 423–425. ISSN: 0003-6951. DOI: 10.1063/1.1653255.

[3] K.C. Kao and G.A. Hockham. 'Dielectric-fibre surface waveguides for optical frequencies'. In: *Proceedings of the Institution of Electrical Engineers* 113.7 (1966), pp. 1151–1158. ISSN: 0020-3270. DOI: 10.1049/piee.1966.0189.

[4] D. J. Richardson et al. 'Optical Amplifiers for SDM Communication Systems'. In: *2017 European Conference on Optical Communication (ECOC)*. IEEE, Sept. 2017, pp. 1–3. ISBN: 978-1-5386-5624-2. DOI: 10.1109/ECOC.2017.8346069.

[5] T. Miya et al. 'Ultimate low-loss single-mode fibre at 1.55 μm'. In: *Electronics Letters* 15.4 (1979), p. 106. ISSN: 00135194. DOI: 10.1049/el:19790077.

[6] R.J. Mears et al. 'Low-noise erbium-doped fibre amplifier operating at 1.54μm'. In: *Electronics Letters* 23.19 (1987), p. 1026. ISSN: 00135194. DOI: 10.1049/el:19870719.

[7] E. Desurvire, J. R. Simpson and P. C. Becker. 'High-gain erbium-doped traveling-wave fiber amplifier'. In: *Optics Letters* 12.11 (Nov. 1987), p. 888. ISSN: 0146-9592. DOI: 10.1364/OL.12.000888.

[8] Sandvine. *Global Internet Phenomena Report - Spring 2011*. Tech. rep. 2011.

[9] Sandvine. *Global Internet Phenomena Report 2018*. Tech. rep. October. 2018.

[10] Cisco. *Cisco Visual Networking Index: Forecast and Trends, 2017–2022*. Tech. rep. 2019.

[11] Amsterdam Internet Exchange (AIX). *Historical Monthly Traffic Volume*.

[12] Peter J. Winzer and David T. Neilson. 'From Scaling Disparities to Integrated Parallelism: A Decathlon for a Decade'. In: *Journal of Lightwave Technology* 35.5 (2017), pp. 1099–1115. ISSN: 07338724. DOI: 10.1109/JLT.2017.2662082.

[13] Rene Jean Essiambre et al. 'Capacity Limits of Optical Fiber Networks'. In: *Journal of Lightwave Technology* 28.4 (Feb. 2010), pp. 662–701. ISSN: 15582213. DOI: 10.1109/JLT.2009.2039464.

[14] C. E. Shannon. 'A Mathematical Theory of Communication'. In: *Bell System Technical Journal* 27.3 (July 1948), pp. 379–423. ISSN: 00058580. DOI: 10.1002/j.1538-7305.1948.tb01338.x.

[15] Peter J. Winzer, David T. Neilson and Andrew R. Chraplyvy. 'Fiber-optic transmission and networking: the previous 20 and the next 20 years [Invited]'. In: *Optics Express* 26.18 (Sept. 2018), p. 24190. ISSN: 1094-4087. DOI: 10.1364/oe.26.024190.

[16] Andrew D. Ellis, Jian Zhao and David Cotter. 'Approaching the Non-Linear Shannon Limit'. In: *Journal of Lightwave Technology* 28.4 (2010), pp. 423–433. ISSN: 15582213. DOI: 10.1109/JLT.2009.2030693.

[17] ITU. *Recommendation ITU-TG.694.1*. Tech. rep. 2012.

[18] Werner Klaus et al. 'Advanced Space Division Multiplexing Technologies for Optical Networks'. In: *Journal of Optical Communications and Networking* 9.4 (Apr. 2017), p. C1. ISSN: 1943-0620. DOI: 10.1364/JOCN.9.0000C1.

[19] S. Iano et al. 'Multicore optical fiber'. In: *Optical Fiber Communication*. Washington, D.C.: OSA, Mar. 1979, WB1. DOI: 10.1364/OFC.1979.WB1.

[20] S. Berdagué and P. Facq. 'Mode division multiplexing in optical fibers'. In: *Applied Optics* 21.11 (June 1982), p. 1950. ISSN: 0003-6935. DOI: 10.1364/AO.21.001950.

[21] A Chralyvy. 'Plenary paper: The coming capacity crunch'. In: *2009 35th European Conference on Optical Communication*. 2009, p. 1.

[22] M. de Boer et al. 'A first demonstrator for a mode group diversity multiplexing communication system'. In: *IEE Seminar on Optical Fibre Communications and Electronic Signal Processing*. Vol. 2005. IEE, 2005, pp. 16–16. ISBN: 0 86341 598 9. DOI: 10.1049/ic:20050554.

[23] S. Schollmann and W. Rosenkranz. 'Experimental equalization of crosstalk in a 2 × 2 MIMO system based on mode group diversity multiplexing in MMF Systems @ 10.7 Gb/s'. In: *33rd European Conference and Exhibition on Optical Communication - ECOC 2007*. Vol. 2007. IEE, 2007, pp. 742–742. ISBN: 978-3-8007-3042-1. DOI: 10.1049/ic:20070268.

[24] An Li et al. 'Reception of Mode and Polarization Multiplexed 107-Gb/s CO-OFDM Signal over a Two-Mode Fiber'. In: *Optical Fiber Communication Conference/National Fiber Optic Engineers Conference 2011*. Washington, D.C.: OSA, Mar. 2011, PDPB8. ISBN: 978-1-55752-906-0. DOI: 10.1364/OFC.2011.PDPB8.

[25] Massimiliano Salsi et al. 'Transmission at 2x100Gb/s, over Two Modes of 40km-long Prototype Few-Mode Fiber, using LCOS based Mode Multiplexer and Demultiplexer'. In: *Optical Fiber Communication Conference/National Fiber Optic Engineers Conference 2011*. Washington, D.C.: OSA, Mar. 2011, PDPB9. ISBN: 978-1-55752-906-0. DOI: 10.1364/OFC.2011.PDPB9.

[26] Nobutomo Hanzawa et al. 'Demonstration of mode-division multiplexing transmission over 10 km two-mode fiber with mode coupler'. In: *Optical Fiber Communication Conference/National Fiber Optic Engineers Conference 2011*. Washington, D.C.: OSA, Mar. 2011, OWA4. ISBN: 978-1-55752-906-0. DOI: 10.1364/OFC.2011.OWA4.

[27] Roland Ryf et al. 'Mode-Division Multiplexing Over 96 km of Few-Mode Fiber Using Coherent 6x 6 MIMO processing'. In: *Journal of Lightwave Technology* 30.4 (Feb. 2012), pp. 521–531. ISSN: 0733-8724. DOI: 10.1109/JLT.2011.2174336.

[28] Sebastian Randel et al. 'Mode-Multiplexed 6×20-GBd QPSK Transmission over 1200-km DGD-Compensated Few-Mode Fiber'. In: *Optical Fiber Communication Conference*. Washington, D.C.: OSA, Mar. 2012, PDP5C.5. ISBN: 978-1-55752-938-1. DOI: 10.1364/OFC.2012.PDP5C.5.

[29] V. A. J. M. Sleiffer et al. 'Optical chopper-based re-circulating loop for few-mode fiber transmission'. In: *Optics Letters* 39.5 (Mar. 2014), p. 1181. ISSN: 0146-9592. DOI: 10.1364/OL.39.001181.

[30] R. Ryf et al. '12 × 12 MIMO Transmission over 130-km Few-Mode Fiber'. In: *Frontiers in Optics 2012/Laser Science XXVIII*. Washington, D.C.: OSA, Oct. 2012, FW6C.4. ISBN: 978-1-55752-956-5. DOI: 10.1364/FIO.2012.FW6C.4.

[31] Jun Sakaguchi et al. '305 Tb/s space division multiplexed transmission using homogeneous 19-core fiber'. In: *Journal of Lightwave Technology* 31.4 (Feb. 2013), pp. 554–562. ISSN: 07338724. DOI: 10.1109/JLT.2012.2217373.

[32] B. Zhu et al. '112-Tb/s Space-division multiplexed DWDM transmission with 14-b/s/Hz aggregate spectral efficiency over a 768-km seven-core fiber'. In: *Optics Express* 19.17 (Aug. 2011), p. 16665. ISSN: 1094-4087. DOI: 10.1364/OE.19.016665.

[33] R. G.H. H. van Uden et al. 'Ultra-high-density spatial division multiplexing with a few-mode multicore fibre'. In: *Nature Photonics* 8.11 (Nov. 2014), pp. 865–870. ISSN: 17494893. DOI: 10.1038/nphoton.2014.243.

[34] Jeff. Hecht. *City of light : the story of fiber optics*. Oxford University Press, 1999, p. 316. ISBN: 0195108183.

[35] A. C. S. Van Heel. 'A New Method of transporting Optical Images without Aberrations'. In: *Nature* 173.4392 (Jan. 1954), pp. 39–39. ISSN: 0028-0836. DOI: 10.1038/173039a0.

[36] Basil I Hirschowitz. 'Flexible light transmitting tube'. In: (Dec. 1956).

[37] N. S. Kapany. 'Fiber Optics VI Image Quality and Optical Insulation*†'. In: *Journal of the Optical Society of America* 49.8 (Aug. 1959), p. 779. ISSN: 0030-3941. DOI: 10.1364/JOSA.49.000779.

[38] Narinder Sing-Kapany. *Fiber optics : principles and applications*. 1967. DOI: b0006boomi.

[39] Y Tamura et al. 'Lowest-ever 0.1419-dB/km loss optical fiber'. In: *2017 Optical Fiber Communications Conference and Exhibition (OFC)*. Mar. 2017, pp. 1–3.

[40] Gerd. Keiser. *Optical fiber communications*. McGraw-Hill Companies, 2011, p. 654. ISBN: 0073380717.

[41] F T Ulaby, E Michielssen and U Ravaioli. *Fundamentals of Applied Electromagnetics*. Always learning. Prentice Hall, 2010. ISBN: 9780132139311.

[42] P Diament. *Wave Transmission and Fiber Optics*. Macmillan Publishing Company, 1990. ISBN: 9780029460870.

[43] D. Gloge. 'Weakly Guiding Fibers'. In: *Applied Optics* 10.10 (1971), p. 2252. ISSN: 0003-6935. DOI: 10.1364/AO.10.002252.

[44] Kenji Kawano and Tsutomu Kitoh. *Introduction to Optical Waveguide Analysis*. New York, USA: John Wiley & Sons, Inc., July 2001. ISBN: 0471406341. DOI: 10.1002/0471221600.

[45] Allan W. Snyder and William R. Young. 'Modes of optical waveguides'. In: *Journal of the Optical Society of America* 68.3 (Mar. 1978), p. 297. ISSN: 0030-3941. DOI: 10.1364/JOSA.68.000297.

[46] Milton Abramowitz and Irene A Stegun. *Handbook of mathematical functions: with formulas, graphs, and mathematical tables*. Vol. 55. Courier Corporation, 1965.

[47] Govind Agrawal. *Nonlinear Fiber Optics*. Elsevier, 2006. ISBN: 9780123695161. DOI: 10.1016/B978-0-12-369516-1.X5000-6.

[48] B. Crosignani, P. Di Porto and C. H. Papas. 'Coupled-mode theory approach to nonlinear pulse propagation in optical fibers'. In: *Optics Letters* 6.2 (Feb. 1981), p. 61. ISSN: 0146-9592. DOI: 10.1364/OL.6.000061.

[49] Max Born and Emil Wolf. *Principles of optics: electromagnetic theory of propagation, interference and diffraction of light*. Elsevier, 2013.

[50] Donald Keck. 'Fundamentals of optical waveguide fibers'. In: *IEEE Communications Magazine* 23.5 (1985), pp. 17–22.

[51] Gordon A. Thomas et al. 'Towards the clarity limit in optical fibre'. In: *Nature* 404.6775 (2000), pp. 262–264. ISSN: 00280836. DOI: 10.1038/35005034.

[52] ITU. *Recommendation ITU-TG.652*. Tech. rep. 2016.

[53] *Corning® SMF-28® Ultra Optical Fiber-product information*. Corning. Nov. 2014.

[54] ITU-T. *Optical system design and engineering considerations*. Tech. rep. 2016.

[55] D Gloge. 'Bending loss in multimode fibers with graded and ungraded core index'. In: *Applied optics* 11.11 (1972), pp. 2506–2513.

[56] Hagen Renner. 'Bending losses of coated single-mode fibers: a simple approach'. In: *Journal of Lightwave technology* 10.5 (1992), pp. 544–551.

[57] Luca Faustini and Giuseppe Martini. 'Bend loss in single-mode fibers'. In: *Journal of lightwave technology* 15.4 (1997), pp. 671–679.

[58] W B Gardner. 'Microbending loss in optical fibers'. In: *The bell system technical journal* 54.2 (1975), pp. 457–465.

[59] Dt Gloge. 'Dispersion in weakly guiding fibers'. In: *Applied optics* 10.11 (1971), pp. 2442–2445.

[60] L G Cohen, Chinlon Lin and W G French. 'Tailoring zero chromatic dispersion into the 1.5–1.6 um low-loss spectral region of single-mode fibres'. In: *Electronics Letters* 15.12 (1979), pp. 334–335.

[61] Lars Gruner-Nielsen et al. 'Dispersion-compensating fibers'. In: *Journal of Lightwave Technology* 23.11 (2005), pp. 3566–3579.

[62] G. P. (Govind P.) Agrawal. *Fiber-optic communication systems*. Wiley, 2010, p. 603. ISBN: 0470505117.

[63] F. Forghieri, R. W. Tkach and A. R. Chraplyvy. 'Fiber Nonlinearities and Their Impact on Transmission Systems'. In: *Optical Fiber Telecommunications IIIA: Third Edition*. 2012. ISBN: 9780123951700. DOI: 10.1016/B978-0-08-051316-4.50012-6.

[64] R H_ Stolen, E P Ippen and A R Tynes. 'Raman oscillation in glass optical waveguide'. In: *Applied Physics Letters* 20.2 (1972), pp. 62–64.

[65] A.G. Striegler and B. Schmauss. 'Fiber-based compensation of IXPM-induced timing jitter'. In: *IEEE Photonics Technology Letters* 16.11 (Nov. 2004), pp. 2574–2576. ISSN: 1041-1135. DOI: 10.1109/LPT.2004.834911.

[66] R W Tkach et al. 'Four-photon mixing and high-speed WDM systems'. In: *Journal of Lightwave Technology* 13.5 (1995), pp. 841–849.

[67] Cristian Antonelli, Mark Shtaif and Antonio Mecozzi. 'Modeling of Nonlinear Propagation in Space-Division Multiplexed Fiber-Optic Transmission'. In: *Journal of Lightwave Technology* 34.1 (Jan. 2016), pp. 36–54. ISSN: 0733-8724. DOI: 10.1109/JLT.2015.2510511.

[68] Francesco Poletti and Peter Horak. 'Description of ultrashort pulse propagation in multimode optical fibers'. In: *Journal of the Optical Society of America B* 25.10 (2008), p. 1645. ISSN: 0740-3224. DOI: 10.1364/josab.25.001645.

[69] S Mumtaz, R Essiambre and G P Agrawal. 'Nonlinear Propagation in Multimode and Multicore Fibers: Generalization of the Manakov Equations'. In: *Journal of Lightwave Technology* 31.3 (Feb. 2013), pp. 398–406. ISSN: 0733-8724. DOI: 10.1109/JLT.2012.2231401.

[70] Frank Gray. 'Pulse code communication'. In: (Nov. 1947).

[71] Alberto Sierra et al. 'On the Use of Delay-Decorrelated I/Q Test Sequences for QPSK and QAM Signals'. In: *IEEE Photonics Technology Letters* 24.12 (June 2012), pp. 1000–1002. ISSN: 1041-1135. DOI: 10.1109/LPT.2012.2192423.

[72] N. G. De Bruijn. 'A combinatorial problem'. In: *Nederl. Akad. Wetensch. Proc.* 49 (1946), pp. 758–764.

[73] Andreas Klein. 'Linear Feedback Shift Registers'. In: *Stream Ciphers*. London: Springer London, 2013, pp. 17–58. DOI: 10.1007/978-1-4471-5079-4_2.

[74] Peter M. Higgins. 'Burrows–Wheeler transformations and de Bruijn words'. In: *Theoretical Computer Science* 457 (Oct. 2012), pp. 128–136. ISSN: 0304-3975. DOI: 10.1016/J.TCS.2012.07.019.

[75] Andrew Klapper Mark Goresky and Andrew Klapper. 'Algebraic shift register sequences'. In: (2012).

[76] K Schuh et al. 'Single carrier 1.2 Tbit/s transmission over 300 km with PM-64 QAM at 100 GBaud'. In: *2017 Optical Fiber Communications Conference and Exhibition (OFC)*. Mar. 2017, pp. 1–3.

[77] Keysight Technologies. *M8196A data sheet.*

[78] D Rafique et al. 'Digital Preemphasis in Optical Communication Systems: On the DAC Requirements for Terabit Transmission Applications'. In: *Journal of Lightwave Technology* 32.19 (Oct. 2014), pp. 3247–3256. ISSN: 0733-8724. DOI: 10.1109/JLT.2014.2343957.

[79] Z Jia et al. 'Performance analysis of pre- and post-compensation for bandwidth-constrained signal in high-spectral-efficiency optical coherent systems'. In: *OFC 2014.* Mar. 2014, pp. 1–3. DOI: 10.1364/OFC.2014.W3K.3.

[80] G Khanna et al. 'A Robust Adaptive Pre-Distortion Method for Optical Communication Transmitters'. In: *IEEE Photonics Technology Letters* 28.7 (Apr. 2016), pp. 752–755. ISSN: 1041-1135. DOI: 10.1109/LPT.2015.2509158.

[81] Harry Nyquist. 'Certain topics in telegraph transmission theory'. In: *Transactions of the American Institute of Electrical Engineers* 47.2 (1928), pp. 617–644.

[82] George Turin. 'An introduction to matched filters'. In: *IRE transactions on Information theory* 6.3 (1960), pp. 311–329.

[83] Friedrich Carl Alwin Pockels. *Lehrbuch der kristalloptik.* Vol. 19. BG Teubner, 1906.

[84] R V Schmidt and I P Kaminow. 'Metal-diffused optical waveguides in LiNbO3'. In: *Applied Physics Letters* 25.8 (1974), pp. 458–460. DOI: 10.1063/1.1655547.

[85] L Thylen. 'Integrated optics in LiNbO/sub 3/: recent developments in devices for telecommunications'. In: *Journal of Lightwave Technology* 6.6 (June 1988), pp. 847–861. ISSN: 0733-8724. DOI: 10.1109/50.4073.

[86] Erik Agrell and Magnus Karlsson. 'Power-efficient modulation formats in coherent transmission systems'. In: *Journal of Lightwave Technology* 27.22 (2009), pp. 5115–5126.

[87] Henning Bulow. 'Polarization QAM modulation (POL-QAM) for coherent detection schemes'. In: *2009 Conference on Optical Fiber Communication-incudes post deadline papers.* IEEE. 2009, pp. 1–3.

[88] Leonardo D Coelho and Norbert Hanik. 'Global optimization of fiber-optic communication systems using four-dimensional modulation formats'. In: *European Conference and Exposition on Optical Communications.* Optical Society of America. 2011, Mo–2.

[89] Sjoerd van der Heide et al. '11,700 km Transmission at 4.8 bit/4D-sym via Four-dimensional Geometrically-shaped Polarization-Ring-Switching Modulation'. In: *arXiv preprint arXiv:1904.12561* (2019).

[90] A H Gnauck et al. 'Efficient Pumping Scheme for Amplifier Arrays with Shared Pump Laser'. In: *ECOC 2016; 42nd European Conference on Optical Communication.* 2016, pp. 1–3.

[91] Lars Gruner-Nielsen et al. 'Few mode transmission fiber with low DGD, low mode coupling, and low loss'. In: *Journal of Lightwave Technology* 30.23 (2012), pp. 3693–3698.

[92] Ming-Jun Li et al. 'Low delay and large effective area few-mode fibers for mode-division multiplexing'. In: *2012 17th Opto-Electronics and Communications Conference*. IEEE. 2012, pp. 495–496.

[93] Takayoshi Mori et al. 'Low DMD four LP mode transmission fiber for wide-band WDM-MIMO system'. In: *Optical Fiber Communication Conference*. Optical Society of America. 2013, OTh3K–1.

[94] Pierre Sillard et al. 'Low-DMGD 6-LP-Mode Fiber'. EN. In: *Optical Fiber Communication Conference*. Washington, D.C.: OSA, Mar. 2014, M3F.2. ISBN: 978-1-55752-993-0. DOI: 10.1364/OFC.2014.M3F.2.

[95] Pierre Sillard et al. 'Low-differential-mode-group-delay 9-LP-mode fiber'. In: *Journal of Lightwave Technology* 34.2 (2015), pp. 425–430.

[96] Pierre Sillard, Marianne Bigot-Astruc and Denis Molin. 'Few-Mode Fibers for Mode-Division-Multiplexed Systems'. In: *Journal of Lightwave Technology* 32.16 (Aug. 2014), pp. 2824–2829. ISSN: 0733-8724. DOI: 10.1109/JLT.2014.2312845.

[97] Pierre Sillard et al. '50 μm multimode fibers for mode division multiplexing'. In: *Journal of Lightwave Technology* 34.8 (2016), pp. 1672–1677. ISSN: 07338724. DOI: 10.1109/JLT.2015.2507442.

[98] B. Y. Kim et al. 'Use of highly elliptical core fibers for two-mode fiber devices'. In: *Optics Letters* 12.9 (Sept. 1987), p. 729. ISSN: 0146-9592. DOI: 10.1364/OL.12.000729.

[99] Ezra Ip et al. 'SDM transmission of real-time 10GbE traffic using commercial SFP + transceivers over 05km elliptical-core few-mode fiber'. In: *Optics Express* 23.13 (June 2015), p. 17120. ISSN: 1094-4087. DOI: 10.1364/oe.23.017120.

[100] F. Parmigiani et al. 'Elliptical Core Few Mode Fibers for Multiple-Input Multiple Output-Free Space Division Multiplexing Transmission'. In: *IEEE Photonics Technology Letters* 29.21 (Nov. 2017), pp. 1764–1767. ISSN: 1041-1135. DOI: 10.1109/LPT.2017.2740499.

[101] Lixian Wang and Sophie LaRochelle. 'Design of eight-mode polarization-maintaining few-mode fiber for multiple-input multiple-output-free spatial division multiplexing'. In: *Optics Letters* 40.24 (Dec. 2015), p. 5846. ISSN: 0146-9592. DOI: 10.1364/OL.40.005846.

[102] G K L Wong et al. 'Excitation of orbital angular momentum resonances in helically twisted photonic crystal fiber.' In: *Science (New York, N.Y.)* 337.6093 (July 2012), pp. 446–9. ISSN: 1095-9203. DOI: 10.1126/science.1223824.

[103] L Rechtman and D M Marom. 'Rectangular versus circular fiber core designs: New opportunities for mode division multiplexing?' In: *2017 Optical Fiber Communications Conference and Exhibition (OFC)*. Mar. 2017, pp. 1–3.

[104] D. Marcuse. 'Derivation of Coupled Power Equations'. In: *Bell System Technical Journal* 51.1 (Jan. 1972), pp. 229–237. ISSN: 00058580. DOI: 10.1002/j.1538-7305.1972.tb01911.x.

[105] Tetsuya Hayashi et al. 'Design and fabrication of ultra-low crosstalk and low-loss multi-core fiber'. In: *Optics Express* 19.17 (Aug. 2011), p. 16576. ISSN: 1094-4087. DOI: 10.1364/OE.19.016576.

[106] Takayuki Mizuno et al. '32-core dense SDM unidirectional transmission of PDM-16QAM signals over 1600 km using crosstalk-managed single-mode heterogeneous multicore transmission line'. In: *2016 Optical Fiber Communications Conference and Exhibition (OFC)*. IEEE. 2016, pp. 1–3.

[107] Y Sasaki et al. 'Single-mode 37-core fiber with a cladding diameter of 248 um'. In: *2017 Optical Fiber Communications Conference and Exhibition (OFC)*. IEEE. 2017, pp. 1–3.

[108] Cen Xia et al. 'Supermodes for optical transmission'. In: *Optics Express* 19.17 (Aug. 2011), p. 16653. ISSN: 1094-4087. DOI: 10.1364/OE.19.016653.

[109] Sercan O. Arik and Joseph M. Kahn. 'Coupled-Core Multi-Core Fibers for Spatial Multiplexing'. In: *IEEE Photonics Technology Letters* 25.21 (Nov. 2013), pp. 2054–2057. ISSN: 1041-1135. DOI: 10.1109/LPT.2013.2280897.

[110] R. Ryf et al. 'MIMO-Based Crosstalk Suppression in Spatially Multiplexed 3x56-Gb/s PDM-QPSK Signals for Strongly Coupled Three-Core Fiber'. In: *IEEE Photonics Technology Letters* 23.20 (Oct. 2011), pp. 1469–1471. ISSN: 1041-1135. DOI: 10.1109/LPT.2011.2162826.

[111] T Hayashi et al. '125-μm-Cladding coupled multi-core fiber with ultra-low loss of 0.158 dB/km and record-low spatial mode dispersion of 6.1 ps/km'. In: *2016 Optical Fiber Communications Conference and Exhibition (OFC)*. Mar. 2016, pp. 1–3.

[112] T. Sakamoto et al. 'Randomly-coupled single-mode 12-core fiber with highest core density'. In: *2017 Optical Fiber Communications Conference and Exhibition (OFC)*. Mar. 2017, pp. 1–3.

[113] Roland Ryf et al. 'Coupled-Core Transmission over 7-Core Fiber'. In: *Optical Fiber Communication Conference Postdeadline Papers 2019*. Washington, D.C.: OSA, Mar. 2019, Th4B.3. ISBN: 978-1-943580-55-2. DOI: 10.1364/OFC.2019.Th4B.3.

[114] Jun Sakaguchi et al. '228-Spatial-Channel Bi-Directional Data Communication System Enabled by 39-Core 3-Mode Fiber'. In: *Journal of Lightwave Technology* 37.8 (Apr. 2019), pp. 1756–1763. ISSN: 0733-8724. DOI: 10.1109/JLT.2019.2895205.

[115] T Sakamoto et al. 'Low-loss and low-DMD few-mode multi-core fiber with highest core multiplicity factor'. In: *2016 Optical Fiber Communications Conference and Exhibition (OFC)*. IEEE. 2016, pp. 1–3.

[116] Daiki Soma et al. '10.16-Peta-bit/s Dense SDM/WDM Transmission over 6-Mode 19-Core Fiber across the C+L Band'. In: *Journal of Lightwave Technology* (2018), pp. 1–1. ISSN: 0733-8724. DOI: 10.1109/JLT.2018.2799380.

[117] Roland Ryf, Nicolas K Fontaine and René-Jean Essiambre. 'Spot-based mode couplers for mode-multiplexed transmission in few-mode fiber'. In: *IEEE Photonics Technology Letters* 24.21 (2012), pp. 1973–1976.

[118] W. Q. Thornburg, B. J. Corrado and X. D. Zhu. 'Selective launching of higher-order modes into an optical fiber with an optical phase shifter'. In: *Optics Letters* 19.7 (Apr. 1994), p. 454. ISSN: 0146-9592. DOI: 10.1364/OL.19.000454.

[119] Waleed Mohammed et al. 'Selective excitation of the LP11 mode in step index fiber using a phase mask'. In: *Optical Engineering* 45.7 (July 2006), p. 074602. DOI: 10.1117/1.2219425.

[120] J Carpenter, B C Thomsen and T D Wilkinson. 'Mode Division Multiplexing of Modes With the Same Azimuthal Index'. In: *IEEE Photonics Technology Letters* 24.21 (Nov. 2012), pp. 1969–1972. ISSN: 1041-1135. DOI: 10.1109/LPT.2012.2220538.

[121] Johannes von Hoyningen-Huene, Roland Ryf and Peter Winzer. 'LCoS-based mode shaper for few-mode fiber'. In: *Optics express* 21.15 (2013), pp. 18097–18110.

[122] Sergio G Leon-Saval et al. 'Multimode fiber devices with single-mode performance'. In: *Optics letters* 30.19 (2005), pp. 2545–2547.

[123] S Yerolatsitis, I Gris-Sánchez and T A Birks. 'Adiabatically-tapered fiber mode multiplexers'. In: *Optics express* 22.1 (2014), pp. 608–617.

[124] Nicolas K. Fontaine et al. 'Geometric requirements for photonic lanterns in space division multiplexing'. In: *Optics Express* 20.24 (Nov. 2012), p. 27123. ISSN: 1094-4087. DOI: 10.1364/OE.20.027123.

[125] Amado M. Velázquez-Benítez et al. 'Scaling photonic lanterns for space-division multiplexing'. In: *Scientific Reports* 8.1 (Dec. 2018), p. 8897. ISSN: 2045-2322. DOI: 10.1038/s41598-018-27072-2.

[126] T. A. Birks et al. 'The photonic lantern'. EN. In: *Advances in Optics and Photonics* 7.2 (Apr. 2015), p. 107. ISSN: 1943-8206. DOI: 10.1364/AOP.7.000107. arXiv: 1303.6810.

[127] Amado M Velázquez-Benitez et al. 'Scaling photonic lanterns for space-division multiplexing'. In: *Scientific reports* 8.1 (2018), p. 8897.

[128] Nicolas K. Fontaine et al. '30×30 MIMO Transmission over 15 Spatial Modes'. EN. In: *Optical Fiber Communication Conference Post Deadline Papers* 1 (Mar. 2015), Th5C.1. DOI: 10.1364/OFC.2015.Th5C.1.

[129] Sergio G Leon-Saval et al. 'Mode-selective photonic lanterns for space-division multiplexing'. In: *Optics express* 22.1 (2014), pp. 1036–1044.

[130] A. M. Velazquez-Benitez et al. 'Six mode selective fiber optic spatial multiplexer'. In: *Optics Letters* 40.8 (Apr. 2015), p. 1663. ISSN: 0146-9592. DOI: 10.1364/OL.40.001663.

[131] N.K. Fontaine et al. 'Mode-selective dissimilar fiber photonic-lantern spatial multiplexers for few-mode fiber'. In: 1 (2013), pp. 1221–1223. DOI: 10.1049/cp.2013.1680.

[132] K Miura Davis et al. 'Writing waveguides in glass with a femtosecond laser'. In: *Optics letters* 21.21 (1996), pp. 1729–1731.

[133] Robert R Thomson, Ajoy K Kar and Jeremy Allington-Smith. 'Ultrafast laser inscription: an enabling technology for astrophotonics'. In: *Optics express* 17.3 (2009), pp. 1963–1969.

[134] Nemanja Jovanovic et al. 'Integrated photonic building blocks for next-generation astronomical instrumentation I: the multimode waveguide'. In: *Optics Express* 20.15 (2012), pp. 17029–17043.

[135] Robert R Thomson et al. 'Ultrafast laser inscription of an integrated photonic lantern'. In: *Optics express* 19.6 (2011), pp. 5698–5705.

[136] Simon Gross et al. 'Three-dimensional ultra-broadband integrated tapered mode multiplexers'. In: *Laser and Photonics Reviews* 8.5 (Sept. 2014), pp. 81–85. ISSN: 18638899. DOI: 10.1002/lpor.201400078.

[137] Haoshuo Chen et al. 'A fully-packaged 3D-waveguide based dual-fiber spatial-multiplexer with up-tapered 6-mode fiber pigtails'. In: *2014 The European Conference on Optical Communication (ECOC)*. IEEE. 2014, pp. 1–3.

[138] Jean-François Morizur et al. 'Programmable unitary spatial mode manipulation'. In: *Journal of the Optical Society of America A* 27.11 (Nov. 2010), p. 2524. ISSN: 1084-7529. DOI: 10.1364/JOSAA.27.002524.

[139] Jesse Lu and Jelena Vučković. 'Objective-first design of high-efficiency, small-footprint couplers between arbitrary nanophotonic waveguide modes'. In: *Optics Express* 20.7 (Mar. 2012), p. 7221. ISSN: 1094-4087. DOI: 10.1364/OE.20.007221.

[140] N K Fontaine et al. 'Design of High Order Mode-Multiplexers using Multiplane Light Conversion'. In: *2017 European Conference on Optical Communication (ECOC)*. 2017, pp. 1–3. DOI: 10.1109/ECOC.2017.8346129.

[141] Guillaume Labroille et al. 'Mode selective 10-mode multiplexer based on multi-plane light conversion'. In: *Optical Fiber Communication Conference*. Optical Society of America. 2016, Th3E–5.

[142] Dan M Marom et al. 'Survey of photonic switching architectures and technologies in support of spatially and spectrally flexible optical networking'. In: *IEEE/OSA Journal of Optical Communications and Networking* 9.1 (2017), pp. 1–26.

[143] Pierre Wall et al. 'WSS switching engine technologies'. In: *OFC/NFOEC 2008-2008 Conference on Optical Fiber Communication/National Fiber Optic Engineers Conference*. IEEE. 2008, pp. 1–5.

[144] Steve Frisken et al. 'Flexible and grid-less wavelength selective switch using LCOS technology'. In: *2011 Optical Fiber Communication Conference and Exposition and the National Fiber Optic Engineers Conference*. IEEE. 2011, pp. 1–3.

[145] R Ryf et al. 'Wavelength-selective switch for few-mode fiber transmission'. In: *39th European Conference and Exhibition on Optical Communication (ECOC 2013)*. IET. 2013, pp. 1–3.

[146] D M Marom et al. 'Wavelength-selective switch with direct few mode fiber integration'. In: *Optics Express* 23.5 (2015), pp. 5723–5737.

[147] Joel Carpenter et al. '1x11 few-mode fiber wavelength selective switch using photonic lanterns'. In: *Optics Express* 22.3 (2014), pp. 2216–2221.

[148] Rajiv Ramaswami, Kumar Sivarajan and Galen Sasaki. *Optical networks: a practical perspective*. Morgan Kaufmann, 2009.

[149] D.C. Hanna et al. 'Continuous-wave oscillation of a monomode ytterbium-doped fibre laser'. In: *Electronics Letters* 24.17 (1988), p. 1111. ISSN: 00135194. DOI: 10.1049/el:19880755.

[150] R. Paschotta et al. 'Ytterbium-doped fiber amplifiers'. In: *IEEE Journal of Quantum Electronics* 33.7 (July 1997), pp. 1049–1056. ISSN: 00189197. DOI: 10.1109/3.594865.

[151] R H Stolen and E P Ippen. 'Raman gain in glass optical waveguides'. In: *Applied Physics Letters* 22.6 (1973), pp. 276–278.

[152] Mohammed N Islam. 'Raman amplifiers for telecommunications'. In: *IEEE Journal of selected topics in Quantum Electronics* 8.3 (2002), pp. 548–559.

[153] R Ryf et al. 'Mode-equalized distributed Raman amplification in 137-km few-mode fiber'. In: *2011 37th European Conference and Exhibition on Optical Communication*. 2011, pp. 1–3.

[154] Mina Esmaeelpour et al. 'Transmission over 1050-km few-mode fiber based on bidirectional distributed Raman amplification'. In: *Journal of Lightwave Technology* 34.8 (2016), pp. 1864–1871.

[155] Keang-Po Ho and Joseph M. Kahn. 'Mode-dependent loss and gain: statistics and effect on mode-division multiplexing'. In: *Optics Express* 19.17 (Aug. 2011), p. 16612. ISSN: 1094-4087. DOI: 10.1364/OE.19.016612.

[156] Nicolas K. Fontaine et al. 'Programmable Gain Equalizer for Multi-Core Fiber Amplifiers'. In: *Optical Fiber Communication Conference: Postdeadline Papers*. Washington, D.C.: OSA, Mar. 2014, Th5C.5. ISBN: 978-1-55752-994-7. DOI: 10.1364/OFC.2014.Th5C.5.

[157] Mitsumasa Nakajima et al. 'SDM-compatible dynamic gain equalizer using spatial and planar optical circuit'. In: *2017 Optical Fiber Communications Conference and Exhibition (OFC)*. IEEE. 2017, pp. 1–3.

[158] Yongmin Jung, Shaif-Ul Alam and David J. Richardson. 'Optical Amplifiers for Mode Division Multiplexing'. In: *Handbook of Optical Fibers*. Singapore: Springer Singapore, 2018, pp. 1–25. DOI: 10.1007/978-981-10-1477-2_49-1.

[159] Yongmin Jung et al. 'Reconfigurable modal gain control of a few-mode EDFA supporting six spatial modes'. In: *IEEE Photonics Technology Letters* 26.11 (2014), pp. 1100–1103.

[160] M Wada et al. 'Core-pumped 10-mode EDFA with cascaded EDF configuration'. In: *ECOC 2016; 42nd European Conference on Optical Communication*. VDE. 2016, pp. 1–3.

[161] K S Abedin et al. 'Amplification and noise properties of an erbium-doped multicore fiber amplifier'. In: *Optics express* 19.17 (2011), pp. 16715–16721.

[162] Jun Sakaguchi et al. '19-core MCF transmission system using EDFA with shared core pumping coupled via free-space optics'. In: *Opt. Express* 22.1 (Jan. 2014), pp. 90–95. DOI: 10.1364/OE.22.000090.

[163] H Ono et al. 'Recent progress on few-mode fiber amplifier'. In: *2016 IEEE Photonics Society Summer Topical Meeting Series (SUM)*. July 2016, pp. 74–75. DOI: 10.1109/PHOSST.2016.7548734.

[164] Y Jung et al. 'Cladding pumped few-mode EDFA for mode division multiplexed transmission'. In: *Opt. Express* 22.23 (Nov. 2014), pp. 29008–29013. DOI: 10.1364/OE.22.029008.

[165] Nicolas K. Fontaine et al. 'Multi-mode Optical Fiber Amplifier Supporting over 10 Spatial Modes'. In: *Optical Fiber Communication Conference Postdeadline Papers*. Washington, D.C.: OSA, Mar. 2016, Th5A.4. ISBN: 978-1-943580-08-8. DOI: 10.1364/OFC.2016.Th5A.4.

[166] Z S Eznaveh et al. 'Ultra-low DMG multimode EDFA'. In: *2017 Optical Fiber Communications Conference and Exhibition (OFC)*. Mar. 2017, pp. 1–3.

[167] S Takasaka et al. 'Increase of Cladding Pump Power Efficiency by a 19-Core Erbium Doped Fibre Amplifier'. In: *2017 European Conference on Optical Communication (ECOC)*. IEEE. 2017, pp. 1–3.

[168] S Jain et al. '32-core Inline Multicore Fiber Amplifier for Dense Space Division Multiplexed TransmissionSystems'. In: *ECOC 2016 - Post Deadline Paper; 42nd European Conference on Optical Communication*. 2016, pp. 1–3.

[169] Benjamin J Puttnam et al. '0.715 Pb/s Transmission over 2,009.6 km in 19-core cladding pumped EDFA amplified MCF link'. In: *Optical Fiber Communication Conference Postdeadline Papers 2019*. Optical Society of America, 2019, Th4B.1. DOI: 10.1364/OFC.2019.Th4B.1.

[170] Qiongyue Kang et al. 'Minimizing differential modal gain in cladding-pumped EDFAs supporting four and six mode groups'. In: *Optics Express* 22.18 (Sept. 2014), p. 21499. ISSN: 1094-4087. DOI: 10.1364/OE.22.021499.

[171] Y Wakayama et al. 'Novel 6-Mode Fibre Amplifier with Large Erbium-Doped Area for Differential Modal Gain Minimization'. In: *ECOC 2016; 42nd European Conference on Optical Communication*. 2016, pp. 1–3.

[172] Antonio Mecozzi, Cristian Antonelli and Mark Shtaif. 'Kramers–Kronig coherent receiver'. In: *Optica* 3.11 (Nov. 2016), p. 1220. ISSN: 2334-2536. DOI: 10.1364/OPTICA.3.001220.

[173] Xi Chen et al. 'Kramers–Kronig Receivers for 100-km Datacenter Interconnects'. In: *Journal of Lightwave Technology* 36.1 (Jan. 2018), pp. 79–89. ISSN: 0733-8724. DOI: 10.1109/JLT.2018.2793460.

[174] Joseph M. Kahn and Keang-Po Ho. 'Linear Propagation Effects in Mode-Division Multiplexing Systems'. In: *Journal of Lightwave Technology, Vol. 32, Issue 4, pp. 614-628* 32.4 (Feb. 2014), pp. 614–628.

[175] Peter J Winzer and Gerard J Foschini. 'MIMO capacities and outage probabilities in spatially multiplexed optical transport systems'. In: *Optics express* 19.17 (2011), pp. 16680–16696.

[176] C R S Fludger and T Kupfer. 'Transmitter Impairment Mitigation and Monitoring for High Baud-Rate, High Order Modulation Systems'. In: *ECOC 2016; 42nd European Conference on Optical Communication*. 2016, pp. 1–3.

[177] Ward Cheney and David Kincaid. 'Linear algebra: Theory and applications'. In: *The Australian Mathematical Society* 110 (2009).

[178] Per-Olov Löwdin. 'On the Non-Orthogonality Problem Connected with the Use of Atomic Wave Functions in the Theory of Molecules and Crystals'. In: *The Journal of Chemical Physics* 18.3 (Mar. 1950), pp. 365–375. ISSN: 0021-9606. DOI: 10.1063/1.1747632.

[179] Irshaad Fatadin, Seb J. Savory and David Ives. 'Compensation of Quadrature Imbalance in an Optical QPSK Coherent Receiver'. In: *IEEE Photonics Technology Letters* 20.20 (Oct. 2008), pp. 1733–1735. ISSN: 1041-1135. DOI: 10.1109/LPT.2008.2004630.

[180] T Tanimura et al. 'A simple digital skew compensator for coherent receiver'. In: *2009 35th European Conference on Optical Communication*. 2009, pp. 1–2.

[181] Seb J. Savory. 'Digital filters for coherent optical receivers'. In: *Optics Express* 16.2 (Jan. 2008), p. 804. ISSN: 1094-4087. DOI: 10.1364/OE.16.000804.

[182] J.J. Shynk. 'Frequency-domain and multirate adaptive filtering'. In: *IEEE Signal Processing Magazine* 9.1 (Jan. 1992), pp. 14–37. ISSN: 1053-5888. DOI: 10.1109/79.109205.

[183] Ruben Andres Soriano et al. 'Chromatic Dispersion Estimation in Digital Coherent Receivers'. In: *Journal of Lightwave Technology* 29.11 (June 2011), pp. 1627–1637. ISSN: 0733-8724. DOI: 10.1109/JLT.2011.2145357.

[184] F. Gardner. 'A BPSK/QPSK Timing-Error Detector for Sampled Receivers'. In: *IEEE Transactions on Communications* 34.5 (May 1986), pp. 423–429. ISSN: 0096-2244. DOI: 10.1109/TCOM.1986.1096561.

[185] M. Oerder and H. Meyr. 'Digital filter and square timing recovery'. In: *IEEE Transactions on Communications* 36.5 (May 1988), pp. 605–612. ISSN: 00906778. DOI: 10.1109/26.1476.

[186] John G Proakis and Masoud Salehi. *Digital communications*. Vol. 4. McGraw-hill New York, 2001.

[187] Roy G. H. van Uden et al. 'MIMO equalization with adaptive step size for few-mode fiber transmission systems'. In: *Optics Express* 22.1 (Jan. 2014), p. 119. ISSN: 1094-4087. DOI: 10.1364/OE.22.000119.

[188] D. Godard. 'Self-Recovering Equalization and Carrier Tracking in Two-Dimensional Data Communication Systems'. In: *IEEE Transactions on Communications* 28.11 (Nov. 1980), pp. 1867–1875. ISSN: 0096-2244. DOI: 10.1109/TCOM.1980.1094608.

[189] Pierre Comon and Christian Jutten. 'Handbook of Blind Source Separation, Independent Component Analysis and Applications'. In: (2010).

[190] A. Belouchrani et al. 'A blind source separation technique using second-order statistics'. In: *IEEE Transactions on Signal Processing* 45.2 (1997), pp. 434–444. ISSN: 1053587X. DOI: 10.1109/78.554307.

[191] Xiang Zhou et al. 'Transmission of 32-Tb/s Capacity Over 580 km Using RZ-Shaped PDM-8QAM Modulation Format and Cascaded Multimodulus Blind Equalization Algorithm'. In: *Journal of Lightwave Technology* 28.4 (Feb. 2010), pp. 456–465. ISSN: 0733-8724. DOI: 10.1109/JLT.2009.2032560.

[192] J. Yang, J.J. Werner and G.A. Dumont. 'The multimodulus blind equalization algorithm'. In: *Proceedings of 13th International Conference on Digital Signal Processing*. Vol. 1. IEEE, pp. 127–130. ISBN: 0-7803-4137-6. DOI: 10.1109/ICDSP.1997.627988.

[193] Bernard Widrow and Marcian E Hoff. *Adaptive switching circuits*. Tech. rep. Stanford Univ Ca Stanford Electronics Labs, 1960.

[194] Timothy M Schmidl and Donald C Cox. 'Robust frequency and timing synchronization for OFDM'. In: *IEEE transactions on communications* 45.12 (1997), pp. 1613–1621.

[195] Andrew Viterbi. 'Nonlinear estimation of PSK-modulated carrier phase with application to burst digital transmission'. In: *IEEE Transactions on Information theory* 29.4 (1983), pp. 543–551.

[196] John P Costas. 'Synchronous communications'. In: *Proceedings of the IRE* 44.12 (1956), pp. 1713–1718.

[197] Timo Pfau, Sebastian Hoffmann and Reinhold Noé. 'Hardware-efficient coherent digital receiver concept with feedforward carrier recovery for M-QAM constellations'. In: *Journal of Lightwave Technology* 27.8 (2009), pp. 989–999.

[198] José Manuel Delgado Mendinueta et al. 'Numerical Investigation of Equalization Enhanced Phase Noise Penalties for MQAM Modulations in Few-Mode Fiber Transmission with Time Domain Equalization'. In: *Advanced Photonics 2017 (IPR, NOMA, Sensors, Networks, SPPCom, PS)*. Washington, D.C.: OSA, July 2017, NeTu2B.1. ISBN: 978-1-943580-30-9. DOI: 10.1364/NETWORKS.2017.NeTu2B.1.

[199] Dawn K. Gifford et al. 'Optical vector network analyzer for single-scan measurements of loss, group delay, and polarization mode dispersion'. In: *Optical Society of America* 44.34 (2005), pp. 7282–7286. ISSN: 0003-6935. DOI: 10.1364/AO.44.007282. arXiv: arXiv:1011.1669v3.

[200] Gregory D. VanWiggeren, Ali R. Motamedi and Douglas M. Baney. 'Single-scan interferometric component analyzer'. In: *IEEE Photonics Technology Letters* 15.2 (2003), pp. 263–265. ISSN: 10411135. DOI: 10.1109/LPT.2002.806100.

[201] Simon Rommel et al. 'Few-mode fiber, splice and SDM component characterization by spatially-diverse optical vector network analysis'. In: *Optics Express* 25.19 (2017), pp. 22347–22361. ISSN: 1094-4087. DOI: 10.1364/OE.25.022347.

[202] Nicolas K. Fontaine et al. 'Characterization of Space-Division Multiplexing Systems using a Swept-Wavelength Interferometer'. In: *Optical Fiber Communication Conference/National Fiber Optic Engineers Conference 2013*. c. 2013, OW1K.2. ISBN: 978-1-55752-962-6. DOI: 10.1364/OFC.2013.OW1K.2.

[203] Koichi Iiyama, Lu-Tang Wang and Ken-Ichi Hayashi. 'Linearizing optical frequency-sweep of a laser diode for FMCW reflectometry'. In: *Journal of lightwave technology* 14.2 (1996), pp. 173–178.

[204] Changho Chong, Atsushi Morosawa and Tooru Sakai. 'High-speed wavelength-swept laser source with high-linearity sweep for optical coherence tomography'. In: *IEEE Journal of Selected Topics in Quantum Electronics* 14.1 (2008), pp. 235–242.

[205] Kazumasa Takada. 'High-Resolution OFDR with Incorporated Fiber-Optic Frequency Encoder'. In: *IEEE Photonics Technology Letters* 4.9 (Sept. 1992), pp. 1069–1072. ISSN: 19410174. DOI: 10.1109/68.157152.

[206] R. Passy et al. 'Experimental and theoretical investigations of coherent OFDR with semiconductor laser sources'. In: *Journal of Lightwave Technology* 12.9 (1994), pp. 1622–1630. ISSN: 07338724. DOI: 10.1109/50.320946.

[207] Tae-Jung Ahn, Ji Yong Lee and Dug Young Kim. 'Suppression of nonlinear frequency sweep in an optical frequency-domain reflectometer by use of Hilbert transformation'. In: *Applied Optics* 44.35 (Dec. 2005), p. 7630. ISSN: 0003-6935. DOI: 10.1364/AO.44.007630.

[208] Gregory D. VanWiggeren and Douglas M. Baney. 'Swept-wavelength interferometric analysis of multiport components'. In: *IEEE Photonics Technology Letters* 15.9 (2003), pp. 1267–1269. ISSN: 10411135. DOI: 10.1109/LPT.2003.816663.

[209] Simon Rommel et al. 'Measurement of Modal Dispersion and Group Delay in a Large Core Count Few-Mode Multi-Core Fiber'. In: *2018 European Conference on Optical Communication (ECOC)*. IEEE, Sept. 2018, pp. 1–3. ISBN: 978-1-5386-4862-9. DOI: 10.1109/ECOC.2018.8535556.

[210] U Glombitza and E Brinkmeyer. 'Coherent Frequency-Domain Reflectometry for Characterization of Singlemode Integratedoptical Waveguides'. In: *Journal of Lightwave Technology* 11.8 (1993), pp. 1377–1384. ISSN: 15582213. DOI: 10.1109/50.254098.

[211] Eric D. Moore and Robert R. McLeod. 'Correction of sampling errors due to laser tuning rate fluctuations in swept-wavelength interferometry'. In: *Optics Express* 16.17 (Aug. 2008), p. 13139. ISSN: 1094-4087. DOI: 10.1364/OE.16.013139.

[212] J. M. (Jonathan M.) Blackledge. *Digital signal processing : mathematical and computational methods, software development, and applications*, p. 813. ISBN: 1904275265.

[213] Matteo Frigo and Steven G Johnson. 'FFTW User ' s Manual'. In: *Library* March (2003).

[214] James E. Gentle. *Numerical linear algebra for applications in statistics*. Springer, 1998, p. 221. ISBN: 0387985425.

[215] B.L. Heffner. 'Automated measurement of polarization mode dispersion using Jones matrix eigenanalysis'. In: *IEEE Photonics Technology Letters* 4.9 (Sept. 1992), pp. 1066–1069. ISSN: 1041-1135. DOI: 10.1109/68.157151.

[216] Justus Bohn et al. 'Characterization of laser inscribed on-chip photonic lanterns with different core distances'. In: *2015 European Conference on Optical Communication (ECOC)*. IEEE, Sept. 2015, pp. 1–3. ISBN: 978-8-4608-1741-3. DOI: 10.1109/ECOC.2015.7341707.

[217] Brian J. Soller et al. 'High resolution optical frequency domain reflectometry for characterization of components and assemblies'. In: *Optics Express* 13.2 (2005), p. 666. ISSN: 1094-4087. DOI: 10.1364/OPEX.13.000666.

[218] T. Sakamoto et al. 'Low-loss and Low-DMD Few-mode Multi-core Fiber with Highest Core Multiplicity Factor'. In: *2016 Optical Fiber Communications Conference and Exhibition (OFC)* 1 (2016), Th5A.2. DOI: 10.1364/ofc.2016.th5a.2.

[219] Jun Sakaguchi et al. 'Spectrally-Efficient Seed-Lightwave-Distribution System using Space-Division-Multiplexed Distribution Channel for Multi-core 3-Mode-Multiplexed DP-64QAM Transmission'. In: *2017 European Conference on Optical Communication (ECOC)*. IEEE, Sept. 2017, pp. 1–3. ISBN: 978-1-5386-5624-2. DOI: 10.1109/ECOC.2017.8345848.

[220] Daiki Soma et al. 'Partial MIMO-based 10-Mode-Multiplexed Transmission over 81km Weakly-coupled Few-mode Fiber'. In: The Optical Society, Mar. 2017, p. M2D.4. DOI: 10.1364/ofc.2017.m2d.4.

[221] Clemens Koebele et al. '40km Transmission of Five Mode Division Multiplexed Data Streams at 100Gb/s with low MIMO-DSP Complexity'. In: *37th European Conference and Exposition on Optical Communications*. Washington, D.C.: OSA, Sept. 2011, Th.13.C.3. ISBN: 978-1-55752-931-2. DOI: 10.1364/ECOC.2011.Th.13.C.3.

[222] P. J. Winzer et al. 'Penalties from In-Band Crosstalk for Advanced Optical Modulation Formats'. In: *2011 37th European Conference and Exhibition on Optical Communication* 1 (2013), Tu.5.B.7. DOI: 10.1364/ecoc.2011.tu.5.b.7.

[223] Jun Sakaguchi et al. 'Large Spatial Channel (36-Core × 3 mode) Heterogeneous Few-Mode Multicore Fiber'. In: *Journal of Lightwave Technology* 34.1 (Jan. 2016), pp. 93–103. ISSN: 0733-8724. DOI: 10.1109/JLT.2015.2481086.

[224] Vincent Sleiffer et al. '73.7 Tb/s (96X3x256-Gb/s) mode-division-multiplexed DP-16QAM transmission with inline MM-EDFA'. In: *European Conference and Exhibition on Optical Communication*. Vol. 20. 26. 2012, Th.3.C.4. ISBN: 978-1-55752-950-3. DOI: 10.1364/ECEOC.2012.Th.3.C.4.

[225] Ezra Ip et al. 'Multiplexed Transmission over 10 × 50-km Spans of Few- Mode Fiber with a Gain-Equalized Few-Mode EDFA'. In: *Ofc* (2013), PDP5A.2.

[226] P. Sillard and D. Molin. 'A Review of Few-Mode Fibers for Space-Division Multiplexed Transmissions'. In: *39th European Conference and Exhibition on Optical Communication (ECOC 2013)*. Institution of Engineering and Technology, 2013, pp. 1–3. ISBN: 978-1-84919-759-5. DOI: 10.1049/cp.2013.1272.

[227] Roy G. H. van Uden et al. 'Time domain multiplexed spatial division multiplexing receiver'. In: *Optics Express* 22.10 (May 2014), p. 12668. ISSN: 1094-4087. DOI: 10.1364/OE.22.012668.

[228] Nevio. Benvenuto and Giovanni Cherubini. *Algorithms for communications systems and their applications*. J. Wiley, 2002. ISBN: 0470843896.

[229] Roy G. H. van Uden et al. '28-GBd 32QAM FMF Transmission With Low Complexity Phase Estimators and Single DPLL'. In: *IEEE Photonics Technology Letters* 26.8 (Apr. 2014), pp. 765–768. ISSN: 1041-1135. DOI: 10.1109/LPT.2014.2305450.

[230] Bernard Widrow and Eugene. Walach. *Adaptive inverse control : a signal processing approach*. IEEE Press, 2008, p. 508. ISBN: 9780470226094.

[231] Bernd Franz et al. 'High speed OFDM data transmission over 5 km GI-multimode fiber using spatial multiplexing with 2×4 MIMO processing'. In: *36th European Conference and Exhibition on Optical Communication*. IEEE, Sept. 2010, pp. 1–3. ISBN: 978-1-4244-8536-9. DOI: 10.1109/ECOC.2010.5621266.

[232] C. P. Tsekrekos et al. 'Design Considerations for a Transparent Mode Group Diversity Multiplexing Link'. In: *IEEE Photonics Technology Letters* 18.22 (Nov. 2006), pp. 2359–2361. ISSN: 1041-1135. DOI: 10.1109/LPT.2006.885282.

[233] H.R. Stuart. 'Dispersive multiplexing in multimode fiber'. In: *Optical Fiber Communication Conference. Technical Digest Postconference Edition. Trends in Optics and Photonics Vol.37 (IEEE Cat. No. 00CH37079)*. Vol. 3. Opt. Soc. America, pp. 305–307. ISBN: 1-55752-630-3. DOI: 10.1109/OFC.2000.868597.

[234] Sergio G. Leon-Saval, Alexander Argyros and Joss Bland-Hawthorn. 'Photonic lanterns: a study of light propagation in multimode to single-mode converters'. In: *Optics Express* 18.8 (2010), p. 8430. DOI: 10.1364/oe.18.008430.

[235] S Wittek et al. 'Mode-Multiplexed Transmission within and Across Mode Groups of a Multimode-Fiber'. In: *2019 Optical Fiber Communications Conference and Exhibition (OFC)*. Mar. 2019, pp. 1–3.

[236] Georg Rademacher et al. 'Long-Haul Transmission Over Few-Mode Fibers With Space-Division Multiplexing'. In: *Journal of Lightwave Technology* 36.6 (Mar. 2018), pp. 1382–1388. ISSN: 0733-8724. DOI: 10.1109/JLT.2017.2786671.

[237] N.S. Bergano and C.R. Davidson. 'Circulating loop transmission experiments for the study of long-haul transmission systems using erbium-doped fiber amplifiers'. In: *Journal of Lightwave Technology* 13.5 (May 1995), pp. 879–888. ISSN: 07338724. DOI: 10.1109/50.387805.

[238] Tobias Fehenberger et al. 'On Achievable Rates for Long-Haul Fiber-Optic Communications'. In: *Optics Express* 23.7 (2015), p. 9183. ISSN: 1094-4087. DOI: 10.1364/OE.23.009183. arXiv: 1501.01495.

[239] Chinlon Lin, L. G. Cohen and H. Kogelnik. 'Optical-pulse equalization of low-dispersion transmission in single-mode fibers in the 13–17-μm spectral region'. In: *Optics Letters* 5.11 (Nov. 1980), p. 476. ISSN: 0146-9592. DOI: 10.1364/OL.5.000476.

[240] Anders Bjarklev et al. 'Optimal design of single-cladded dispersion-compensating optical fibers'. In: *Optics Letters* 19.7 (Apr. 1994), p. 457. ISSN: 0146-9592. DOI: 10.1364/OL.19.000457.

[241] Haoshuo Chen and A. M. J. Koonen. 'Spatial Division Multiplexing'. In: Springer, Cham, 2017, pp. 1–48. DOI: 10.1007/978-3-319-42367-8_1.

[242] S Randel et al. 'Complexity analysis of adaptive frequency-domain equalization for MIMO-SDM transmission'. In: *39th European Conference and Exhibition on Optical Communication (ECOC 2013)*. 2013, pp. 1–3. DOI: 10.1049/cp.2013.1540.

[243] S Randel et al. 'First real-time coherent MIMO-DSP for six coupled mode transmission'. In: *2015 IEEE Photonics Conference (IPC)*. Oct. 2015, pp. 1–2. DOI: 10.1109/IPCon.2015.7323761.

[244] A M J Koonen et al. 'Silicon photonic integrated mode multiplexer and demultiplexer'. In: *IEEE Photonics Technology Letters* 24.21 (2012), pp. 1961–1964.

[245] N K Fontaine et al. 'Packaged 45-Mode Multiplexers for a 50-μm Graded Index Fiber'. In: *2018 European Conference on Optical Communication (ECOC)*. 2018, pp. 1–3. DOI: 10.1109/ECOC.2018.8535302.

[246] K Shibahara et al. 'Space-time coding-assisted transmission for mitigation of MDL impact on mode-division multiplexed signals'. In: *Optical Fiber Communication Conference*. Optical Society of America. 2016, Th4C–4.

[247] Elie Awwad, Ghaya Rekaya-Ben Othman and Yves Jaouën. 'Space-time coding schemes for MDL-impaired mode-multiplexed fiber transmission systems'. In: *Journal of Lightwave Technology* 33.24 (2015), pp. 5084–5094.

[248] *100G PSM4 Specification Version 2.0*. PSM4 MSA Group. 2014.

[249] Vijay Vusirikala. *A quick hop across the pond: Supercharging the Dunant subsea cable with SDM technology*. 2019.

[250] Tetsuya Hayashi et al. 'Field-Deployed Multi-Core Fiber Testbed'. In: 2019.

List of Acronyms

3DWG	3D-waveguide
ADC	analog-to-digital converter
AIR	achievable information rate
AOM	acousto-optic modulator
AR	achievable rate
ASE	amplified spontaneous emission
ASIC	application-specific integrated circuit
ASK	amplitude-shift keying
AWGN	additive white Gaussian noise
BER	bit error rate
BPD	balanced photo-detector
BPS	blind phase search
BPSK	binary phase-shift keying
CAGR	compound annual growth rate
CCF	coupled-core fibre
CD	chromatic dispersion
CMA	constant modulus algorithm
CPE	carrier phase estimation
CUT	channel under test
CW	continuous wave
DAC	digital-to-analog converter
DCF	dispersion compensated fibre
DD	direct detection
DD-LMS	decision-directed least mean square
DFB	distributed feedback
DGD	differential group delay
DMD	differential mode delay
DMG	differential modal gain
DMGD	differential mode group delay
DML	directly-modulated laser
DPLL	digital phase-locked loop
DRA	distributed Raman amplifier
DSF	dispersion-shifted fibre
DSO	digital sampling oscilloscope
DSP	digital signal processing
DUT	device under test
DWDM	dense wavelength-division multiplexing
ECL	external cavity laser
EDFA	erbium doped fibre amplifier
ENOB	effective number of bits
FDE	frequency domain equaliser
FEC	forward error-correction
FFT	fast Fourier transform
FIR	finite-impulse response
FMF	few-mode fibre
FM-MCF	few-mode multi-core fibre
FPGA	field-programmable gate array

FWM four-wave mixing

GD group delay
GFF gain flattening filter
GI graded-index
GNSE generalized nonlinear Schrödinger equation
GVD group velocity dispersion

HD-FEC hard-decision forward error-correction

IF intermediate frequency
IFFT inverse fast Fourier transform
IL insertion loss
IM-DD intensity-modulation and direct-detection
IO input/output
IOT Internet of Things
IP internet protocol
IQ-MOD IQ-modulator
IR infra-red
ISI intersymbol interference
ITU International Telecommunications Union

KK Kramers-Kronig
KKRX Kramers-Kronig receiver

LCoS liquid crystal on Silicon
LEAF large effective area fibre
LFSR linear-feedback shift register
LMS least means square
LO local oscillator
LP linearly polarised
LSPS loop-synchronised polarisation scrambler

M2M machine to machine
MCF multi-core fibre
MDG mode dependent gain
MDL mode dependent loss
MDM mode-division multiplexing
MEMS micro-electro-mechanical systems
MI mutual information
MIMO multiple-input multiple-output
MMA multi-modulus algorithm
MMF multi-mode fibre
MMSE minimum mean squared error
MPLC multi-plane light conversion
MZI Mach-Zehnder interferometer
MZM Mach-Zehnder modulator

NA numerical aperture
NF noise figure
NLSE nonlinear Schröding equation
NRZ non-return-to-zero

ODE ordinary differential equation
OEO optical-electrical-optical
OOK on-off keying
OPLL optical phase-locked loop
OSA optical spectrum analyser
OSNR optical signal-to-noise ratio
OTDR optical time-domain reflectometry
OTF optical tunable filter
OVNA optical vector network analyser

PAM pulse-amplitude modulation
PBC polarisation beam combiner
PBS polarisation beam splitter
PCVD plasma chemical vapor depostion
PD photodetector
PD-CRX polarisation-diverse coherent receiver
PDL polarisation dependent loss
PL photonic lantern
PLL phase-locked loop
PMD polarisation mode dispersion

PON passive-optical network
PRBS pseudorandom bit sequence
PSK phase-shift keying
PSP principal states of polarisation

QAM quadrature amplitude modulation
QPSK quadrature phase shift keying

ROADM reconfigurable optical add-drop multiplexer
RRC root-raised-cosine
RZ return-to-zero

SBS stimulated Brillouin scattering
SD-FEC soft-decision forward error-correction
SDM space-division multiplexing
SE spectral efficiency
SLM spatial light modulator
SMF single-mode fibre
SNR signal-to-noise ratio
SPM self-phase modulation
SRS stimulated Raman scattering
SSMF standard single-mode fibre
STL swept tunable laser
SVD singular value decomposition
SWI swept wavelength interferometry

TDE time domain equaliser
TDM-SDM time-domain multiplexed space-division multiplexing
TE transverse electric
TIA trans-impedance amplifier
TM transverse magnetic

VOA variable optical attenuator

WDM wavelength-division multiplexing
WGA weakly guiding approximation
WGN white Gaussian noise
WSS wavelength selective switch

XPM cross-phase modulation

List of Publications

Journal papers

[J1] Yetian Huang, Haoshuo Chen, Hanzi Huang, Zhengxuan Li, Nicolas K. Fontaine, Roland Ryf, Juan Carlos Alvarado Zacararias, Rodrigo Amezcua-Correa, **John van Weerdenburg**, Chigo Okonkwo, Ton Koonen, Yingxiong Song and Min Wang. 'Mode- and Wavelength-Multiplexed Transmission with Crosstalk Mitigation Using a Single Amplified Spontaneous Emission (ASE) Source'. In: *Photonics Research* (Accepted for publication).

[J2] Simon Rommel, **John van Weerdenburg**, José Manuel Delgado Mendinueta, Werner Klaus, Jun Sakaguchi, Juan José Vegas Olmos, Ton. Koonen, Yoshinari Awaji, Chig Okonkwo, Idelfonso Tafur Monroy and Naoya Wada. 'Polarization equalization in optical vector networkanalysis for SDM fiber characterization'. In: *IEEE Photonics Technol. Lett.* (Under review).

[J3] **J.J.A. van Weerdenburg**, S. Rommel, J.M. Delgado Mendinueta, W. Klaus, J. Sakaguchi, J.J. Vegas Olmos, A.M.J. Koonen, Y. Awaji, T. Tafur-Monroy, C.M. Okonkwo and N. Wada. 'Enhanced Modal Dispersion Estimation Enabled by Chromatic Dispersion Compensation in Optical Vector Network Analysis'. In: *Journal of Lightwave Technology* (Aug. 2019), p. 1. ISSN: 0733-8724. DOI: 10.1109/JLT.2019.2923112.

[J4] Laura Martin González, Sjoerd van der Heide, Xuwei Xue, **John van Weerdenburg**, Nicola Calabretta, Chigo Okonkwo, Josep Fàbrega and Michela Svaluto Moreolo. 'Programmable adaptive BVT for future optical metro networks adopting SOA-based switching nodes'. In: *Photonics* 5.3 (Aug. 2018), p. 24.

[J5] **John van Weerdenburg**, Roland Ryf, Juan Carlos Alvarado-Zacarias, Roberto Alejandro Alvarez-Aguirre, Nicolas Keith Fontaine, Haoshuo Chen, Rodrigo Amezcua-Correa, Yi Sun, Lars Grüner-Nielsen, Rasmus V Jensen, Robert Lingle, Ton Koonen and Chigo Okonkwo. '138-Tb/s Mode- and Wavelength-Multiplexed Transmission Over Six-Mode Graded-Index Fiber'. In: *J. Lightwave Technol.* 36.6 (Mar. 2018), pp. 1369–1374.

[J6] Jochem Verbist, Jing Zhang, Bart Moeneclaey, Wouter Soenen, **John van Weerdenburg**, Roy van Uden, Chigo Okonkwo, Johan Bauwelinck and Gunther Roelkens. 'A 40-GBd QPSK / 16-QAM Integrated Silicon Coherent Receiver'. In: *IEEE Photonics Technol. Lett.* 28.19 (Oct. 2016), pp. 2070–2073. ISSN: 10411135. DOI: 10.1109/LPT.2016.2582799.

[J7] J. Zhang, J. Verbist, B. Moeneclaey, **J.J.A. van Weerdenburg**, R.G.H. van Uden, H. Chen, J. van Campenhout, C.M. Okonkwo, X. Yin, J. Bauwelinck and G. Roelkens. 'Compact Low-Power-Consumption 28-Gbaud QPSK/16-QAM Integrated Silicon Photonic/Electronic Coherent Receiver'. In: *IEEE Photonics Journal* 8.1 (Feb. 2016), pp. 1–10. ISSN: 1943-0655. DOI: 10.1109/JPHOT.2015.2505609.

[J8] **John van Weerdenburg**, Amado Velàzquez-Benitez, Roy van Uden, Pierre Sillard, Denis Molin, Adrian Amezcua-Correa, Enrique Antonio-Lopez, Maxim Kuschnerov, Frans Huijskens, Hugo de Waardt, Ton Koonen, Rodrigo Amezcua-Correa and Chigo Okonkwo. '10 Spatial mode transmission using low differential mode delay 6-LP fiber using all-fiber photonic lanterns'. In: *Optics Express* 23.19 (Sept. 2015), p. 24759. ISSN: 1094-4087. DOI: 10.1364/OE.23.024759.

Conference contributions

[J9] Bin Chen, Yi Lei, Sjoerd van der Heide, **John van Weerdenburg**, Alex Alvarado and Chigo Okonkwo. 'First Experimental Verification of Improved Decoding of Staircase Codes using Marked Bits'. In: *Optical Fiber Communication Conference*. 1. Optical Society of America. Mar. 2019, pp. 2–4.

[J10] **John van Weerdenburg**, Simon Rommel, José Manuel Delgado Mendinueta, Werner Klaus, Jun Sakaguchi, Juan José Vegas Olmos, Ton Koonen, Yoshinari Awaji, Idelfonso Tafur Monroy and Chigo Okonkwo. 'Chromatic Dispersion Analysis and Compensation in a Large Core-Count Few-Mode Multi-Core Fiber Based on Optical Vector Network Analysis'. In: *Optical Fiber Communication Conference*. Optical Society of America. Mar. 2019, M1E–2.

[J11] Haoshuo Chen, Nicolas K. Fontaine, Roland Ryf, Juan Carlos Alvarado-Zacarias, **John van Weerdenburg**, Rodrigo Amezcua-Correa, Chigo Okonkwo and Ton Koonen. 'Optical Crosstalk Reduction using Amplified Spontaneous Emission (ASE)'. In: *2018 Optical Fiber Communications Conference and Exposition (OFC)*. IEEE. Mar. 2018, pp. 1–3.

[J12] Roland Ryf, **John van Weerdenburg**, Roberto A. Alvarez-Aguirre, Nicolas K. Fontaine, Rene-Jean Essiambre, Haoshuo Chen, Juan Carlos Alvarado-Zacarias, Rodrigo Amezcua-Correa, Ton Koonen and Chigo Okonkwo. 'White Gaussian Noise Based Capacity Estimate and Characterization of Fiber-Optic Links'. In: *2018 Optical Fiber Communications Conference and Exposition (OFC)*. Mar. 2018, pp. 1–3.

[J13] Sjoerd van der Heide, **John van Weerdenburg**, Marianne Biqot-Astruc, Adrian Amezcua-Correa, Jose Antonio-Lopez, Juan Carlos Alvarado-Zacarias, Huug de Waardt, Ton Koonen, Pierre Sillard, Rodrigo Amezcua-Correa and Chigo Okonkwo. 'Single Carrier 1 Tbit/s Mode-Multiplexed Transmission Over Graded-Index 50u Core Multi-Mode Fiber Employing Kramers-Kronig Receivers'. In: *2018 European Conference on Optical Communication (ECOC)*. IEEE. IEEE, Sept. 2018, pp. 1–3. ISBN: 978-1-5386-4862-9. DOI: 10.1109/ECOC.2018.8535491.

[J14] **John van Weerdenburg**, Roland Ryf, Roberto Alvarez-Aguirre, Nicolas K. Fontaine, René-Jean Essiambre, Haoshuo Chen, Juan Carlos Alvarado-Zacarias, Rodrigo Amezcua-Correa, Simon Gross, Nicolas Riesen, Michael Withford, David W. Peckham, Alan McCurdy, Robert Lingle, Ton Koonen and Chigo Okonkwo. 'Mode-multiplexed 16-QAM transmission over 2400-km large-effective-area depressed-cladding 3-mode fiber'. In: *2018 Optical Fiber Communications Conference and Exposition (OFC)*. IEEE. Mar. 2018, pp. 1–3.

[J15] N.K. Fontaine, H. Chen, R. Ryf, D. Neilson, J.C. Alvarado-Zacarias, **J.J.A. van Weerdenburg**, R. Amezcua-Correa, C.M. Okonkwo and J. Carpenter. 'Programmable Vector Mode Multiplexer'. In: *2017 European Conference on Optical Communication (ECOC)*. Sept. 2017, pp. 1–3. DOI: 10.1109/ECOC.2017.8346099.

[J16] **John van Weerdenburg**, Roland Ryf, Juan Carlos Alvarado-Zacarias, Roberto A. Alvarez-Aguirre, Nicolas K. Fontaine, Haoshuo Chen, Rodrigo Amezcua-Correa, Ton Koonen and Chigo Okonkwo. '138 Tbit/s transmission over 650 km graded-index 6-mode fiber'. In: *2017 European Conference on Optical Communication (ECOC)*. IEEE. Sept. 2017, pp. 1–3.

[J17] **John van Weerdenburg**, Alex Alvarado, Juan Carlos Alvarado-Zacarias, Enrique Antonio-Lopez, Jochem Bonarius, Denis Molin, Marianne Bigot-Astruc, Ton Koonen, Adrian Amezcua-Correa, Pierre Sillard, Rodrigo Amezcua-Correa and Chigo Okonkwo. 'Spatial pulse position modulation for multi-mode transmission systems'. In: *2017 Optical Fiber Communications Conference and Exhibition (OFC)*. Mar. 2017, pp. 1–3.

[J18] Wang Miao, **John van Weerdenburg**, Roy van Uden, Huug de Waardt, Ton Koonen, Chigo Okonkwo and Nicola Calabretta. 'Low Latency Optical Label Switched Add-Drop Node for Multi-Tb/s Data Center Interconnect Metro Networks'. In: *ECOC 2016; 42nd European Conference on Optical Communication*. VDE. Sept. 2016, pp. 1–3. ISBN: 9783800742745.

[J19] Wang Miao, **John van Weerdenburg**, Roy van Uden, Huug de Waardt, Ton Koonen, Chigo Okonkwo and Nicola Calabretta. 'Optical label switched add-drop node for low latency and high capacity data center interconnect metro networks'. In: Nov. 2016.

[J20] **John van Weerdenburg**, Amado Velázquez-Benítez, Roy van Uden, Enrique Antonio-Lopez, Pierre Sillard, Denis Molin, Marianne Bigot-Astruc, Adrian Amezcua-Correa, Frans Huijskens, Frank Achten, Huug de Waardt, Ton Koonen, Rodrigo Amezcua Correa and Chigo Okonkwo. '10 Spatial Mode Transmission over 40km 50μm Core Diameter Multimode Fiber'. In: *Optical Fiber Communication Conference*. Washington, D.C.: OSA, Mar. 2016, Th4C.3. ISBN: 978-1-943580-07-1. DOI: 10.1364/OFC.2016.Th4C.3.

[J21] **John van Weerdenburg**, Roy van Uden, Eric Sillekens, Huug de Waardt, Ton Koonen and Chigo Okonkwo. 'Cluster Analysis of Received Constellations for Optical Performance Monitoring'. In: *ECOC 2016; 42nd European Conference on Optical Communication; Proceedings of*. c. VDE. Sept. 2016, pp. 779–781. ISBN: 9783800742745.

[J22] **John van Weerdenburg**, Enrique Antonio-lopez, Juan Carlos Alvarado-zacarias, Denis Molin, Marianne Bigot-Astruc, Roy van Uden, Huug de Waardt, Ton Koonen, Rodrigo Amezcua-Correa, Pierre Sillard and Chigo Okonkwo. 'Exploiting Selective Excitation of Strongly Coupled Modes to Reduce DMGD in Multi-mode Transmission Systems'. In: *42nd European Conference and Exhibition on Optical Communications*. 1. VDE. Sept. 2016, pp. 292–294. ISBN: 9783800742745.

[J23] Jochem Verbist, Jing Zhang, Bart Moeneclaey, Wouter Soenen, **John van Weerdenburg**, Roy van Uden, Chigo Okonkwo, Xin Yin, Gunther Roelkens and Johan Bauwelinck. 'A 40 GBaud Integrated Silicon Coherent Receiver'. In: *European Conference On Integrated Optics (ECIO)*. Warsaw, May 2016, pp. 22–23.

[J24] Dawei Yu, **John van Weerdenburg**, Eric Silekens, Roy. van Uden, Ming Tang, Deming Liu, Amado Velazquez-Benitez, Pierre Sillard, Denis Molin, Marianne Bigot-Astruc, Rodrigo Amezcua Correa, Huug de Waardt, Ton Koonen, Songnian Fu and Chigo Okonkwo. 'Trellis Coded Modulation Transmission over 40km 6-LP Mode Fiber'. In: *Optical Fiber Communication Conference*. Vol. 1. Washington, D.C.: OSA, Mar. 2016, Th4C.5. ISBN: 978-1-943580-07-1. DOI: 10.1364/OFC.2016.Th4C.5.

[J25] Eric Sillekens, Roy van Uden, **John van Weerdenburg**, Maxim Kuschnerov, Huug de Waardt, Ton Koonen and Chigo Okonkwo. 'Experimental demonstration of 8 state Turbo Trellis coded modulation employing 8 phase shift keying'. In: *2015 European Conference on Optical Communication (ECOC)*. Vol. 2015-Novem. IEEE. IEEE, Sept. 2015, pp. 1–3. ISBN: 978-8-4608-1741-3. DOI: 10.1109/ECOC.2015.7341943.

[J26] **J.J.A. van Weerdenburg**, A..M. Velazquez-Benitez, R.G.H. van Uden, P. Sillard, D. Molin, A. Amezcua-Correa, J.E. Antonio-Lopez, M. Kuschnerov, F.M. Huijskens, H. de Waardt, A.M.J. Koonen, R. Amezcua-Correa and C.M. Okonkwo. '10 Spatial mode transmission over low differential mode group delay fibre employing all-fibre photonic lanterns'. In: *2015 European Conference on Optical Communication (ECOC)*. Vol. 2015-Novem. 1. IEEE, Sept. 2015, pp. 1–3. ISBN: 978-8-4608-1741-3. DOI: 10.1109/ECOC.2015.7341841.

[J27] Jochem Verbist, Jing Zhang, Bart Moeneclaey, **John van Weerdenburg**, Roy van Uden, Chigo Okonkwo, Xin Yin, Johan Bauwelinck and Gunther Roelkens. '112 Gbit/s single-polarization silicon coherent receiver with hybrid-integrated BiCMOS linear TIA'. In: *European Conference on Optical Communication, ECOC*. Vol. 2015-Novem. IEEE, Sept. 2015, pp. 1–3. ISBN: 9788460817413. DOI: 10.1109/ECOC.2015.7341771.

[J28] Dawei Yu, Songnian Fu, **John van Weerdenburg**, Zizheng Cao, Ming Tang, Perry Shum, Deming Liu, Ian Giles, Ton Koonen and Chigo Okonkwo. 'Experimental Characterization of Rayleigh Backscattering in Few-Mode Fiber Using All-Fiber Photonic Lanterns'. In: *Asia Communications and Photonics Conference 2015*. c. Washington, D.C.: OSA, Nov. 2015, AM2B.4. ISBN: 978-1-943580-06-4. DOI: 10.1364/ACPC.2015.AM2B.4.

Acknowledgements

As I am writing this last part of my thesis, I am thinking back on the path travelled to arrive were I am today. On this journey, I have received support from numerous people, for which I would like to express my gratitude in this section.

Just as it is difficult to predict the next main driver for future bandwidth demand, I would not have foreseen me finishing a PhD in optical fibre communications. My interest for this field was raised during one of my last bachelor courses, leading to the broadband telecommunications master track. After one of the lectures of dr.ir. Huug de Waardt, I contacted him for possibilities of an internship abroad, preferably South Korea. However, Huug convinced me that Nokia Siemens Networks in Munich would be a better choice. Unfortunately, due to a reorganization, my assignment was cancelled. Not long thereafter, he managed to arrange a project at ADVA Optical Networking in Meiningen. Not the most exciting place to live, but joining the team of dr.-Ing. Micheal Eiselt definitely was. Huug, thank you for arranging this headstart into the field of optical communications, and supervision of my master's and PhD.

Barely back in Eindhoven, dr. Chigo Okonkwo offered me a graduation assignment. Some ambitious, and perhaps slightly ridiculous plan to exceed his recently established transmission record. In the end, his record managed to survive, but the project definitely resulted in some noticeable results. During the many hours we spent in the lab, I got to know Chigo as a supervisor who can be excited about the smallest steps of progress and at the same time motivates you to reach for the best possible result. He always managed to support me in whatever way possible, whether it was by thoroughly criticising my papers, managing equipment, or arranging internships. This thesis would never be realised without the dedication of Chigo, for which I will be ever grateful. Chigo's inexhaustible enthusiasm made it an easy task to convince students to join his group for an internship or graduation assignment, which greatly contributed to the great working atmosphere. I would like to thank Sjoerd van der Heide in particular for the many discussions, joint experimental work, and enjoyable conference trips.

Another key person for my PhD is prof.ir. Ton Koonen, who managed the general direction of the research and despite his busy schedule made the time to comment on my papers, conference contributions, and this thesis. Ton, thank you for your support and offering me this position in your group. Furthermore, I would like to thank the secretary of the group, José Hakkens-Jansen, for managing the bureaucracy around this project. I would likely have missed an important deadline without her reminders.

'A good start is half the battle' also holds for a PhD. In a very short time, dr. Vincent Sleifer and dr. Roy van Uden trained me to take over their work of the Mode Gap project and run the lab by myself. Not long thereafter, dr. Fausto Gomez-Agiz joined the group for a year. His experience from industry was a valuable source for practical solutions to many of the problems encountered in the lab. Also, the temporary position held by Jochem Bonarius-de Hoop gave some great insight into the complexity of the digital signal processing algorithms. For all information theory related questions, I could always ask dr. Alex Alvarado who together with Chigo formed a bridge between the ECO and SPS groups. I also appreciated and enjoyed the discussions and brainstorms with dr. Simon Rommel which greatly improved the research presented in this thesis.

Without the novel fibres designed by dr. Pierre Sillard and his group at Prysmian and the mode multiplexers fabricated by the group of dr. Rodrigo Amezcua Correa at the CREOL group of the university of Central Florida this research would not have been as successful. Thank you for providing the components and for the many discussions. I would like to thank dr. Amado Velázquez-Benétez and Juan-Carlos Alvarado Zacarias in particular for fabricating the photonic lanterns and close collaboration.

During my PhD, I spend some time outside TU/e, at two renowned research labs. The first being Nokia Bell Labs in Crawford Hill, where I had the opportunity to talk to many researchers that are typically too busy at conferences and gain a closer look at their research. I also managed to obtain strong results for this thesis, which would not have been possible without dr. Roland Ryf. Outside the slightly unconventional working hours of Roland, I could always count on support from dr. Nicolas Fontaine and dr. Haoshuo Chen. Although most time was spent in the lab, I would like to thank to Nick and his wife Maxine for hosting me in their house.

My second internship brought me to the other side of the planet, at the National Institute of Information and Communications Technology (NICT) in Tokyo. With great support from Dr. José Manuel Delgado Mendinueta and dr. Werner Klaus, I enjoyed every minute spent in the Photonic Network System Group of dr. Naoya Wada. Outside "office hours" I was always welcome to join dr. Benjamin Puttnam, dr. Ruben Luís, dr. Georg Rademacher, dr. Tobias Eriksson and their partners for some social activities. どうもありがとうございます。

Het leven van een PhD student bestaat meestal uit lange dagen die niet altijd stressvrij verlopen. Gelukkig kon ik daarom rekenen op mijn Bestuursgenoten van het 53e die mij soms uit het lab sleepten voor onvergetelijke bestuursweekenden, maandelijkse borrel of andere activiteiten. Bedankt daarvoor en excuses voor de

keren die ik heb gemist vanwege deadlines. Daarnaast ben ik blij deel uit te maken van Electrical Engineering generatie 2007. Gezamenlijk blokken voor de lastige vakken, organiseren van vele activiteiten of gezellig aan de bar van het Walhalla zitten zorgden voor een onvergetelijke tijd aan de TU/e.

Als laatste, maar zeker niet het onbelangrijkste wil ik mijn ouders bedanken. Al meer dan dertig jaar kan ik op ze rekenen en staan ze voor mij klaar. Altijd kan ik terecht voor advies en hulp, maar ben ik ook vrij om mijn eigen keuzes te maken. Ook al is dat soms haaks op hun eigen belang. Samen met mijn broertje Niels zorgden zij ervoor dat ik Wamel altijd als warm thuis kan beschouwen waar ik weer even tot rust kon komen of toch nog even wat werk af te maken.

Curriculum Vitae

J.J.A. (John) van Weerdenburg was born on October 17, 1987 in West Maas en Waal, the Netherlands. He received his B.Sc. And M.Sc. in Electrical Engineering from Eindhoven University of Technology (TU/e) in 2012 and 2015, respectively. His master's thesis was entitled "Mode Selective, Full Mode Mixed Launching in Multi-mode Fiber Transmission Systems" was conducted at the electro-optical communications (ECO) group at TU/e. He also obtained the Broadband Telecommunications Technologies certificate as part of his master's studies.

From September 2015, he started a PhD project in the electro-optical communications (ECO) group at Eindhoven University of Technology of which the results are presented in this dissertation. His research has been funded by the Dutch research funding organization, Nederlandse Organisatie voor Wetenschappelijk onderzoek (NWO) Photonics Graduate program. His research interests are focused on the combination of novel fibers and components with digital signal processing to achieve high capacity optical transmission.

He has (co-)authored more than 25 publications in top scientific journals and international conferences. His work was selected for the Corning Outstanding Student Paper Competition in 2018. He has served as a reviewer for IEEE Photonics Technology Letters and the IEEE/OSA Journal of Lightwave Technology and is a student member of IEEE and OSA.